THE SINTHESYS AND CHARACTERIZATION OF GLASS-CERAMIC BASED ON TERARY SYSTEM MgO-B_2O_3 SiO_2

Urban Došler

Doctoral Dissertation
Jožef Stefan International Postgraduate School
Ljubljana, Slovenia, February 2011

Evaluation Board:

Prof. Dr. Dragoljub Uskoković,Principal Research Fellow, Institute of Technical Sciences of SASA, Knez-Mihailova 35/IV P.O. BOX 377, 11000 Belgrade, Serbia

Assis. Prof. Dr. Miran Čeh, Nanostructured Materials Department, Jožef Stefan Institute, Jamova 39, 1000 Ljubljana, Slovenia

Assis.Prof. Dr. Boštjan Jančar, Advanced Materials Department, Jožef Stefan Institute, Jamova 39, 1000 Ljubljana, Slovenia

MEDNARODNA PODIPLOMSKA ŠOLA JOŽEFA STEFANA
JOŽEF STEFAN INTERNATIONAL POSTGRADUATE SCHOOL

Urban Došler

THE SINTHESYS AND CHARACTERIZATION OF GLASS-CERAMIC BASED ON TERARY SYSTEM $MgO-B_2O_3$ SiO_2

Doctoral Dissertation

SINTEZA IN KARAKTERIZACIJA STEKLO-KERAMIKE NA OSNOVI TERNARNEGA SISTEMA $MgO-B_2O_3$ SiO_2

Doktorska disertacija

Supervisor: Prof. Dr. Danilo Suvorov

Co-Supervisor: Dr. Marjeta Maček Kržmanc

Ljubljana, Slovenia, February 2011

Table of Contents

Abstract

The past fifteen years has seen the rapid development of various wireless communication devices, which operate at microwave or milimeterwave frequencies (mobile phones, wireless local-area networks (LAN), Bluetooth, etc.). At the same time, this progress has stimulated the development of new materials and process technologies, which enable the size reduction and increased functionality of electronic components. Low-temperature co-fired ceramic (LTCC) technology is one of the most promising approaches for fabrication of low-cost, miniaturised and integrated electronic components. Due to simultaneous co-firing of the substrates and electrodes the most commonly used dielectric substrates are based on glass-ceramics materials. In spite of very advanced features of the LTCC technology, the development of new LTCC modules is accompanied by several challenges and new materials that could fulfil various demands. In the scope of this dissertation $MgO\text{-}B_2O_3\text{-}SiO_2$ (MBS) based glass and its transformation to glass-ceramics was systematically investigated in order to evaluate this material for potential dielectric LTCC substrate applications. Among the compounds that are expected to crystallize from the $MgO\text{-}B_2O_3\text{-}SiO_2$ glass the borates ($Mg_2B_2O_5$, $Mg_3B_2O_6$) have not been so intensively investigated in terms of dielectric properties as silicates ($MgSiO_3$, Mg_2SiO_4). However, the knowledge of the dielectric properties of individual crystalline components is important for the interpretation of the properties of the $MgO–B_2O_3–SiO_2$ glass-ceramics. From this reason the first part of the dissertation is dedicated to the synthesis, sintering and dielectric characterization of $Mg_2B_2O_5$ and $Mg_3B_2O_6$ ceramics. $Mg_2B_2O_5$ (6.2-7.0) and $Mg_3B_2O_6$ (6.8 - 7.4) did not differ significantly in permittivity, while nearly 10-times difference was observed in Qxf-values. With regard to the Qxf values $Mg_3B_2O_6$ (240 000 GHz) surpasses the $Mg_2B_2O_5$ ceramics, which exhibited Qxf-values 10 000-30 000 GHz. The microstructural characteristics and the synthesis conditions for the preparation of high-Q $Mg_3B_2O_6$ ceramics was investigated in details. Scanning electron microscopy of the $Mg_3B_2O_6$ ceramics sintered at 1310 °C revealed the presence of anisotropic, exaggeratedly grown grains with a crystallographic fault that extends along the direction of the anisotropy. The anisotropic grains were examined by electron backscatter diffraction (EBSD). The analysis of the Kikuchi pattern showed that the crystallographic fault is a (011) twinning plane.

The control over the microstructure and dielectric properties of the glass-ceramics is

possible when the nucleation and crystallization processes are well understood. The overall crystallization processes in MBS glass were studied by means of non-isothermal analysis technique, X-ray diffraction and scanning electron microscopy. For MBS glass nucleation occurred in the temperature range from 600 to 750 °C with the maximum nucleation rate at 700 °C, whereas the nucleation and crystal growth processes overlapped at 700 ≤ T ≤ 750 °C. The analyses of the non-isothermal data by the most common models (Ozawa, Kissinger, Matusita, Ozawa-Chen, Šatawa) revealed that the crystallization of $Mg_2B_2O_5$ was three-dimensional bulk with diffusion controlled crystal growth rate with n = m = 1.5 and activation energy for crystallization (E) of 420-450 kJ/mol. The addition of TiO_2 nucleating agent to the MBS glass in an amount of 10 wt.% was found to facilitate the formation of nuclei and changed the crystallization mechanism to bulk crystallization with an increasing number of nuclei (m = 3, n = 4).

The crystallization product obtained during non-isothermal experiment differed from that obtained after isothermal heat-treatment at the temperatures higher than 950 °C. In the time-scale of dynamic differential scanning calorimetry (DSC) measurement only $Mg_2B_2O_5$ crystallize, while the silicon remained in the glassy matrix till the melting. In contrast, during isothermal heat-treatment, the main crystalline phases of $Mg_2B_2O_5$ and $MgSiO_3$ appeared at 800 and 950 °C, respectively. Warwickite ($Mg_3TiB_2O_8$) and boron doped rutile ($TiB_{0.024}O_2$) phase additionally crystallized in TiO_2-added MBS glass at 1000 °C.

The addition of TiO_2 nucleating agent was found to increase the permittivity and improve the Qxf-values. The permittivity increased from 6.1 in MBS glass to 6.9 in MBS Glass with 10 wt.% of TiO_2. The improvement of the Qxf-values, which reached the maximum value of 16 5000 GHz in TiO_2-added glass-ceramics was ascribed to the enhanced crystallization caused by the TiO_2 addition. The results of dielectric characterization showed that MgO-B_2O_3-SiO_2 based glass-ceramics in some respect surpass the commercially used glass-ceramics substrates.

Povzetek

Zadnjih petnajst let je zaznamoval hiter razvoj različnih brezžičnih komunikacijskih naprav, ki delujejo v mikro oziroma milimetrskih valovnih frekvencah (mobilni telefoni, brezžična omrežja lokalnega območja (LAN), Bluetooth, itd.). Hkrati pa je ta napredek spodbudil razvoj novih materialov in procesne tehnologije, ki omogoča zmanjšanje velikosti in večjo funkcionalnost elektronskih komponent. Tehnologija nizko temperaturne sočasno sintrane keramike (LTCC) omogoča izdelavo nizko cenovnih, miniaturiziranih in integriranih elektronskih komponent. Zaradi sočasnega žganja substratov z elektrodami se najpogosteje uporabljajo dielektrični substrati, ki temeljijo na steklo-keramičnih materialih. Kljub zelo napredni LTCC tehnologiji, je razvoj novih LTCC modulov odvisen od številnih izzivov in novih materialov, ki lahko izpolnijo željene zahteve. V sklopu moje disertacije sem natančno raziskal steklo in pripadajočo steklo-keramiko sistema MgO-B_2O_3-SiO_2 (MBS) z namenom dokazati potencial tega materiala kot dielektričnega substrata z možnostjo uporabe v LTCC tehnologiji. Med spojinami, ki kristalizirajo v sistemu MBS stekla, so dielektrične lastnosti magnezijevih boratov ($Mg_2B_2O_5$, $Mg_3B_2O_6$) slabše raziskane kot magnezijevi silikati ($MgSiO_3$, Mg_2SiO_4). Vendar pa je poznavanje dielektričnih lastnosti posameznih kristalnih spojin, pomembno za interpretacijo steklo-keramičnih lastnosti celotnega ternarnega MBS sistema. Zaradi tega razloga je prvi del disertacije namenjen sintezi, sintranju in dielektrični karakterizaciji $Mg_2B_2O_5$ in $Mg_3B_2O_6$ keramiki. Dielektrična konstanta $Mg_2B_2O_5$ (6,2 – 7,0) in $Mg_3B_2O_6$ (6,8 – 7,4) se bistveno ne razlikuje, medtem ko je razlika v Qxf vrednostih 10 kratna. Qxf vrednosti $Mg_3B_2O_6$ keramike (240 000 GHz) močno presegajo Qxf vrednosti $Mg_2B_2O_5$ keramike, ki so v območju med 10 000 in 30 000 GHz. Podrobno smo raziskali mikrostrukturne karakteristike in sintezne pogoje za pripravo $Mg_3B_2O_6$ keramike z visokimi Q vrednostmi. Z vrstičnim elektronskim mikroskopom smo $Mg_3B_2O_6$ keramiki sintrani pri 1310 °C odkrili prisotnost pretirane rasti anizotropnih zrn s kristalografsko napako vzdolž anizotropne smeri. Anizotropna zrna so bila raziskana s povratno sipano elektronsko difrakcijo (EBSD) s katero smo s pomočjo analize Kikuchi-jevih črt dokazali dvojčično ravnino (011). Pregled nad mikrostrukturnim in dielektričnim lastnostim steklo-keramike je možen le, če zelo dobro poznamo procese nukleacije in kristalizacije stekla. S pomočjo ne-izotermnih analiznih tehnik, rentgenske difrakcije in vrstične elektronske mikroskopije smo proučevali nukleacijske in kristalizacijske procese. Nukleacija stekla v MBS sistemu poteka v

temperaturnem območju od 600 do 750 °C, z najvišjo stopnjo nukleacije pri 700 °C, medtem ko se proces rasti nukleusov in kristalov prekriva v območju med 700 in 750 °C. Analize ne-izotermnih, najpogosteje uporabljenih modelov (Ozawa, Kissinger, Matusita, Ozawa-Chen in Šatava) kažejo na volumsko kristalizacijo $Mg_2B_2O_5$ keramike z difuzijsko kontrolirano rastjo kristalov, ki se pojavijo pri konstantnem številu nukleusov in sicer je n = m = 1,5. Aktivacijska energija kristalizacije (E) volumskih vzorcev je med 420-450 kJ/mol. Z dodatkom 10 ut.% TiO_2 nukleacijskega sredstva MBS steklu smo pospešili tvorbo jeder in s tem spremenil kristalizacijski mehanizem v volumsko kristalizacijo z naraščajočim številom jeder (m = 3, n = 4). Sestava kristalizacijskih faz pridobljenih v ne-izotermnih eksperimentih je drugačna kot tista, ki nastane v izotermnih pogojih nad 950 °C. Pri diferencialni dinamični kalorimetriji (DSC) kristalizira samo $Mg_2B_2O_5$, medtem ko po taljenju silicij ostane v matrici stekla. Med izotermno toplotno obdelavo $Mg_2B_2O_5$ in $MgSiO_3$ kristalizirata kot primarni fazi pri ≈ 800 oziroma ≈ 950 °C. Pri vzorcih MBS stekla z več kot 1 ut.% TiO_2 pri temperaturah višjih od 1000 °C sta bila z rentgensko praškovno difrakcijo dokazani dodatni fazi: warwickite ($Mg_3TiB_2O_8$) in rutil dopiran z borom ($TiB_{0,024}O_2$). Ugotovili smo, da smo z dodatkom TiO_2, povečali dielektrično konstanto in izboljšali Qxf vrednosti. Dielektrična konstanta je iz 6,1 v MBS steklu narasla na 6.9 v MBS steklu z dodatkom 10 ut.% TiO_2. Izboljšanje Qxf vrednosti, ki so dosegle najvišjo vrednost 16 500 GHz pri vzorcu MBS stekla z 10 ut.% dodatka TiO_2 pripisujemo povišani stopnji kristalizacije zaradi dodanega nukleacijskega sredstva. Rezultati dielektričnih lastnosti kažejo, da je steklo-keramika MBS sistema v določenih pogledih presegla komercialno uporabne steklo-keramične substrate.

Abbreviations

LAN	=	Local Area Network
GPS	=	Global Positioning System
ITS	=	Intelligent Transport System
LTCC	=	Low Temperature Co-fired Ceramic
ASTM	=	American Society for Testing and Materials
IC	=	Integrated Circuit
MCM	=	Multi-Chip Module
MCIC	=	Multi-Chip Integrated Circuit
HTCC	=	High Temperature Co-fired Ceramic
TCE	=	Thermal Coefficient of Expansion
P_i	=	Interfacial or Space Polarization
P_d	=	Dipole Polarization
P_a	=	Atomic or Ionic Polarization
P_e	=	Electronic Polarization
UV	=	Ultraviolet
CVD	=	Chemical Vapour Deposition
IR	=	Infrared
MBS	=	$MgO\text{-}B_2O_3\text{-}SiO_2$
XRD	=	X-ray Powder Diffraction
SEM	=	Scanning Electron Microscope
TEM	=	Transmission Electron Microscope
EBSD	=	Electron Back Scatter Diffraction
DSC	=	Differential Scanning Calorimetry
DTA	=	Differential Thermal Analyses
STA	=	Simultaneous Thermal Analyses
TG	=	Thermogravimetry
MS	=	Mass Spectrometry
DSC	=	Differential Scanning Calorimetry
JMA	=	Johnson-Mehl-Avrami
RF	=	Radio Frequency

LCR = Inductance, Capacitance, and Resistance Meter

MW = Microwave

ICP = Inductively Coupled Plasma

AES = Atomic Emission Spectroscopy

EDS = Energy Dispersive Spectroscopy

1 Introduction

The rapid development of the telecommunication and satellite broadcasting technology industry[1] today requires low volume and low cost circuit fabrication, while at the same time demands excellent electrical performance, reliability, circuit miniaturization, integration and surface mounting techniques. Recently, microwave and millimetre-wave dielectric materials have been developed for wide application in wireless telecommunications such as mobile phone, wireless local area network (LAN), Global Positioning System (GPS), Bluetooth, Intelligent Transport System (ITS)[2] and in low volume high performance application in military, space and car industry. The utilizable region of communication frequency has expanded from microwave to millimetre wave region, where the speed for signal propagation velocity within the material is higher which in applications means ultra high speed wireless LAN and ITS.

Many materials have been developed and modified, according to the needs of the specific applications. Low temperature co-fired ceramic (LTCC) technology is one of the latest widely investigated solution for the fabrication of 3-Dimensional multilayer material modules. Several LTCC microwave dielectric ceramics system such as Al_2O_3-(Ca-Al-B-Si-O glass), Bi_2O_3-TiO_2-TeO_2, BaO-TiO_2-WO_3, $MTiO_3$ (M = Mg, Zn, Ca), $ZnAl_2O_4$-TiO_2, $Li_3AlB_2O_6$, CaO-B_2O_3-SiO_2, $Ba_2Ti_9O_{20}$-glass, $Ca_{1-x}Mg_xSiO_3$ (x = 0.1-0.5), $ZnNb_2O_6$, have been investigated over the years.[3, 4, 5, 6, 7, 8, 9, 10, 11, 12, 13 and 14]

The LTCC systems available on the market fall into two major categories: glass + ceramics (multiphase ceramics)[15,16,17,18,19] and glass-ceramics (crystallisable glass)[20,21,22,23]. In the former technique low-softening temperature glass powder is added into crystalline ceramics powder to reduce the sintering temperature and increase the densification. In the latter system crystalline components crystallized from glass matrix during firing. The amorphous crystallisable glass is usually prepared by conventional glass making technique such as mixing the pure components of the glass in the desired ratio, firing the mixture to form a homogeneous melt and then quenching the melt to obtain glass. Crystallization of so prepared glass could be controlled by heat-treatment. The quantity of crystalline phases formed during firing significantly influences properties of the glass-ceramics materials including the dielectric properties. The glass-ceramics are due to lower dielectric losses more attractive to researchers' for designing LTCC substrate systems than glass and ceramic

mixtures.

In our study the glass-ceramic approach was adopted to investigate and developed a new potential material for the use as a substrate material in LTCC technology. In contrast to numerous of glass-ceramic materials, which are precisely investigated and described in the literature, the recrystallization of MgO-B_2O_3-SiO_2 system and their dielectric properties have not been reported, yet.

In the following chapter I will provide a general overview of the present knowledge of nucleation and crystallization of glasses. The LTCC technology and the known characteristic of MgO-B_2O_3-SiO_2 system are described in details.

1.1 The glass

Natural glass has existed since the beginnings of the time, during formation of the earth. Siliceous melts of rocks occasionally, during volcanic eruption when penetrated the surface, cooled quickly and froze to the natural glasses. The foaming melt became solid natural glass foam, since high viscosity prevented the escape of bubbles.

Humans have been producing glasses by melting of raw materials for thousands of years. The first cases of glassware date from at least 5000 B.C. were found in Egypt and Mesopotamia. Initially the glass products were used for tools, weapons and jewels as beads. In the third millennium, in the central Mesopotamia, the basic raw materials of glass were being used principally to produce glazes on pots and vases. Development and consequently the usage of glass products were simultaneously developed through the time. Today, the use of glass is in wide range, with application in the architectural, engineering electronics, telecommunications and aerospace industry.

With nucleation and crystallization of glass the crystallites is embedded in a glass matrix and these affect on the physical and chemical properties of the so-called glass-ceramic. Glass ceramic materials are polycrystalline solids containing from nanometres to micrometers size crystals embedded in a residual glass matrix.

1.1.1 Definition of glass

After ASTM[24] the glass definition, which was purposed in 1949 is as follows: “The glass is an inorganic product of fusion which has been cooled to a rigid condition without crystallization.” There are several definitions of the glass and the most widely used is definition given by Morey[25]: “Glass is an inorganic substance in a condition which is

continuous with, and analogous to, the liquid state of that substance, but which, as the result of a reversible change in viscosity during cooling, has attained so high a degree of viscosity as to be, for all practical purposes rigid." Both organic and inorganic materials may form glasses if their structure is non-crystalline, which means lack of long-range order.

1.1.2 The glass formation

Glasses are usually formed by cooling a liquid fast enough to prevent detectable crystallization. The structure of the glasses can be clearly distinguished from that of liquids, since glass structure is effectively independent of temperature. The glass formation is best understood by examining Figure 1, in which the enthalpy or specific volume of the crystal, liquid and glass is a function of the temperature. Starting with cooling the liquid at a high temperature. If there is a discontinuous change in enthalpy or volume at the melting point Tm, then the liquid is crystallized. The crystallization belongs to 1^{st} order phase transition, which are accompanied by the volume and enthalpy change. However, if no spontaneous crystallization and solidification occurred, the material may remain in a liquid state at a temperature below its freezing point Tm. Material can be then identified as a metastable supercooled liquid. Further reducing of the temperature rapidly increases the viscosity of the supercooled liquid and converts it to the glassy state. Change from a supercooled liquid to a non-crystalline solid glass occurs over a temperature range, referred to the glass transition temperature Tg. The definition of the glass transition temperature Tg, is as follows: "The temperature at which the viscosity reaches an arbitrary value of $\sim 10^{13}$ Poise (1 Poise = 0,1 Pas), delineating a change in behaviour from Newtonian liquid to Hookean solid." It is well known that Tg is not a constant, but is a function of the cooling rate from the liquid to the glassy state. If slower cooling rates are used so that the time available for the structure to relax is increased, the supercooled liquid persists to a lower temperature, what results in glass with higher density. Similarly, by heating the glassy material in the annealing range, in which slow relaxation can occur, the glass structure in time approaches an equilibrium density corresponding to the supercooled liquid at this temperature. However, a slow cooling allows enough time for a viscous liquid to alter its local atomic arrangement to attain the minimum free energy at the corresponding temperature, whereas a rapid cooling causes an increase of viscosity that is too quick for the local atomic arrangement to follow and results in a transition into a glass at a higher temperature. The structure of a rapidly cooled glass is more open than that of a slowly cooled one because the "freezing-in" of the atomic arrangement occurs at a higher temperature. The properties of a glass are therefore different from glass to glass, depending on the thermal history, even if the chemical composition is the same.

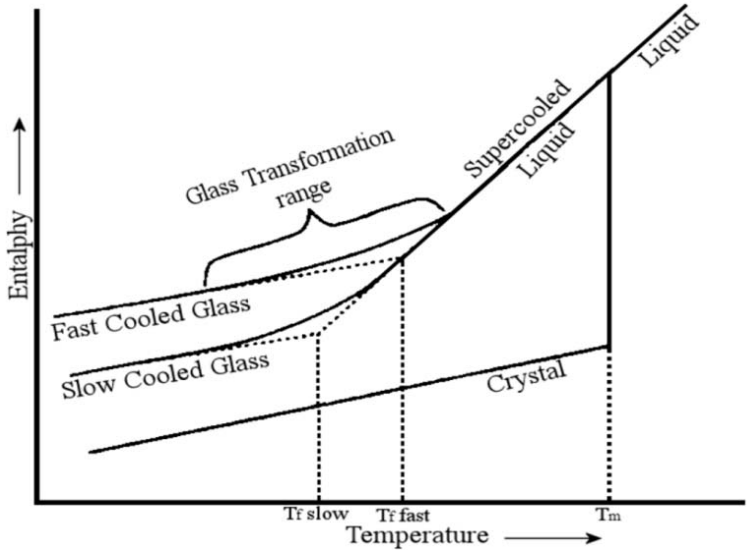

Figure 1. *Effect of temperature on the enthalpy of a glass forming melt and crystal relations.*

It should be emphasized that different cooling rates, corresponding to different relaxation times, have different impacts on the glassy state which is equivalent to different temperature ranges along the curve for the supercooled liquid as illustrated in Figure 2. A faster rate of cooling freezes structural rearrangement at higher glass transition temperature Tg and specific volumes of the glasses which are formed. The specific volume of the glass at the temperature T_0 can be V_1 or V_2 or V_3, depending on which of the three cooling rates was used in forming the glass.

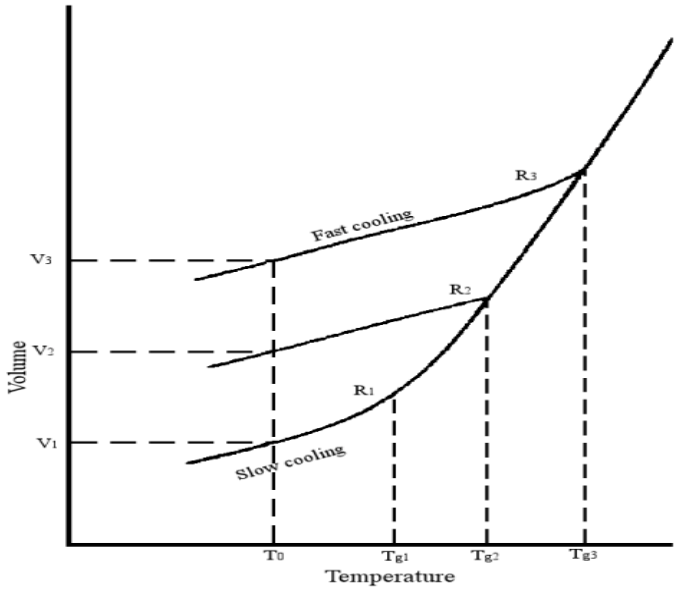

Figure 2. *Specific volume of the glass as a function of the cooling rate.*

Changes in the viscosity of the glass are in accordance with the changes in enthalpy and specific volume shown in Figure 1 and Figure 2. Glasses are often characterized by the

temperature at which certain glasses reach standard viscosity reference points that are important in glassmaking. For instance, the working point, the temperature where the forming process is possible is equivalent to the temperature at which viscosity is $\eta = 10^3$ Pas. The softening point, at which the glass may slump under its own weight is defined by a viscosity $\eta = 10^{6,6}$ Pas. The annealing point is a viscosity at which internal stress can be substantially relieved in approximately 15 minutes and is defined as $\eta = 10^{12,4}$ Pas. The viscosity at the glass transition is 10^{12}-$10^{13,5}$ Pas for oxide glasses and represents a limit above which structural rearrangements cannot take place at normal cooling rates.

1.1.3 Structure of glasses

The first theory of the glass formation was based on Tamman[26] research in 1903. He defined glass as a supercooled melt. He found that crystallization of a super cooled liquid is controlled by two basic factors. The first of these is the nucleation rate, i.e. the number of nuclei formed in a unit volume per unit time; the second is the rate of crystal growth, i.e. the rate of shift of the phase boundary of the crystalline phase in the liquid. Several years later around 1926 Goldschmidt[27] founded simple theory that glass formation was based on the oxide general formula R_nO_m that could easily formed when the ionic radius (r) ratio of the cations to the oxygen ion lies in the range from 0,2 to 0,4. This condition is fulfilled for the oxides, which are shown in the Table 1 and which are today known as glassmakers.

Table 1. *Radius ratios for typical glass – formers.*

Compound	Radius Ratio (r_k/r_A)
SiO_2	$r_{Si} : r_O = 0.39Å : 1.4Å \approx 0.28$
B_2O_3	$r_B : r_O = 0.20Å : 1.4Å \approx 0.15$
P_2O_5	$r_P : r_O = 0.34Å : 1.4Å \approx 0.25$
GeO_2	$r_{Ge} : r_O = 0.44Å : 1.4Å \approx 0.31$
BeF_2	$r_{Be} : r_F = 0.34Å : 1.36Å \approx 0.25$

Since radius ratios in this range tend to produce cations surrounded by four oxygen ions in the form of tetrahedral, Goldschmidt therefore believed that only melts containing tetrahedrally – coordinated cations formed glasses during cooling. This contention was purely empirical, with no attempt to explain why tetrahedral coordination should be so favourable to glass formation.

The network hypothesis proposed by Zachariasen[28] and reinforced by Warren's[29] X – ray diffraction represented a leap forward in the knowledge about the structure of glasses. Zachariasen claimed that the silicate crystals, which readily form glasses instead of recrystallizing after melting and cooling, have a network, as opposed to close – packed, structures. These networks consist of tetrahedra connected at all four corners, just as in corresponding crystals Figure 3a, but the networks are not periodic and symmetrical as it is shown in Figure 3b. These networks extend in all three dimensions. The properties of glasses are isotropic due to the natural consequence of the absence of symmetry in the network. The ultimate condition for glass formation is assured with the ability to form such networks. The atomic arrangement in glass is characterized by an extended 3-dimensional network, which lacks of symmetry and periodicity. The energy of a glass will be higher than that of the corresponding crystal due to the non-structurally equivalent atoms in the glass network (Figure 1).

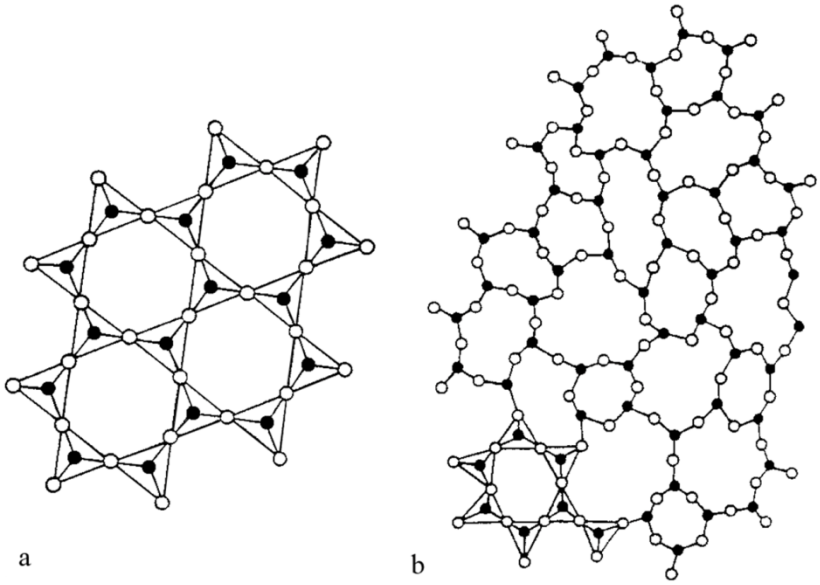

Figure 3. *SiO_4 tetrahedron linkage in crystallized and amorphous SiO_2, a regularly ordered netting of SiO_4 building blocks in crystalline SiO_2 (rock crystal), b Disordered netting of SiO_4 building blocks on SiO_2 glass (molten rock crystal).*

Today the most commonly used models for glass structure are based on the original conception of Zachariasen which are grouped under the term of the random network theory. The following rules for glass formation are valid for the formation of a continuous 3 – dimensional network, with no indication of the degree of long-range order of that network. Zachariasen is according to the adopted hypothesis that a glass should have energy similar to that of the corresponding crystal considered the conditions for constructing a random network such as shown in Figure 3 and suggested four rules for the formation of an oxide glasses.

Zachariasen's rules for glass formation in simple oxides MxOy:

- Each oxygen atom should be linked to not more than two cations.
- The oxygen coordination number of the network must be small, 3 or 4.
- Oxygen polyhedra share only corners and not edges or faces.
- At least three corners of each oxygen polyhedron must be shared in order to form a 3 – dimensional network.

In fact, these rules adequately describe the structures of many crystalline phases such as SiO_2, B_2O_2, P_2O_5, GeO_2, As_2S_3, and BeF_2 known as glass network formers. Some components can also participate in glass formation as occupiers of random position distributed through the structure located to provide local charge neutrality as pictured in Figure 4. Since their major function is viewed as providing additional oxygen ion, which modifies the network structure, they are called network modifiers. However, these components do not form networks but occupy thermodynamically stables sites or act as a replacement for a part of network former. Thereby causing a decrease of viscosity, lowering the melting point and increase of the electrical conductivity.

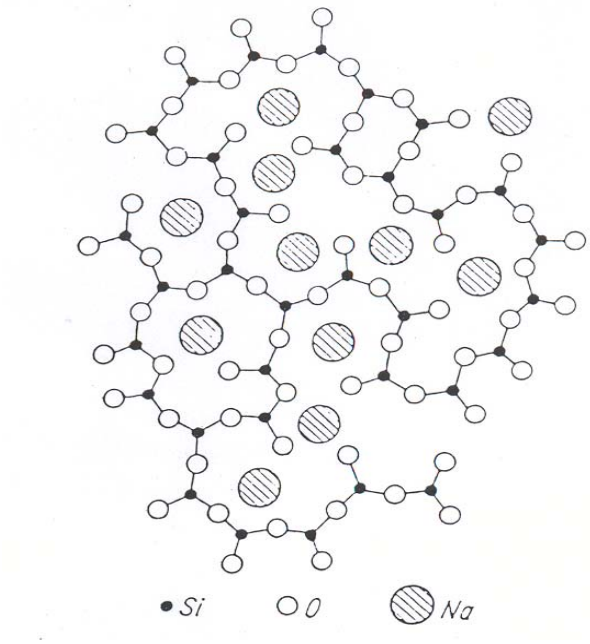

Figure 4. *Arrangement of atoms (or ions) in a sodium silicate glass. When Na_2O is incorporated, the large sodium ions are after rupture of oxygen bridges, located in the new, larger cavities.*

The cations, which can be interpolated into the network structure as a modifiers or partially substitute the glass formers although they do not belong to form glasses are referred as intermediate ions. In Figure 5 is schematically represented an example of an intermediate ion interpolated into the glass structure. If the intermediate ion Al^{3+} is interpolated into the network structure instead of the glass former Si^{4+}, another alkali ion M^{+} is interpolated in order to satisfy the electroneutrality.

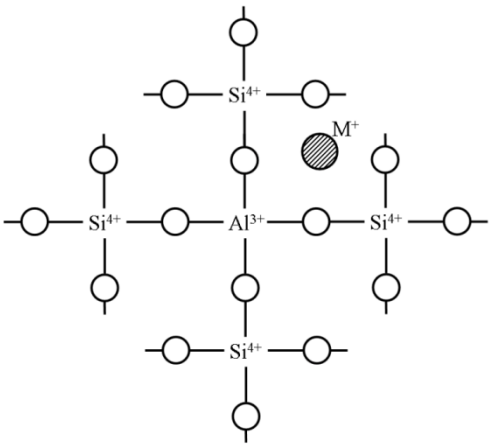

Figure 5. *Interpolation of intermediate Al-ion into the glass matrix.*

On the basis of Zachariasen – Warren concept numerous properties of conventional glasses can be explained or predicted. As an increase in large cations breaks bridges in the fundamental network, the increased mobility of the building units and the modifiers easily account for decreasing viscosity and melting range, as well as increasing electrical conductivity.

Dietzel[30] extended Goldschmidt's considerations of the role of size and polarizability of constituent ions to that of their charges. Essentially he included the influence of the interaction of forces between cations and anions during solidification of a melt. Applying the fundamental relation of physics for the attraction or repulsion (P) between electrical charges (Q) at distance (a):

$$P = \frac{QQ}{a^2} \tag{1}$$

and for anions and cations next equation is valid:

$$K = \frac{Z_C Z_a e^2}{(r_c + r_a)^2} = \frac{Z_c Z_a e^2}{a^2} \tag{2}$$

where (K) describes, the interacting forces; (Z_c), (Z_a) are the valences of cation and anion; (e)

is the elementary charge; (r_c), (r_a) are the radii of cation and anion, and ($a = r_c + r_a$).

Dietzel introduced the term “field strength”

$$F = \frac{Z_c}{a^2} \tag{3}$$

For characterization the effect of a single cation, he assumed that the anion is oxygen ($a = r_c + r_{O2-}$). For non-oxide glasses, other values for (a) have to be introduced.

According to Dietzel,[26] stable compounds require a difference of field strength ΔF between two cation of a binary system exceeding 0.3. With a further increase, the number of compounds, but also the tendency to glass formation, increases. Melts of binary systems with ΔF of the constituent ions exceeding 1.33 usually solidify as glasses.

In general the role of cations depends on valence and coordination number and the related value of field strength at distance of oxide ion, as illustrated in Table 2. The fact is that Zachariasen’s classification of ions as network formers, modifiers, and intermediates may be clearly related to their field strength:

for network modifiers	F ≈ 0.1 to 0.4;
for intermediates	F ≈ 0.5 to 1
for network formers	F ≈ 1.4 to 2

Table 2. *Classification of cations according to their field strength.[26]*

Element	Valence Z	Ionic Radius (for CN = 6 r in Å [a]	Most Frequent Coordination Number CN	Ionic Distance for Oxides a in Å	Field Strength at Distance of O^2 Ions Z/a^2	Function in Glass Structure
K	1	1.33	8	2.77	0.13	
Na	1	0.98	6	2.30	0.19	
Li	1	0.78	6	2.10	0.23	
Ba	2	1.43	8	2.86	0.24	
Pb	2	1.32	8	2.74	0.27	Network-modifier
Sr	2	1.27	8	2.69	0.28	$Z/a^2 \approx 0.1 \ldots 0.4$
Ca	2	1.06	8	2.48	0.33	
Mn	2	0.91	6	2.23	0.40	
Fe	2	0.83	6	2.15	0.43	
Mn	2	0.83	4	2.03	0.49	
Mg	2	0.78	6	2.10	0.45	
			4	1.96	0.53	
Zr	4	0.87	8	2.28	0.77	
Be	2	0.34	4	1.53	0.86	Intermediate
Fe	3	0.67	6	1.99	0.76	$Z/a^2 \approx 0.5 \ldots 1.0$
			4	1.88	0.85	
Al	3	0.57	6	1.89	0.84	
			4	1.77	0.96	
Ti	4	0.64	6	1.96	1.04	
B	3	0.20	4	1.50	1.34	
Ge	4	0.44	4	1.66	1.45	
Si	4	0.39	4	1.60	1.57	Network-former
P	5	0.34	4	1.55	2.1	$Z/a^2 \approx 1.5 \ldots 2.0$
B	3	0.20	3		1.63	

[a] 1 Å = 10^{-8} cm

1.2 Crystallization of glasses

1.2.1 General

The previous section contains the explanation of the conditions for the glass formation, whereas the nucleation and crystallization processes of the glasses will be described in this chapter. Glass is metastable and will transform to the stable crystalline state if enough thermal energy is available. This transformation is called devitrification or crystallization, and occurs owing to nucleation, which is prerequisite for crystal growth process. It is well known that virtually any material will form a glass, if cooled so rapidly that insufficient time is provided to allow the reorganization of the structure into the periodic arrangement required by crystallization. Crystallization of glass is a process resulting in an ordered crystal network in the less-ordered random network.[24] Crystallization is predicted on the formation of nuclei,

which occurs in the important state of transition between the liquid melt and the crystalline solid state. As the glass is heated the viscosity decreases, which increases the tendency for structural rearrangement and crystallization. When the temperature is increased high enough usually just slightly above the softening point, crystal nuclei begin to form. The nuclei are simply tiny regions in the glass structure where the crystalline structure has formed. As the temperature is further increased the rate of nuclei formation, or nucleation, increases to a maximum at some temperature, depending on the composition. At higher temperatures additional thermal energy causes the nuclei to grow by crystal growth mechanisms. The rate of crystal growth increases with increasing temperature to a maximum at some temperature, and then the rate decreases to zero at the liquidous temperature.

In silicates, as well as in organic polymers, nucleation and crystallization will not occur spontaneously, as in salt melts, even when the saturation or freezing temperature is passed slowly. As shown in Figure 6 it is necessary to pass a second curve ("curve of supersaturation") at temperatures below those of the saturation or freezing curve before nuclei and crystals will form.

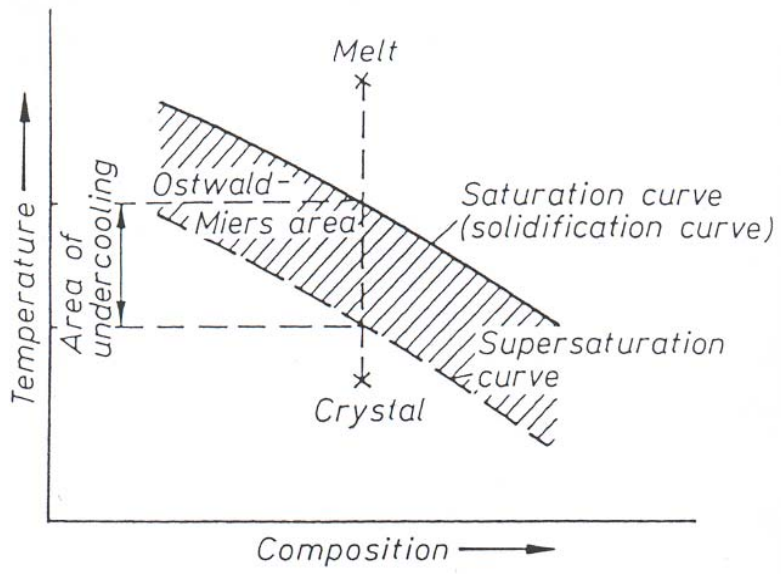

Figure 6. *Schematic presentation of the transition from a highly viscous melt to the crystalline state.*

1.2.2 Nucleation

The nucleus can be homogeneous, when the formation occurs spontaneously within the melt, or heterogeneous, where nucleation occurs from preferred sites, such as surfaces, grain boundaries, second-phase particles, and other discontinuities in the structure. Heterogeneous nucleation dominates, because there are always defects and impurities present. The term crystallization is actually separate into two distinct physical processes: formation of submicroscopic nuclei and their growth into macroscopic crystals. These two processes are called nucleation and crystal growth. If nuclei are not present, crystal growth cannot occur and the material will form a glass. The terminology glass is used even when extremely small nucleus and low volume fraction of the nuclei prevents their detection and consequently the crystal growth has not been defined. Nucleation and crystal growth can occur within bulk glass or on the surface, referred as bulk and surface crystallization, respectively. Most commercial glass compositions tend to crystallize mainly on the surface by expanding into the glass matrix, because of the heterogeneities on the surface. If the crystallization is uncontrolled, the large crystals usually grows, which strongly impairs the mechanical properties of the particular glass ceramic. In contrast to the spontaneous crystallization, small grains at the controlled crystallization were observed. The temperature dependence of nucleation and crystallization of glasses has been described by Tammann.[31] He discovered that the transformation of a melt to a crystalline state consists of two different processes: the nucleation and crystal growth. When a melt is cooled below the melting point, crystals do not form spontaneously in the entire volume. At first, submicroscopic crystalline aggregates of a definite size, i.e., the nuclei, must form, and only then can crystal growth occur upon these nuclei.

A nucleus is an entity that already belongs to the new phase but is unstable equilibrium with respect to the supersaturated matrix phase. [32] Thermodynamics and kinetics must be additional assistance for further description of the formation of this nucleus.

1.2.2.1 Homogeneous nucleation

In classical homogeneous nucleation the nuclei are formed with equal probability throughout the bulk of the melt. Nuclei are not usually detected directly due to extremely small size. Their concentration is usually determined by a complex procedure involving an isothermal heat treatment at the nucleation temperature. The sample is quenched to freeze the nuclei, and then reheated to the temperature where the nuclei can grow to a detectable size for analysis. Two significant barriers exist for the nucleus formation. First, the thermodynamic barrier,

which involves the free energy, change in the system when a nucleus is formed. Secondly, the kinetic barrier which is the result of the requirement that mass moves or rearranges in space, allowing the growth of a crystal from the melt.

Nucleation is a thermodynamic process of the phase transition, associated with a decrease in the free enthalpy ΔG. The total free enthalpy consists of a volume contribution (ΔG_V) and a surface contribution (ΔG_O).

$$\Delta G = -\Delta G_V + \Delta G_O \tag{4}$$

The ΔG_v is the free enthalpy change per unit volume, which corresponds to, gained portion of the energy produced by the formation of nuclei and it is negative. Based on the assumption of the spherical particles, the G_V is calculated according to the Eq 5.

$$-\Delta G_V = -\frac{4}{3}\pi r^3 \Delta g_V \tag{5}$$

where r is the radius of the nucleus and Δg_V the change in free volume enthalpy during phase transition.

The surface contribution ΔG_O corresponds with the energy to be provided when a nucleus is formed.

$$\Delta G_O = 4\pi r^2 \sigma(\Delta g_O) \tag{6}$$

where σ is a surface tension. The free enthalpy of the interface Δg_O can be neglected. Thus the free total enthalpy becomes:

$$\Delta G = -\frac{4}{3}\pi r^3 \Delta g_V + 4\pi r^2 \sigma \tag{7}$$

where the first term represents the change in volume free energy and the second term represents the change in surface energy. ΔG will be positive, referring to Eq.7, when size of the nucleus (r) are small and consequently the surface term will dominate. However, as r increases the volume term will dominate and ΔG will become negative. In the case when the surface term is smaller than the volume term the critical nucleus size r* is achieved.

The theoretical derivation of nuclei with the critical radius is expressed as:[33]

$$r^* = -\frac{2\sigma}{\Delta g_V} \tag{8}$$

The critical nucleus size r* corresponds to the critical free enthalpy ΔG*. The critical free energy change for the formation of supercritical nuclei is determined by:

$$\Delta G^* = \frac{16\pi\sigma^3}{3(\Delta g_V)^2} \tag{9}$$

The individual terms and their sum in the Eq 7 are shown in correspondence of the crystal radius r to the ΔG in Figure 7. There is a maximum of free enthalpy ΔG* at critical nucleus size r*, beyond free energy decreases with increasing r. Nucleus disintegration happened bellow r* when ΔG decreases with decreasing of r. Newly formed particles of the critical nuclei size r* and even larger size called supercritical nuclei are capable of growing. Particles that are smaller than r* are called embryo or subcritical particles and are incapable of growing and eventually disintegrate.

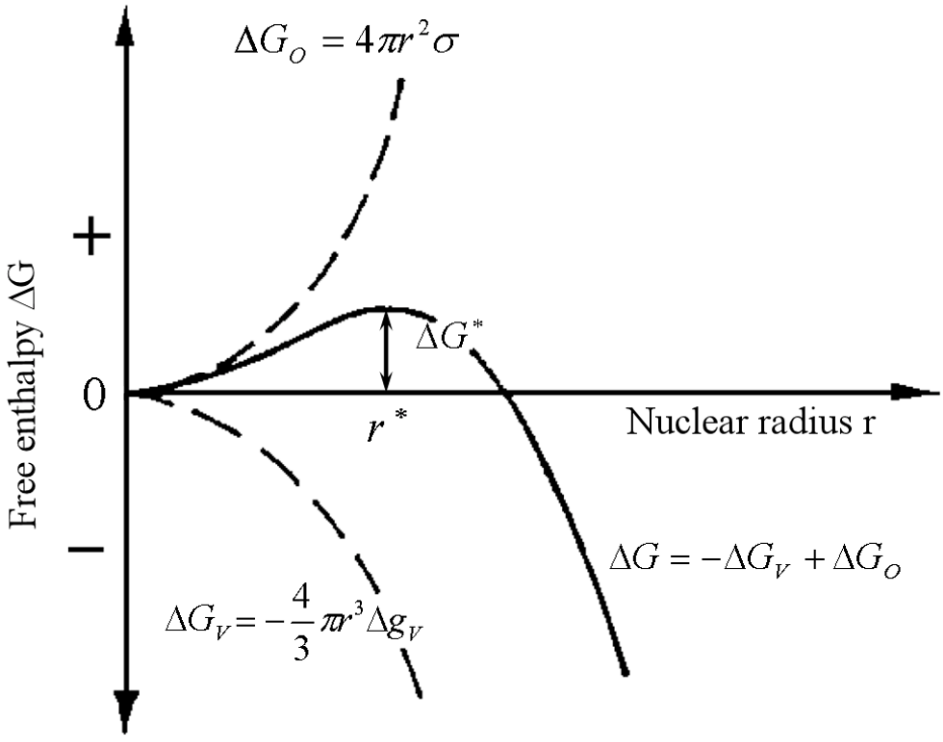

Figure 7. *Free enthalpy of a crystalline nucleus as a function of its radius.*

Considering the kinetic processes, which are useful for investigating the balance between the formation and dissolution of nuclei, steady and non-steady state processes must be distinguished. In a steady-state process the reaction rate is invariant with time. In a non-steady state process, a time lag occurs before the steady – state reaction rate is reached.

The rate of nucleation is expressed in terms of the number of nuclei formed in unit volume per unit time. If the number of nuclei is equal to the equilibrium number, then it is expressed:

$$n^* = n \exp\left(-\frac{\Delta G^*}{kT}\right) \tag{10}$$

where n* is number of nuclei of critical size, n is number of molecules per unit volume and k is Boltzman constant.

If the process of nucleus growth to supercritical size is sufficiently slow, then the number of nuclei at steady state can be considered as roughly equivalent to the equilibrium number. Then the nucleation rate I_0 for steady-state nucleation can be expressed as:

$$I_0 = K_v \exp\left(-\frac{\Delta Ga + \Delta G^*}{kT}\right) \tag{11}$$

where K_v is a constant and ΔGa is activation energy for the diffusion of ions from a homogeneous solution to the location of nucleation.

1.2.2.2 Heterogeneous nucleation

The process of heterogeneous nucleation is stimulated by the presence of impurity particles, phase boundaries, special catalyst and foreign substrates. Nuclei are usually formed on the walls of the reaction vessels. If nucleation occurs at a phase boundary between the vessel surface or air and the glass, then crystallization proceeds from this surface into the bulk of the sample and it is termed as surface crystallization

The entire theory of critical free energy used for forming critical size nuclei in heterogeneous nucleation is derived from the contact or wetting angle (Θ) relationship of Young's equation and is given by:

$$\Delta G_S^* = \Delta G^* f(\Theta) \tag{12}$$

where the contact angle is

$$f(\Theta)=\frac{(2+\cos\theta)(1-\cos\theta)^2}{4} \tag{13}$$

Heterogeneous nucleation is based on the spherical cup model depicted in Figure 8. Three specific situations will be explained on the basis of that model. First if the heterogeneous substrate (S) is not wetted, the contact angle (Θ) equals 180° and consequently f(Θ) equals 1. These phenomena return to a homogeneous nucleation process. Second, if the surface (S) is completely wetted and the contact angle (Θ) is approximating to 0°, then $f(\Theta)\geq 0$ and ΔG_S^* are very small. Therefore at $\Theta <$ 180° heterogeneous nucleation will rather occur than homogeneous nucleation.

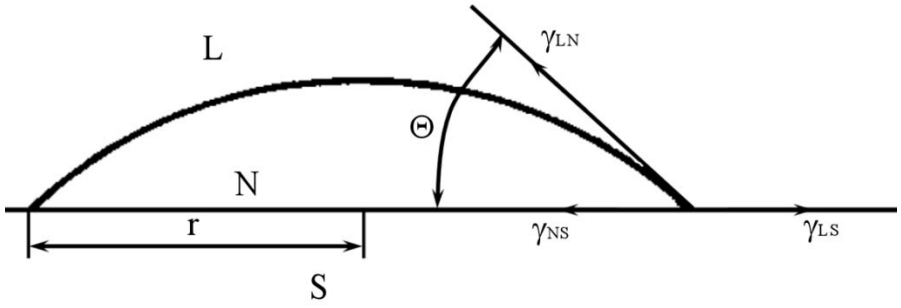

Figure 8. *Schematic expose of a spherical cup model for the heterogeneous nucleation.*

If we assumed that nucleus is formed on the primarily separated solid phase in the supersaturated liquid, then the free energy is connected with formation of the surface of two new boundaries is extend by the following relationship

$$\Delta Gs = \gamma_{LN} A_{LN} + \pi r^2 (\gamma_{NS} - \gamma_{LS}) \tag{14}$$

where are the interfacial energies liquid-nucleus (γ_{LN}), nucleus-solid (γ_{NS}) and liquid solid phase (γ_{LS}) and A_{LN} is the surface area of the liquid-nucleus phase boundary.

If $\gamma_{LS} > \gamma_{NS}$ then it follows from equation Eq 12 that ΔG_S is smaller than ($\gamma_{LN}A_{LN}$) and the overall free energy connected with formation of the nuclear surface is smaller than that for homogeneous nucleation ($\gamma_{LN}A_{LN}$). Assuming equilibrium of energy conditions at the boundary of two solid and one liquid phase, according to Figure 8 it holds that

$$\gamma_{LS} = \gamma_{NS} + \gamma_{LN} \cos\Theta \tag{15}$$

If we Eq 13 insert into the Eq 12, we get this expression:

$$\Delta Gs = \gamma_{LN} A_{LN} - \pi r^2 \gamma_{LN} \cos\Theta \tag{16}$$

The expression for the thermodynamic barrier to heterogeneous nucleation is obtained similarly as for homogeneous nucleation:

$$\Delta G^*_{HET} = \frac{16\pi\gamma^3_{LN}}{3(\Delta G_V)^2} \frac{(2+\cos\Theta)(1-\cos\Theta)^2}{4} \tag{17}$$

The rate of heterogeneous nucleation is then given by the relationship:

$$I_{HET} = K_s \exp\left(-\frac{\Delta G^*_{HET} + \Delta G_a}{kT}\right) \tag{18}$$

This expression is similar to its counterpart for homogeneous nucleation, but with the number of molecules per unit volume or area in contact with the substrate. ΔG_a is the activation energy required to disengage an atom or molecule from the liquid phase and move it across the interface to the foreign surface.

The effect of nucleation and crystallization rate observed from higher toward lower temperature is schematically illustrated in Figure 9.

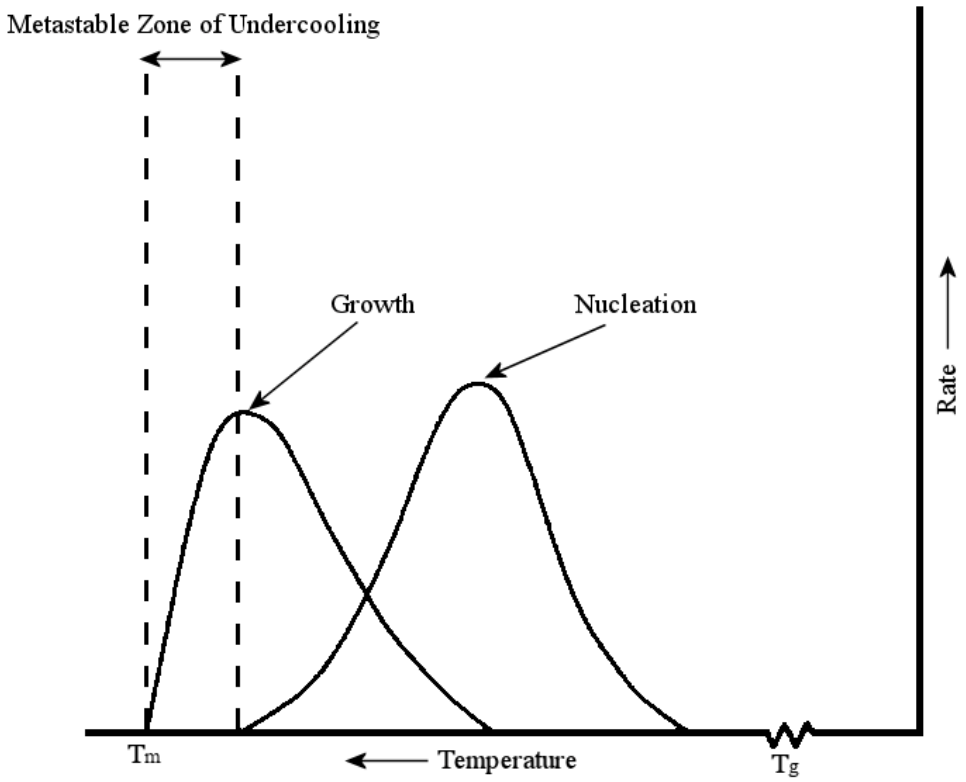

Figure 9. *The influence of temperature on the rates of nucleation and crystal growth for a glass forming melt.*

If the temperature of the melt is above T_m, there will be no tendency toward formation of a nucleus. As the temperature decreases to $\leq T_m$, the nucleus can become stable due to the change of the free energy of the system. As long as the temperature is close to the T_m, the value of Δg_V is very small. Regarding to the approximated relation (Eq 19), which is valid only for small under cooling's.

$$\Delta g_V = \Delta Hg \frac{(Tm - T)}{Tm} \tag{19}$$

It follows theoretically that the critical radius (r*) given from the Equation 8 for a stable nucleus will be very large. Practical probability of reaching large size nucleus is extremely low, and the melt will remain free of nuclei even though the temperature is below T_m. With further cooling Δg_V will increase, consequently the value of the critical nucleus size (r*) is reduced. Eventually the critical radius will become so small, that the probability of formation of a nucleus large enough to exceed the critical radius will become significant, and nuclei will begin to form in detectable quantities. A metastable zone of undercooling exists because small detectable nuclei posses considerably lower temperature of melting than greater mass of material. Once the temperature of the cooling melt passes below the lower limit of the metastable zone, the thermodynamic barrier will decrease with decreasing temperature, allowing nuclei to form at an ever increasing rate.

The growth and nucleation rate can be also explained differently from above discussion. Shape of the nucleation curve can be qualitatively explained with the help of equations (5-11). Small undercooling rates indicate high ΔG^* due to small difference of Δg_V and therefore the nucleation rate is small. The maximum nucleation rate is reached when subsequent undercooling increases Δg_V to the point where ΔG^* is not the same as ΔG_a. Further decreasing of the nucleation rate occurred because higher undercooling and ΔG^* became negligible compared to ΔG_a.

1.3 LTCC

1.3.1 Development of LTCC technology

Microelectronics in the last 15 years became a profitable industry worldwide. Successful combination of a broad spectrum of technologies with the remarkable advancements in materials science result in various range of products such as mobile phones, wireless communication systems, portable computers, DVD players, flat panel displays, storage medias, etc. [6] Microelectronics packaging is technology, which combines performance, reliability and cost reduction. Whether it is an integrated circuit (IC) on a silicon chip (e.g. solid state devices, logic and memory components of computers, etc.) or a microsystem on a multi-chip module (MCM), which are the basic functional segments of such devices, packaging plays an important role by providing mechanical support, robustness, hermeticity, power and signal transmission to/from ICs, in addition to many other functions. [34] However one of the major differences between microsystem packaging and IC packaging is that the microsystem generally interacts with the environment in which it is placed. Therefore the protection is important due to the contamination of the environment; mainly this is valid for the sensors used in biomedical, pharmaceutical and food industries.

Microelectronic packages are consisted form ICs flip-chipped or bonded on a substrate which present planar interconnect board. This type of packaging, in which the multiple ICs and various components are confined into single module, is called MCM (Figure 10). [35]

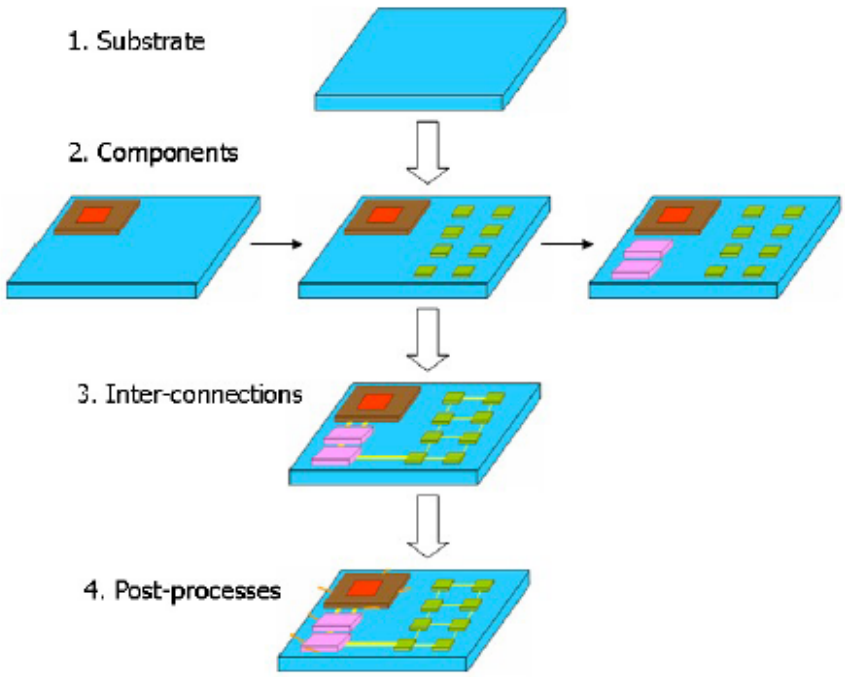

Figure 10. *A simple microelectronic package: components confined into one single layer.*

On the other hand the integration of active and passive electronic components such as filters, resistors, inductors, and capacitors etc… into the multilayer ceramic module is called Multi-Chip Integrated Circuit (MCIC). These components embedded and buried onto the surface layers are facilitating the fabrication of a monolithic structure with increased performance and reliability. MCIC technology is divided into three main groups: Thick-film, Low Temperature Co-fired Ceramic (LTCC) and High Temperature Co-fired Ceramic (HTCC).

At the beginning the LTCC-based MCIC technology was commonly used for the production of high volume microwave devices. Nowadays LTCC technology is well introduced both for low volume high performance application (military, space) and high volume low cost application (wireless communication, car industry). [36] The major RF opportunities are in the fields of mobile telecommunication devices (0.9-2 GHz), wireless local networks such as Bluetooth (2.4 GHz), global positioning systems such as GPS (1.6 GHz) and in broad band access connection systems (5.8-40 GHz). [37] All of these extensive options for applications are based on highly functional, reliable and low-cost electronic devices. It is evident that immense progress has been achieved by using advanced materials systems, which play the major role in the production of microelectronic packages.

A typical LTCC module consists of dielectric tapes, connecting vias, external and internal conductors and passive components (resistors, capacitors, inductors). Standard thick film conductor, resistor and capacitor materials are used in LTCC circuits as buried (two or three dimensional 3D) or surface components.

The conductor and passive components are deposited by screen printing method which is typical for thick film technology. Thick or thin film components can be made on both sides of the fired module. Additional active or passive components are added to the top or bottom part of the fired structure using various assembling methods. Typical soldering, flip chip and wire bonding techniques are used for this purpose. The schematic cross-section of the LTCC module is shown in Figure 11.

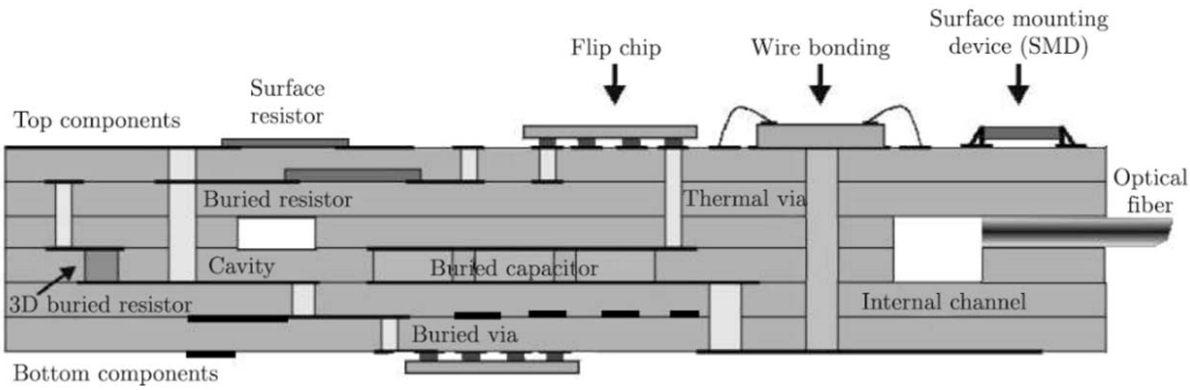

Figure 11. *Cross-section of the LTCC module.[36]*

1.3.2 Substrate material properties

One of the most important applicable products of LTCC technology is substrate, which is fundamental component of any microelectronic package. The circuits are attached on the substrate and the electrodes facilitate the connection between these devices. In a typical LTCC module, the substrate is the fired LTCC sheet, whereas all other active and passive electronic components are the functional elements of the system integrated or virtually screen-printed into the thin layers of ceramic resulting in three-dimensional (3D) multilayer module. Such multilayer devices require a low sintering temperature below 950 °C with the intention of co-firing with inexpensive and highly conductive electrodes such as silver (Ag) and copper (Cu) with the melting points 961 and 1081 °C, respectively.[38] Ag/Pd is also known as a highly interesting conductor due to complete miscibility and thus a wide range of melting temperatures that can be manipulated by changing the Ag/Pd ratio. However the oxidation of Palladium leads to the expansion of the electrode and consequently the tendency to interact with the surrounding dielectric substrate. The firing temperature of densification or crystallization of the proposal LTCC composite below 800 °C is undesirable because this can prevent the evaporation of the organics and solvents used in conductive pastes and binder and thus cause residual carbon traces in the microstructure. [18,39] The residual carbon that may remains after the binder decomposition would adversely affect dielectric performance of LTCC package. The disadvantages related to carbon removal make the selection of the glass-ceramic and identification of a suitable composition even more challenging. This is not valid only for low sinterable glass-ceramics but also for the ceramics where sintering temperature is decreased by the sintering aids.

Furthermore, there are beside appropriate sintering temperature some other important characteristics required for a dielectric substrate material such as low dielectric constant for fast signal transmission, high quality factor Q which is the inverse of the dielectric loss factor tanδ for selectivity, high dielectric strength, low dissipation factors particularly at high frequencies, well-matched thermal coefficient of expansion (TCE) to that of printed components, high mechanical strength, smooth surfaces, free of surface distortion, visual defects, physical and chemical compatibility, low cost in high volume production. [40] Some of these particular demands will be hereinafter explained in details. Most of the substrates used in microelectronics are ceramic or glass-ceramics. LTCC substrates fulfil most of these prerequisites, in addition to other benefits such as flexibility in design and fabrication, low firing temperatures, etc. The production of LTCC circuit is connected to several very

fundamental and sophisticated techniques of the ceramics processing science such as ceramic powder preparation, [41] colloidal processing [42] and tape-casting [43].

1.3.2.1 Dielectric constant (permittivity), ε

Materials with low dielectric constant (ε_r) from 4 to 12 are mostly used as substrate layers while high dielectric constant materials are used mainly for capacitor layers or resonating structures. Signal propagation is one of the most important aspects in electronic packaging. This is a direct function of the relative permittivity. Enhancing the velocity (reducing the propagation delay time) is closely related to the improvement of the media speed and reduction of the device size. In the case of ceramic packages, the relative permittivity of the ceramic over and within the metal lines is deposited or embedded governs the propagation delay (t_d), which is given by: [44]

$$t_d = \frac{l\sqrt{\varepsilon_r}}{c} \tag{20}$$

where l is the line length, ε_r is the relative permittivity of the substrate and c is the speed of light. The media speed (ν) is a function of propagation delay and their relation is given by:

$$\nu = \frac{l}{t_d} \tag{21}$$

Therefore the substrates with low dielectric constant are required to increase the speed of the signal propagation and thus reducing the delay time. [18,45,46] Figure 12 presents the propagation delay as a function of the dielectric constant of the ceramic materials. [18,39] Advantage of low dielectric constant materials is that the frequency dependence is commonly very low.

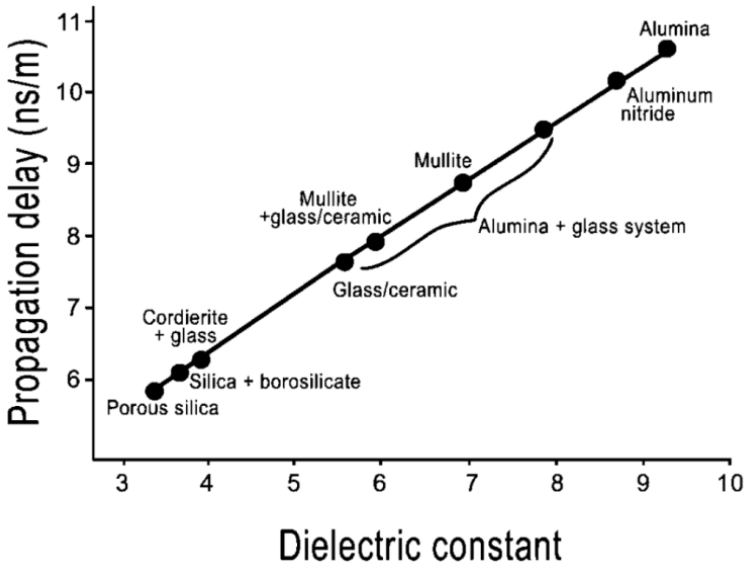

Figure 12. *Propagation delay as a function of the dielectric constant with different ceramic materials.*

High dielectric constant ($\varepsilon_r > 20$) means that LTCC technology enables miniaturization of small embedded resonators, capacitors, filters and antennas. The resonant frequency (f_0) of the resonator of the cylindrical shape is related to the permittivity, by the following equation:

$$f_0 \approx \frac{c}{\lambda_d \sqrt{\varepsilon_r}} \approx \frac{c}{D\sqrt{\varepsilon_r}} \tag{22}$$

where λ_d is the wave length of the standing wave along diameter (D) of a resonator. If the permittivity is increased, the size of the resonator may be decreased while still maintaining a specific resonant frequency, hence it follows that larger permittivities enable miniaturization.[47,48]

1.3.2.2 Quality factor, Q

The quality factor of common LTCC materials is expressed with inverse of dielectric loss factor tanδ and is required for achieving high frequency selectivity and stability of microwave components.[2] However, definition of Q as 1/ tanδ is not particularly useful for visualizing how Q relates to microwave communications. More precisely, the quality factor of the dielectric media is determined as the resonant frequency (f_0) divided by the bandwidth, Δf_0, measured at 3 dB below the maximum height at resonance, Figure 13.[48]

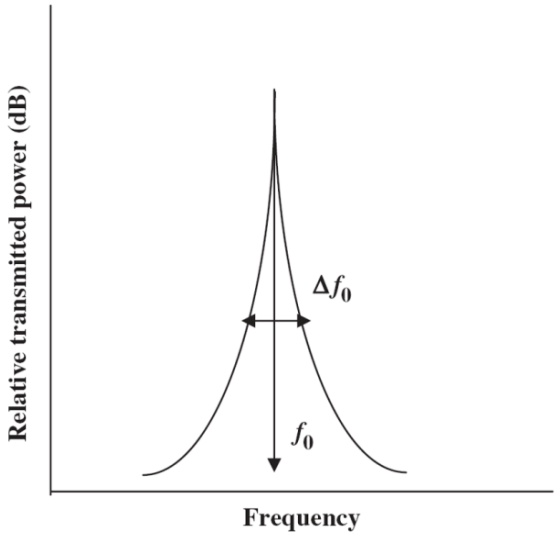

Figure 13. *Schematic relation of resonant peak with associated parameters.*

It is clear from this definition that Q value is the criteria of the selectivity of a resonator at a given frequency. With the higher Q values we avoid the risk of cross-talk within a frequency range. In the microwave region Q value decreases with increasing frequency.[49] However theoretically Qxf values of any given material is supposed to be constant in the broad frequency range. In order to enable the comparison between different ceramics, the Qxf values and not Q-values are most commonly reported in the literature. [50] In practice, their interdependence is evidently different; samples measured at higher frequency above 5 GHz always give higher Qxf values than identical materials measured at lower frequency. It is assumed that the precise reason for this is related to processing. Larger parts, which resonate at lower frequencies statistically, contain more flaws and defects than smaller ceramic bodies. Qxf values measured below 5 GHz are more relevant, however, representing how the material may perform in a real MW circuit.

Considering the substrate material, the quality factor of a multilayer ceramic device is inversely related to the transmission line energy loss of a wave signal. The signal loss mainly relies on the conduction loss of the internal electrode in high frequency ranges, whereas it depends on the dielectric loss of the substrate in low frequency ranges.[51] Therefore for high frequency regions, high conductive electrodes such as Ag and Cu are more effective to use. From this reason low firing temperature of substrate is required regarding to the low melting temperatures of such metal electrodes.

1.3.2.3 Temperature coefficient of resonant frequency, τ_f

Temperature coefficient of resonant frequency (τ_f) of the resonator material or substrate dielectric should be close to zero for thermal stability of the device frequency. Furthermore the important elements integrated in a MCIC, such as the filters and resonators, also need to be very stable under the fluctuation of the temperatures. τ_f measures the shift of resonant frequency of a dielectric resonating circuit over a temperature change. The dielectric is expected to have a τ_f value close to zero, so that the components in the package demonstrate stable dielectric properties under temperature fluctuations and provide high quality filtering.[52] The τ_f is related to the temperature coefficient of the permittivity, (τ_ε) and to the coefficient of the thermal expansion α (CTE) by the following equation:[53]

$$\tau_f = -\frac{1}{2}\tau_\varepsilon - \alpha \tag{23}$$

In practice, to adjust the τ_f to zero, there is an option to add the appropriate amount of crystalline phase with the opposite sign of τ_f.[54,55] Dai et al.[52] in Motorola developed a low loss and near zero τ_f LTCC (T2000), which was achieved by compensating negative value of τ_f with addition of TiO_2 possessing a positive value.

1.3.3 Present and future prospects

The rapid growth of wireless telecommunications, personal communication networks, and sensor applications has lead to a dramatic increase in the regimes of microwave and millimetre wave systems. Growing demand on advanced data transference extended the progress of communication technologies. On the other side, competitions between the manufacturers of the wireless communication components have been accelerated in parallel to the widening of the marketplaces as in the cases of PCS (personal communication system), GPS (global positioning system), SBS (satellite broadcasting system), Internet etc. Therefore the manufacturers are focusing attention on improving the electronic devices in terms of lighter weight, lower cost, multi-functionality, miniaturization, higher efficiency and performance. These demands can be achieved by establishing manufacturing techniques with high predictability and reliability. As a result, low temperature cofired ceramic (LTCC) systems have been adopted as a solution for advanced microelectronic packaging for high frequency applications. The LTCC technology is in production mainly in Japan, USA, Austria and Germany. Companies such as Ferro, Dupont, Huges, Motorola, Nokia, Epcos etc. are the

major corporations, which develop appropriate materials for wireless, space, car and military needs.

Recent developments and future perspectives in LTCC materials development are driven by two major factors: materials compatibility issues and new application areas, imposing additional restrictions on the chemistry of the tapes. Glass-free, lead-free, zero shrinkage LTCC tapes systems and pressure-assisted sintering, at this point, are some of the popular research interests.

1.4 Dielectrics in electromagnetic field

Important properties of microwave dielectric materials used as various components of integrated circuits in LTCC technology are mainly dielectric constant (ε), dielectric losses (tanδ) and temperature coefficient of resonance frequency (τ_f). The frequency range depends on dimensions of ceramic component and dielectric constant of the material from which the component is made. New consumer demands for more efficient devices continually increases the frequency range. Al the abovementioned dielectric parameters are precisely described and discussed in following sections.[33,50,56]

1.4.1 Capacitance and dielectric constant

Capacitance is defined as the capability of a capacitor to store the charge of a voltage (electrical energy). If electric charge is transferred between two initially uncharged conductors, both become equally but opposite charged, one positively, the other negatively, and a potential difference is established between them. In a parallel plate capacitor the capacitance (C) is a measure of the ability of any two conductors in proximity to store a charge (Q), when a voltage (V) is applied across them. This relation is described with following equation:

$$C = \frac{Q}{V} \tag{24}$$

The capacitance of a parallel plate capacitor in vacuum is determined by the consideration of the area (A) of the plates and distance (d) between these two plates (Figure 14a)

$$C_0 = \frac{\varepsilon_0 A}{d} \tag{25}$$

where ε_0 is defined as the permittivity (dielectric constant) of vacuum and is equal to 8.854 10^{-12} C^2/m^2. When insulating material which reduces the voltage because of its effect on the

electric field is inserted between the conductors the capacity is increased. Such materials are called dielectrics with the other words we can describe material as a substance with no free charges (Figure 14b). When the electric field is applied molecules of a dielectric are in stirring state, their negatively charged electrons separate slightly from their positively charged cores and they are pulled in the opposite direction of the electric field. The separation of charges continues till the external electric fields are balanced by the internal forces. This creates two new centres of charge, the molecule is said to be polarized and is known as induced electric dipole. The dipole moment so acquired is known as induced electric dipole moment.

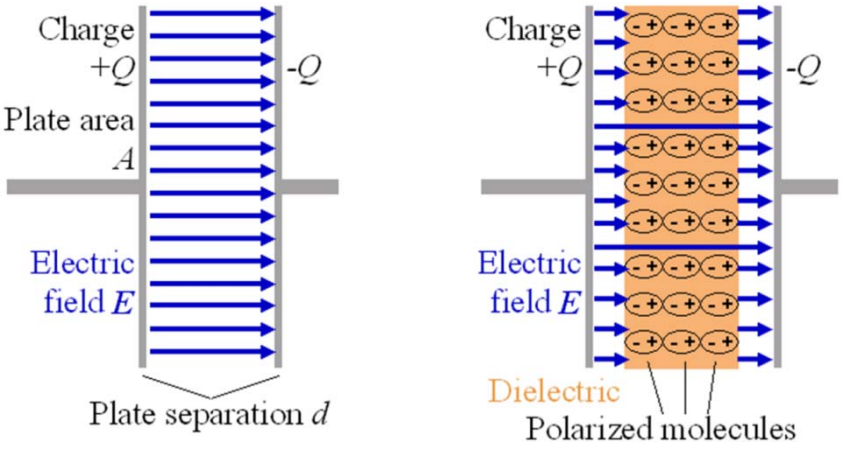

Figure 14. *Charge on a parallel-plane capacitor with (a) vacuum as a dielectric and (b) as a dielectric material between plates.*

The dielectric constant (k) is a physical measure of the electric polarizability of a material and is defined as the ratio of the capacitance of a capacitor, with a dielectric between the plates to that with a vacuum between the plates.

$$k = \frac{C}{C_o} = \frac{\frac{\varepsilon A}{d}}{\frac{\varepsilon_0 A}{d}} = \frac{\varepsilon}{\varepsilon_0} \tag{26}$$

where ε is defined as the permittivity of dielectric material. The dielectric constant (k) can be also called the relative permittivity (ε_r). In order to avoid the confusion of these two terms with similar meaning, the term relative permittivity will be used in the continuation.

1.4.1.1 Mechanisms of polarizations

When an electric field is applied to an ideal dielectric material there is no long-range transport of charge but only a limited rearrangement such that the dielectric acquires a dipole moment and is said to be polarized. The polarization effect is that the capacitor plates with an intermediate layer of dielectrics can store more charge than in the case where the vacuum is between plates. Quantity of stored charges in the condenser with contained dielectric is frequency dependent and bounded to the motion of four different carrier of polarization. Each mechanism involves a short-range motion of charge and contributes to the total polarization of the material. The polarization mechanisms are:

Interfacial or space charge polarization (P_i), occurs when mobile charge carriers are stopped by a physical barrier (Figure 15) that inhibit charge migration, possibly a grain or phase boundary, porous, dislocations etc. The charges are pile up at the barrier producing a localized polarization of the material that increases capacitance and dielectric constant. At this type of polarization the frequency range of sensitivity is very low, only a few 10 kHz and it is presented in Figure 16.

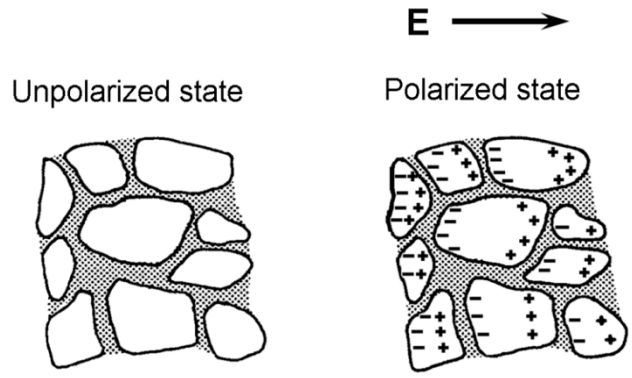

Figure 15. *Schematic representation of interfacial polarization mechanism.*

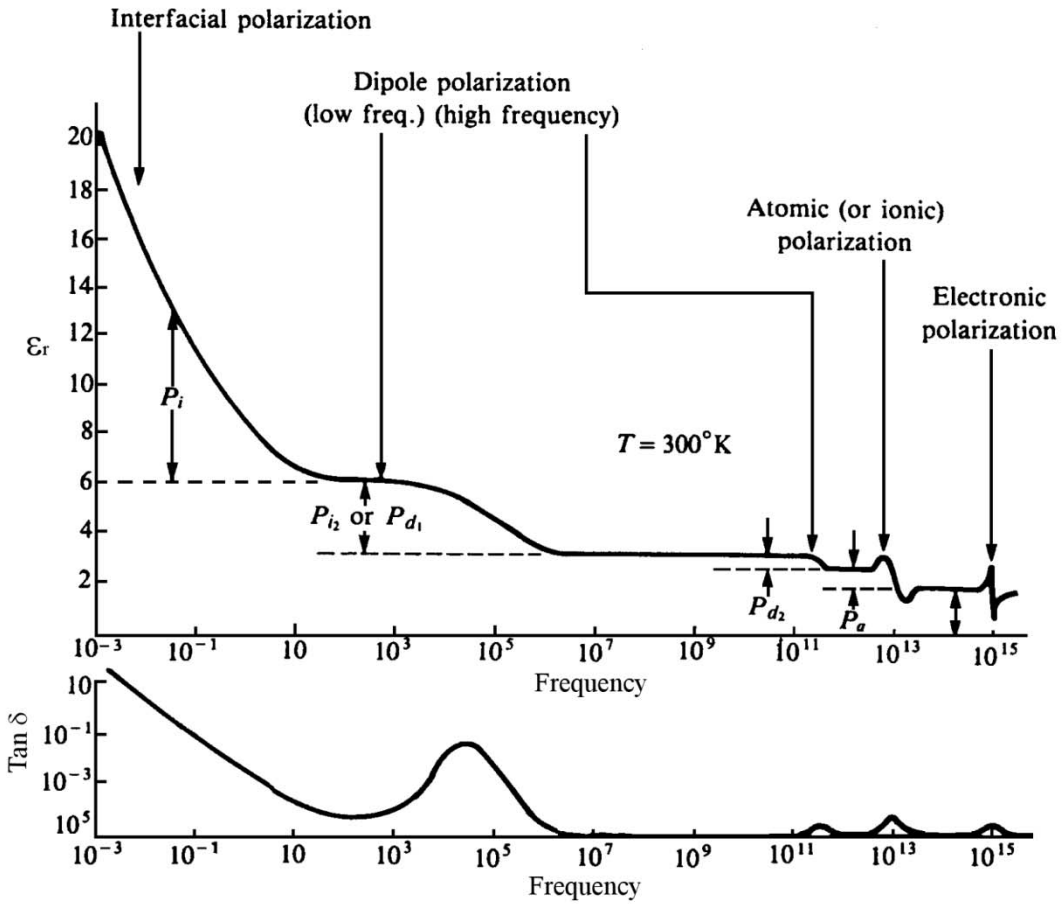

Figure 16. *Frequency dependence of the polarization mechanism in dielectrics with contribution to the dielectric constant and to the log tanδ.*

Dipole polarization (P_d) occurs when permanent dipoles in asymmetric molecules are orientated in the direction of the applied electric field (Figure 17) and it is characteristic for frequencies lower than 10^9 Hz. Presence of permanent electric dipoles exists even when the electric field is removed, which is particular for ferroelectrics. It is well known that motion of dipoles is temperature dependent; therefore the dipole polarization is likewise temperature dependent. In some literatures the dipole polarization is also known as oriental polarization.

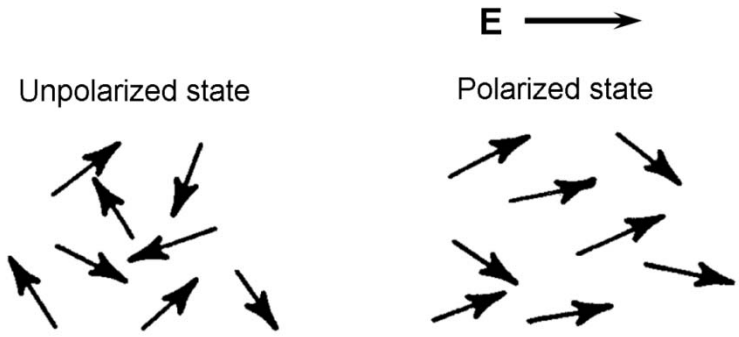

Figure 17. *Schematic representation of dipole polarization mechanism.*

Atomic or ionic polarization (P_a) occurs when adjacent positive and negative ions response with stretching under an applied electric field, such as shown in Figure 18. This is performed at frequencies lower than 10^{13} Hz (Figure 16). Resonance absorption occurs at a frequency characteristic of the bond strength between the ions.

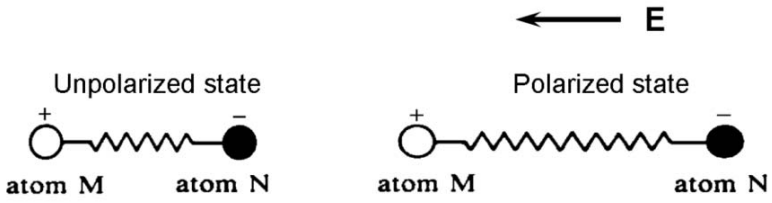

Figure 18. *Schematic representation of atomic polarization mechanism.*

A relation between the polarizability and the dielectric constant ε of a dielectric substance describe the Clausius-Mossotti equation which in expressed as:

$$\frac{\varepsilon-1}{\varepsilon+2}=\frac{4\pi}{3}N\alpha \tag{27}$$

where N is the number of molecules per unit volume, α is the polarizability of the molecules.

Electronic polarization (P_e) is due to the shift of the negative electron cloud of the ions within the material with respect to the positive atom nucleus in an electric field as shown in Figure 19. This mechanism occurs at very high frequencies above 10^{15} Hz which are in the ultraviolet optical range shown in Figure 16.

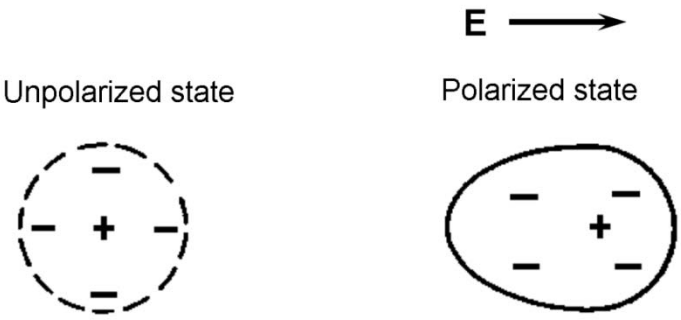

Figure 19. *Schematic representation of electronic polarization mechanism.*

In all cases, the polarization associated with the charge migration of polarization, therefore the certain time (relaxation time) is needed for reorganization of dipoles in the material. Different relaxation times of various polarization mechanisms are the reason for the frequency

dependence of polarization (Figure 16). This frequency dependence reflects the fact that a material's polarization does not respond instantaneously to an applied field. The response must always arise after the applied electric field which can be represented by a phase difference. At low frequencies of agitation, all the mechanisms of polarization might follow the changing of the electric field. With further increasing of frequency of the excitation, elimination of the space charge polarization occurred due to the highest relaxation time. Continuation of the excitation frequency growth first exclude the dipole and later ionic polarization therefore at the highest frequency range only electronic polarization is present.

The polarization (P) ie equal to the total dipole moment induced in the material by the electric field:[57]

$$P = N\overline{\mu} \tag{28}$$

where N is the number of dipole moment per unit volume and ($\overline{\mu}$) is the average dipole moment. The average dipole moment of the charged particles is proportional to the local electric field (E'), which acts on the particles:

$$\overline{\mu} = \alpha E' \tag{29}$$

where proportional factor (α) is the polarizability of average dipole moment per unit of local field strength. The expression for polarization considering the dipole moment is:

$$P = N\alpha E' \tag{30}$$

For insulating dielectric materials, polarization of the surrounding medium substantially effects the magnitude of the local field. Mossotti was the first to derive the local field contribution by the integration of the normal component of the polarized vector over the surface of a spherical cavity in the material, which enables following Clausius-Mossotti equation.

$$\frac{\varepsilon_r - 1}{\varepsilon_r + 2} = \frac{1}{3\varepsilon_0}\left[N_e\alpha_e + N_a\alpha_a + N_d\alpha_d + N_i\alpha_i\right] \tag{31}$$

Clausius-Mossotti equation connects the relative permittivity (ε_r) with the total number of polarizable species (N), and the total values of polarizability of the species (α). The Clausius-Mossotti equation shows explicitly how dielectric constant depends on composition and crystal structure through polarizability and molar volume. Dielectric constant depends on the

contribution of all four types of polarizations. The dielectric polarizability at high frequency range includes both ionic and electronic components. The electronic polarizability is related to the refractive index (n) by the Lorenz-Lorentz equation:[58]

$$P_e = \frac{3V_m}{4\pi} \cdot \frac{n^2 - 1}{n^2 + 2} \tag{32}$$

where V_m is the molar volume.

The contribution of ionic polarization can be experimentally determined and the ionic polarization of the random compound can be calculate with the help of the ion additivity rule:[58]

$$\alpha(M_2M'X_4) = 2\alpha(M) + \alpha(M') + 4\alpha(x) \tag{33}$$

Ion polarizabilities can be used to estimate the dielectric constant of complex ternary oxides and fluorides whose values have not been experimentally determined. There is good agreement between the calculated and experimentally measured values for many ternary systems including borates, silicates, aluminates, germinates, phosphates.

1.4.2 Dielectric losses

Energy losses in the material occur because of the processes which are dependent on the frequency of electro-magnetic field and nature of the material (Figure 16). At frequency at around 1kHz the energy losses occurs due to migration of ions, therefore ion conductivity appear or individual ions leap from one to another potential minimum. The vibration and deformation of ions prevail in the microwave frequency region. The dielectric losses, which appear due to the electronic polarization, are in this frequency region negligible and become considered only in UV region.

Consider a capacitor that consists of two parallel electrodes and a sinusoidal potential applied to the dielectric

$$V = V_0 e^{i\varpi t} \tag{34}$$

leads to the charging current (I_c) appear:

$$I_c = \frac{dQ}{dt} = \frac{CdV}{dt} = i\varpi CV = \varpi CV_0 e^{\left[i\left(\omega t + \frac{\pi}{2}\right)\right]} \tag{35}$$

where $\omega = 2\pi f$ is the angular velocity and C is capacitance.

In an ideal dielectric the charging current, which is associated with storage of electric by dipoles leads the applied voltage by a phase angle 90°. This relationship is vectorially described in Figure 20.

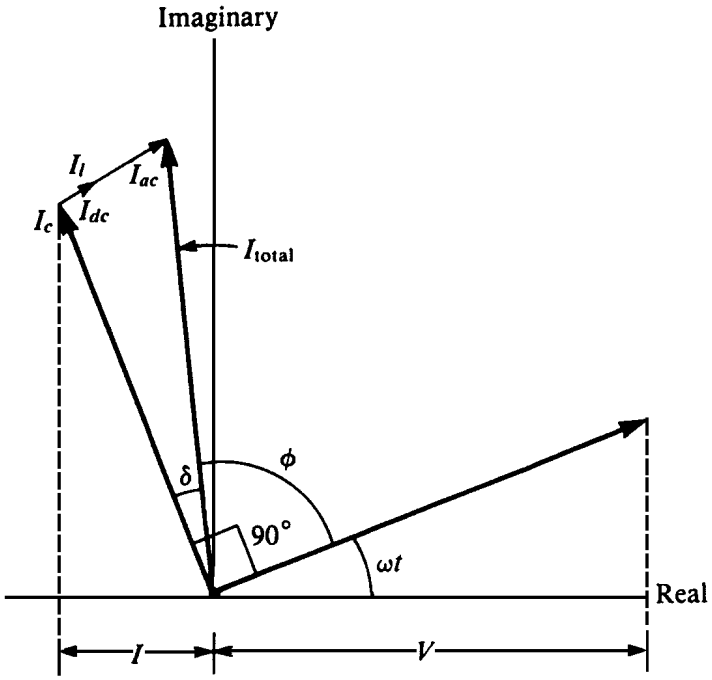

Figure 20. *Vector diagram of charging, loss and total currents in a dielectric.*

In real dielectrics loss current must be considered due to the formation of time delay. The loss current arises from the long-range migration of charges which leads to the origin of direct current (dc) and from the dissipation of energy associated with rotation or oscillation of dipoles. The latter contribution to the dielectric losses is a consequence of the charged particles having a specific mass and therefore an inertial resistance being moved. Both ac and dc conduction are in phase with the applied voltage. Loss current (I_l) in the dielectric can be written:

$$I_l = \left(G_{dc} + G_{ac}\right)V \tag{36}$$

where V is the voltage, G_{dc} is the direct current conductance and G_{ac} is the alternating current conductance. The total current (I_t) is the sum of Eq. 35 and Eq. 36:

$$I_T = I_c + I_l = \left(i\varpi C + G_{dc} + G_{ac}\right)V \tag{37}$$

The total current in real dielectric is a complex quantity, which leads the applied voltage by an angle (90°-δ) and not by 90° where δ is called the loss angle. Loss tangent δ representing the deviation from ideality of the losses in the dielectric material and from Figure 20 is

evident that tan δ defined as coefficient between loss and charging current.

The dielectric constant of a real dielectric might be expressed as a complex permittivity:

$$\varepsilon^* = \varepsilon' - i\varepsilon'' \tag{38}$$

Considering the Eq 26, Eq 34, Eq 35 and Eq 38 the total current can be defined as:

$$I = \frac{CdV}{dt} = \varepsilon_r C_0 i\varpi V = (\varepsilon' - i\varepsilon'')C_0 i\varpi V_0 e^{[i\varpi t]} \tag{39}$$

and thus

$$I_T = i\varpi\varepsilon' C_0 V + \varpi\varepsilon'' C_0 V \tag{40}$$

where ε' is the charging constant or often just dielectric constant and ε'' are referred to as the dielectric or relative loss factor. The first term on the right-hand side of Eq 37 describes charge storage in dielectric; second term refers to dielectric losses. The dissipation factor, loss angle or most commonly loss tangent (tan δ), is defined as:

$$\tan\delta = \frac{\varepsilon''}{\varepsilon'} \tag{41}$$

The quality factor (Q) is often used for extending dielectric losses at high-frequency insulation applications. The Q-value is defined as reciprocal of the tan δ.[59]

$$Q = \frac{1}{\tan\delta} = 2\pi \frac{Maximum\,energy\,stored\ \ per\ cycle}{Average\ energy\ dissipated\ \ per\ cycle} \tag{42}$$

It is known that the total dielectric loss is the sum of: intrinsic loss due to the interaction of the ac electric field with the phonons of the material and extrinsic loss owing to the coupling of the microwave field with defects.[60,61,62] Gurevich and Tagantsev developed a complete theory of intrinsic dielectric losses.[63] According to the theory of quantum mechanics, the intrinsic loss mainly corresponds to the absorption of the energetic quantum of the electromagnetic field in collisions with the thermal phonons. The intrinsic losses depend on the crystal symmetry, ac field frequency and temperature. These intrinsic losses fix the lover limit of losses in defect-free single crystals or ideal pure materials. On the other hand, the extrinsic dielectric losses are associated with imperfections in the crystal lattice such as impurities, microcraks, porosity, random crystallite orientation micro structural point (vacancies), linear (dislocations) and/or planar (grain boundaries) defects.[64] However, the extrinsic losses are caused by lattice defects and therefore can be in reduced or eliminated by

proper material processing. The losses due to the different types of defect show different frequency and temperature dependents symmetry.[59]

1.4.3 Temperature coefficient of resonant frequency

One of the most selective characteristic of dielectric materials is temperature coefficient of resonant frequency (τ_f), which describes the relative changes of resonance frequency of dielectric resonator in defined temperature range. The values of τ_f are usually predicted by empirical methods and its relation with the temperature coefficient of permittivity (τ_ε) is described by Equation 23. Relative permittivity is related to the physical-structural characteristics of crystal (polarizability, molar volume), which is given by Clausius-Mosotti equation (Eq 31). The τ_ε can be expressed by differentiating the Clausius-Mosotti equation with respect to temperature at constant pressure:[65,66]

$$\frac{1}{(\varepsilon_r-1)(\varepsilon_r+2)}\left(\frac{\partial\varepsilon_r}{\partial T}\right)_p=-\frac{1}{3V}\left(\frac{\partial V}{\partial T}\right)_p+\frac{1}{3\alpha_D^T}\left(\frac{\partial\alpha_D^T}{\partial V}\right)_T\left(\frac{\partial V}{\partial T}\right)_p+\frac{1}{3\alpha_D^T}\left(\frac{\partial\alpha_D^T}{\partial T}\right)_V \tag{43}$$

and

$$\frac{1}{(\varepsilon_r-1)(\varepsilon_r+2)}\left(\frac{\partial\varepsilon_r}{\partial T}\right)_p=A+B+C \tag{44}$$

The A, B and C terms describe physical processes. Term A is related to the thermal expansion coefficient (α_l) and increasing of the temperature effect on the volume expansion result in lower concentration of polarizable particles per unit volume. Due to the positive thermal expansion coefficient, term A is almost always negative. Term B describes the variation in polarizability of a constant number of particles as a result of variation in volume with the temperature, and term C describe direct dependence of polarizability with the temperature at constant volume.

1.4.4 Prediction of the dielectric properties of the composite ceramics

Predicting the effective dielectric properties of the glass-ceramic composites is very important for design the composite materials. Several quantitative rules of the mixture models have been proposed for prediction of the dielectric properties of the multi-component systems. The most commonly used equation for predicting the dielectric constant of the mixture composition is the Maxwell–Wagner's equation shown in Eq. (45)[67]

$$\varepsilon_c = \nu_1 \varepsilon_1 + \nu_2 \varepsilon_2 \tag{45}$$

where ν and ε are the volume fraction and relative dielectric constant of phase.

Lichtenecker suggested more accurate logarithmic model (Eq. 46) for the determination of the dielectric constant of the mixture described with following equation:[68]

$$\ln \varepsilon_c = \upsilon_1 \ln \varepsilon_1 + \upsilon_2 \ln \varepsilon_2 \tag{46}$$

The Lichtenecker logarithmic mixing rule is an inference equation that combines the parallel connection and series connection model, and the Lichtenecker logarithmic mixing rule can be thought to be composed of dielectric spheres with permittivity ε_2 uniform dispersed in a continuous medium with permittivity ε_1, where $\varepsilon_2 > \varepsilon_1$.[69]

More recently, Jayasundere–Smith suggested more accurate formula, which considered interactive effects between the fields of neighbouring spheres. According to this model, permittivity of mixed ceramic composition can be predicted as follows[70]

$$\varepsilon_c = \frac{\varepsilon_1 \nu_2 + \varepsilon_2 \nu_2 \left[\frac{3\varepsilon_1}{\varepsilon_2 + 2\varepsilon_1}\right]\left[1 + \frac{3\nu_2(\varepsilon_2 - \varepsilon_1)}{\varepsilon_2 + 2\varepsilon_1}\right]}{\nu_1 + \nu_2 \left[\frac{3\varepsilon_1}{\varepsilon_2 + 2\varepsilon_1}\right]\left[1 + \frac{3\nu_2(\varepsilon_2 - \varepsilon_1)}{\varepsilon_2 + 2\varepsilon_1}\right]} \tag{47}$$

For small volume fractions, these interactive effects of neighbouring spheres can be negligible.

The resultant dielectric loss of the mixture composed of two kinds of materials, can be expressed in the form of

$$\tan \delta = \upsilon_1 \tan \delta_1 + \upsilon_2 \tan \delta_2 \tag{48}$$

where $\tan \delta_1$ and $\tan \delta_2$ are the dielectric losses of the two components, respectively.

From Eqs. (42) and (48) the following relation for the Q value as a semi-empirical model was obtained:

$$\frac{1}{Q} = \frac{\upsilon_1}{Q_1} + \frac{\upsilon_2}{Q_2} \tag{49}$$

where Q_1 and Q_2 are the Q values of the two components and Q is the resultant Q value of the mixture.

To calculate the temperature coefficient of resonant frequency (τ_f) of mixture phase, a empirical model was proposed as follows:[71]

$$\tau_{f,mixture} = \upsilon_1 \tau_{f1} + \upsilon_2 \tau_{f2} \tag{50}$$

where τ_{f1} and τ_{f2} are the temperature coefficient of the two components and $\tau_{fmixture}$ is the resultant temperature coefficient of mixture. Generally variation of τ_f in a random mixture is proportional to the molar variation of the constituent phases.

1.5 Binary system $MgO\text{-}B_2O_3$

In the far past a lot of research were done in the $MgO\text{-}B_2O_3$ system. Phase relations in the system $MgO\text{-}B_2O_3$ were first examined by Toropov and Konovalov[72] in the 1940. Their work was based on the cooling curve analyses and they reported about the existence of the congruently melting compounds $3MgO{\cdot}B_2O_3$ (1400 °C), $2MgO{\cdot}B_2O_3$ (1381 °C), and $MgO{\cdot}B_2O_3$ (1183 °C). The phase diagram was revised by Davis and Knight[73] and they are mostly agreed with the general features of Toropov and Konovalov report, except that $MgO{\cdot}B_2O_3$ was shown to melt incongruently at 988 °C and the liquids temperatures were lower by 40 °C. The authors[72] also report about low-temperature exothermic break at 780 °C, for the phase which is poorer in MgO than $MgO{\cdot}B_2O_3$. That effect was not observed by Davis and Knight or any other researcher who was later involved in study of this phase diagram. Kuzel,[74] which subsequently synthesized the $MgO{\cdot}2B_2O_3$ compound also reported that $MgO{\cdot}B_2O_3$ compound does not exist as such but rather was a mixture of $MgO{\cdot}2B_2O_3$ and $2MgO{\cdot}B_2O_3$. Kuzel's research was confirmed by Fletcher et. al.,[75] who also detected no solid solutions in the system. Finally it was proved that the $MgO{\cdot}B_2O_3$ compound does not exist.[74,75,76,77] The compound $MgO{\cdot}2B_2O_3$, which was first reported by Kuzel, was lately confirmed by many authors[76,77]. All the above mentioned researcher agreed about the existence of $3MgO{\cdot}B_2O_3$ and $2MgO{\cdot}B_2O_3$ compounds. In the Table 3 there are names of all reported compounds and investigators in the system $MgO\text{-}B_2O_3$. Phase equilibria were revised

in the system $MgO-B_2O_3$ as the result of a study using DTA and quenching method by Mutluer and Timucin[77]. They corrected and constructed the phase diagram (Figure 21) in the central portion due to the peritectic transformation of $2MgO \cdot B_2O_3$ at 1312 °C. Although Davis and Knight[73] found at 57.7 wt.% MgO and 1313 °C the eutectic between pyroborate ($2MgO \cdot B_2O_3$) and orthoborate ($3MgO \cdot B_2O_3$).

Table 3. *Names of compounds and investigators in the system $MgO-B_2O_3$.[76]*

Compound	Investigators	
	Confirmed by	Not Confirmed by
$MgO \cdot B_2O_3$	Davis and Knight, Toropov and Konovalov, Yamaguchi	Kuzel, Fletcher, Watanabe, Stevenson and Whitaker
$MgO \cdot 2B_2O_3$	Fletcher, Stevenson and Whitaker, Kuzel, Nakamura	Davis and Knight, Toropov and Konovalov, Okawara and Yamaguchi,
$3MgO \cdot B_2O_3$	Davis and Knight, Nefedov	
$2MgO \cdot B_2O_3$	Davis and Knight, Nefedov , Mrose, Toropov and Konovalov, Watanabe, Fletcher, Stevenson and Whitaker, Okawara and Yamaguchi, Takeuchi, Kuzel, Nakamura, Berger , White	

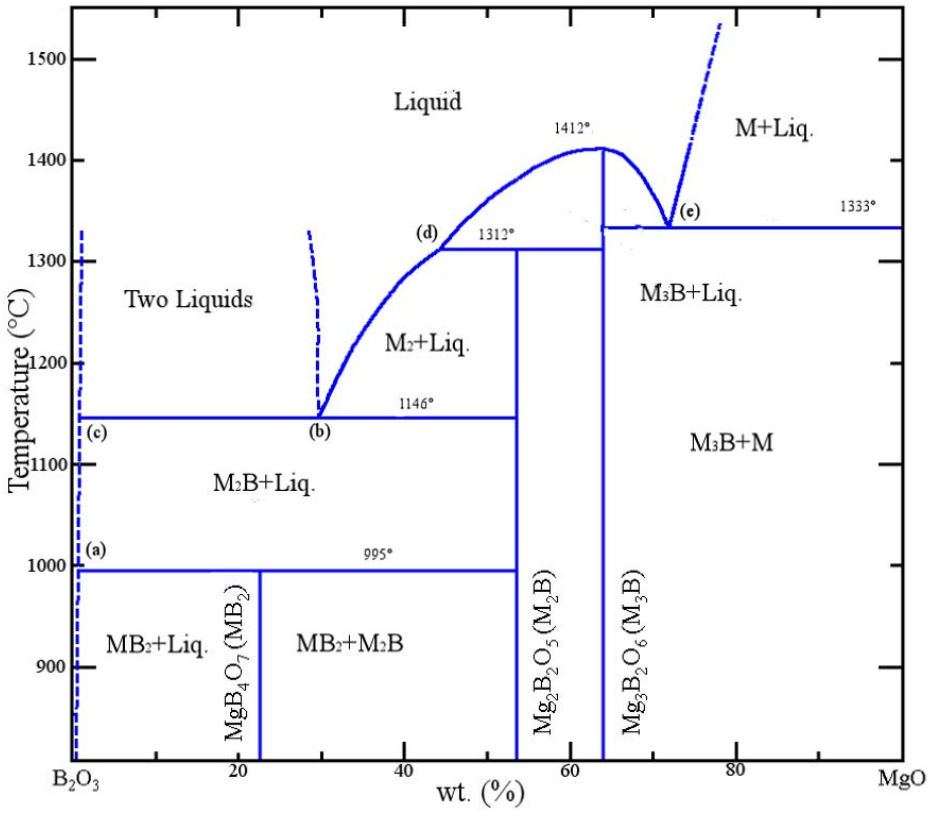

Figure 21. *The phase diagram $MgO-B_2O_3$.*

The system $MgO\text{-}B_2O_3$ contains 4 invariant points, such as:
peritectic at 995 °C,

$$\mathbf{MgO{\cdot}2B_2O_3\,(s) \leftrightarrow Liquid\ (a) + 2MgO{\cdot}B_2O_3\,(s)} \quad (51)$$

a monotectic at 1146 °C,

$$\mathbf{Liquid\ (b) \leftrightarrow Liquid\ (c) + 2MgO{\cdot}B_2O_3\,(s)} \quad (52)$$

a second peritectic at 1312 °C

$$\mathbf{2MgO{\cdot}2B_2O_3\,(s) \leftrightarrow Liquid\ (d) + 3MgO{\cdot}B_2O_3\,(s)} \quad (53)$$

and a eutectic at 1333 °C

$$\mathbf{Liquid\ (e) \leftrightarrow 3MgO{\cdot}2B_2O_3\,(s) + MgO\,(s)} \quad (54)$$

where (a)-(e) designate the equilibrium liquids in Figure 21. First two reactions (Eq 51 and Eq 52) and the temperature at which they occur are similar to those found by Davis and Knight,[73] except that the incongruently melting compound in first (Eq 51) is $MgO{\cdot}2B_2O_3$ rather than $MgO{\cdot}B_2O_3$ and the monotectic liquid in Eq 52 contains 30 wt.% MgO rather than 36 wt.%.

According to Toropov and Konovalov[72] and Davis and Knight[73] the $2MgO{\cdot}B_2O_3$ compound, would melt congruently at 1381 °C and at 1340 °C, respectively. Later on Mutluer and Timucin[77] refuted that theory and with the additional DTA analyses they showed, $2MgO{\cdot}B_2O_3$ compound melts incongruently at 1312 °C and is related to $3MgO{\cdot}B_2O_3$ by a peritectic reaction, as opposed to the eutectic reaction predicted by previous investigators. Researchers[73,77] agrees well with the melting temperature of $3MgO{\cdot}B_2O_3$, (1410 °C) determined by Toropov and Konovalov[72]. On the basis of Mutluer and Timucin[77] isothermal determination of the eutectic temperature, which is lower for about 30 °C than previous estimates. The composition of the eutectic liquid is the same in all the proposed diagrams. The steep slope of the MgO liquidus, which is inferred above 1450 °C, suggests that small additions of B_2O_3 to MgO decrease the melting point of the latter rather rapidly, thus deteriorating its refractoriness.

Magnesium borates such as MgB_4O_7, $Mg_2B_2O_5$ and $Mg_3B_2O_6$ referring to previously mentioned $MgO{\cdot}2B_2O_3$, $2MgO{\cdot}B_2O_3$ and $3MgO{\cdot}B_2O_3$, respectively are very remarkable ceramic materials due to their interesting mechanical properties, attractive thermal properties, thermo-luminescent properties,[78,79] its high resistance to corrosion and good antiwear

behaviour[80]. Various synthesis methods for preparation of magnesium borate have been proposed up to now. In recent years, several nanostructure forms of $Mg_2B_2O_5$, such as nanowires, nanotubes, nanobelts and whiskers, have been synthesized through chemical vapour deposition CVD method,[81] catalyst-free method,[82] high temperature solid-state synthesis method,[83,84] solvothermal method[85] respectively. Bando et al. prepared MgB_4O_7 nanowires[86] and $Mg_3B_2O_6$ nanotubes[87] via thermal evaporation and IR irradiation methods, respectively. Zhang et al.[88] synthesized single crystalline $Mg_3B_2O_6$ nanobelts by heating a mixture of boron and MgO powders under flowing Ar/H_2O gases.
However, numerous methods have been used recently for the synthesis of magnesium borates for different applications. In our work we synthesized $Mg_2B_2O_5$ and $Mg_3B_2O_6$ with the solid state reaction and the dielectric properties of binary compounds, which have not been known yet, were also determined.

1.5.1 $Mg_2B_2O_5$

Magnesium pyroborate ($Mg_2B_2O_5$) is in nature known as a suanite mineral and it was first found by Watanabe[89] in North Korea mine, as a fibrous aggregate of monoclinic crystals. Crystal structure of $Mg_2B_2O_5$ was determined by Takeuchi [90] in 1952, and its properties $Mg_2B_2O_5$ and structure have been compiled by Mrose et al.[91]. The synthetic $Mg_2B_2O_5$ was obtained usually as a mixture of monoclinic and triclinic structures. The monoclinic as well as the triclinic form of $Mg_2B_2O_5$ is heteromorphic, which means that the structure differing from standard form. The monoclinic structure (space group $P2_1/c$) of $Mg_2B_2O_5$ is described by G. C. Guo et al.[92] shown in Figure 22 where the large circles represent Mg atoms, medium circles O atoms, and small circles B atoms. The structure of the monoclinic form of $Mg_2B_2O_5$ is based on Mg_4O_{18} tetramers, composed of four Mg octahedra linked by three shared edges, and connected by sharing four O···O edges to form chains extending along [010]. The B atoms hold the chains together and form B_2O_5 (double-triangle) groups. The Mg···Mg distances in the Mg_4O_{18} tetramers are 3.148 (3) and 3.152 (3) Å. The O atoms of each B_2O_5 group are not quite coplanar; the dihedral angle between the two slanting trigonal-planar BO_3 groups is 14.90 °.

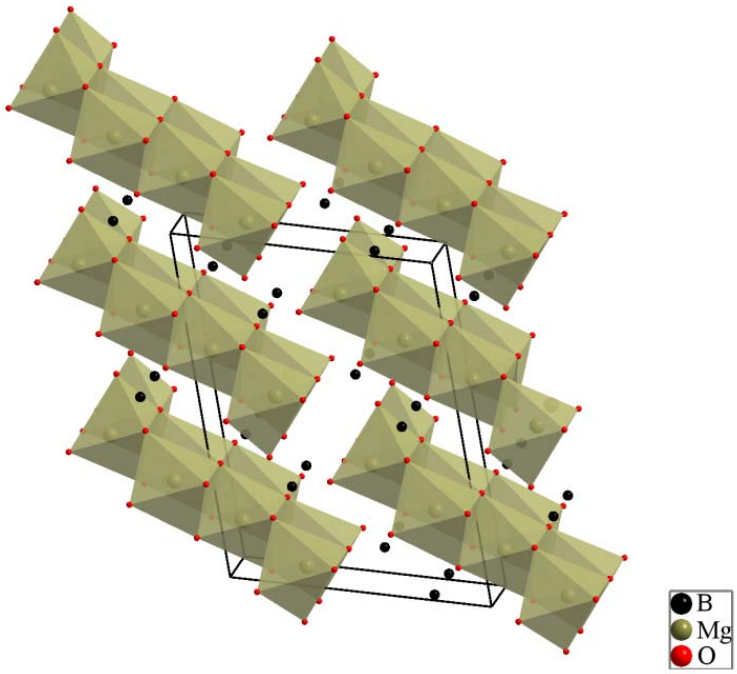

Figure 22. *The structure of $Mg_2B_2O_5$ viewed along [010].*

Likewise as the monoclinic form also the single-crystal structure of triclinic (space group Pī) magnesium pyroborate $Mg_2B_2O_5$ was determined by G. C. Guo et al.[93] The structure of triclinic $Mg_2B_2O_5$ is illustrated in Figure 23 where the large open circles represent Mg atoms, small open circles O atoms and small black circles B atoms. The triclinic $Mg_2B_2O_5$ structure is based on $[Mg_4O_{18}]$ tetramers, composed of four octahedra linked by three shared edges, connected, through sharing four O-O edges, into chains extended along (001). The B atoms hold the chains together and form B_2O_5 (double-triangle) groups. In the Mg octahedral polymer $[Mg_4O_{18}]$, the Mg···Mg distances are 3.175(2) and 3.131(2) Å. The O atoms of the B_2O_5 group are not quite coplanar; the dihedral angle between the two slanting trigonal planar BO_3 groups is 9.84 °.

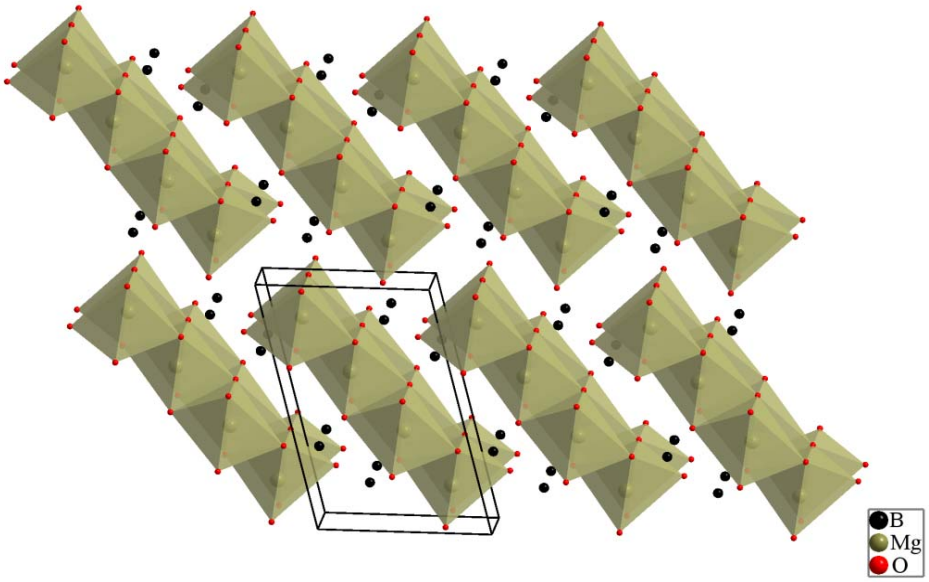

Figure 23. *The structure of $Mg_2B_2O_5$ projected on [001].*

1.5.2 $Mg_3B_2O_6$

$Mg_3B_2O_6$ is known as a Kotoite mineral and it was discovered and described by mineralogist Takeo Watanabe [89] in 1939. He was investigating the ores from North Korean Hol Kol mine. Effenberger and Perttlik[94] produced and studied the single crystal forms of the three compounds $M_3(BO_3)_2$ (M = Mg, Co and Ni) and compared with crystal system of $Mn_3(BO_3)_2$[95]. They found that all of the synthesized metal orthoborates were crystallized in the kotoite form. The mineral Kotoite with space group *Pnmn* is an orthorhombic crystal where each Mg atom is surrounded by an octahedron of oxygen atoms. Boron atoms are surrounded by three oxygen atoms, BO_3, in a triangular configuration shown in Figure 24.

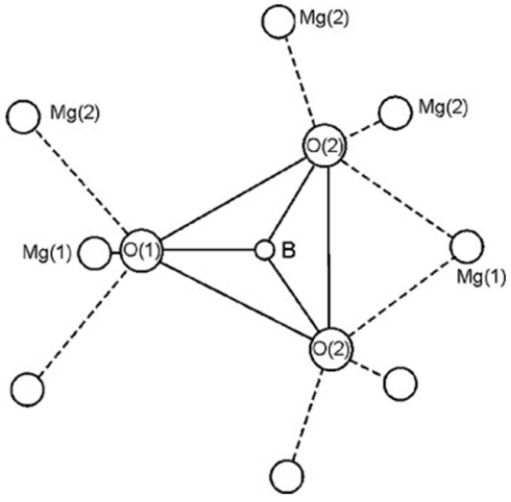

Figure 24. *BO_3 coordination of atoms in $Mg_3B_2O_6$.*

However magnesium occupies the centre of an octahedron and boron occupies the centre of a triangle. The crystal structure of magnesium orthoborates has been also analyzed by Berger[96] who found that isomorphous orthoborates of cobalt and magnesium is orthorombic in the unit cell.

1.6 Ternary $MgO-B_2O_3-SiO_2$ system

The phase equilibrium diagram for the $MgO-B_2O_3-SiO_2$ system was first established by Kuzel[97] in 1963, illustrated in Figure 25. Therefore this phase diagram has been evaluated from data obtained essentially by the quenching method using ternary compositions. The melting was performed in platinum crucible. Kuzel[97] determined the phase diagram by means of differential thermal analysis and X-ray diffraction. Within the investigated part of the diagram, the components and compounds MgO, $2MgO\cdot SiO_2$, $MgO\cdot SiO_2$, SiO_2, $3MgO\cdot B_2O_3$ and $2MgO\cdot B_2O_3$ posses primary fields. Vaporization of boric acid was substituted with the addition of boric acid until theoretical compositions were achieved. The fields of cristobalite (SiO_2), protoenstatite ($MgO\cdot SiO_2$) and the compound of $2MgO\cdot B_2O_3$ lie predominantly under a large region of liquid immiscibility. The wide region of $MgO\cdot SiO_2$, $2MgO\cdot B_2O_3$ and the compound of $2MgO\cdot SiO_2$ contains two ternary eutectics at 1186 and 1203 °C, respectively. These regions extend across the diagram between the magnesia-silica side and the magnesia-boric oxide side. Two from five triangle systems contains single ternary eutectic. The sub-systems such as $MgO-3MgO\cdot B_2O_3-2MgO\cdot SiO_2$ and $3MgO\cdot B_2O_3-2MgO\cdot B_2O_3-2MgO\cdot SiO_2$ comprise ternary eutectic at 1327 and 1270 °C, respectively. The fifth triangle $2MgO\cdot B_2O_3-B_2O_3-SiO_2$ assumedly possess eutectic at very low level of MgO. In abovementioned sub-system there are two melts and two solid binaries $Mg_2B_2O_5$ and $Mg_2B_2O_4$, respectively. The latter composition was later on confirmed by many researchers as a non-existent. In the whole equilibrium diagram $MgO-B_2O_3-SiO_2$ was no indication for a ternary compound.

Suanite $Mg_2B_2O_5$ crystallizes in ternary as well as in binary sub-system always as a triclinic modification. Kuzel in his paper evidently affirmed that monoclinic Suanit was not obtained in any case.

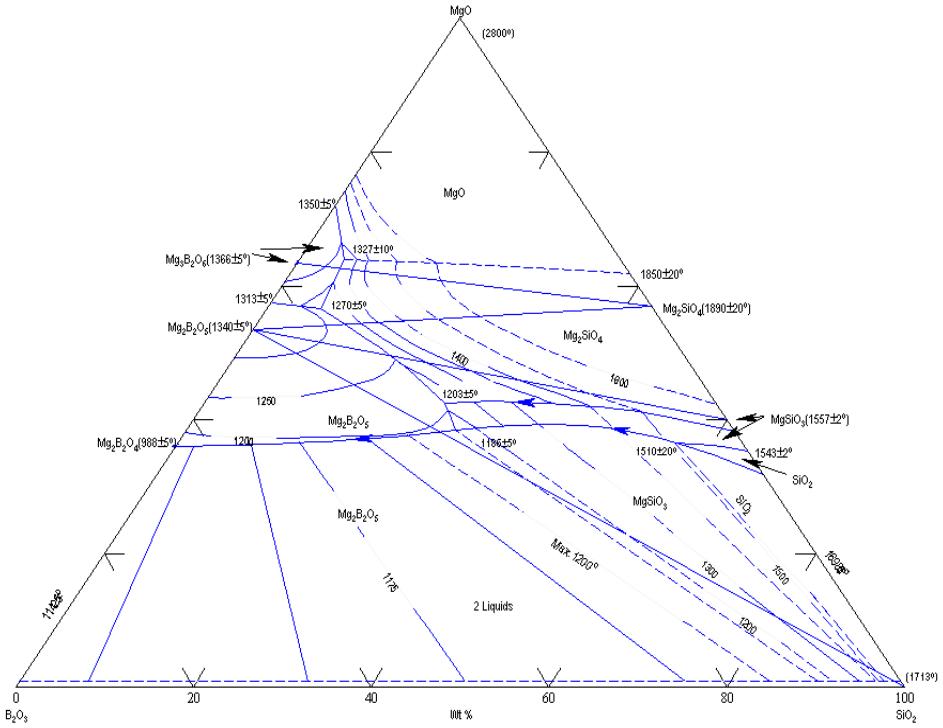

Figure 25. *MgO-B_2O_3-SiO_2 ternary phase diagram.*

2 Aims and Hypothesis

Glasses and glass-ceramics materials have been widely investigated for various technological applications in optics and electronics. Glass-ceramics are also constituents of advanced microelectronic packaging, where they are mainly used as low-temperature co-fired ceramic (LTCC) dielectric substrates. Taking into account the dielectric requirements of low permittivity ($\varepsilon < 8$) and high quality factor ($Q = 1/\tan\delta$), the pure ceramic materials would be more appropriate for the dielectric substrate applications than glass-ceramics. However, low-permittivity ceramics materials sinter at high temperatures (> 1000 °C), while the glass-ceramics compositions enable the sintering at the LTCC sintering conditions (< 900 °C). Due to the incomplete crystallization of glass, glass-ceramics still contain some glass, which lower the Q-values. The high Q-value of the glass-ceramics could be achieved firstly by decreasing the amount of the glassy phase and secondly by the selection of the system with high Q crystallisable phases. Minimizing of the glassy phase content is attained by controlled crystallization, which is possible only with the knowledge of the nucleation and the crystallization processes. For the selection of the glass-ceramics system for LTCC substrate applications not only the type, but also the number of crystallisable phases is important. Namely, the probability for the reaction with the electrodes and other co-fired materials increase with the number of phases.

Taking into account the above-mentioned reasons, $MgO\text{-}B_2O_3\text{-}SiO_2$ (MBS) system was selected to investigate as potential material for LTCC substrate applications. Depending on the composition $MgSiO_3$, Mg_2SiO_4, $Mg_2B_2O_5$ or $Mg_3B_2O_6$ are expected to crystallize from MBS glass. $MgSiO_3$ and Mg_2SiO_4 have been already reported to exhibit high Qxf values of 120 000 and 240 000 GHz, respectively. The investigations, which were performed in the scope of this study, revealed promising dielectric properties of $Mg_2B_2O_5$ and $Mg_3B_2O_6$. In particular, $Mg_3B_2O_6$ was found to exhibit high Qxf values of 100 000 - 240 000 GHz. The conditions for the preparation of $Mg_3B_2O_6$ with Qxf values over 200 000 GHz as well as microstructural phenomena of exaggerated grown grains were investigated in details.

It is well known that the complete densification and the high crystallinity are indispensible for good mechanical strength and for high Qxf values of glass-ceramics materials. The tailoring of these properties becomes possible when the processes during transformation from the glass to the glass-ceramics are well understood. In order to enhance the crystallization,

TiO_2 nucleating agent was added to MBS glass. With the use of verified methods for the analysis of non-isothermal data we attempted to determine the following important characteristics of the MBS and TiO_2-added MBS glass: (i) the temperature range of nucleation, (ii) temperature of maximum nucleation rate (iii) the eventual overlapping of the nucleation and crystallization processes and (iv) kinetic parameters. Additionally, the crystallization mechanism for both glasses was inferred from non-isothermal DSC data and scanning electron microscopy measurements. The correctness of the determined values of Avrami parameter (n) and dimensionality of the crystal growth (m) were indirectly confirmed by employing of different methods for the analysis of the thermo analytical data (Kissinger, Matusita, Ozawa-Chen). The study of crystallization kinetics was performed for bulk and powder MBS glass. Due to the mixed crystallization mechanism (surface and bulk) in the powder glass the meaningful value of activation energy were obtained only for the bulk glass.

Based on the knowledge about the nucleation and crystallization processes, the synthesis and the sintering of MBS glass-ceramics was optimized and finally the dielectric and the structural characterization of the MBS glass-ceramics was performed. The influence of TiO_2 nucleating agent on the crystallization and consequently on the dielectric properties was examined.

3 Materials and Methods

3.1 Glass and ceramic preparation

3.1.1 Chemical used

Magnesium oxide (Sigma Aldrich) with 98 % purity, boron oxide (Alfa Aesar) with 99.98 %, silicon oxide (Alfa Aesar) with 99.8 % purity and titanium (IV) oxide rutile (Alfa Aesar) with 99.99 % were used as starting materials Table 4.

Table 4. *Raw materials for glass preparation and melting temperatures.*

	Magnesium oxide, MgO	Boron oxide, B_2O_3	Silicon oxide, SiO_2	Titanium oxide, TiO_2
Melting temperature (°C)	2852	450	1710	1843
Chemical composition	MgO 98% SO_4^{2-},SO_3^{2-} 0.02% Cl^- ≤0.01% NO_3^- ≤0.005% Na ≤0.5% Ca ≤0.05% Fe ≤0.01% K ≤0.005% Sr ≤0.005% Ba ≤0.005% Mn ≤5 ppm	B_2O_3 99.98% NO_3^- ≤0.005% Cl^- ≤0.002% Na ≤0.5% Ca ≤0.05% Fe ≤0.01% K ≤0.005% Sr ≤0.005% Ba ≤0.005% Mn ≤5 ppm	SiO_2 99.8% Al_2O_3 0.001 Fe_2O_3 0.0005 K_2O 0.0005 Na_2O 0.0005 Fe^{3+} ≤1 ppm	TiO_2 99.99% Al_2O_3 0.001 CaO 0.042 Fe_2O_3 0.001 K_2O 0.006 MgO 0.008 P_2O_5 0.07 SiO_2 0.015 ZrO_2 <0.005 Na_2O 0.009 SO_3 0.001

3.1.2 Preparation of $MgO – B_2O_3 – SiO_2$ glass

The initial oxides were dried at 150 °C at conventional hot air drier and homogenized with zirconia balls (d = 5 mm) in plastic jars using turbula mill for 60 minutes. The samples were stored in desiccator filled with silica-gel to keep them in a dry environment. According to the phase diagram of the MgO-B_2O_3-SiO_2 system[97] the ratios of chosen components were 43

wt.% MgO, 35 wt.% B_2O_3 and 22 wt.% SiO_2. After homogenization dried powders were melted in a corundum and platinum crucible, respectively. Each batch was melted in an electric furnace (Nabertherm) at 1350 °C exceptionally 1500 °C when the nucleating agent TiO_2 was added. The melt was held at the maximum temperature for 30 minutes where the viscosity of the melt was low enough so that the melt could be easily poured onto a graphite plate to avoid occurrence of any crystallization. The glass was crushed with vibrational mill in order to ensure complete homogenization of the glass the whole melting procedure was repeated. This melting regime was found sufficient to yield bubble free, transparent and colourless quenched glass frit with no visible crystalline inclusions, which was also confirmed by X-ray analyses (Figure 26). Subsequently, the glass powders prepared for sintering were milled in acetone region with Y-stabilized ZrO_2 balls (d = 3 mm) in planetarium ball mill (Fritsch, Pulverisette 5) at various milling time. The pulverized glass powders were dried and uniaxially pressed at about 100 MPa to obtain green compacts with a diameter of 12 mm and thickness of around 4 mm. The prepared samples were characterized by different methods: XRD, DSC, heating microscope, dielectric measurements and Archimedes' density.

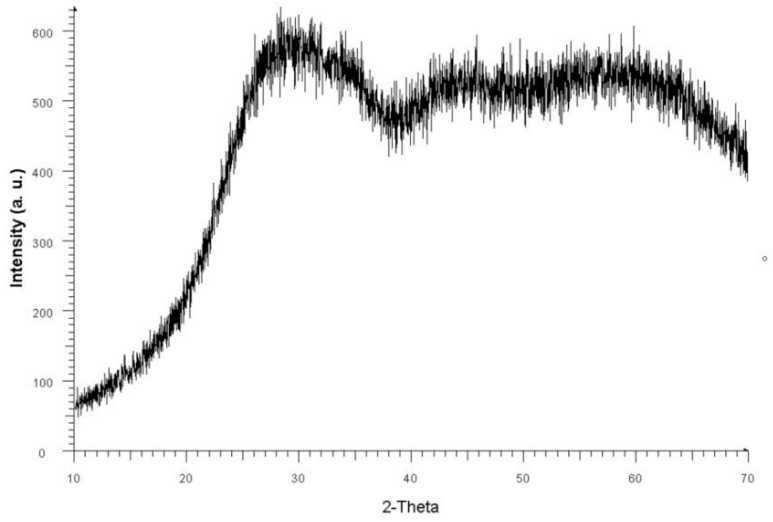

Figure 26. *X-ray analysis of glass with the following composition 43 wt.% MgO, 35 wt.% B_2O_3 and 22 wt.% SiO_2.*

3.1.3 Synthesis of the $Mg_2B_2O_5$ and $Mg_3B_2O_6$ ceramic sample

The ceramic compounds $Mg_2B_2O_5$ and $Mg_3B_2O_6$ from the binary MgO-B_2O_3 system were synthesized using solid-state reaction techniques. Prior to weighing (Mettler H35AR analytical balance), the initial oxide powders MgO and B_2O_3 were dried for 12 h at 500 °C and 100 °C, respectively. These dried powders were then homogenized in acetone regime and repeatedly pre-reacted with intermediate grinding and milling. Detailed pre-reaction conditions for the $Mg_2B_2O_5$ and the $Mg_3B_2O_6$ are represented in Table 5.

Table 5. *Pre-reactions and sintering conditions of $Mg_3B_2O_6$ and $Mg_2B_2O_5$ ceramics.*

Material	Pre-reactions temperatures (°C)	Sintering temperature (°C)	Structure
$Mg_3B_2O_6$	600, 900, 1000, 1100, 1200	1200-1300	S.G.: Pnm
$Mg_2B_2O_5$	600, 900, 1000, 1100, 1200	1250-1280	S.G. $P\bar{1}$

The loss of B_2O_3, which occurred during the pre-reactions, was compensated by weighing an 11 wt.% and a 14 wt.% excess of B_2O_3 for the $Mg_3B_2O_6$ and the $Mg_2B_2O_5$, respectively. Prior to the sintering, the powders were milled in a planetary ball mill (Fritsch, Pulversette 5) with Yttria-stabilized ZrO_2 balls, at 200 rpm for 2 hours. The size of the particles after the milling was analyzed using a HR 850 Alcatel Cilas laser granulometer, which showed that the median particle size (d_{50}) was up to 1 μm. The milled powders were dried in Kambic drier then uniaxially pressed under a pressure of the 100 MPa to obtain a green compacts with a diameter of 12 mm and a thickness of around 4 mm. The sintering of the compressed samples in order to defined the sintering conditions were observed by means of the heating microscope (EM 201, Hesse Instruments), with a heating rate of 10 °C/min. The green pellets were sintered at different temperatures for various periods of time and then cooled to the room temperature. The sintering was performed in a tube furnace in an air atmosphere with 10 °C/min heating rate. The cooling rate from the sintering temperature (T_s) was either fast or slow, with the latter being a controlled cooling rate of 2 °C/min. Fast cooling refers to uncontrolled cooling in the furnace as a result of natural convection, conduction and radiation from the sintering temperature to the room temperature. The density of the sintered glass-ceramic specimens as a function of sintering temperature were evaluated by the Archimedes immersion liquid displacement method using an analytical balance an acetone as the reference liquid. The literature data of 3.086 g/cm^3 (PDF 38-1475) and 2.91 g/cm^3 (PDF 15-0537) were used for the theoretical densities of the $Mg_3B_2O_6$ and the $Mg_2B_2O_5$.[98] The relative densities (ρ_r) were obtained by comparing the measured densities with the theoretical ones.

3.2 Characterization methods

3.2.1 X-ray powder diffraction

X-ray powder diffraction (XRD) is a very effective technique for the investigation of the crystal structure and phase analyses of the material. The degree of the crystallinity and the identification of the phases developed after the crystallization were examined by X-ray powder diffraction analyses of crystalline samples. A mortar and pestle were used to grind the

glass-ceramic and ceramic samples into a fine powder that were tested by XRD. In principle, X-rays are directed to the powder sample where they interact with the crystalline material and diffract at different angles. These diffracted beams are then directed to the detector, e.g., scintillation, proportional or solid state detector, which measures the beam intensity. Namely, the detector collects x-ray photon and then converts them into a measurable signal or eventually to the X-ray diffraction pattern. For the identification of the crystalline phases present in the sample, position and intensity matching of the spectrum is performed with reference to the established ICDD (International Centre for Diffraction Data) database. This latter task is normally carried out with the aid of the accompanied software. XRD analysis was used to identify the crystalline phase(s) that forms in the prepared glass-ceramic and ceramic material. The analysis was performed on pulverized specimens of the ceramic and glass-ceramic materials, and was carried out using a D4 Endeavor, Bruker AXS, powder diffractometer with a 2θ scan range between 10 ° and 90 °. Step size and counting time were changing regarding to demand of preciseness of measurement. XRD patterns were also recorded on a PAN alytical X'Pert PRO diffractometer with CuKα radiation in configuration with Johanson's monochromator to remove the $CuK\alpha_2$ radiation. In this case step size was 0.008 ° and counting time 100 s. Used diffractometers differ in counting time.

3.2.2 Microstructure analyses

For the following analyses the sample preparation technique distinguishes according to the microscope and consequently to the desired information.

3.2.2.1 Optical microscope

The surface topographies of the produced vitreous and sintered glass-ceramic materials which were previously polished and then chemically or thermally etched were analyzed using an Olympus BX 60 Microscope equipped with Olympus DP soft image Analyzer. The surface was scanned and images were taken to reveal the visible changes appeared from the heat treatment. The topography information's were prerequisite for the further characterization.

3.2.2.2 Scanning electron microscope (SEM)

The usual procedure of specimen preparation for metallographic examination involves grinding on progressively finer silicon carbide (SiC) papers and polishing with a polishing cloth and a polycrystalline diamond powder paste (Struers) with 3 and ¼ μm roughness. The selected samples were mounted in a conventional metallographic mounting medium technovit (Demotec 30) to increase stability during grinding and polishing. During mounting, the

samples were carefully positioned so the polished cross-section surface was perpendicular to the cut surface. The metallographic procedure was done on a Struers RotoPol-21. After polishing vitreous, glass-ceramic and ceramic specimens were thermally or chemically etched. The polished ceramic $Mg_3B_2O_6$ and $Mg_2B_2O_5$ materials were thermally etched 50 °C bellow the sintering temperatures for 20 minutes. The glass and glass-ceramic were chemically etched with an aqueous solution of 10 ml HNO_3, 20 ml of H_2O and 5 ml of HF for 2 minutes in order to dissolve a thin layer of glass and reveal the crystalline phases that were formed. With the help of optical microscope we kept the control of etching. Due to the material's non conductive nature, the samples had to be coated with a thin layer of carbon.

The microstructures of so prepared specimens were characterized and observed using scanning electron microscope (SEM JEOL JXA 840A, JSM 5800 and FE-SEM 7600), which were operating at different accelerating voltage from 5 to 20 keV. Scanning electron micrographs with the help of an image-tool program were used to determine the grain size area on a polished cross-section.

3.2.2.3 A transmission electron microscope (TEM)

A transmission electron microscope (TEM) (JEM 2100, JEOL, Tokyo, Japan) equipped with a Gatan ORIUS SC1000 CCD camera was utilized to examine the grain boundaries. Prior to the TEM investigation, the samples were cut into 3-mm-diameter discs, ground to a thickness of approximately 120 μm, dimple ground to 20 μm and ion milled to electron transparency using Ar ions at 3.8 kV.

3.2.2.4 Electron back scatter diffraction (EBSD)

Electron Back-Scatter Diffraction (EBSD) is another important analytical technique used to obtain information about crystallographic orientation of the specimen. However, EBSD employs an electron beam for acquiring a diffraction pattern and is performed using a Scanning Electron Microscope (SEM). Unlike conventional SEM, the EBSD setup requires that a sample be tilted at 70 ° from the horizontal position so that it is slanted as it is being bombarded by the descending electron beam. Moreover, the system needs to be equipped with a fluorescent phosphor screen detector to capture the pattern by the diffracted electrons. This pattern consists of intersecting lines, also referred to as Kikuchi bands. The complex matching of these Kikuchi bands is automated, and is usually achieved with reference to the databases accompanied with the software. EBSD analysis can only be considered for materials associated with crystalline phases that generate Kikuchi patterns. A non-crystalline material, such as glass, will not be suited for such an analysis since it cannot generate Kikuchi patterns.

In our case field-emission scanning electron microscopy (JSM 6500-F, JEOL, Tokyo,

Japan) with an EBSD Inca Crystal 300 with the corresponding software for the analysis of the Kikuchi patterns was used to determine the crystallographic orientation relationships of the $Mg_3B_2O_6$ twins.

3.2.3 Differential scanning calorimetry

Differential scanning calorimetry (DSC) was helpful in determining the crystallization and glass transition temperature of the glasses. Consequently on the basis of these data the proper heat treatment procedure could be established for the preparation of the glass-ceramics with the target properties. The crystallization is an exothermic process. This results from the fact that the crystalline phase has lower free energy than disorder glass. On the contrary, the melting of the crystalline phase is accompanied by the absorption of energy, which results as an endothermic peak in thermogram. The glass transition temperature is a second-order transition, which is accompanied by the change of heat capacity, what is noticed as the deviation of the baseline.

Differential scanning calorimetry was used to study the nucleation and crystallization phenomena of MgO-B_2O_3-SiO_2 system and calculate the activation energy of crystallization. Thermogravimetric (TG) and differential scanning calorimetry (DSC) analyses were performed on a Jupiter 449 simultaneous thermal analysis (STA) instrument coupled with a 403C Aëoloss mass spectrometer (MS) (Netzsch). Prior to measurements, the temperature of the DSC was calibrated using Au, In, Bi and Sn standards. The TG/DSC measurements were performed using a constant weight powder or bulk samples in an alumina crucible in argon 80 wt.% oxygen 20 wt.% atmosphere with various heating rates from 5 to 20 °C/min and the temperatures range was from room temperature to 1100 °C. Alumina powder was used as a reference material.

3.2.3.1 Determination of the temperature for maximum nucleation

Very important for the accurate crystallization of the glass is the knowledge of the nucleation process. The bulk samples were prepared with pouring melt on the graphite model covered with the holes with slightly smaller diameter compared to the diameter of alumina crucible used for DSC measurement. The size of the bulk samples is very important due to equal weight of the samples as well as the shape of the bulk should be flat because of better contact with the bottom of the measuring crucible. In the case of powder specimen the good thermal contact is assured.

The range of nucleation was determined with the help of differential scanning calorimetry of raw glass sample. Matusita[99] affirmed that the rate of crystal nucleation in glass usually

reaches the maximum at a temperature somewhat higher than the glass transition temperature and then decreases rapidly with increasing temperature. The procedure for determination of the temperature for maximum nucleation was as follows: the bulk glass – samples were nucleated at certain temperatures in the temperature range between the glass – transition temperature and crystallization on – set temperature. These nucleated samples were then heated with the heating rate of 10 °C/min in the DSC instruments to crystallize. The position of the crystallization peak maximum (T_p) and also its height depend on the number of nucleus formed during nucleation.[100,101] In the case of larger number of nuclei, the position of T_p is shifted to the lower temperature and its height increases. The temperatures of maximum nucleation rate were obtained from the plots of $100/T_p$ and peak height versus nucleation temperature.

3.2.3.2 Theoretical basics

Several analytical models[102,103,104,105,106,107,108] are available to analyze differential thermal analyses (DTA) or DSC data for determine the activation energy for crystallization of the glass. Despite that DTA and DSC being well established techniques there is considerable controversy and some confusion over the use of these methods for determining the kinetic parameters. Different methods can produce conflicting data which are not preferable because of mistrust and confusion.

3.2.3.2.1 Isothermal studies

The isothermal crystallization data are interpreted using the formal theory of transformation kinetics developed by Johnson-Mehl-Avrami (JMA)[109] and also by a similar approach of Kolomogroff[110] and it is described with following equation:

$$-\ln(1-\alpha) = (kt)^n \tag{55}$$

where α is the volume fraction crystallized at a given temperature in time t, k is the reaction rate constant for the whole transformation process, the dimensionless quantity n is the Avrami exponent, which depends on the nucleation and crystal growth. The reaction rate constant, k, is related to the activation energy for the overall crystallization process (E), through the Arrhenius temperature dependence

$$k = Ae^{\left(-\frac{E}{RT}\right)} \tag{56}$$

where A is a frequency factor, R is the universal gas constant and T is the isothermal absolute temperature. The values k and n are determined using the relationship:

$$\ln\left[\ln\left(\frac{1}{1-\alpha}\right)\right] = \ln k + n\ln t \tag{57}$$

Experimentally k and are determined from the plots [ln(1/1-α)] versus ln(t). A plot of ln(k) against 1/T for different isothermal temperatures is subsequently employed to determine a value for E. The overall effective activation energy E is expressed by equation:

$$E = \frac{\left(E_N + mE_G\right)}{n} \tag{58}$$

where, E_N and E_G is the activation energy for nucleation and crystal growth, respectively. The dimensionality of crystal growth is described by m[106] which is often used as a morphology index. If the nucleation frequency is negligible over the temperature range supported by investigation then

$$E \approx \frac{m}{n}E_G \tag{59}$$

and with the assumption that nucleation reach the maximum nuclei in the sample then $E = E_G$. On the contrary, if the nucleation frequency cannot be ignored and the nuclei are formed during the isothermal treatment then n = m + 1.

3.2.3.2.2 Non-isothermal studies

Such as isothermal also non-isothermal techniques have been used for determination of activation energies for crystallization generally for kinetics data. Kissinger analytical model[102] is the most frequently used technique to describe the variation of the peak crystallization temperature with heating rate.

$$\ln\left(\frac{\beta}{T_p^2}\right) = -\left(\frac{E_G}{RT_p}\right) + \text{constant} \tag{60}$$

where *E* is the apparent activation energy for crystallization, β is the DSC heating rate, T_p is the peak crystallization temperature and R is the gas constant. The slope of the plot of $\ln(\beta/T_p^2)$ versus $1/T_p$ gives the apparent activation energy of the corresponding process. The existence of a good linearity indicates the validity of the use of the Kissinger plot. However, when surface crystallization and bulk crystallization occur simultaneously, the crystallization

mechanism is governed by the heating rate, that is, domination of the surface crystallization at higher heating rate but domination of the bulk crystallization at lower heating rate.

Matusita and etc.[105,106,107] have affirmed that Kissinger equation is valid only when crystal growth occurs on a fixed number of nuclei. If a majority of the nuclei are formed during the DSC measurement, so that the number of nuclei continuously varies with β then incorrect values for the activation energy are obtained. The Matusita proposed the modified Kissinger equation which requires the knowledge of the nucleation mechanism. Supplemented equation is:

$$\ln\left(\frac{\beta^n}{T_p^2}\right) = -1{,}052\left(\frac{mE_G}{RT_p}\right) + \text{constant} \tag{61}$$

where n is a numerical factor depending on the nucleation process known as the Avrami parameter, and m is the number of dimensions in which the crystal grows. The values m and n are closely related, namely when the number of nuclei in the glass are constant during crystallization and DSC measurements at different heating rates (β) then m = n. In the case, when glass crystallizes predominantly by surface crystallization it follows that m = n = 1 in both instances the Kissinger equation is valid. This means that, analysis of the crystallization data using Kissinger equation will yield the correct value for the activation energy, i.e., E = E_G. When the number of nuclei increases during DSC runs and nuclei number is inversely proportional to β then m = n – 1. Values ascribed to n and m according to the different crystallization behaviour is summarized in the Table 6.[111] Only with the knowledge of the crystallization mechanism of the particular glass system allows the determination of the n and m values and with the help of DSC plots the activation energy can be determined.

Many studies reported in the literature, which are using the non-isothermal methods for determining kinetic parameters of inorganic glass systems, have unfortunately ignored the knowledge of the connection between n and m parameters and have also assumed that the Kissinger approach could be applicable for any system.

Table 6. *Numerical values for n and m used in the determination of activation energies for crystallization.*

CRYSTALLIZATION MECHANISM	n	m
Bulk crystallization with a constant number of nuclei	**n = m**	
Three-dimensional growth of crystals	3	3
Two-dimensional growth of crystals	2	2
One-dimensional growth of crystals	1	1
Bulk crystallization with a constant number of nuclei with crystal growth rate proportional to $t^{-0,5}$ (diffusion controlled)		
Three-dimensional growth of crystals	1,5	1,5
Two-dimensional growth of crystals	1	1
One-dimensional growth of crystals	0,5	0,5
Bulk crystallization with an increasing number of nuclei	**n = m + 1**	
Three-dimensional growth of crystals	4	3
Two-dimensional growth of crystals	3	2
One-dimensional growth of crystals	2	1
Bulk crystallization with an increasing number of nuclei with crystal growth rate proportional to $t^{-0,5}$ (diffusion controlled)		
Three-dimensional growth of crystals	2,5	1,5
Two-dimensional growth of crystals	2	1
One-dimensional growth of crystals	1,5	0,5

The value of n is determined from the Ozawa[108] equation:

$$\left.\frac{d\ln(-\ln(1-\alpha))}{d\ln\beta}\right|_T = -n \tag{62}$$

where α is the volume fraction crystallized at a temperature T, which was determined from the DSC exotherm shown in Figure 27. The crystallized volume fraction α is the ratio of the partial area, S (at T), to the total area S_o of the crystallization exotherm. From the plotting of ln[ln(1-α)] versus lnβ, where α is obtained at the same temperature from a number of crystallization exotherms, taken at different heating rates, the value n is obtained. This plot, according to Eq. 62, should be a straight line, from the slope of which n can be calculated. There are several other methods for determination of activation energy. Ozawa – Chen: [112]

$$\left.\frac{d\ln\beta}{d\left(\frac{1}{T}\right)}\right|_\alpha = -1{,}052\frac{mE_G}{nR} \tag{63}$$

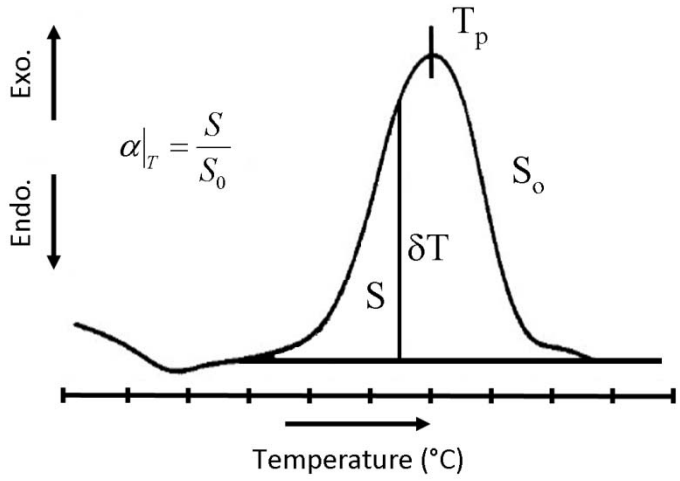

Figure 27. *Typical DSC crystallization exotherm where volume fraction of crystallized glass α_T at T could be calculated.*

The activation energy E_G can be also evaluated from the single crystallization exotherm with the Šatava method:[113]

$$\left.\frac{d\ln(-\ln(1-\alpha))}{d\ln\left(\frac{1}{T}\right)}\right|_{\beta} = -1{,}052\frac{mE_G}{R} \tag{64}$$

The volume fraction α is recommended to lie in the range of 0.1-0.9. From the linear line of the ln (-ln (1 - α)) versus ln (1/T) the mE_G can be obtained. This method is the least accurate for the determination of the activation energy.

In our case DSC runs at heating rates of 5, 7, 10, 12, 15, and 20 °C/min for the activation energy analysis. In all cases, each glass was heated for ten hours at optimum nucleation temperature, cooled down and then heated to full crystallization. With the nucleation we tried to ensure that the determined activation energy represents only the activation energy for crystal growth.

3.2.4 Dielectric measurements

The radio-frequency (RF) dielectric measurements were performed at 1 MHz on Au-plated disk capacitors using a high-precision LCR meter (Agilent 4284 A). The permittivity measured at 1 MHz was used to determine the appropriate $TE_{01\delta}$ mode in the microwave (MW) frequency range. The MW dielectric properties were characterized using the dielectric resonator method, described by Krupka et al.[114], using a network analyzer (HP 8719C).

The permittivity and dielectric losses (tan δ) were calculated at the resonant conditions. The Q values were calculated from the tan-δ values in accordance with the equation Q = 1/tan δ. To determine the temperature coefficient of resonant frequency (τ_f) the test cavities were inserted into a temperature-controlled chamber. The dielectric characteristics of the samples were analyzed in the temperature range from 20 to 60 ºC.

4 Results and discussion

4.1 Binary system $MgO-B_2O_3$

Based on the Mutluer and Timucin[77] work, the binary system $MgO-B_2O_3$ should have three thermodynamically stable compounds MgB_4O_7, $Mg_2B_2O_5$ and $Mg_3B_2O_6$. The synthesis of MgB_4O_7, $Mg_2B_2O_5$ and $Mg_3B_2O_6$ from stoichiometric ratios of initial oxides MgO and B_2O_3 did not result in a single-phase ceramics. Boron oxide melts in the broad range around 450 °C. Due to the low melting temperature and consequently higher vapour pressure of B_2O_3 considerable amount of B_2O_3 evaporates during annealing. This requires adequate selection of the synthesis conditions. Both initial oxides B_2O_3 and MgO absorb water from air humidity. From this reason prior to weighing B_2O_3 and MgO were dried at 120 °C and 500 °C, respectively. The drying temperatures were chosen on the basis of the TG-DSC and MS measurements (Figure 28). For the preparation of single phase MgB_4O_7, $Mg_2B_2O_5$ and $Mg_3B_2O_6$ ceramics the loss of B_2O_3, has to be compensated by adding the excess of B_2O_3. The appropriate amount of B_2O_3 was determined experimentally by the preparation of various compositions with the excess of B_2O_3. The amount of B_2O_3 needed for the compensation of the evaporated B_2O_3 was then selected on the basis of the single phase product determined by the XRD.

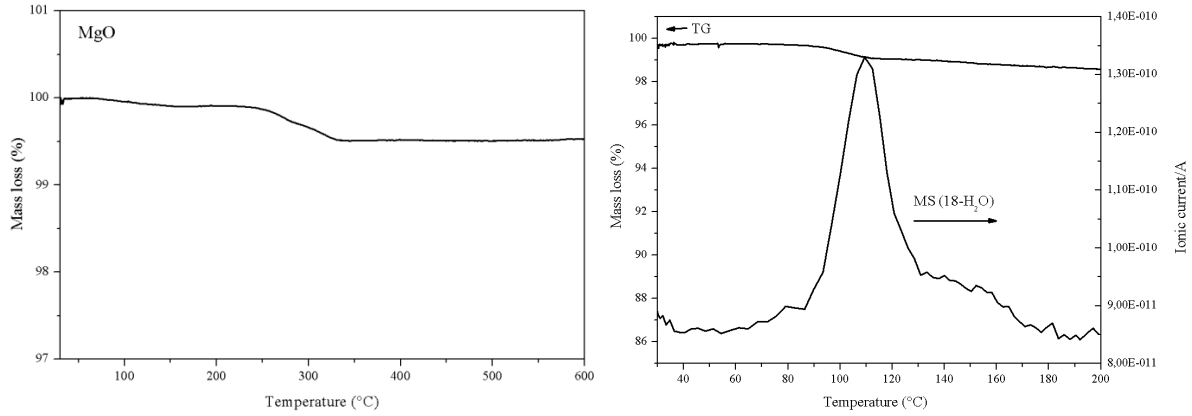

a) b)

Figure 28. *TG (—) and DSC (---) curves of initial oxides. MgO is shown in graph (a) while the B_2O_3 is presented in graph (b).*

4.1.1 MgB_4O_7

For the first preparation of MgB_4O_7 ceramic dried MgO and B_2O_3 were weighed and homogenized in the stoichiometric ratio. The events that occur during the heating of this mixture were monitored by the heating microscope. Variation in the cross-sectional area curve indicates significant variation in the sample volume during heating Figure 29. On the basis of the TG/DSC-MS analysis the shrinkage between 200-400 °C and enlargement between 400-600 °C were attributed to the decomposition and melting of boric acids (H_3BO_3 and HBO_2) and B_2O_3, respectively. H_3BO_3 formed during homogenization in air because B_2O_3 absorbs water from air humidity.

Hydrolysis of boron oxide which is very hydroscopic material gives us orthoboric acid, H_3BO_3 which is a very weak monobasic acid and acts exclusively by hydroxylion acceptance rather than proton donation:

$$\mathbf{B(OH)_3 + 2H_2O \leftrightarrow H_3O^+ + B(OH)_4^-} \quad (65)$$

Partial dehydration of H_3BO_3 above 100 °C yields metaboric acid HBO_2 which can exist in several crystalline modifications:

		Coordination number of Boron	Density (g/cm^3)	Melting point (°C)
	Orthorhombic HBO_2	3	1,784	176
	↑ Rapid quench			
$B(OH)_3$ 140°C	Monoclinic HBO_2	3 and 4	2,045	201
175°C	Cubic HBO_2	4	2,487	236

According to the XRD measurements (Figure 30), HBO_2 and H_3BO_3 phases were present in the pre-reacted powders up to 400 °C. This means that B_2O_3, which melts during heating and then solidify during cooling, absorb again the humidity from the atmosphere. During the synthesis of bigger amount of the sample, the enlargement in the sample volume that was observed by the heating microscope measurements (Figure 29, red curve) can cause the problems because the material can creep out of the crucible. Large quantities that stick on the walls of the crucible are also lost for further synthesis procedure. We found experimentally

that the enlargement in the sample volume can be considerably reduced by annealing of the $MgO{\cdot}2B_2O_3$ mixture at 100 °C and 300 °C (Figure 29, green and blue curve).

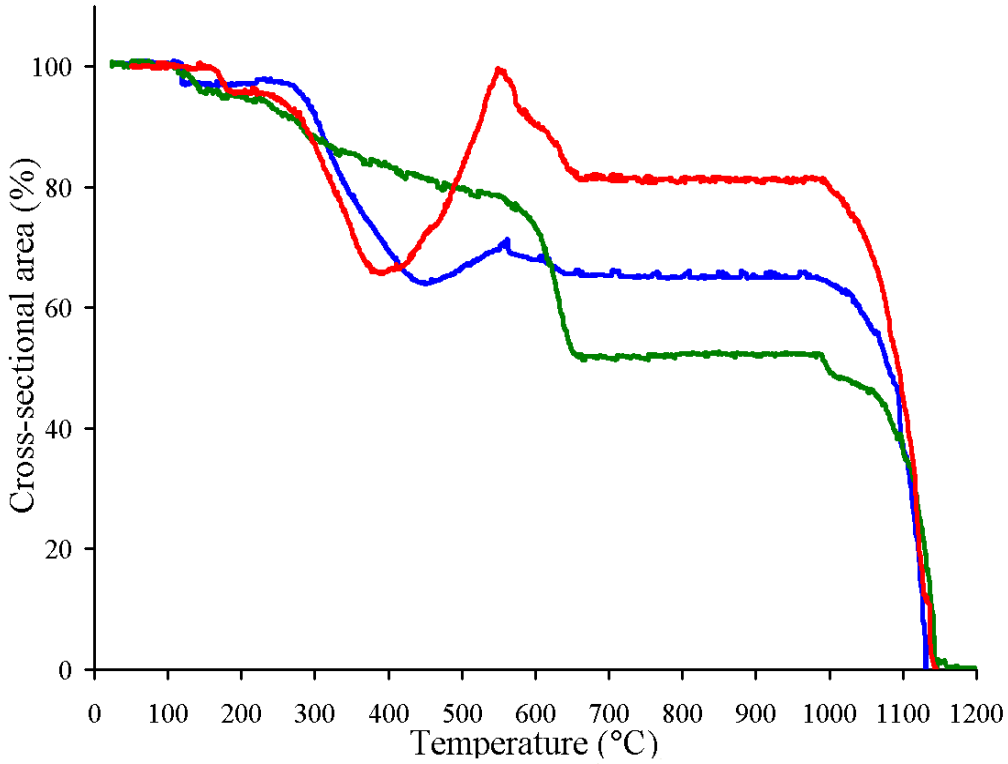

Figure 29. *Heating curve of the MgB_4O_7 composition. Red curve indicate raw MgB_4O_7, blue curve presented 100 °C for 4 hours and green curve is obtained for sample fired at 100 °C 4 hours, 300 °C 1hour.*

The XRD pattern of the $MgO{\cdot}2B_2O_3$ stoichiometric mixture, which was pre-reacted several times (100-950 °C) (Figure 30, curve c) or directly annealed at 950 °C (Figure 30, curve b) shows the presence of the $Mg_2B_2O_5$ in addition to the MgB_4O_7 phase (Figure 30, curve b). These results showed that an excess of B_2O_3 is needed in order to ensure single-phase MgB_4O_7.

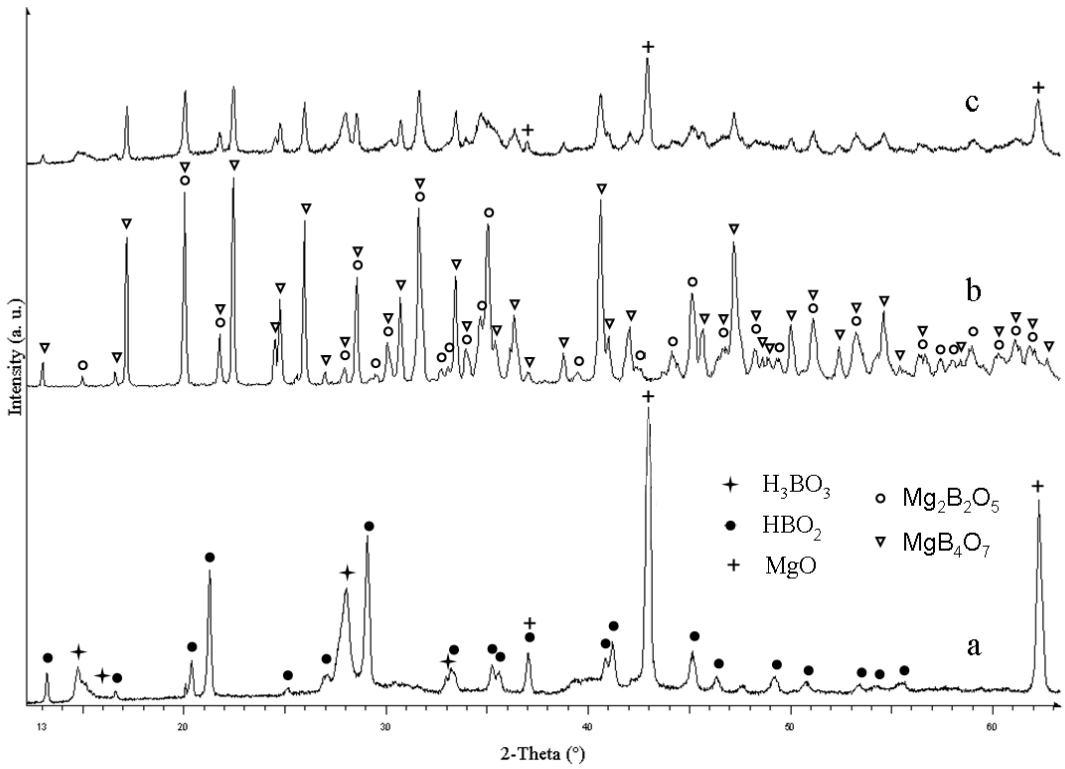

Figure 30. *X-ray powder diffraction pattern of the MgB_4O_7 at different heating conditions: pre-reaction at 400 °C heated for 4 hours (a), pre-reaction at 100 °C heated for 4 hours and 300 °C heated for 1 hour (b), fired for 10 hours at 950 °C (c) and after pre-reaction at 100 °C for 4 hours and 300 °C, 700 °C and 800 °C for 1 hour, then sintered at 950 °C for 10 hours (d). Denotation of crystalline phases: (✦) H_3BO_3, (●) HBO_2, (+) MgO, (▽) MgB_4O_7, (○) $Mg_2B_2O_5$.*

The required amount of excess B_2O_3 was experimentally determined by the preparation of initial mixtures with different excess of B_2O_3. These initial mixtures were pre-reacted under conditions precisely described in Table 7. In the XRD (Figure 31, curve a) pattern of MgB_4O_7 with 21 wt.% excess of B_2O_3 pre-reacted at 100, 300 and 600 °C MgB_4O_7 and $Mg_2B_2O_5$ phase and large amount of non-reacted MgO were present. MgB_4O_7 phase formed during further annealing at 700, 800 and 900 °C (Figure 31, curve b). MgO phase and most probably boron oxide-rich glassy phase were still present at this temperature. By increasing the temperature to 950 °C single-phase of MgB_4O_7 was obtained (Figure 31, curve c). This shows that 21 % excess of B_2O_3 is sufficient for single phase MgB_4O_7.

Table 7. *Pre-reaction and heating conditions of MgB_4O_7.*

Material	Heating at low-temperatures	Annealing temperature (°C)
MgB_4O_7	100 °C (5h) and 300 °C (0.5h)	600, 700, 800, 900 and 950
The time of each pre-reaction was 10h.		

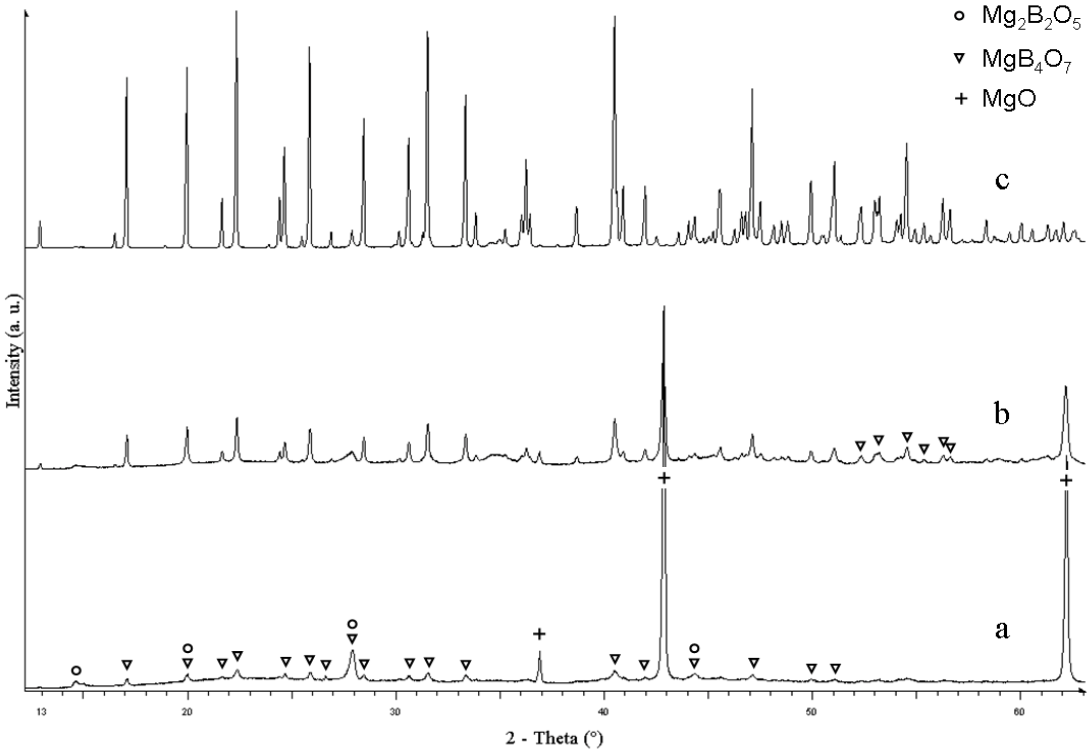

Figure 31. *X-ray powder diffraction pattern of the MgB_4O_7 with 21 wt.% excess of B_2O_3 after pre-reaction at 100 and 300 °C, calcinated at 600 °C (a), additional calcination at 700 °C (b) and additional calcination at 800 and 900 °C and annealed at 950 °C. Denotation of crystalline phases: (▽) MgB_4O_7, (○) $Mg_2B_2O_5$ (+) MgO.*

According to phase diagram of Mutluer and Timucin[77] MgB_4O_7 decomposes to $Mg_2B_2O_5$ and liquid phase at 995 °C. Since we were not able to prepare dense MgB_4O_7 ceramics below this temperature, the MgB_4O_7 ceramics was not dielectrically and microstructurally characterized.

4.1.2 $Mg_2B_2O_5$

4.1.2.1 Synthesis

The $Mg_2B_2O_5$ based ceramics was synthesized by a standard solid-state reaction technique. Dried powders were mixed in a 2:1 molar ration, homogenized in acetone and repeatedly pre-reacted with grinding and milling.

On the basis of the exothermic DSC peak at 600–800 °C, which belongs to the crystallization of the magnesium borates, we chose the temperature for the first pre-reaction at 600 °C. In addition to the crystallization peaks above 600 °C, the DSC curve of the homogenized, initial powders also revealed two strong endothermic peaks below 200 °C (Figure 32). The mass spectrometry of the evolved gas revealed that the mass loss in the TG curve and these endothermic peaks coincided with the removal of water. Taking into account the literature data, these processes below 200 °C could be attributed to the decomposition of the H_3BO_3.[115] Although the B_2O_3 was dried before weighing, B_2O_3 bound water during the homogenization in air, forming H_3BO_3.

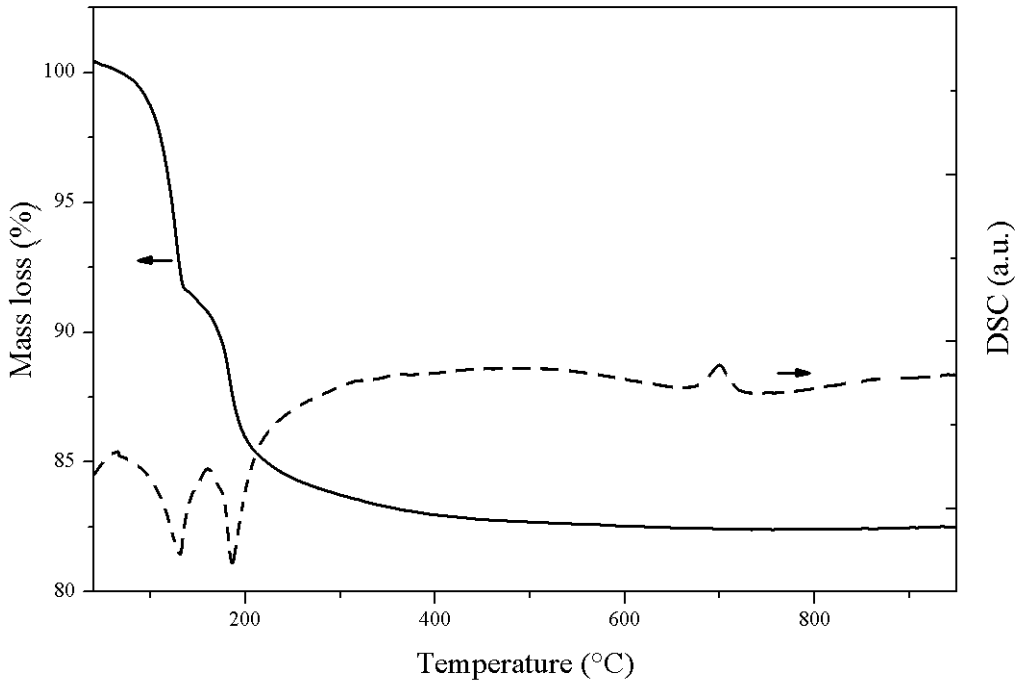

Figure 32. *TG (—) and DSC (---) curves of homogenized $Mg_2B_2O_5$ (denoted as M2B2) powders with 14 wt.% of B_2O_3.*

The synthesis of $Mg_2B_2O_5$ from stoichiometric ratios of the initial oxides MgO and B_2O_3 did not lead to single-phase ceramics. The presence of $Mg_3B_2O_6$ in the $Mg_2B_2O_5$ ceramics could be an indication of the evaporation of B_2O_3 during the pre-reactions and sintering. The loss of B_2O_3 was compensated by the addition of excess B_2O_3 at the beginning of the

synthesis. The required amounts of excess B_2O_3 were determined experimentally by the preparation of initial mixtures with a 10–15 wt.% excess of B_2O_3 (Figure 33). These initial mixtures were pre-reacted under the conditions described in Table 8. The required amount of excess B_2O_3 for $Mg_2B_2O_5$ was selected on the basis of the single-phase composition of the powders after annealing at 1250 °C.

Table 8. *Pre-reactions and sintering conditions of $Mg_2B_2O_5$. The pre-reaction time at each temperature was 10 hours.*

Material	Pre-reactions temperatures (°C)	Sintering temperature (°C)	Structure
$Mg_2B_2O_5$	600, 900, 1000, 1100, 1200	1250-1280	S.G. $P\bar{1}$

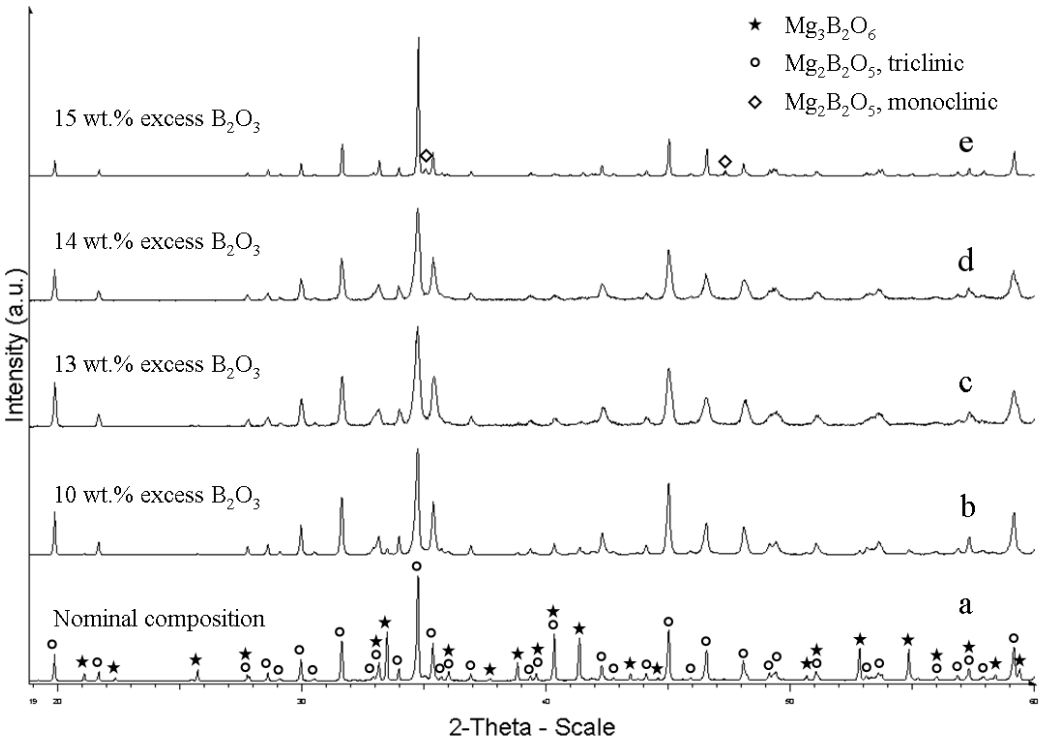

Figure 33. *X-ray powder diffraction pattern of the $Mg_2B_2O_5$ nominal composition and $Mg_2B_2O_5$ with various excess of B_2O_3 (10 – 15 wt.%), all sintered at 1250 °C for 10 hours.*

In the XRD pattern of the nominal composition of the $Mg_2B_2O_5$ a considerable amount of $Mg_3B_2O_6$ was present after sintering at 1250 °C for 10 hours (Figure 33, curve a). With the addition of 10 wt.% of excess of B_2O_3 the amount of $Mg_3B_2O_6$ has been drastically reduced (Figure 33, curve b). In case of 13 wt.% of excess of B_2O_3 the secondary phase $Mg_3B_2O_6$ was still present (Figure 33, curve c). According to the XRD pattern we confirmed that 14 wt.% of excess of B_2O_3 led to the single phase $Mg_2B_2O_5$ ceramics at 1200 °C and at 1250 °C (Figure

33, curve d). In the case of 15 wt.% of excess B_2O_3 the monoclinic $Mg_2B_2O_5$ phase appears (Figure 33, curve e).

The investigations of the phase formation during the pre-reactions of $Mg_2B_2O_5$ (with 14 % of excess B_2O_3) revealed the formation of MgB_4O_7 and $Mg_2B_2O_5$ phase at 600 °C. Both phases in addition to H_3BO_3 phases were present in a small quantity (Figure 34). The strongest diffraction lines belong to MgO. B_2O_3 melts at 450 °C and after pre-reaction at 600 °C most probably exists in the mixture in the form of amorphous oxide. In the XRD pattern of the $Mg_2B_2O_5$ (with 14 wt.% of excess B_2O_3) powder pre-reacted at 900 °C the diffraction lines of all the magnesium borates (MgB_4O_7, $Mg_2B_2O_5$ and $Mg_3B_2O_6$) were present in addition to traces of MgO. With the subsequent pre-reaction at 1000 °C the MgB_4O_7, $Mg_3B_2O_6$ and MgO phases disappeared and $Mg_2B_2O_5$ became single phase. The monoclinic (S.G. $P2_1/a$) and triclinic (S.G. $P\bar{1}$) crystal modifications of the $Mg_2B_2O_5$ were present up to 1000 °C. Only the triclinic modification was found in the samples annealed at T ≥ 1100 °C.

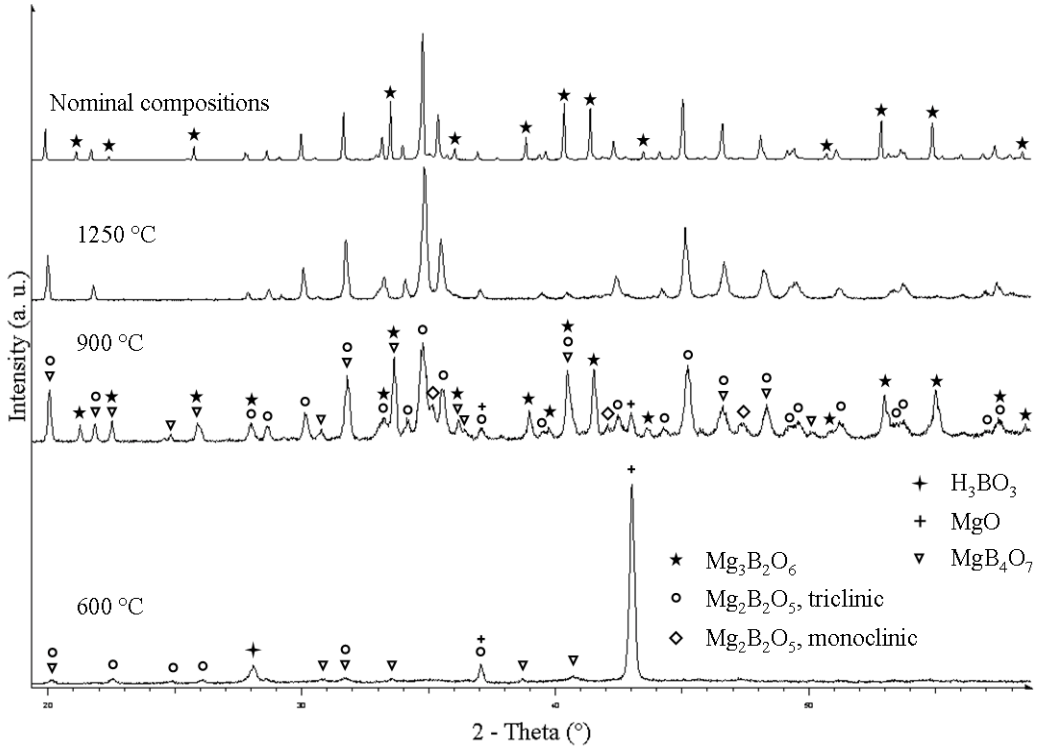

Figure 34. *X-ray powder diffraction pattern of the $Mg_2B_2O_5$ (nominal composition (1250 °C), and $Mg_2B_2O_5$ with a 14 wt.% excess of B_2O_3 after pre-reaction at 600 °C, 900 °C and 1250 °C. Denotation of the crystalline phases: ★ $Mg_3B_2O_6$, ○ $Mg_2B_2O_5$ (triclinic), ◇ $Mg_2B_2O_5$ (monoclinic), + MgO, ✦ H_3BO_3, ▽ MgB_4O_7.*

4.1.2.2 Sintering and microstructural characteristics

According to sintering behaviour observed by means of the heating microscope densification of the $Mg_2B_2O_5$ started above 950 °C (Figure 35). The change of the pellets' silhouettes monitored during the heating up with a defined heating profile is assumed to be isothropic. This implies that the shrinkage of the pellet during sintering is the same in all directions. The cross-sectional area of the $Mg_2B_2O_5$ decreased for 28 % up to 1200 °C (Figure 35). Due to the further shrinkage the cross-sectional area decreased for 43 and 48 %, when the temperature increased to 1250 and 1280 °C, respectively (Figure 35). The first signs of melting such as round upper edges and spread lower edges of the cylindrical pressed sample start at ~1300 °C (Figure 35). This observation is in a rather good agreement with the phase diagram reported by Mutluer and Timucin, where $Mg_2B_2O_5$ incongruently melts at 1312 °C.[77] In order to prepare ceramics with high density, $Mg_2B_2O_5$ was sintered at 1250 and 1280 °C.

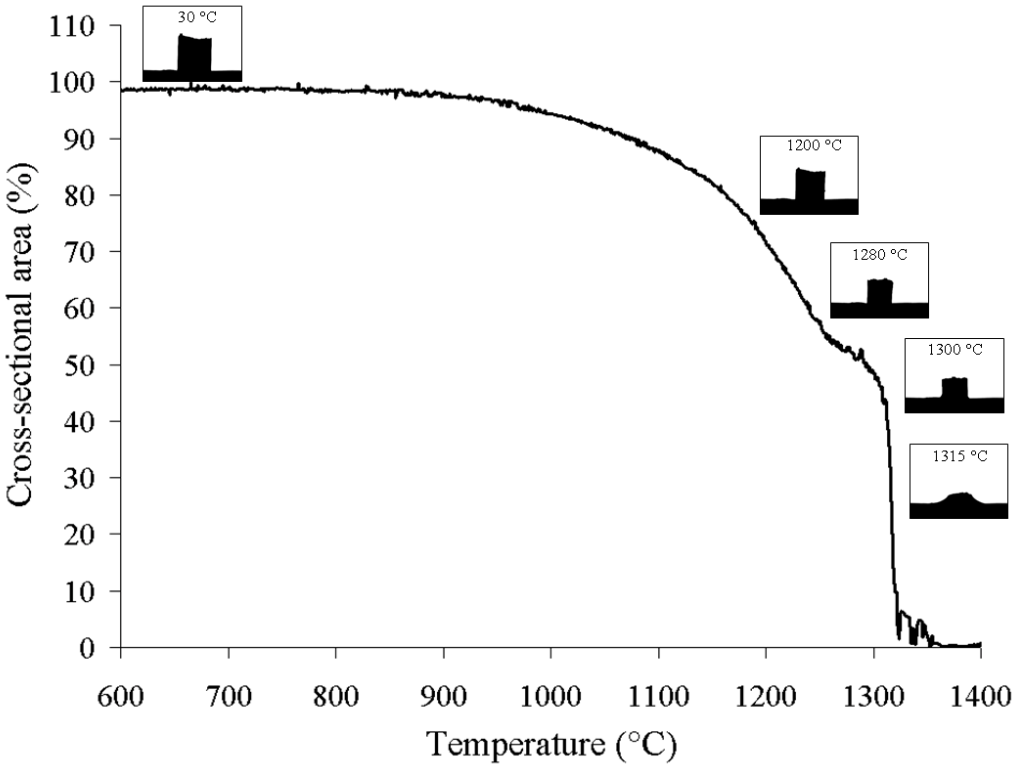

Figure 35. *Sintering profiles of the milled $Mg_2B_2O_5$ lastly calcinated at 1200 °C observed with heating microscope.*

The microstructures of $Mg_2B_2O_5$ ceramics were observed using scanning electron microscope. SEM micrograph of a thermally etched sample sintered at 1280 °C revealed grains with a size of ~10 μm. Some of the grains in the fast-cooled sample (Figure 36 a) are

euhedral, while in the slow-cooled sample they are more anhedral (Figure 36 b). The single-phase structure of $Mg_2B_2O_5$ ceramics observed by X-ray powder diffraction was also confirmed with the microstructure analyses. The secondary or the glassy phase was not perceived from the micrographs (Figure 36). We assumed that all of the amorphous B_2O_3 reacted or evaporated during synthesis.

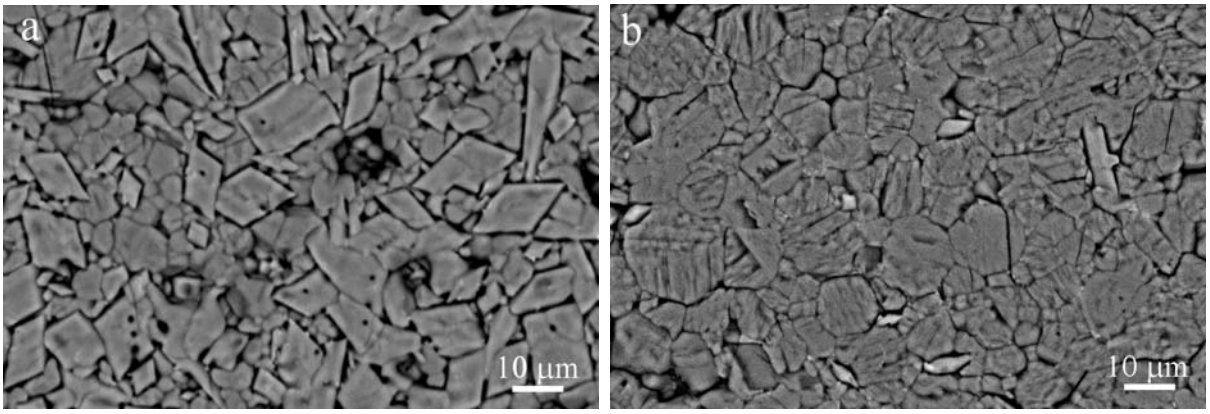

Figure 36. *Scanning electron micrographs of the thermally etched $Mg_2B_2O_5$ ceramics sintered at 1280 °C for 10 hour, cooled fast (a) and sintered at 1280 for 20 hours cooled with a slow cooling rate of 2 °C /min (b).*

4.1.2.3 Microwave dielectric characterization

The samples for microwave characterization were prepared in a cylindrical shape with height/diameter ratio of 0.4 and sintered at 1250 and 1280 °C, respectively. Density measurements (Archimedes' method in acetone) of the sintered $Mg_2B_2O_5$ revealed that it was very difficult to prepare ceramics with relative density higher than 97 %. The literature data of 2.91 g/cm^3 (PDF 15-0537) was used as the theoretical densities of the $Mg_2B_2O_5$.[98]

The microwave dielectric properties of $Mg_2B_2O_5$ together with the density data are presented in Table 9. It is well known that the measured permittivity depend on intrinsic characteristics such as ionic polarizability and molar volume of the constituent phases and also on extrinsic property like porosity. With the pre-reactions at 600, 900, 1000, 1100 and 1200 °C we ensured single-phase $Mg_2B_2O_5$ ceramics. The density of sintered ceramics was in the range from 94 to 97 %. Taking into account the observations of many authors the permittivity is significantly influenced by the porosity when the relative density is smaller than 96 %.[116] The density data in the Table 9 do not support our expectations that sintering at higher temperature and prolongation of sintering lead to ceramics with higher density and permittivity.

Table 9. *Microwave dielectric properties and density data's of $Mg_2B_2O_5$.*

Material	$Mg_2B_2O_5$			
Ts (°C)	1250°C/10h	1250°C/20h	1280°C/10h	1280°C/20h
Cooling	fast	fast	fast	2°C/min
ε	7.0	6.6	6.6	6.2
Qxf (GHz)	18 400	19 100	19 800	32 100
f_o (GHz)	12.0	11.9	12.3	12.6
τ_f (ppm/°C)	-41	-46	-41	-18
ρ_r (%)	95	97	94	95

The permittivity for the $Mg_2B_2O_5$ ceramics varied from 6.2 to 7.0 and the Qxf values from 18 400 GHz to 32 100 GHz. Many factors are believed to affect the microwave dielectric losses and they can be also divided into two categories: intrinsic and extrinsic losses.[117] While the intrinsic losses are related to the crystal structure and bonding character of the material, extrinsic losses appear due to imperfections in the material such as impurities, grain boundaries, second phases, oxygen vacancies, densification and porosity. Due to the scattering of the results of the Qxf-values (Table 9), we believe that these measured values contain some extrinsic contribution. The τ_f values of $Mg_2B_2O_5$ were in the range from -18 to -45 ppm/°C.

4.1.3 $Mg_3B_2O_6$

4.1.3.1 Synthesis

The synthesis procedure for the preparation of $Mg_3B_2O_6$ ceramics was similar to that of $Mg_2B_2O_5$ ceramics, what is precisely described in the previous chapter. In order to understand the reactions during the synthesis procedure, differential scanning calorimetry and thermogravimetric analyses were performed for $3MgO{\cdot}B_2O_3$ initial homogenized mixture. The results, which are shown in Figure 37, are similar to that obtained for the $2MgO{\cdot}B_2O_3$ initial mixture. Two strong DSC endothermic peaks below 200 °C and one exothermic peak at 600-800 °C belong to boric acid decomposition and crystallization of magnesium borates, respectively. Boric acid formed from B_2O_3 during the homogenization in air. The thermogravimetric analysis showed that ~10 % of mass loss resulted from the decomposition of H_3BO_3. Based on the broad crystallization peak at 600-800 °C the pre-reaction was started at 600 °C.

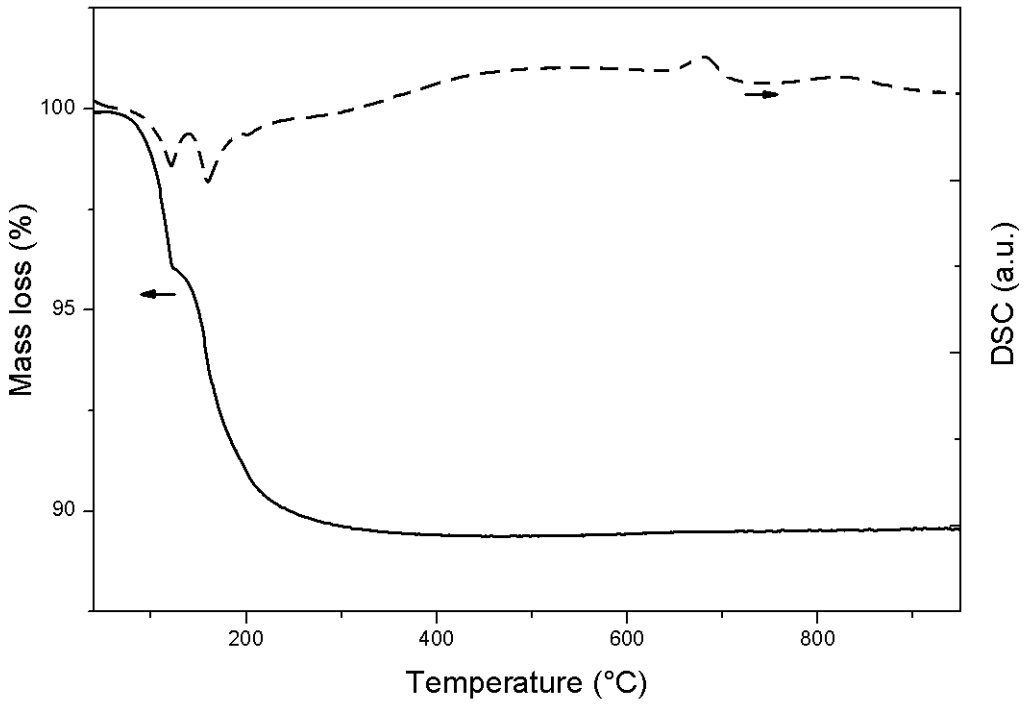

Figure 37. *TG(—) and DSC (---) analysis of the $Mg_3B_2O_6$ ceramics powder with 11 wt.% of B_2O_3 denoted as M3B2.*

Due to the evaporation of boron oxide, the mixture of initial oxides weighted in the stoichiometric ratio expectedly did not lead to the single $Mg_3B_2O_6$ phase ceramics. MgO phase was always present as the secondary phase, its amount even increase with the annealing temperature and time. As for the synthesis of single phase $Mg_2B_2O_5$ the single phase $Mg_3B_2O_6$ was tried to prepare by the addition of excess B_2O_3 at the beginning of the synthesis. In order to find the proper amount of excess B_2O_3, the compositions with a 5-13 % excess of B_2O_3 were prepared. These initial compounds were pre-reacted under the conditions described in Table 10. The required amount of excess B_2O_3 for $Mg_3B_2O_6$ was selected on the basis of the single-phase composition of the powders annealed at 1200 and 1300 °C. In the X-ray powder diffraction pattern of $Mg_3B_2O_6$ with 5 wt.% of excess of B_2O_3 the secondary phase of MgO was still present (Figure 38). The same was observed also for 10 wt.% excess of B_2O_3. In the case of 13 wt.% excess of boron oxide the $Mg_2B_2O_5$ phase started to form. The $Mg_3B_2O_6$ with 11 wt.% of excess B_2O_3 annealed at 1200 °C, as well as at 1300 °C, was found to be single phase with regard to the XRD.

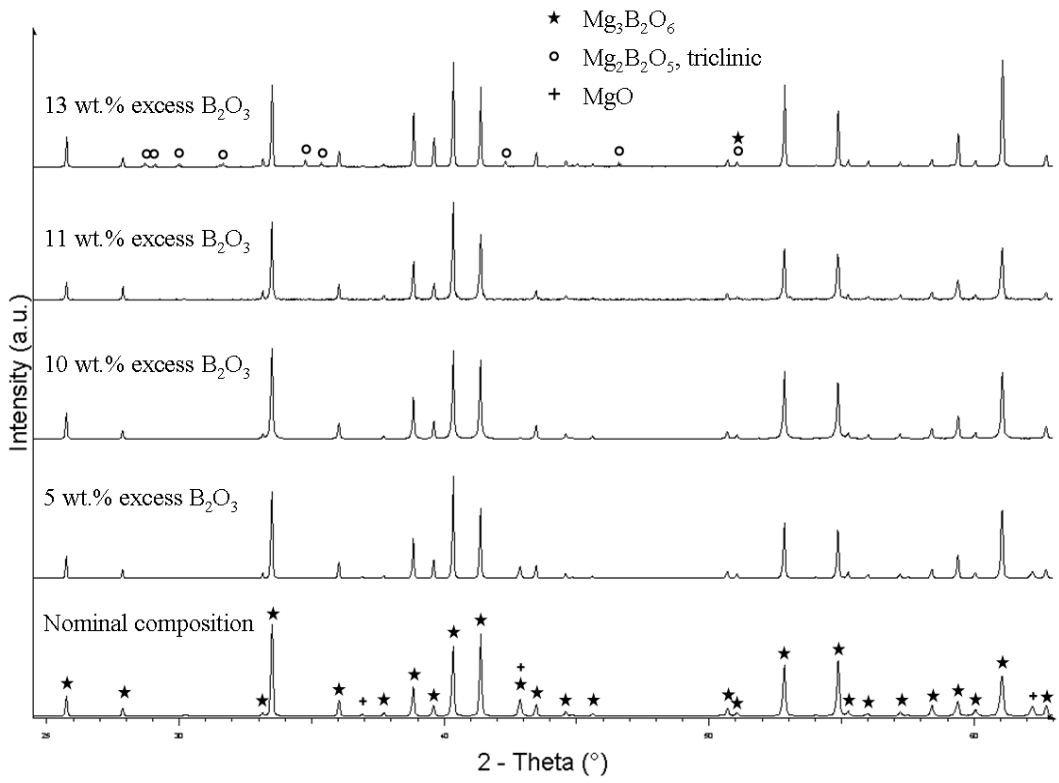

Figure 38. *X-ray powder diffraction pattern of the $Mg_3B_2O_6$ nominal composition and $Mg_3B_2O_6$ with 5 – 13 wt.% excess of B_2O_3, all sintered at 1300 °C for 10 hours. Denotation of the crystalline phases: ★ $Mg_3B_2O_6$, ○ $Mg_2B_2O_5$ triclinic and + MgO.*

Table 10. *Pre-reactions and sintering conditions of $Mg_3B_2O_6$. The pre-reaction time at each temperature was 10 hours.*

Material	Pre-reactions temperatures (°C)	Sintering temperature (°C)	Structure
$Mg_3B_2O_6$	600, 900, 1000, 1100, 1200	1200-1300	S.G. P*nm*

The phase evolution during the synthesis of single phase $Mg_3B_2O_6$ from homogenized mixture with 11 wt.% excess of B_2O_3 was followed by XRD measurements after each pre-reaction step; 600, 900, 1000, 1100 and 1200 °C. These XRD patterns are shown in Figure 39. During the pre-reaction of the homogenized powder with a stoichiometry of $Mg_3B_2O_6$ (11 wt.% excess of B_2O_3) at 600 °C the MgB_4O_7 phase started to form. A significant amount of unreacted MgO and traces of H_3BO_3 were also present in the pre-reacted powder at this temperature. We believed that at this temperature the majority of the B_2O_3 phase is in the amorphous form. Moreover, with the increasing pre-reaction temperature up to 900 °C, the $Mg_3B_2O_6$ appeared as the dominant phase. The secondary phases identified at this temperature were MgO and $Mg_2B_2O_5$; however, both of them completely disappeared at 1200 °C. Single

phase $Mg_3B_2O_6$ ceramic were obtained on the basis of X-ray diffactometry for the sample annealed at 1200 and 1300 °C.

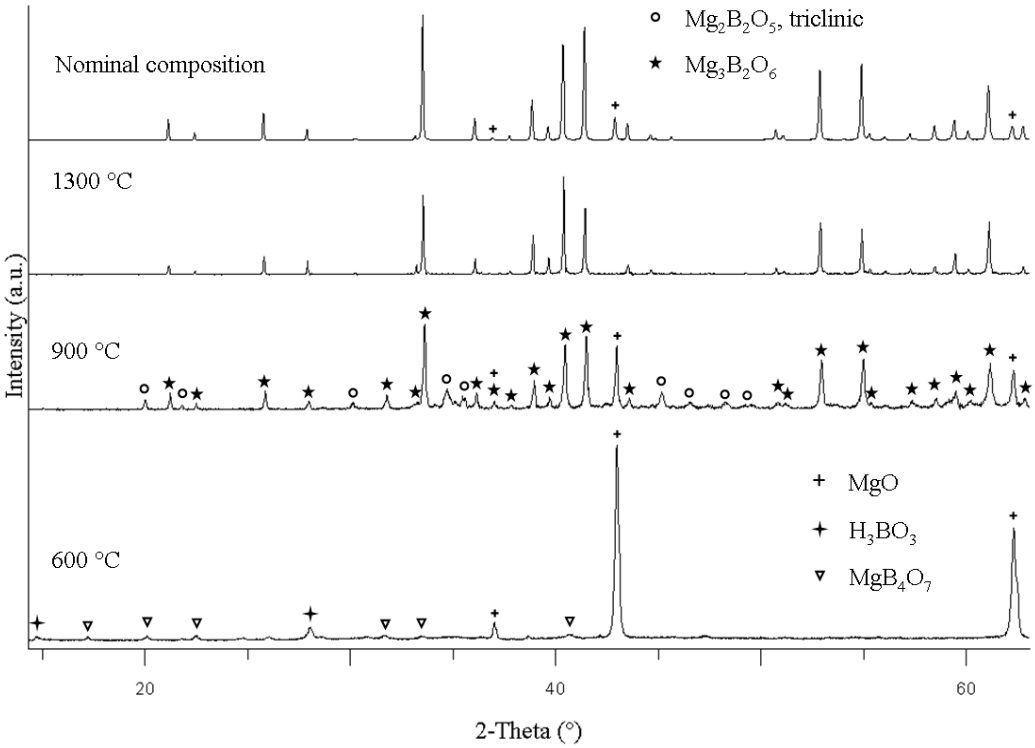

Figure 39. *X-ray powder diffraction pattern of the $Mg_3B_2O_6$ nominal composition sintered at 1300 °C and $Mg_3B_2O_6$ with an 11 wt.% excess of B_2O_3 after pre-reaction at 600 °C, 900 °C and 1300 °C. Denotation of the crystalline phases: ★ $Mg_3B_2O_6$, ○ $Mg_2B_2O_5$, + MgO, ✦ H_3BO_3, ▽ MgB_4O_7.*

4.1.3.2 Sintering and microstructural characteristics

Heating microscope measurements of the pellet pressed from the single phase $Mg_3B_2O_6$ milled powder were performed in order to obtain the data about the optimal sintering temperature for the preparation of dense $Mg_3B_2O_6$ ceramics. It can be seen from Figure 40 that the densification of the $Mg_3B_2O_6$ ceramics started above 1000 °C, while the maximal densification rate was achieved in the temperature region from 1200 to 1300 °C.

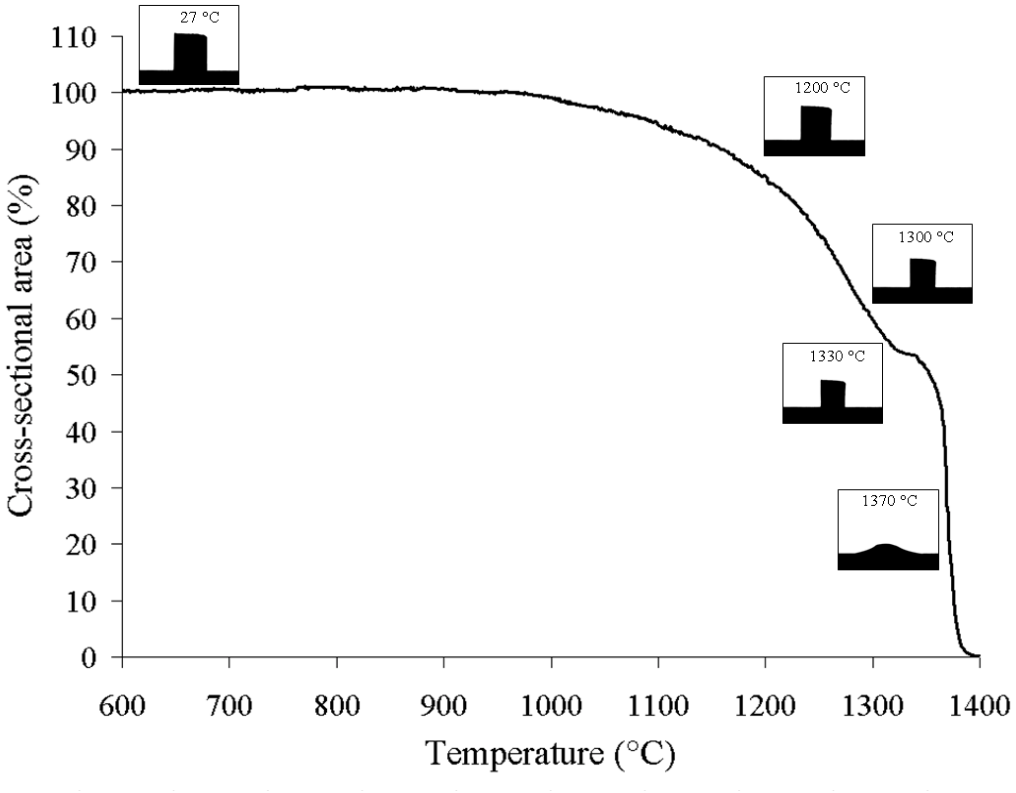

Figure 40. *Densification of the $Mg_3B_2O_6$ ceramics observed with a heating microscope.*

The pellets silhouettes monitored at 1330 °C indicate the beginning of the melting due to the change of the sample edges. According to the heating curve, melting occurred at around 1370 °C.

In order to prepare ceramics with high density, $Mg_3B_2O_6$ was sintered at 1200 and 1300 °C. When the microstructures of the $Mg_3B_2O_6$ ceramics sintered under various conditions were compared considerable differences in the grain size and the porosity were observed. The ceramics sintered at 1300 °C (20 hours) and cooled slowly consisted of ~1000-μm grains, containing some closed porosity (Figure 41 a, b). In the $Mg_3B_2O_6$ ceramics sintered for a shorter time (10 hours) at 1300 °C and cooled rapidly the grain sizes are in a broad range from 10 μm to 1000 μm. In addition to the large elongated grains there are also areas with smaller grains of a few tens of μm (Figure 41 c and d). Only small grains of 10–50 μm were present in the ceramics sintered at 1200 °C (Figure 41 e). These ceramics showed porous microstructures and the closed porosity was replaced by open porosity. Intensive grain growth and closed porosity, as it is present in the $Mg_3B_2O_6$ ceramics sintered at 1300 °C (Figure 41 a, b and c), usually occur as a consequence of liquid-phase formation. With regard to the phase diagram reported by Mutluer et al.[77] the admixture of MgO or $Mg_2B_2O_5$ to $Mg_3B_2O_6$ decreases the melting temperature, and the reported eutectic temperature between $Mg_3B_2O_6$ and MgO is 1333 °C. On the basis of this we assume that the admixture of MgO

could not cause the formation of a liquid phase during sintering at 1300 °C. The reported temperature of the incongruent melting of $Mg_2B_2O_5$ at 1312 °C is much closer to our sintering temperature at 1300 °C. Since we did not detect any $Mg_2B_2O_5$ by XRD we assume that its concentration is below 2 %. Another reason for the liquid-phase formation could also be the low-melting-point glassy phase, which is often present in systems based on B_2O_3. Although the reasons for grain growth are not entirely understood, the majority of investigations indicate that the temperature and the duration of annealing have bigger influence on the grain growth than the cooling rate.

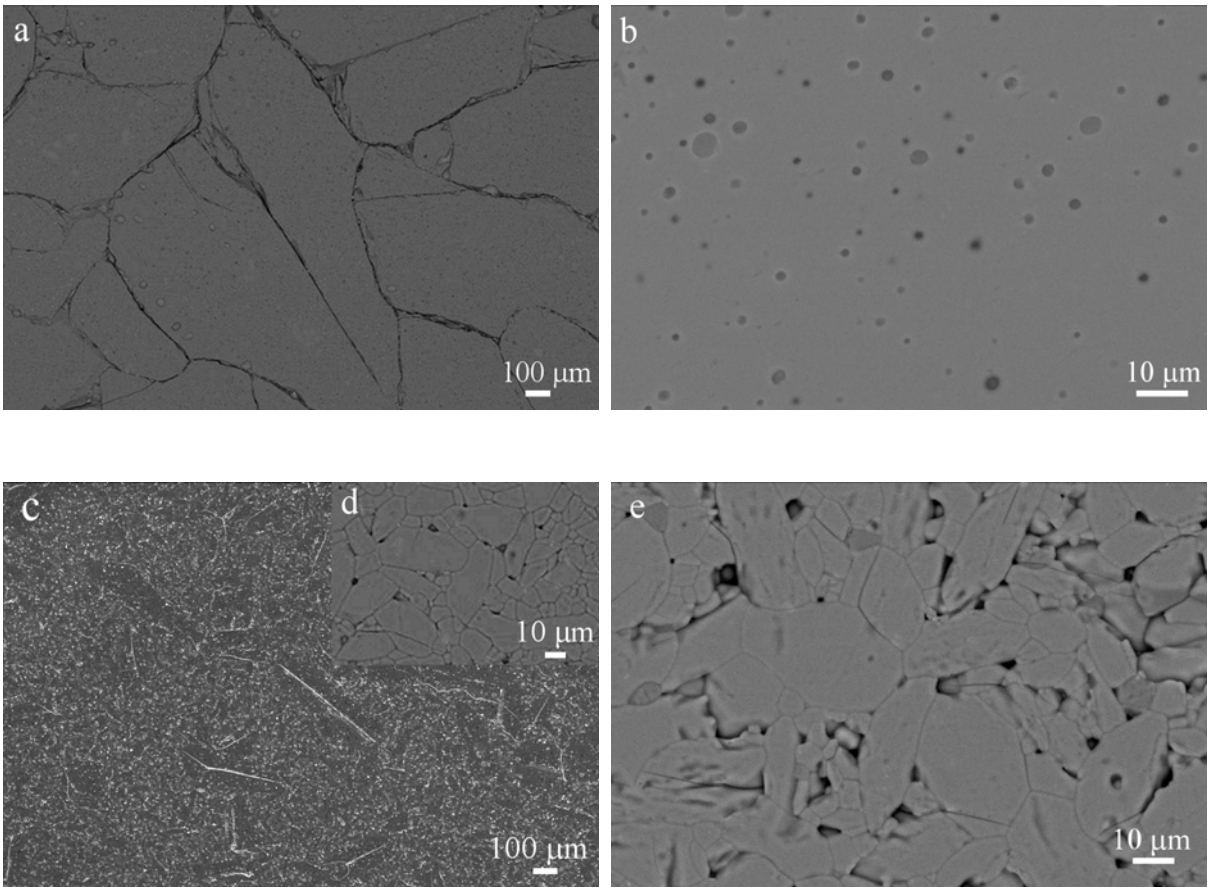

Figure 41. *Scanning electron micrographs of the thermally etched $Mg_3B_2O_6$ ceramics sintered at 1300 °C for 20 hours and cooled with a cooling rate of 2 °C/min (a, b), sintered at 1300 °C for 10 hours and cooled fast (c, d) and sintered at 1200 °C for 10 hours and cooled fast (e).*

4.1.3.3 Microwave dielectric characterization

It is generally known that an extrinsic phenomenon such as porosity causes a detrimental deviation from the intrinsic dielectric properties of the materials. A low level of porosity (< 5 %) decreases the permittivity but does not have a major influence on the microwave dielectric

losses. In addition, a porosity of more than 5 % also has a detrimental effect on the dielectric losses. In contrast to the permittivity and the dielectric losses the τ_f is reported to be less sensitive to the porosity.[19] Density measurements on the sintered $Mg_3B_2O_6$ ceramics revealed that it was very difficult to prepare ceramics with relative densities higher than 97 %. The microwave dielectric properties, together with the density data, are presented in Table 11. In accordance with the higher density, the permittivity (ε = 7.2) of the $Mg_3B_2O_6$ ceramics sintered at 1300 °C was higher than the permittivity (ε = 6.8) of the ceramics sintered at 1200 °C (Table 11). The permittivity of the $Mg_3B_2O_6$ varied from 6.8 to 7.4.

Table 11. *Microwave dielectric properties of $Mg_3B_2O_6$ ceramics.*

Material	$Mg_3B_2O_6$			
Ts (°C)	1200°C/10h	1300°C/10h	1300°C/10h	1300°C/20h
Cooling	fast	fast	2°C/min	2°C/min
ε	6.8	7.4	7.0	7.2
Qxf (GHz)	57 900	150 000	230 900	220 300
f_o (GHz)	12.1	11.9	11.8	11.6
τ_f (ppm/°C)	-37	-36	-42	-45
ρ_r (%)	91	97	95	96

The $Mg_3B_2O_6$ ceramics sintered at 1300 °C showed considerably higher Qxf values than the ceramics sintered at 1200 °C (Table 11). Besides the different densities, these two types of ceramics also exhibited a large difference in the grain size. The highest Qxf values over 220 000 GHz (at 11.8 GHz) were observed for the ceramics that were sintered at 1300 °C for 10 or 20 hours and cooled slowly from the sintering temperature with a controlled cooling rate of 2 °C/min. These ceramics consisted of large grains (~1000 μm) with some closed porosity. According to the density measurements the porosity was about 4–5 %. Porosities in this range were reported to have no significant influence on the dielectric losses.[118] The ceramics sintered at 1300 ºC (10 hours) and cooled rapidly contained areas of large (500–1000 μm) and small grains (10–50 μm) (Figure 41 c and d). The Qxf value of this ceramic was 150 000 GHz. In the ceramics sintered at 1200 °C the grains were only a few tens of μm in size (Figure 41 e) and the Qxf value was 57 900 GHz. $Mg_3B_2O_6$ was already reported to exhibit a high Qxf value of 150 000 GHz,[119] but the properties of the ceramics prepared in this study exceeded this value. The ceramics that exhibited a Qxf > 200 000 GHz consisted of

500–1000 μm grains, whereas the Qxf values fell below 150 000 GHz in the case of a few 10 μm grains. It is known that grain boundaries increase the dielectric losses, and that there is a smaller concentration of grain boundaries in the ceramics with large grains. Nevertheless, further investigations are needed to find out whether the variation in the grain size is the only reason for this large difference in the Qxf values.

4.1.4 The correlation between dielectric losses and grain size of $Mg_3B_2O_6$ ceramics

Several repetitions of the synthesis of $Mg_3B_2O_6$ revealed that the microstructural development and Qxf values were very repeatable within the same synthesis batch. Nevertheless, differences in the Qxf values and the grain size, in particular in the degree of the exaggerated grain growth, were noticed between the different synthesis runs. Based on our previous study, we assumed that these differences appeared due to the various admixtures of the intermediate phases, such as glass and $Mg_2B_2O_5$, which are all below the detection limit of the XRD.[120] We assume that the liquid phase, which formed due to the presence of both phases, was the reason for the exaggerated grain growth. We believed that the liquid phase could occur because of melting of glassy phase which is often present in the systems containing B_2O_3. An amorphous layer with a thickness of 5-40 nm between the grain boundaries was confirmed by the TEM investigations, which also revealed the presence of some separate crystallites within this amorphous layer (Figure 42 a, b). Based on this we can infer that the liquid phase formed at high temperatures. We assume that the majority of the liquid phase solidified to form an amorphous glassy phase, which then segregates at the grain boundaries during the cooling. The crystallites within the amorphous layer are most probably the consequence of the partial crystallization during slow cooling. Another reason for the liquid phase source could be the presence of small amount of $Mg_2B_2O_5$, which according to the reported phase diagram incongruently decompose into $Mg_3B_2O_6$ and a liquid at the sintering temperature of 1312 °C.[77] In the continuation we investigated the influence of $Mg_2B_2O_5$ addition on the grain growth and, consequently on the Qxf values.

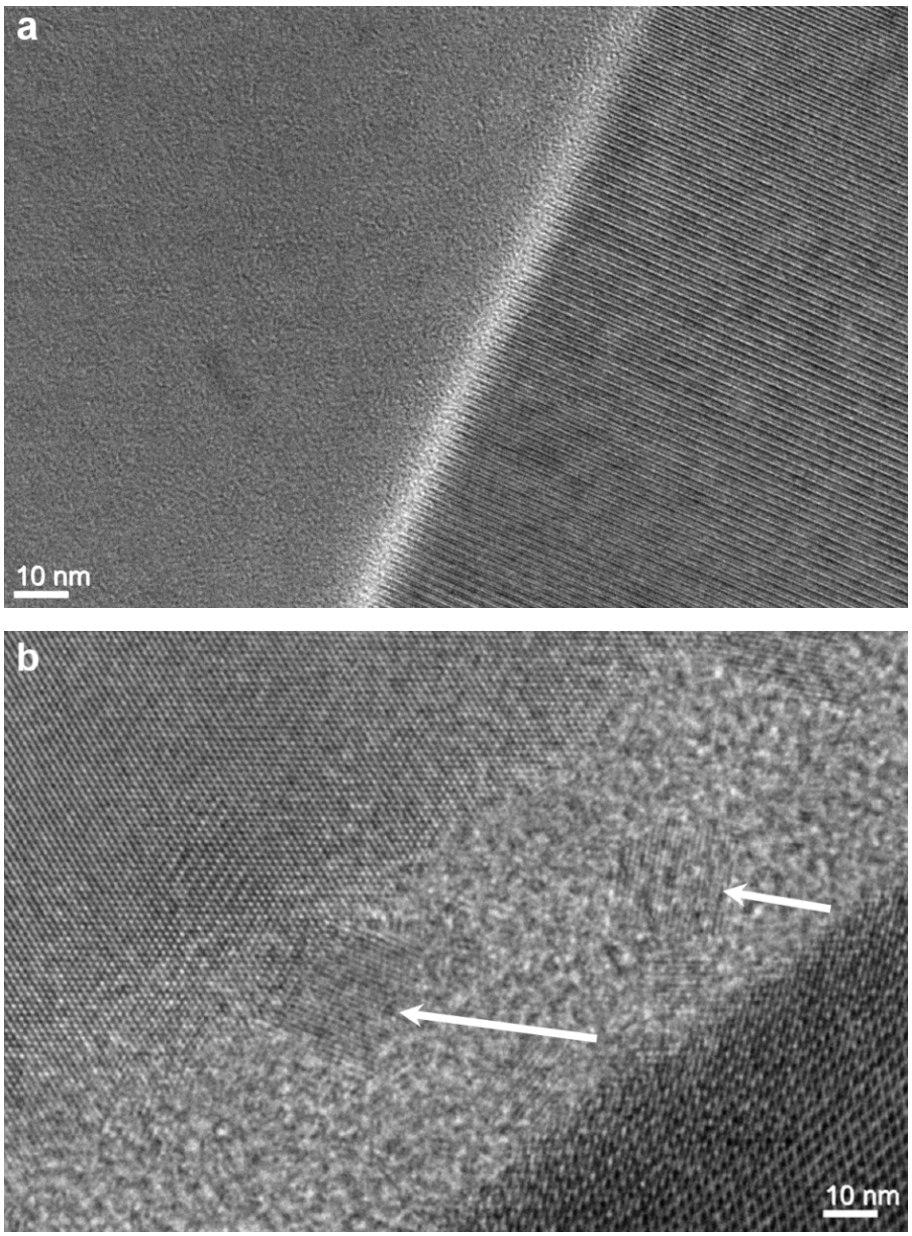

Figure 42. *HRTEM micrograph of the grain boundary with an amorphous layer (a) and the amorphous layer with the crystallite, which is denoted by the arrow (b).*

4.1.4.1 The $Mg_3B_2O_6$ ceramics with the addition of 0-5 wt.% $Mg_2B_2O_5$

In order to control the grain growth we varied the amount of added $Mg_2B_2O_5$ (1 and 5 wt.%) and annealing time. I have to mention here that the study of the correlation between the grain size and Qxf-values was done with the $Mg_3B_2O_6$ prepared from another synthesis batch than $Mg_3B_2O_6$ described in the previous chapter, because of that the microstructural development as well as dielectric properties differed. The procedure of preparing the samples for the study of the correlation between the grain size and Qxf values started with the sintering of the green pellets at 1310 °C for 20 hours which were then cooled slowly with a controlled cooling rate

of 2 °C/min. In the next step we measured microwave dielectric properties after 24 hours of the completion of the annealing process. The pellets were afterwards polished and thermally etched at 1250 °C for 20 min and the microstructure was then examined with a scanning electron microscope. The procedure of annealing, dielectric and microstructural characterization was repeated up to eight times to determine the effect of time and temperature. Due to the pronounced anisotropic shape of the grains, the grain size was determined by measuring the grain area on a polished cross-section. The average grain size was determined from scanning electron micrographs with the help of an image-tool program.

The microstructural investigations of the polished and thermally etched sample revealed a bimodal distribution of the grain sizes. The large, mostly anisotropic, grains occupied approximately 16 % of the polished surface (Figure 43).

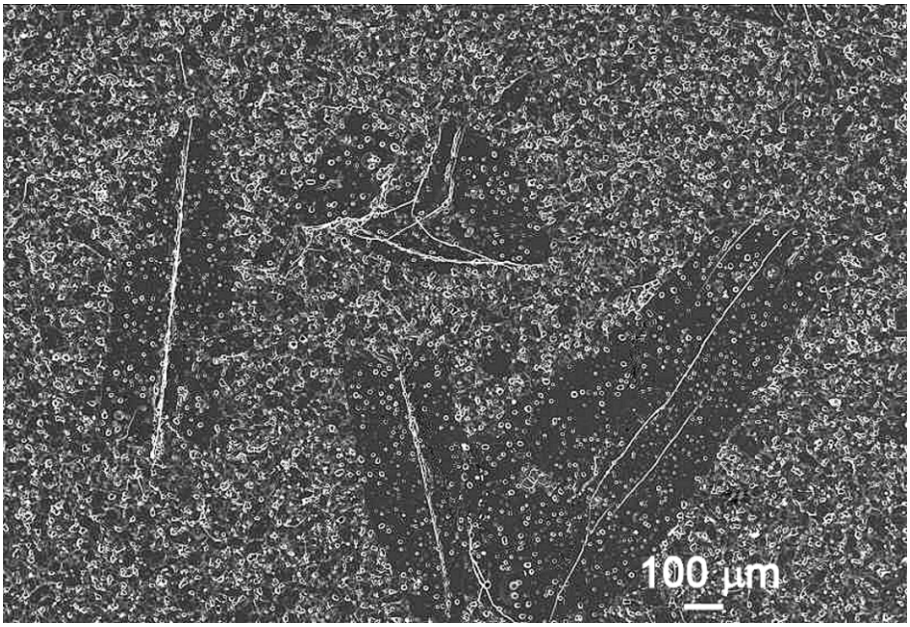

Figure 43. *Scanning electron micrograph of the thermally etched $Mg_3B_2O_6$ sintered at 1310 °C for 20 hours.*

The rest of the polished surface was covered with grains that had an average diameter of 10 µm. Although the grain diameter is the most commonly used in the literature for the description of grain size, in the text that follows the average area of the grain in the polished cross-section is used as a measure for the average grain size. The reason for such a decision was the anisotropic character of the grains in the $Mg_3B_2O_6$ samples. Large grains were considered as those grains with a cross-section area greater than 0.01 mm^2. With subsequent firings, the number of large grains as well as the portion of the polished surface covered with these grains increased (Figure 44). After 160 hours, more than 40 % of the polished surface

was covered with large grains (Figure 45 curve a). Apart from the areas of the large grains there were also regions with considerably smaller grains (Figure 44 b).

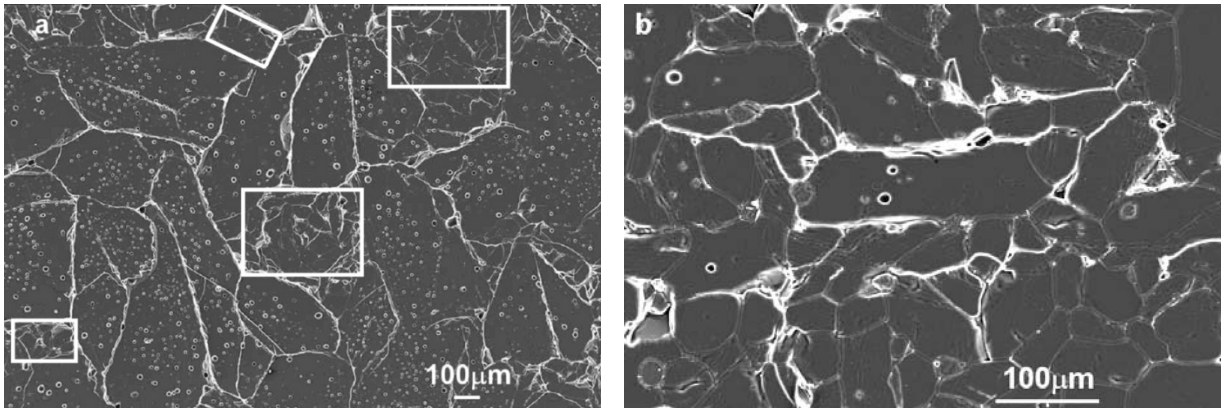

Figure 44. *Scanning electron micrograph of the thermally etched $Mg_3B_2O_6$ annealed 8 times at 1310 °C for 20 hours. The rectangles in "a" denote the areas with smaller grains. An example of such an area is shown in "b".*

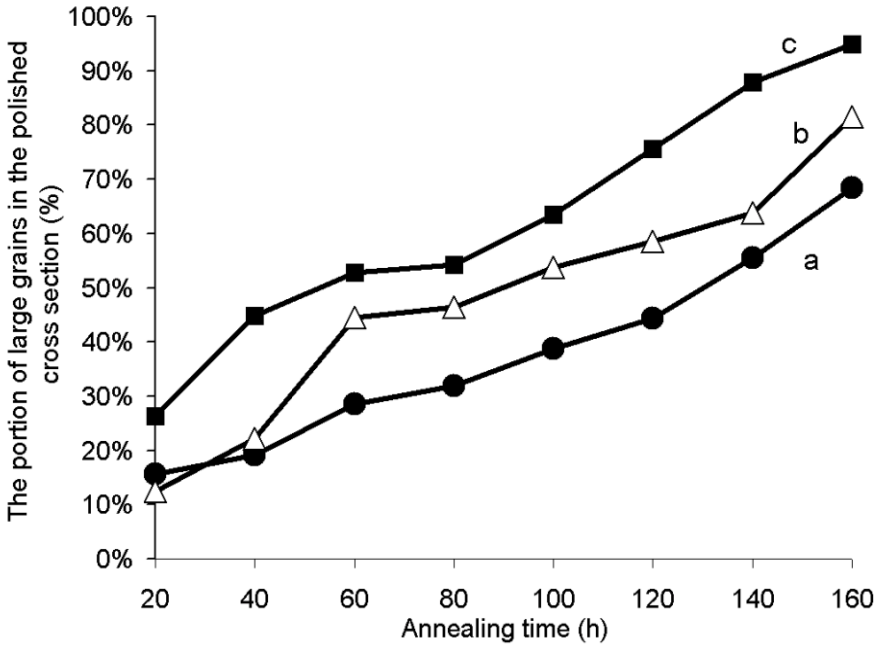

Figure 45. *The portion of large grains in the polished cross-section as a function of annealing time at 1310 °C; curve a: $Mg_3B_2O_6$ (—•—), curve b: $Mg_3B_2O_6$ with 1 wt.% of $Mg_2B_2O_5$(—△—), curve c: $Mg_3B_2O_6$ with 5 wt.% of $Mg_2B_2O_5$(—■—).*

Figure 46 illustrates how one particular large grain of $Mg_3B_2O_6$ ceramics without additive grows with the annealing time. We fired the sample at 1310 °C and every 20 hours we scan the image of this particular grain at the same magnification with the electron microscope. The

grain size was monitored with special image-tool program.

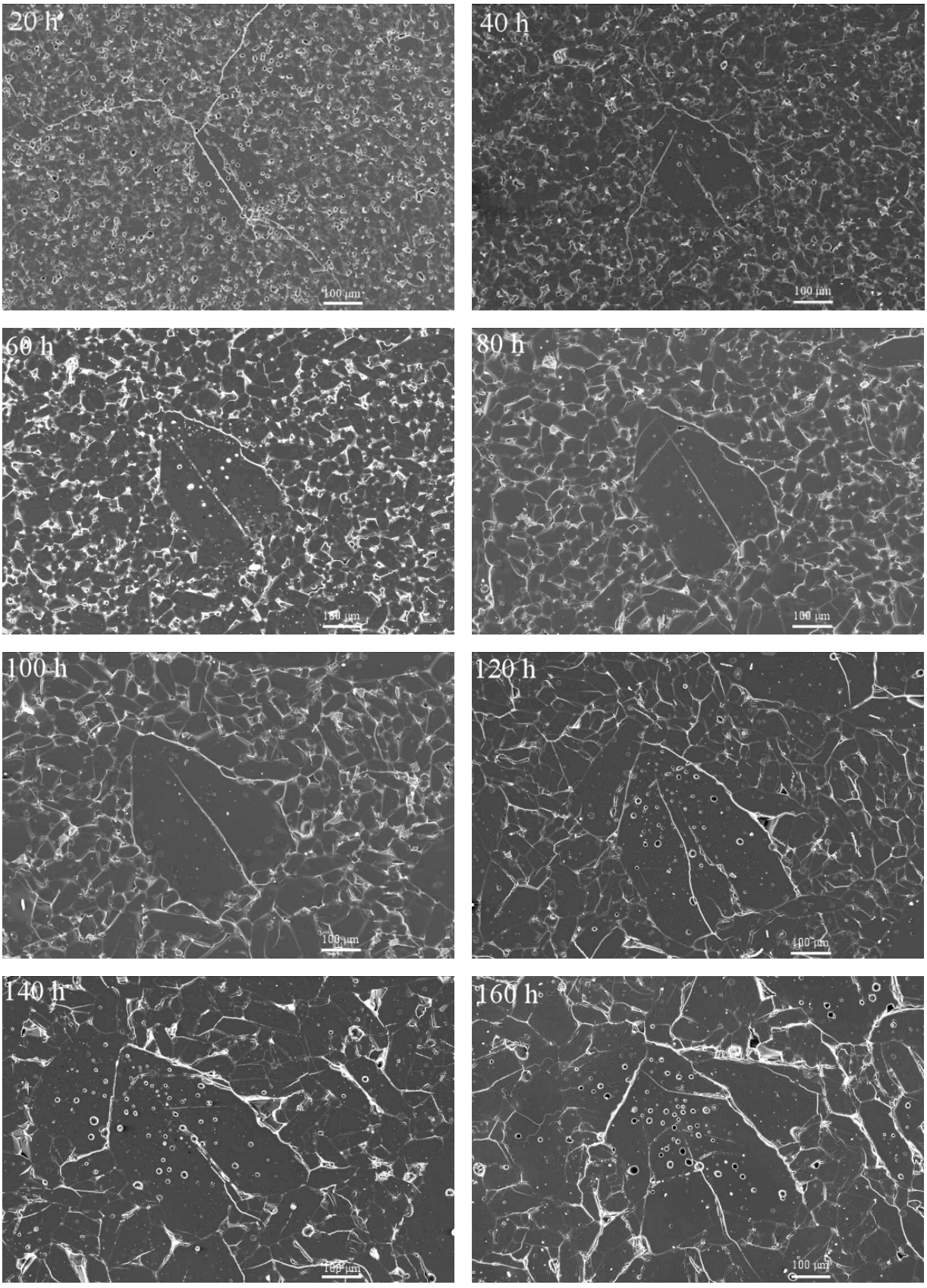

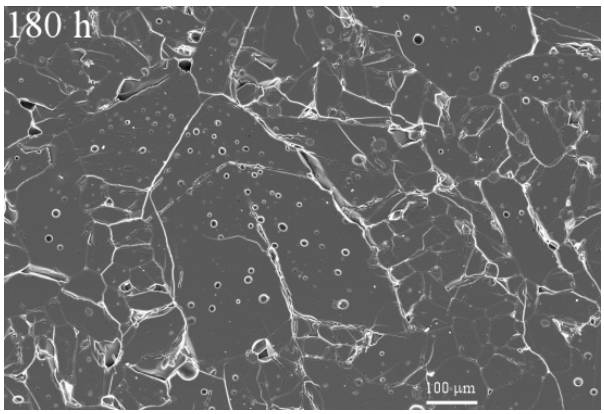

Figure 46. *Scanning electron micrographs of the one particular grain of $Mg_3B_2O_6$ sample annealed at 1310 °C for various time from 20 to 180 hours.*

When the size of one of the abnormally growing grains was monitored over time a linear increase in the grain size was observed (Figure 47). This is typical for grain growth in the presence of a liquid phase.[121]

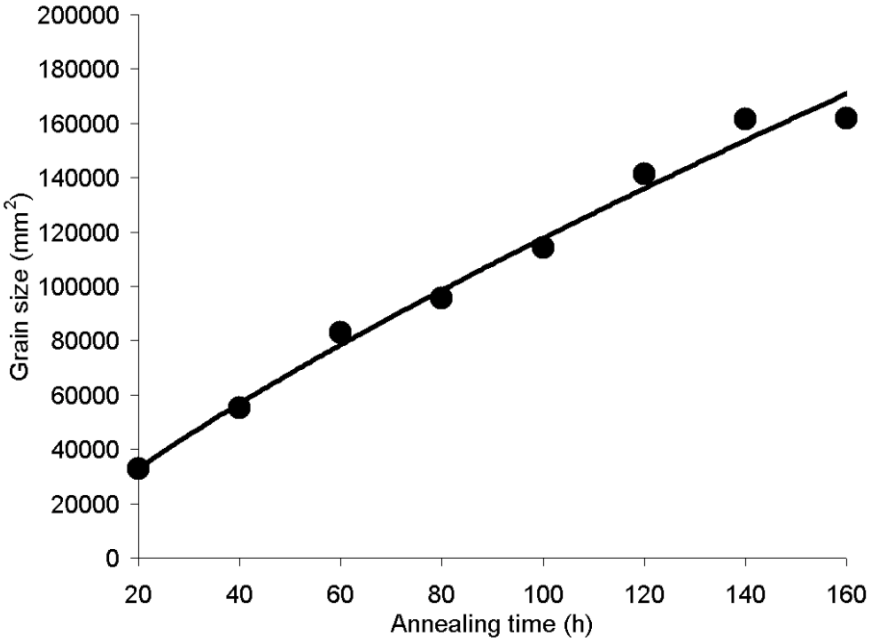

Figure 47. *The size of the single large grain of $Mg_3B_2O_6$ as a function of annealing time at 1310 °C.*

In the second step the grain growth of the $Mg_3B_2O_6$ ceramics was intentionally accelerated by the small addition of $Mg_2B_2O_5$. The liquid phase, which formed due to the incongruent decomposition of the $Mg_2B_2O_5$, is believed to cause the abnormal grain growth.[122] After a first annealing (20 hours at 1310 °C) the addition of $Mg_2B_2O_5$ only slightly influenced the average grain size. Nevertheless, the average grain size increased in the expected order, being

the largest in the $Mg_3B_2O_6$ sample with 5 wt.% of $Mg_2B_2O_5$. In this sample a significantly higher portion of the polished surface was covered by large grains in comparison with the samples with 0 and 1 wt.% of added $Mg_2B_2O_5$ (Figure 45 and Figure 48).

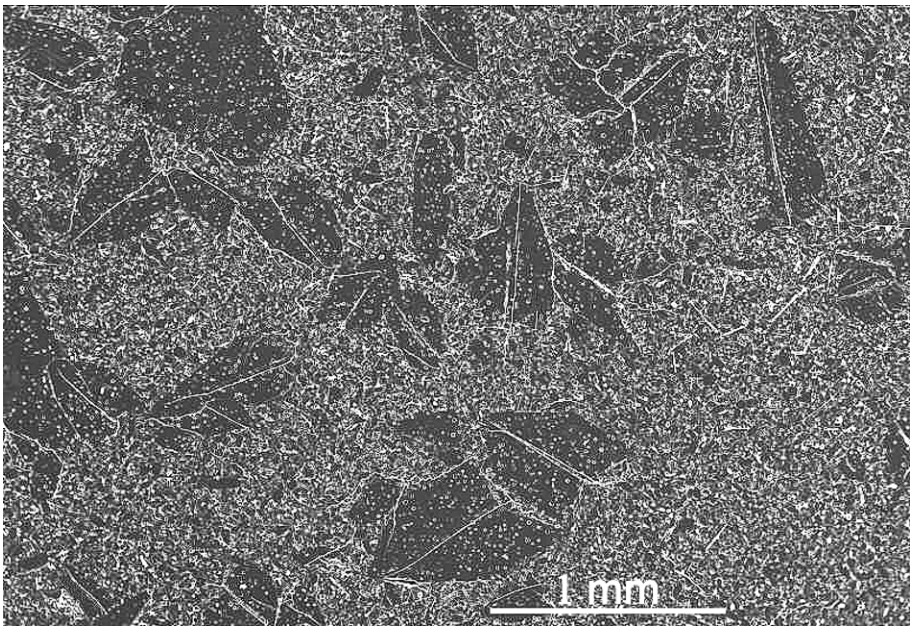

Figure 48. *Scanning electron micrograph of the thermally etched $Mg_3B_2O_6$ with 5 wt.% of $Mg_2B_2O_5$ sintered at 1310 °C for 20 hours.*

The increase in the average grain size and the portion of large grains with a prolongation of the annealing were observed for all the samples (Figure 45 and Figure 49). As expected, the fastest grain growth was observed for the $Mg_3B_2O_6$ sample with 5 wt.% of $Mg_2B_2O_5$ (Figure 50). After final annealing the average grain size in this sample was about 10 times larger than the samples with a smaller amount of $Mg_2B_2O_5$. More than 90 % of the polished surface was covered with large grains (Figure 45, curve c, Figure 49).

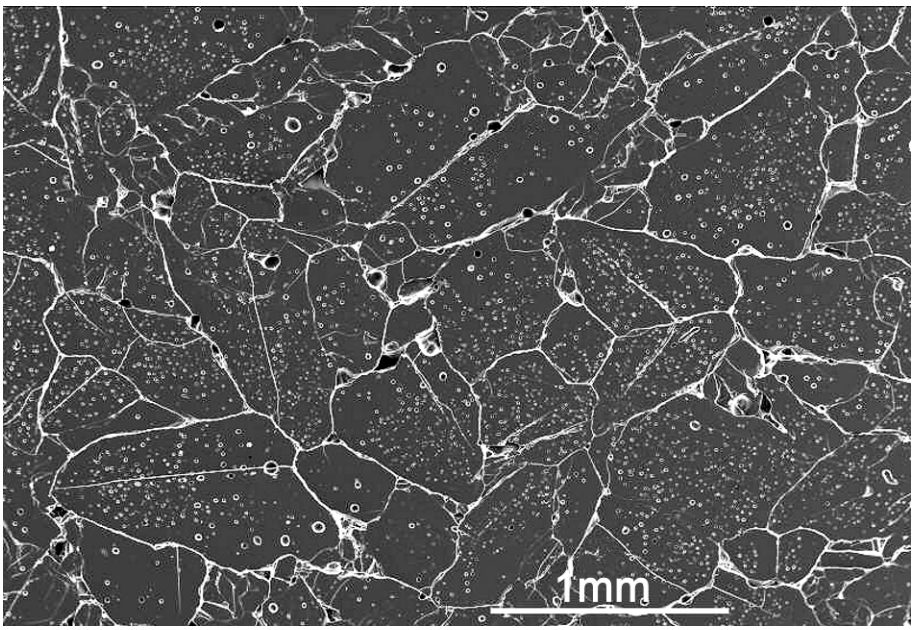

Figure 49. *Scanning electron micrograph of the thermally etched $Mg_3B_2O_6$ with 5 wt.% of $Mg_2B_2O_5$ annealed 8 times at 1310 °C for 20 hours.*

The contribution of the fast-growing large grains to the average grain size of the $Mg_3B_2O_6$ with various amounts of $Mg_2B_2O_5$ was significant, and because of that the time dependence of the average grain size was closer to the proportional growth rate than to the normal growth rate (Figure 50).

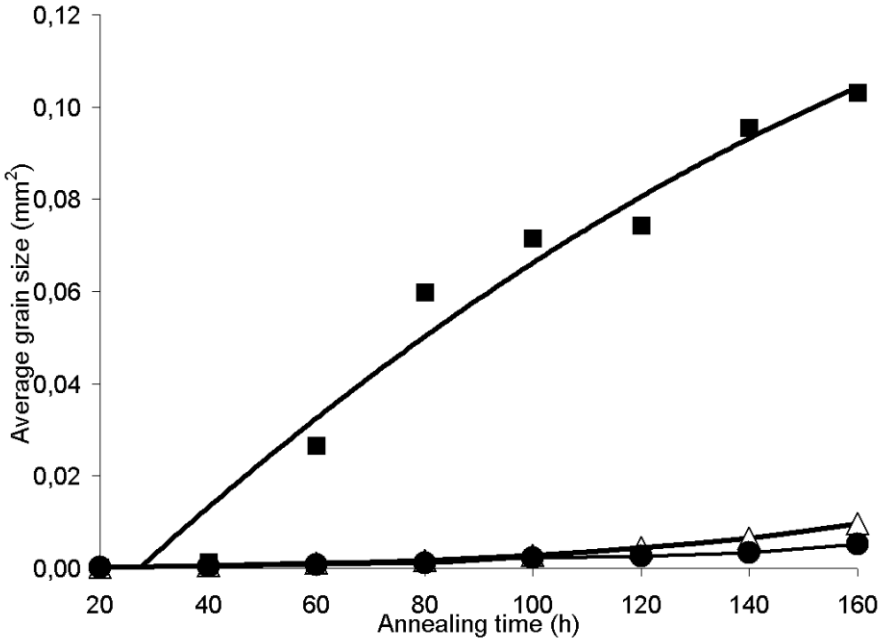

Figure 50. *The average grain size as a function of annealing time at 1310 °C; $Mg_3B_2O_6$ (—•—), $Mg_3B_2O_6$ with 1 wt.% of $Mg_2B_2O_5$(—△—),$Mg_3B_2O_6$ with 5 wt.% of $Mg_2B_2O_5$(—■—).*

The SEM imaging of the $Mg_3B_2O_6$ ceramics revealed that the exaggeratedly grown anisotropic grains contain the fault that extends along the anisotropic grain (Figure 43 and Figure 51). In several different ceramics the exaggerated anisotropic grain growth was observed for the grains containing the crystal defect, which extends along the anisotropy. Recnik et al. have studied the anisotropic grain growth in BaO-doped $CaTiO_3$ and proved that the grains containing polytypic faults grow preferentially along the direction of fault plane. The formation of the polytypic faults was assumed to be related to the local deviation from the stoichiometry, which was produced by the dopant.[123] A typical exaggeratedly grown anisotropic grain with a crystal defect that stretches along the direction of anisotropy is shown in Figure 51. Usually, a transmission electron microscope (TEM) would be used to identify the nature of such defects; however, the size of most of the anisotropic grains in the case of $Mg_3B_2O_6$ ceramics is in the vicinity of 1 mm, which makes the sample preparation cumbersome. We therefore applied electron back-scatter diffraction (EBSD) to obtain information about the crystallographic orientation of the parts of the grain on either side of the defect. EBSD known also as back-scatter Kikuchi diffraction is now regarded as the optimum technique for the routine measurement of microtexture, except for special cases where TEM is necessary.[124] The essential requirement for the generation of an EBSD pattern is that the specimen must be tilted so that the electron beam strikes it at a small angle, thus achieving a large fraction of electrons which have been diffracted (backscattered) by the lattice planes in the specimen.

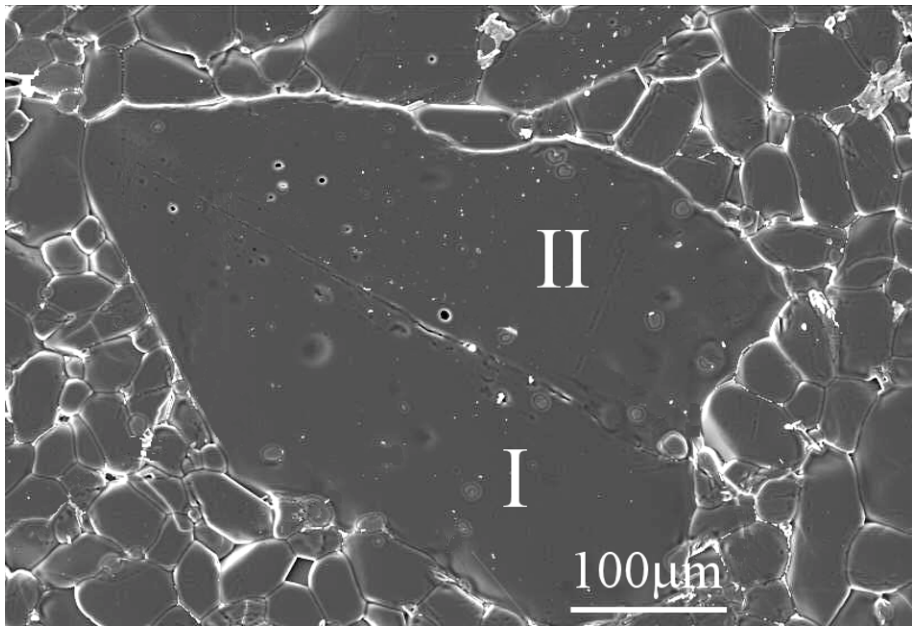

Figure 51. *Scanning electron micrograph of the exaggerated grown anisotropic grain with a twin boundary.*

The typical backscatter Kikuchi patterns obtained from both sides are shown in Figure 52. Essentially Kikuchi patterns are projection of the geometry of lattice planes in crystal.[125] The individual Kikuchi bands were indexed in the Pnnm setting, based on the bandwidth measurements using the INCA Crystal software. The conclusive information we derived from the indexation is based on a determination of the parallel poles between the two parts of the grain. It appears that the $[-1-11]_I$ is parallel to the $[1-11]_{II}$ and the $[0-11]_I$ is parallel to the $[0-11]_{II}$ (Figure 52). Such an orientation relationship implies that crystal parts I and II are related via a 180 º rotation about the normal to the (0-11) plane, which for a centrosymmetric Pnnm space group equals a reflection across (011). Based on these findings it can be concluded that the defect stretching along the anisotropic grains is a (011) twin boundary. The misorientation of the two parts of the grain in terms of reciprocal space is shown schematically in Figure 53. Further investigations of the local chemistry are needed in order to find the reasons for the formation of such a twin boundary.

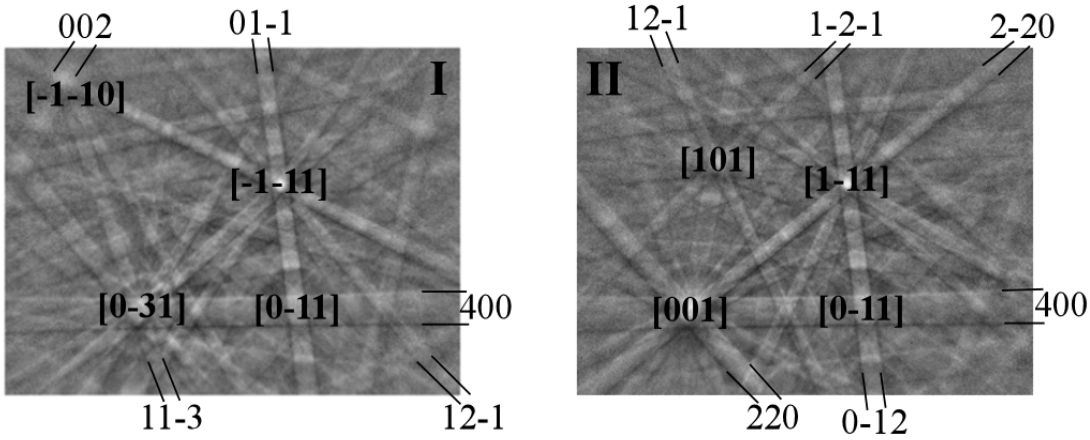

Figure 52. *EBSD patterns corresponding to the regions I and II from Figure 49.*

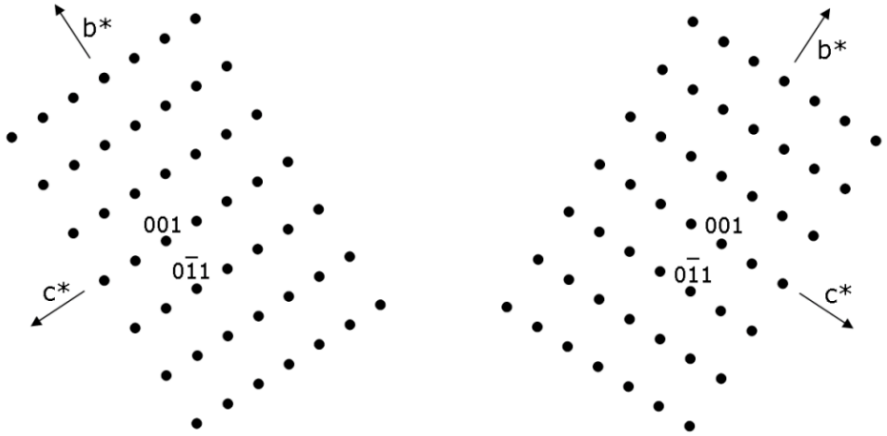

Figure 53. *Misorientation of the parts of the grain across the (011) twin boundary, in terms of the reciprocal lattice.*

4.1.4.1.1 Microwave dielectric properties of $Mg_3B_2O_6$ ceramics with various amounts of $Mg_2B_2O_5$ and different annealing times.

After the first annealing the samples with different amounts of $Mg_2B_2O_5$ did not differ significantly in terms of their Qxf values, permittivity and density (Table 12). The dielectric measurements, which were performed after each annealing and cooling step, showed that the Qxf values for all the $Mg_3B_2O_6$ samples increased with a prolongation of the annealing time, while the permittivity remained at 7. In addition, the density did not change significantly with annealing. We observed that the closed porosity increased, while the open porosity decreased during the grain growth. However, the overall porosity did not change and remained in the range 3-4 % for all the samples. It was also observed that the $Mg_3B_2O_6$ sample with the 5 wt.% of $Mg_2B_2O_5$ always exhibited the highest Qxf values. The maximum Qxf value of 240 000 GHz was obtained for this kind of sample after annealing for 160 hours at 1310 °C (Table 12, Figure 54). This value was the same, regardless of whether the sample was continuously annealed for 160 hours or annealed eight times for 20 hours with intermediate cooling. In both cases this high Qxf value was not improved with further annealing. Figure 54 also shows that the increase in the Qxf values in the $Mg_3B_2O_6$ sample with 5 wt.% of $Mg_2B_2O_5$ was accompanied by a much larger increase in the grain size compared to that in the $Mg_3B_2O_6$ with 1 wt.% and without addition of $Mg_2B_2O_5$, where a Qxf value of over 200 000 GHz was measured for the much more fine-grained ceramics. This implies that not only the grain size but also other factors influence the Qxf values. Since the smaller grains are preferable in terms of the mechanical strength, investigations of $Mg_3B_2O_6$ should focus on the simultaneous prevention of the exaggerated grain growth and the preservation of high Qxf values. This would be possible by decreasing the amount of amorphous and $Mg_2B_2O_5$ phases in the synthesized $Mg_3B_2O_6$ powder. The improvement of the Qxf values with annealing could be attributed to a decrease in the amount of the amorphous phase during annealing.

Table 12. *Qxf values of $Mg_3B_2O_6$ annealed under different annealing conditions and with various amounts of $Mg_2B_2O_5$.*

FIRING	Qxf		
1310°C/20h	$Mg_3B_2O_6$ with add. of $Mg_2B_2O_5$		
cooling 2°C/min	0 wt.%	1 wt.%	5 wt.%
1x	108000	101000	111000
2x	128000	135000	154000
3x	156000	158000	170000
4x	160000	175000	186000
5x	180000	189000	197000
6x	199000	212000	222000
7x	212000	225000	229000
8x	200000	237000	241000

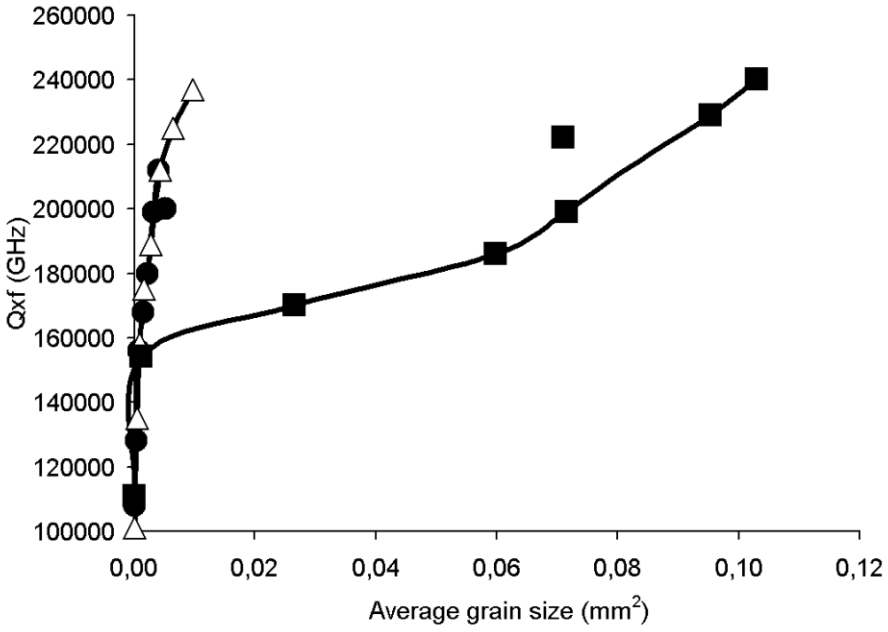

Figure 54. *Qxf values as a function of average grain size; $Mg_3B_2O_6$ (—●—), $Mg_3B_2O_6$ with 1 wt.% of $Mg_2B_2O_5$(—△—),$Mg_3B_2O_6$ with 5 wt.% of $Mg_2B_2O_5$(—■—).*

4.2 Ternary system $MgO-B_2O_3-SiO_2$ (MBS)

Taking into account several low permittivity and high Q compounds (Mg_2SiO_4, $MgSiO_3$, $Mg_3B_2O_6$ and $Mg_2B_2O_5$) that crystallize in the $MgO-B_2O_3-SiO_2$ system, the glass-ceramics based on $MgO-B_2O_3-SiO_2$ is expected to be a good alternative to commercially used $CaO-B_2O_3-SiO_2$ glass-ceramics.

However, the crystallization of $MgO-B_2O_3-SiO_2$ glass and the dielectric properties of the corresponding glass-ceramics have not been widely investigated yet. The $CaO–B_2O_3–SiO_2$ glass-ceramics is promising LTCC substrate material because of low dielectric loss, low firing temperature and compatibility with several metal electrodes.[10,20,21,126,127] Ferro A6 LTCC material is the commercial representative from $CaO-B_2O_3-SiO_2$ system. In the following chapters we intend to introduce new $MgO-B_2O_3-SiO_2$ (MBS) based glass-ceramics material with competitive dielectric performance. Our investigation was focused on the 43 wt.% MgO-35 wt.% B_2O_3-22 wt.% SiO_2 composition. The main purpose of the work was to study the sintering and crystallization behaviour in correlation with the microwave dielectric properties. The influence of the TiO_2 nucleating agent on the crystallization and microwave dielectric properties of this glass-ceramics was also examined and discussed.

4.2.1 Preliminary evaluation of the 43 wt.% MgO – 35 wt.% B_2O_3 – 22 wt.% SiO_2 glass-ceramic as a potential low – permittivity substrate prepared in corundum (Al_2O_3) crucible

The glass composition contained 43 wt.% MgO–35 wt.% B_2O_3–22 wt.% SiO_2 was chosen according to the preliminary studies and phase diagram[97]. At the beginning the glass was prepared in a corundum crucible which was later replaced by platinum crucible. The typical events that occurred during the transformation from glass to glass-ceramics are well visible in the DSC curve of MBS glass illustrated in Figure 55. The inflection at 650 °C is attributed to the glass transition temperature. The exothermic peak at 780 °C was attributed to the crystallization of $Mg_2B_2O_5$, while the weak exothermic peak at 950 °C presumably corresponds to crystallization of the cordierite ($Mg_2Al_4Si_5O_{18}$). The crystallization of $Mg_2B_2O_5$ was confirmed by the XRD analysis of the powder obtained in the separate DSC experiment, which was stopped at the temperature of the crystallization peak.

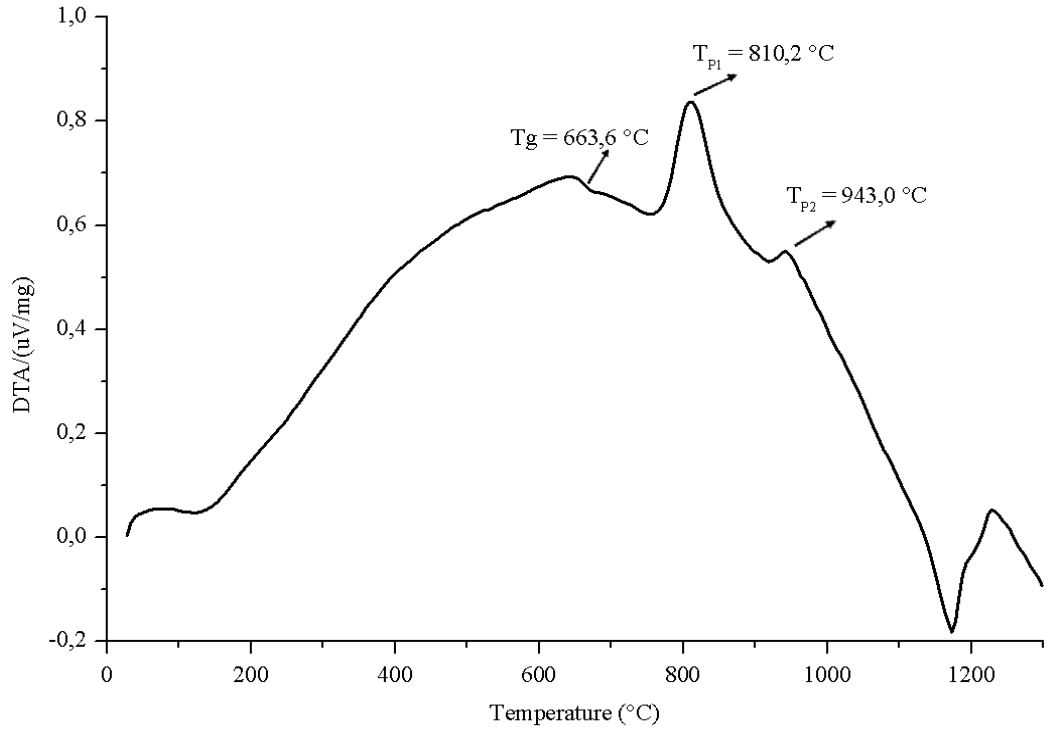

Figure 55. *DSC curve for a MBS glass powder prepared in corundum crucible heated at 10 °C/min heating rate. (Tg, glass transition temperature; T_{p1}, T_{p2}, peak crystallization temperature.)*

The sintering behaviour of milled glass powder was examined by heating microscope (HM) measurements (Figure 56). Since this method monitors the change of the pellet's silhouette during heating, any shrinkage and enlargement of the pellet results in decrease and increase of its cross – sectional area, respectively. According to the heating microscope measurements, sintering starts at around 660 °C, what is in accordance with the glass-transition temperature (Tg) in the DSC curve (Figure 55). Sintering of glass powder compact generally starts at temperatures slightly higher than Tg due to viscous flow, which stimulates coalescence of the powder and removes the pores from the bulk of materials.[128] After the steep decrease of the cross-sectional area due to the sintering, the cross-sectional area does not change between 750 and 1000 °C (Figure 56). According to the DSC curve the crystallization takes place in this temperature range (Figure 55). At temperatures greater than 1050 °C the cross-sectional area increases as the result of the deformation of the pellet. The melting was observed as steep decrease in the cross-sectional area at T > 1100 °C and as endothermic peak at 1170 °C in the DSC curve.

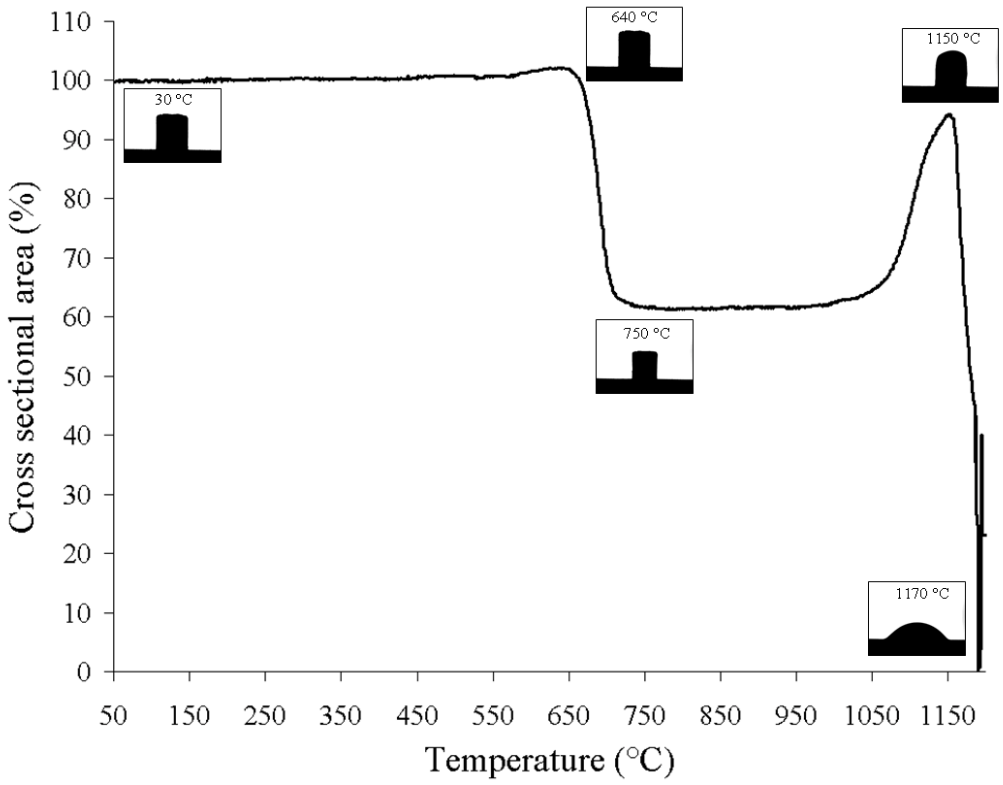

Figure 56. *Shrinkage curve of glass composition 43 wt.% MgO – 35 wt.% B_2O_3 – 22 wt.% SiO_2 melted in a corundum crucible as a function of sintering temperature, fired at a heating rate of 10 °C/min in air.*

Properties of the polycrystalline materials depend on the quantity and composition of the crystalline phases. The phase evolution during isothermal annealing at various temperatures from 600-1000 °C was followed by X – ray powder diffraction showed in Figure 57. At the temperatures below 800 °C the crystallization didn't occur. The XRD pattern of the glass-ceramics obtained by annealing at 800 °C for 10 hours revealed the crystallization of monoclinic (S.G. *P*21/*a*) and triclinic (S.G.*P*1) crystal modifications of the $Mg_2B_2O_5$. The peak intensity of monoclinic modification decreased with increasing the sintering temperature. When the annealing temperature was increased up to 900 °C the cordierite (indialite) phase started to form. Indialite is the hexagonal modification and high temperature polymorph of cordierite and has identical stoichiometry: $Mg_2Al_4Si_5O_{18}$.[129] The reason of cordierite formation was the diffusion of aluminium from corundum (Al_2O_3) crucible to the melt during melting process. The involvement of aluminium in new phase indicated that part of it participated in the crystallization reaction. We expected that the cordierite could influence also the material properties. The reaction of the melt with alumina crucible was consistent with the observations reported by Y. J. Seo et. al.[130] The proximity of some $Mg_2B_2O_5$ and cordierite diffractions caused the broadening of the corresponding XRD lines

(Figure 57). With increasing the annealing temperature up to 950 °C the 2 – Theta peaks become wider due to the formation of $MgSiO_3$ phase. This is the most evident for the diffraction at 2θ between 34-36 °. The level of $MgSiO_3$ crystallinity increased at 1000 °C whereas the amount of cordierite phase considerably was reduced at this temperature.

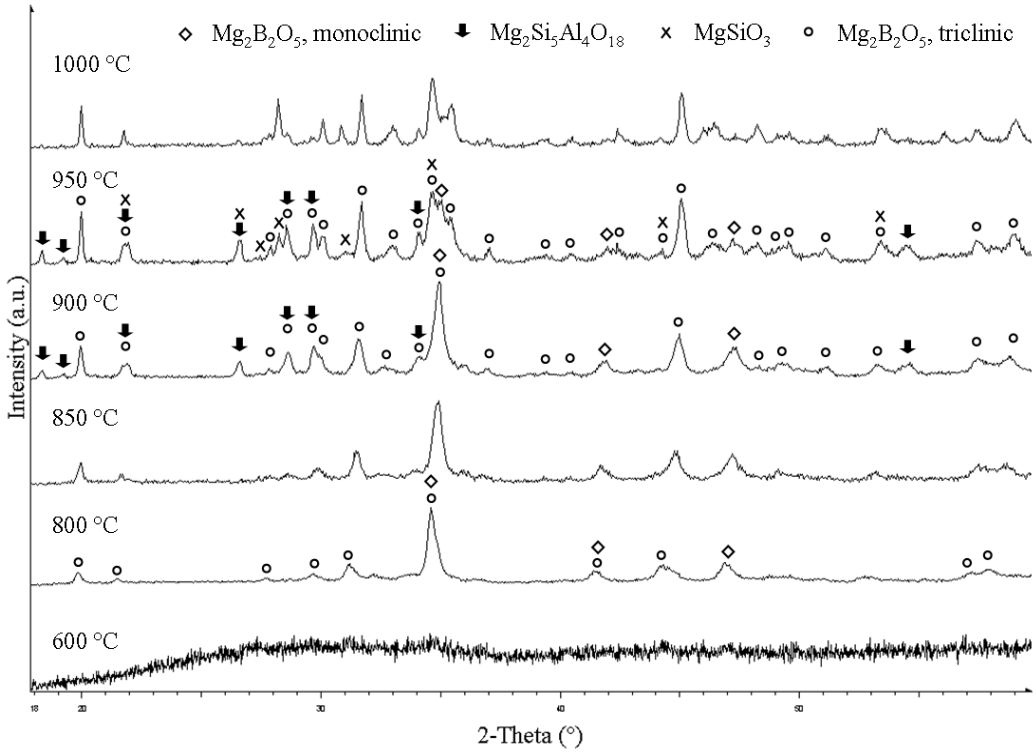

Figure 57. *X – ray powder diffraction results for the glass and glass – ceramic composition 43 wt.% MgO – 35 wt.% B_2O_3 – 22 wt.% SiO_2 prepared in corundum crucible. Denotation of the crystalline phases: ⬇ $Mg_2Si_5Al_4O_{18}$, ○ $Mg_2B_2O_5$ - triclinic, x $MgSiO_3$, ◇ $Mg_2B_2O_5$ - monoclinic.*

The elemental chemical analysis of the molten glass was done to confirm the contamination with aluminium during glass melting. The chemical analysis performed by inductively coupled plasma atomic emission spectroscopy (ICP - AES) revealed that the glass –ceramics contained 2.9 wt.% of aluminium (Table 13).

Table 13. *Chemical analysis (by ICP method) of glass composition 43 wt.% MgO – 35 wt.% B_2O_3 – 22 wt.% SiO_2 melted in a corundum crucible.*

Constituents of the glass	Mg	B	Si	Al
Content (wt.%)	24.4	9.7	9.3	2.9

4.2.1.1 Microstructure studies

The general study of MBS glass heated at different temperatures between 800 and 1000 °C for 5 hours indicated the formation of $Mg_2B_2O_5$ as main crystalline phase, while cordierite and $MgSiO_3$ were present as secondary phases. The relative amount of the phases depended on the annealing temperature. Due to the difficulties of the quantitative determination of boron by the EDS, the amount of crystalline phases was estimated from the XRD pattern. SEM micrographs of the polished and chemically etched glass-ceramics, which was previously sintered at 800-1000 °C, are shown in Figure 58. Although the sample for SEM were prepared by chemical etching (HF and HNO_3), the residual glassy phase still remained. According to microstructure, we believe that obtained glass – ceramics containing large portion of amorphous phase. In the glass-ceramics annealed at higher temperature (850, 900 and 950 °C) quite uniform distribution of spherical particles was obtained. The density measurements revealed (Table 14) slight increase of porosity with the increase of sintering temperature from 800 to 950 °C. At 1000 °C the density suddenly dropped from 2.72 (800 °C) to 2.21 g/cm^3 (1000 °C). This decrease in density for nearly 20 % is visible also in the microstructure (Figure 58, e).

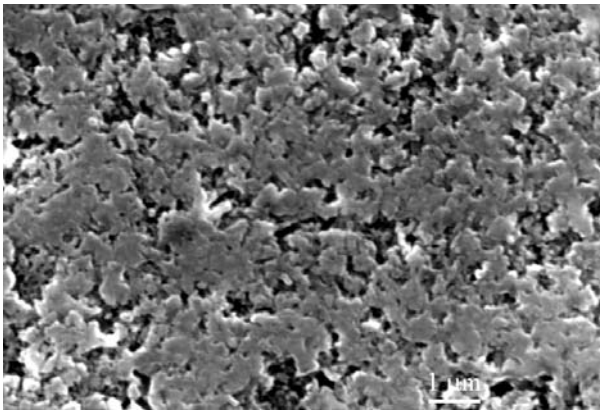

(a) 800 °C

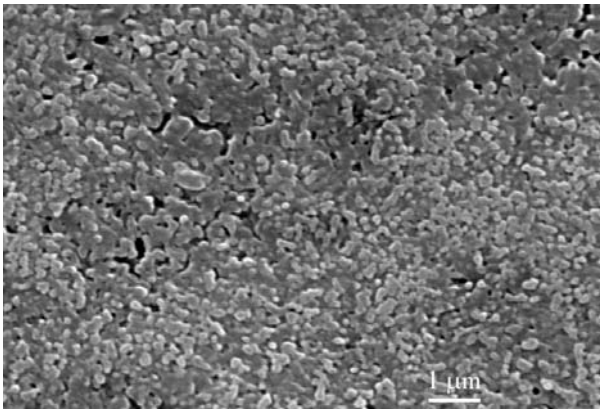

(b) 850 °C

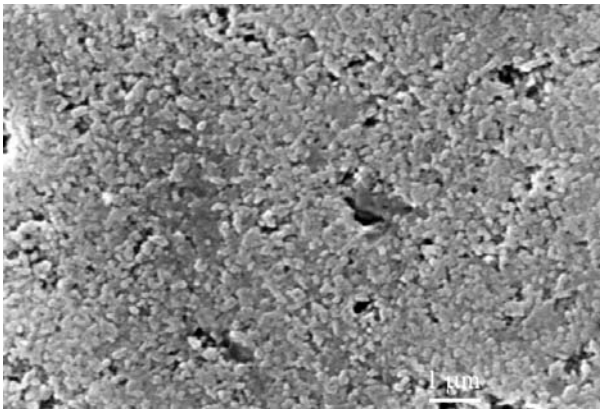

(c) 900 °C

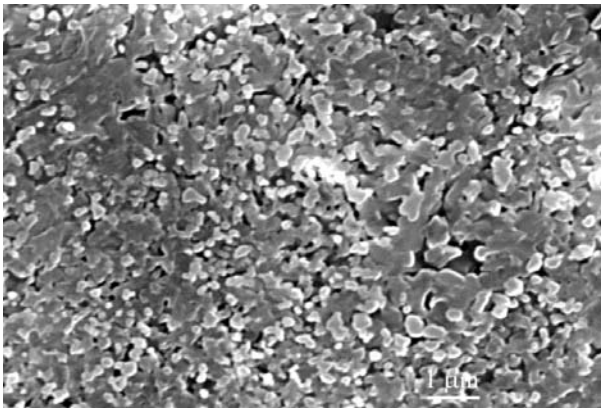

(d) 950 °C

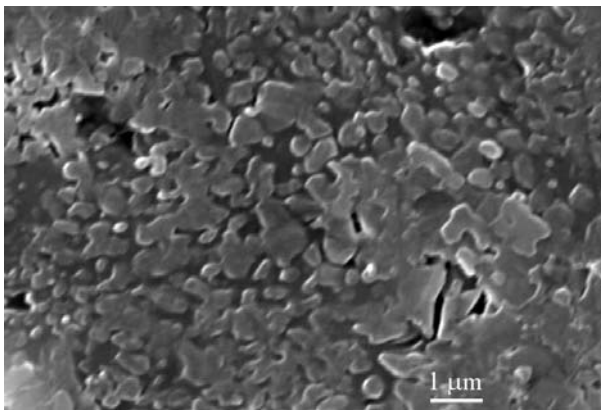

(e) 1000 °C

Figure 58. *SEM images after chemical etching of 43 wt.% MgO – 35 wt.% B_2O_3 – 22 wt.% SiO_2 glass – ceramics sintered sample at: (a) 800 °C, (b) 850 °C, (c) 900 °C, (d) 950 °C, (e) 1000 °C.*

Table 14. *Dielectric characterization of 43 wt.% MgO – 35 wt.% B_2O_3 – 22 wt.% SiO_2 composition as a function of sintering temperature and duration of milling.*

	Sintering conditions	**Shrinkage (%)**	**Permittivity (/)**	**Qxf (GHz)**	**Density (g/cm^3)**
Crushed	800°C/5h	14	6.4	2454	2.68
	850°C/5h	14	6.2	3745	2.67
	900°C/5h	14	5.9	5328	2.66
	950°C/5h	14	5.7	8178	2.62
	1000°C/5h	11	5.4	5726	2.50
		Shrinkage (%)	**Permittivity (/)**	**Qxf (GHz)**	**Density (g/cm^3)**
Milled 1h	800°C/5h	18	6.4	1836	2.69
	850°C/5h	18	6.3	2694	2.68
	900°C/5h	18	6.0	5415	2.66
	950°C/5h	17	5.8	7940	2.62
	1000°C/5h	14	5.2	5981	2.36
		Shrinkage (%)	**Permittivity (/)**	**Qxf (GHz)**	**Density (g/cm^3)**
Milled 2h	800°C/5h	20	6.5	2919	2.72
	850°C/5h	20	6.4	3794	2.72
	900°C/5h	20	6.0	2415	2.69
	950°C/5h	18	5.6	9357	2.58
	1000°C/5h	13	4.7	9135	2.21

Milling was performed in planetarium mill in acetone media.

4.2.1.2 Microwave dielectric properties

Microwave dielectric properties of the MBS glass-ceramics sintered at 800-1000 °C are summarized in the Table 14. The glass-ceramics for dielectric characterization was prepared from the powders with different median particle size, what was achieved by variation of milling time. The purpose was to optimize the milling conditions in order to prepare the ceramics with the optimal dielectric properties. The prolongation of milling time increased contraction of the glass – ceramic from 14 to 20 % which resulted in a slight increase in densities. Sintering temperature between 800 and 950 °C did not significantly effect the densities regardless of the milling time.

A glass-ceramic material is usually comprised of one or several crystalline phases distributed in a glassy matrix. Therefore it can be expected that the dielectric properties of the material are influenced by the content, composition, particle sizes and the way of distribution of its constituent phases. The crystalline phases, glass matrix and the interfacial region existing between them each may have its own contribution to the polarization processes occurring in the glass ceramic material as a whole. In order to illuminate the effects of sintering temperature on the microwave dielectric properties, the variation of dielectric constant and Qxf value of MBS glass-ceramics versus sintering temperatures was examined (Figure 59 and Figure 60, Table 14). It is well known that finely ground material obtained by milling have a large impact on the density and consequently on dielectric properties. Therefore, it is not surprising that the prolonged milling (2h) led to the ceramics with the highest density, permittivity and Qxf-values. The dielectric constant of the samples varied from 6.5 to 4.7 with increasing the sintering temperatures from 800 to 1000 °C, respectively. The significant decrease of dielectric constant at 1000 °C is in accordance with the increase of porosity (Figure 58, e). The increase of Q×f values with the sintering temperature was observed for all three types of glass-ceramics up to 950 °C (Figure 60, Table 14). This improvement of the Qxf values is most probably related with better crystallization at higher temperature, what consequently results in smaller glass content. The network formers in the remaining glass can profoundly absorb the microwave power at high frequencies, which caused the degradation of the Q×f values of glass–ceramic.[127] The highest Qxf value of 9357 GHz was obtained for the glass-ceramics prepared from the finest powder (2-hour milled) which was sintered at 950 °C. At 1000 °C the Qxf values suddenly decreased (Figure 60, Table 14). This could be the consequence of partial melting, what increased the amount of glassy phase. Another reason for this deterioration of Qxf values could be related with the decrease of the cordierite phase (Figure 57). Figure 61 shows the temperature coefficient of resonant frequency τ_f of glass–ceramic sintered at different temperature for 5 h. The τ_f values

of glass–ceramic increased non – uniformly from - 25 to - 45 ppm/°C with the increase of sintering temperature from 800 to 1000 °C.

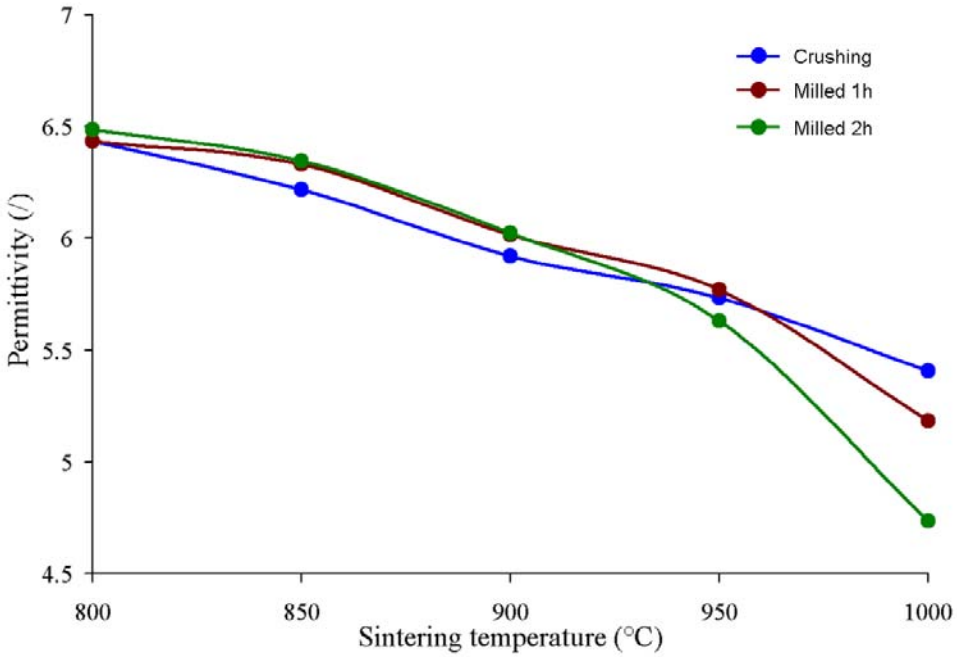

Figure 59. *Dielectric constant of the 43 wt.% MgO – 35 wt.% B_2O_3 – 22 wt.% SiO_2 glass – ceramic prepared in corundum crucible as a function of sintering temperature at various milling conditions.*

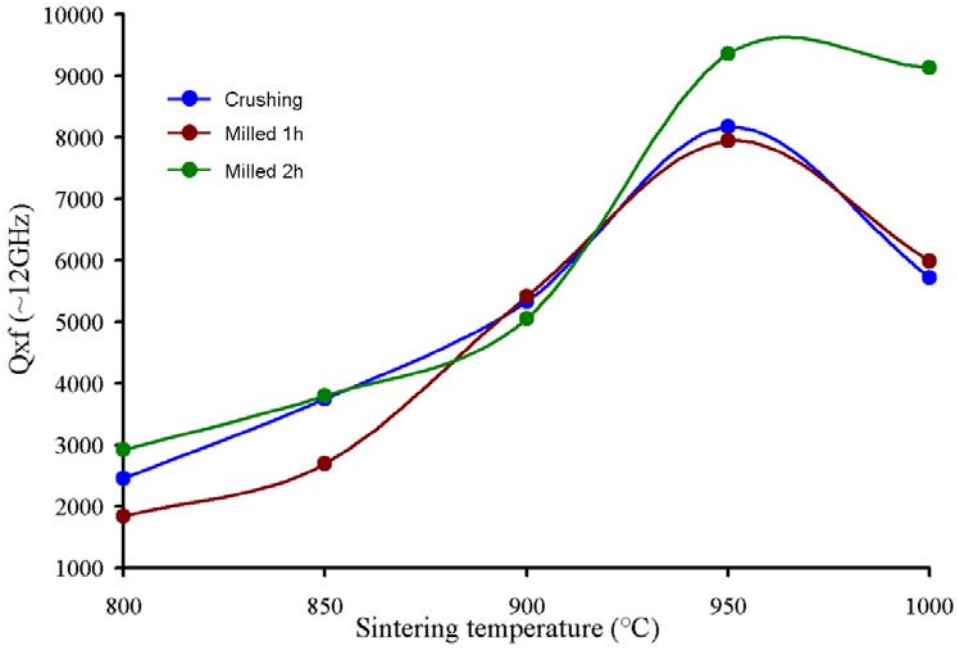

Figure 60. *Quality values of the 43 wt.% MgO – 35 wt.% B_2O_3 – 22 wt.% SiO_2 glass – ceramic prepared in corundum crucible as a function of sintering temperature at various milling conditions.*

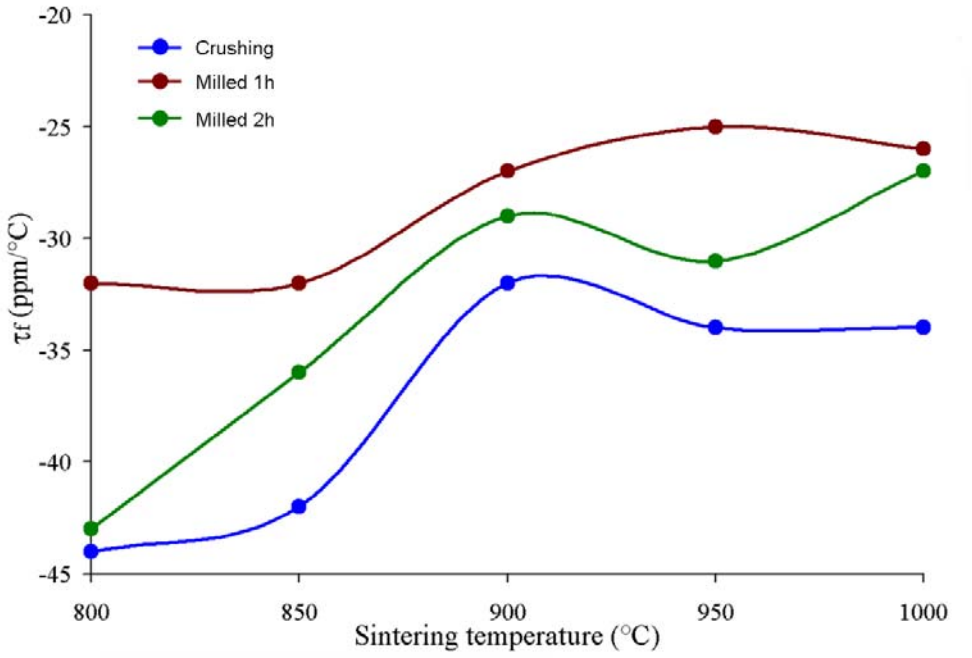

Figure 61. *Temperature coefficient of resonant frequency of the 43 wt.% MgO – 35 wt.% B_2O_3 – 22 wt.% SiO_2 glass-ceramic prepared in corundum crucible as a function of sintering temperature at various milling conditions.*

4.2.2 The synthesis of the 43 wt.% MgO–35 wt.% B_2O_3–22 wt.% SiO_2 (MBS) glass-ceramic composition prepared in platinum crucible

In order to avoid the diffusion of aluminium from the crucible to the glass, the whole glass preparation procedure was repeated in the Pt-crucible. Although cordierite exhibits very promising dielectric properties we tried to avoid its formation. During the preparation of MBS glass the cordierite formed as the reaction product between the melt and crucible and because of that it is difficult to control its amount. The procedure for preparation of the glass composition with 43 wt.% MgO–35 wt.% B_2O_3–22 wt.% SiO_2 in platinum crucible was completely the same as in the case of melting in the corundum crucible and it is described in chapter 4.2.1. The DSC analysis of glass powder (Figure 62) clearly shows the glass transition temperature (Tg) and the exothermic crystallization peak. Comparison between the samples melted in different crucible revealed that glass transition temperatures are almost identical in both cases. However, a glass sample melted in platinum crucible showed only a single crystallization peak (T_{p1} = 869.5 °C) while a glass from corundum crucible comprised two crystallization peaks. In both cases the strongest peak belongs to the $Mg_2B_2O_5$ crystallization. In case of glass melted in platinum crucible, this crystallization peak appeared at higher

temperature than that for the glass melted in corundum crucible ($T_{p(corundum)}$ = 810.2 °C, $T_{p(platinum)}$ = 869.5 °C). The reason for this difference could be attributed to different size of the particles.

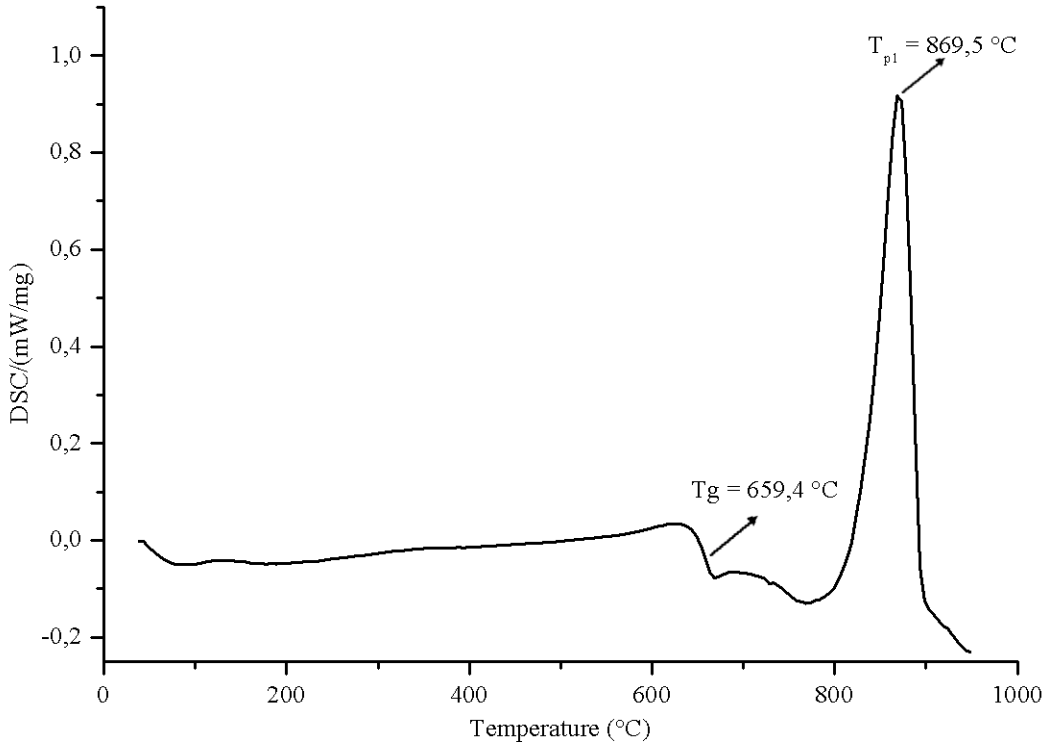

Figure 62. *DSC curve for a MBS glass powder prepared in platinum crucible heated at 10 °C/min heating rate. (Tg, glass transition temperature; T_{p1}, peak crystallization temperature.)*

The comparison between the data obtained by heating microscope and DSC give us very useful information about that how the processes such as densification, crystallization and melting followed during the heat-treatment procedure. For the preparation of any dense glass-ceramics material it is very important that the densification takes place before the crystallization starts. The temperature interval between the Tg and on-set of crystallization is very important for further applications of glass. According to the heating microscope measurements of MBS melted in platinum crucible (Figure 63) sintering started at approximately 640 °C and the densification is finished at 700 °C. The temperature plateau from 700 to 1100 °C was stable relating to further densification. Above 1100 °C the glass-ceramic sample started to melt.

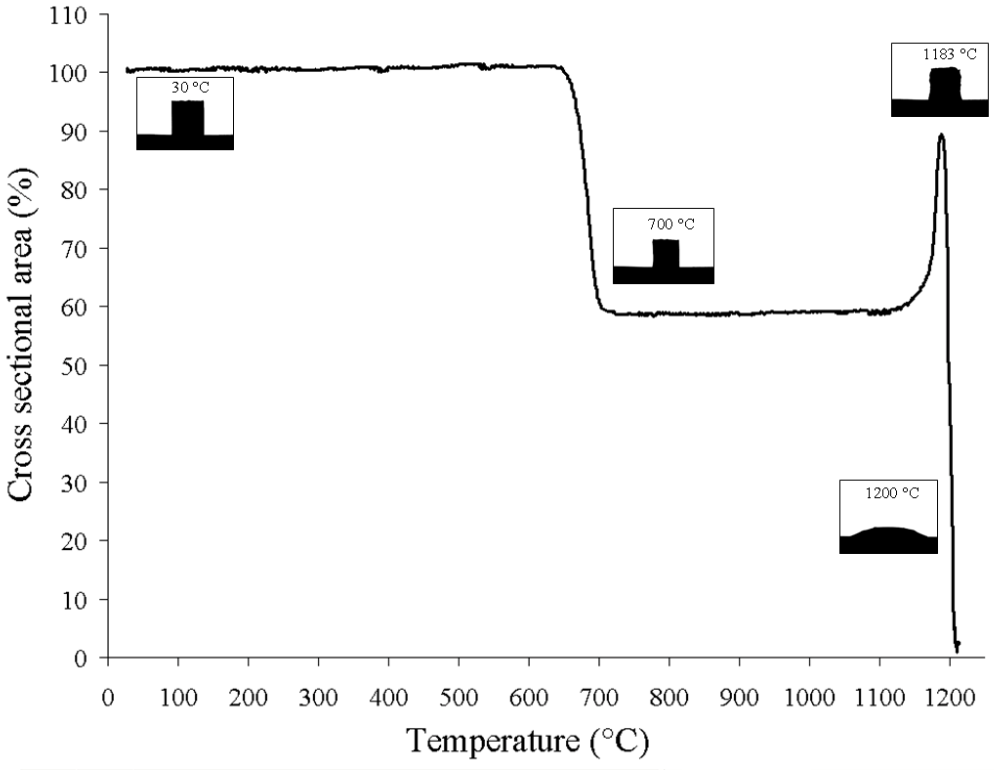

Figure 63. *Shrinkage curve of glass composition 43 wt.% MgO – 35 wt.% B_2O_3 – 22 wt.% SiO_2 melted in platinum crucible as a function of sintering temperature, fired at a heating rate of 10°C/min in air.*

4.2.3 Crystallization of MBS glass

The dielectric properties of low-permittivity LTCC substrates, what is the targeted application of MBS glass-ceramics, in great extend depend on the type and amount of the crystalline phases. In order to understand the crystallization process in the MBS glass we investigated the mechanism and the kinetics of the nucleation and crystal growth. The aim of this study was to establish the technical criteria for the optimization of the dielectric properties of the MBS glass. Knowing the nucleation rate at different temperatures for glass-forming melts has both scientific and technological importance, especially, the temperature where the nucleation rate is a maximum. However, these data are important to prepare glass-ceramics with desired microstructures by controlled nucleation and crystallization, as well as to understand the stability of a glass for practical applications where the formation of nuclei and their subsequent growth to crystal must be avoided (such as in optical fibers, laser glasses, optical switching glasses).[131] The procedure commonly used to determine the nucleation rate is to heat the glass at a certain temperature for a selected period of time, thereby developing some number of nuclei within the glass. The glass is then heated to a higher temperature for a short time, where detectable crystals grow on these nuclei. Assuming that each crystal grows from a

single nucleus and that no new nuclei form or dissolve during crystal growth, the number of nuclei per unit volume of the glass can be determined by counting the number of crystals in a given volume. The nucleation rate is determined at different temperatures by repeating the same procedure at various temperatures and times. This method is very time consuming. The development of the thermoanalytical techniques such as DTA or DSC enabled much faster determination of the nucleation rate as well as other kinetic parameters such as activation energy (E_G) and Avrami exponent (n). Nevertheless, the results obtained by the thermal analysis methods depend on sample characteristics (particle size, thermal conductivity, heat capacity) and also on instrumentation (furnace size, sample holder material, thermocouple location etc). The influence of these factors could be eliminated by the calibration of the instrument.

The non-isothermal DTA and DSC techniques are experimentally simple and quick, and give comparable results with isothermal techniques. However, the correct interpretation of the non-isothermal DTA and DSC results requires the knowledge of the crystallization mechanism.

The investigation of the nucleation and crystallization mechanisms are presented in the following chapter, which is divided in two parts: the first part is dedicated to the MBS glass while the second part is related to the influence of nucleating agent TiO_2.

4.2.3.1 Determination of the nucleation temperature range for MBS glass

The MBS glass was prepared by the method (described in Chapter 3.1.2. and 3.2.3.1.), which ensures that all bulk samples possess similar mass, shape and flat surface on one-side. The preliminary results revealed that the shape of the sample and also the particle size strongly influenced the position of the crystallization peak. In case of larger particles and bulk samples the crystallization peak was shifted to higher temperature compared to that of powder samples. This is expected because the shape of the particles and size influence the heat transfer. Irregular-shaped sample, which is not in good contact with the bottom of the crucible and large particles have greater heat transfer resistance than powder samples. The shape and the position of crystallization peak also depend on crystallization mechanism. For example, the powders with the prevailing surface crystallization show broader peaks than the samples with bulk crystallization mechanism. The surface crystallization is usually recognized by broad peaks, which position depends on particle size. The similar particle size is very important to retain the control over the conditions and effects of surface and bulk crystallization.[132]

Taking into account the non-isothermal solid-state phase-transformation theory[133] the maximum of the DSC crystallization peak (T_p) is related to the number of nuclei per unit volume (N) by the following equation:

$$\ln N = \left(\frac{mE_c}{RT_p} \right) + \text{constant} \tag{66}$$

The inverse of the temperature corresponding to the maximum of the DSC crystallization peak, $1/T_p$, obtained for the MBS glass nucleated at different T_n, for 10 h, is shown in Figure 64. Values for the as-quenched glass are also shown. It is well known that the nucleation rate is a function of temperature and becomes maximum at a temperature near the middle of the temperature range where nucleation can occur. Equation (66) shows that $1/T_p$ is proportional to N in the glass. Therefore, the change in T_p, (Figure 64) with the temperature of nucleation heat-treatment ($T_{n)}$ is primarily due to a change in N in the glass. It can be seen from Figure 64 that $1/T_p$, is constant and the same as for as-quenched glass till the glass was nucleated below 600 °C. This indicates that the nucleation rate for this glass in the temperature range from 0 to 600 °C is so low that no detectable numbers of new nuclei are formed in 10 h. Crystallization therefore occurred on the nuclei that were initially present in the as-quenched glass. Figure 64 further shows that the temperature where the nucleation can occur in the MBS glass ranges from 600 to 750 °C with the maximum nucleation rate at 725 °C.

Taking into account the experimental results of Chandra S. Ray et al.[131] for $Li_2O_2{\cdot}SiO_2$ glass the height of the crystallization peak (δT_p) is also proportional to N. Our investigations revealed that this relationship is valid for MBS glass, too. The temperature for maximum nucleation determined from (Peak height) versus T_n (Figure 65) is for 25 °C lower than that determined from $1/T_p$ versus T_n (Figure 64). It was observed also for other glasses that the method (Peak height) versus T_n gave slightly lower values for the temperature of maximum nucleation than the method of $1/T_p$ versus T_n.[132] The explanation for this lies in the partial crystallization of the sample during nucleation heat treatment at higher temperatures. Since the peak height is proportional to maximum phase transformation rate as well as to the volume fraction crystallized during the DSC run, the crystalline phase, which formed already during nucleation heat treatment causes the lowering of the peak height in the DSC run. Visual observations supported the nucleation temperature of 700 °C and not 725 °C. Namely, when the nucleation heat treatment temperature was higher than 700 °C the samples became opaque, indicating partial crystallization.

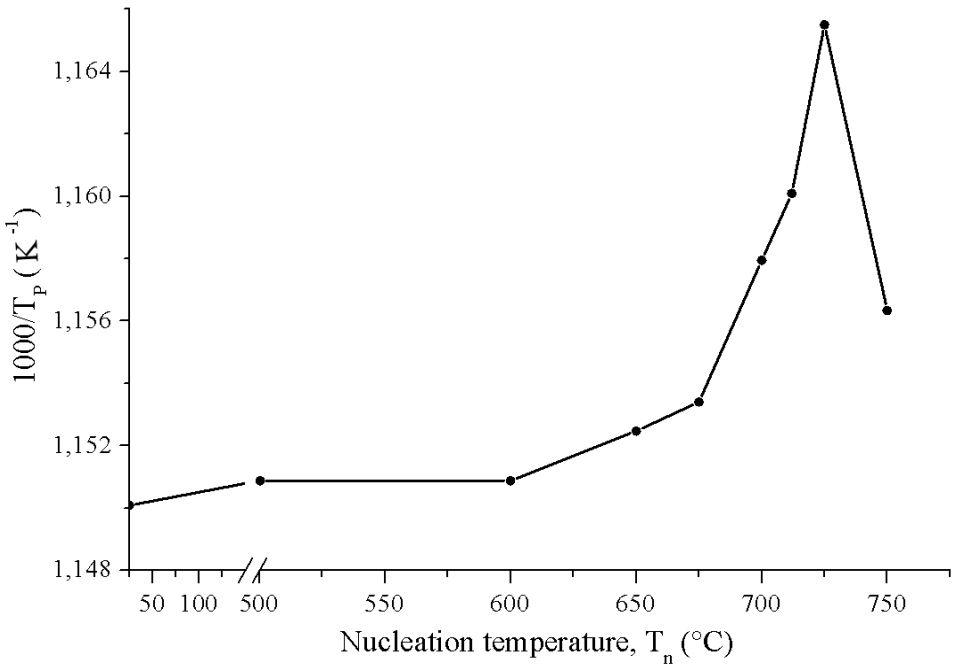

Figure 64. *Inverse of T_p for the MBS glass as a function of T_n. Particle size and weight of each sample were held constant at 4.5 mm and ≈ 60 mg, respectively. Each sample was held at T_n for 10 h and β = 10 °C/min.*

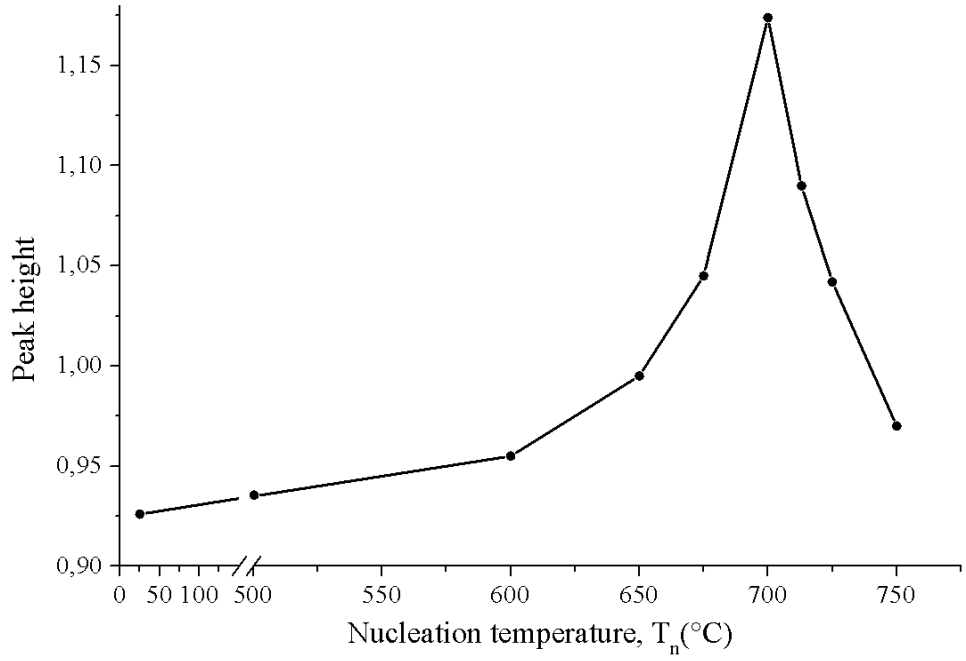

Figure 65. *Height of the DSC crystallization peak, (δT_p), for the MBS glass as a function of nucleating temperature T_n, for 10 h. Particle size and weight of each sample were held constant at 4.5mm and ≈ 60 mg, respectively.*

4.2.3.2 Study of the crystallization kinetics of MBS glass by non-isothermal DSC

In order to understand the crystallization mechanism of MBS glass the DSC investigations were performed for bulk and powder MBS glass samples with and without previous nucleation heat-treatment (Figure 66).

The surface crystallization is expected prevailing crystallization mechanism when the particle size of the glass powder is smaller than 50 μm. The crystallization exotherm of the MBS glass powder (< 50 μm) is not broader but even slightly narrower than that of bulk sample. Based on this we assumed that the bulk crystallization prevailed over surface crystallization also in powder MBS glass. The main difference between the powder and the bulk samples was observed in the temperature of crystallization. Namely, the on-set of the crystallization (Tx) and crystallization temperature peak (T_p) were for nearly 100 °C higher for bulk than for powder samples. This effect could be attributed to the slower heat transfer in the bulk samples compared to that in powders. Since there is only one exothermic peak in the DSC curve the crystallization of one phase is expected. The XRD measurements of the samples after the DSC scans revealed that the crystallization exotherms were in all samples associated with the crystallization of $Mg_2B_2O_5$. It can be seen from Figure 66 that the exothermic peak shifts toward lower temperature when both powder and bulk samples were heat-treated at 700 °C. This effect results from an increase of the number of nuclei during nucleation heat treatment.

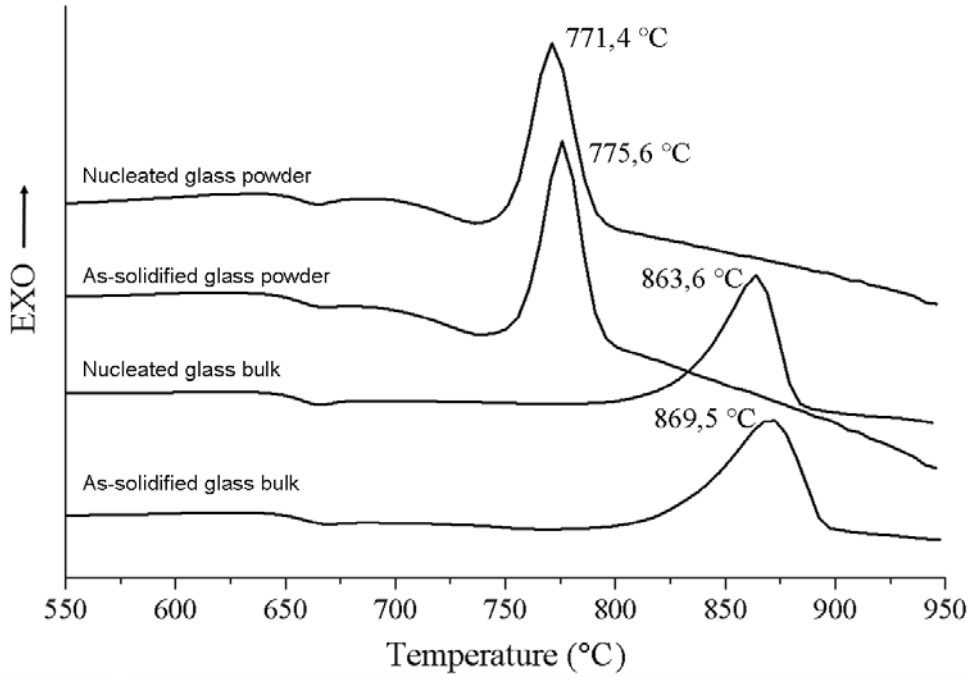

Figure 66. *DSC curves of MBS glass with various nucleation time and different shape of sample (nucleation temperature: 700 °C, heating rate 10 °C/min).*

Figure 67 represents the typical exothermic peaks with variation of heating rates ranging from 5 to 20 °C/min for the MBS glass sample that was nucleated at 700 °C for 10 h. The exothermic peak shifts to lower temperature as the heating rate decreases. We believe that peak shift shown in Figure 67 is attributed to the change in the heating rate and not to the difference in number of nuclei, since the saturation of the sample with the nuclei was achieved during nucleation (700 °C, 10h).

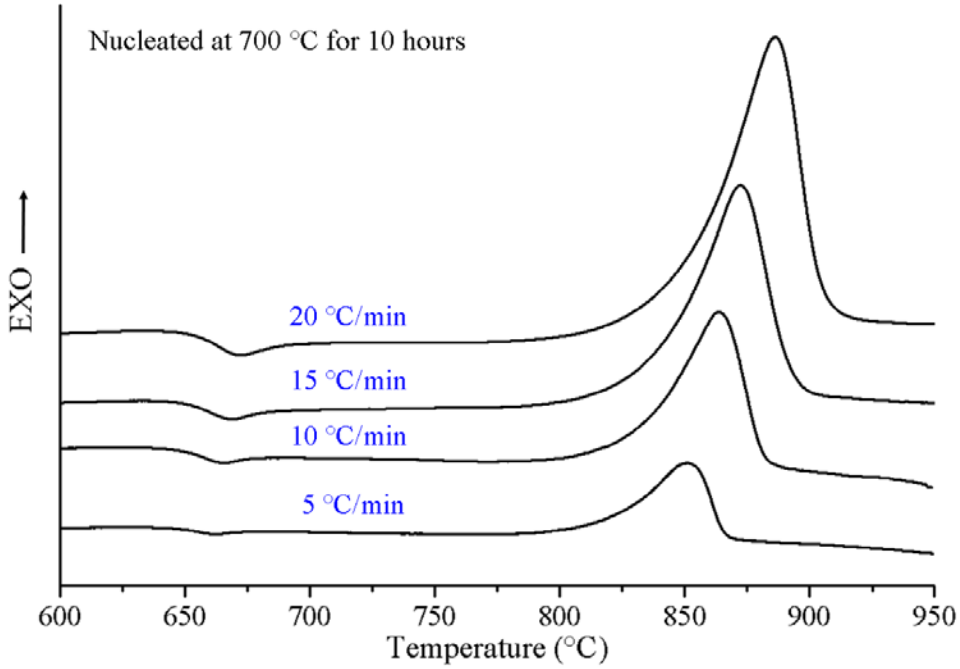

Figure 67. *DSC curves for bulk MBS glass, pre-nucleated 10 hours at 700 °C and scanned at different heating rates.*

The knowledge of the Avrami exponent (n) is prerequisite for the further analyses of DSC data with the various methods such as Kissinger, Matusita and Sakka, Ozawa-Chen and Šatava. The Avrami exponent (n) value can also be independently determined from the DSC results. From the Eq 62, the slope of the plot of $\ln[-\ln(1-\alpha)]$ versus $\ln\beta$ yields the value of n. The plot is shown in Figure 68 and the value of n is estimated to be between 1.5 and 1.6 for temperatures ranging between 849 and 857 °C. These result suggest bulk crystallization and the formation of three-dimensional crystals from a constant number of nuclei with the diffusion controlled crystal growth rate, which is proportional to $t^{-0.5}$.

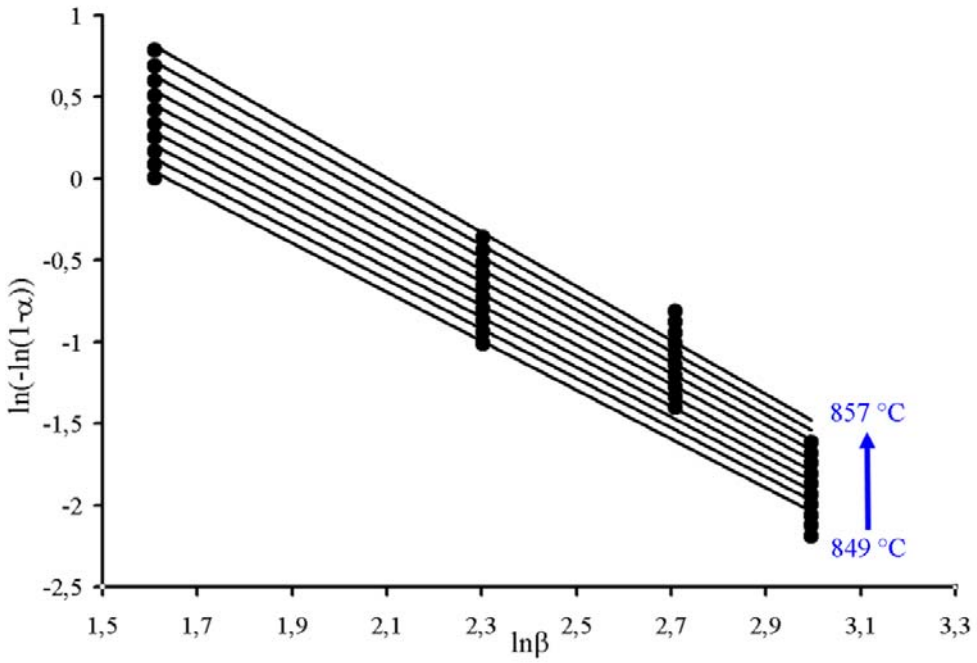

Figure 68. *Plot of ln[-ln(1-α)] versus lnβ for determining the value of n. The calculated results are obtained from Figure 67.*

From the shift of the crystallization peak temperature (T_p) with heating rate the activation energy for crystallization (Eg) could be determined using the Kissinger equation (Eq 60). According to this equation, a plot of $\ln(T_p^2/\beta)$ versus $1/T_p$ yields a straight line in which the slope is proportional to the activation energy of crystallization. The plots for the bulk sample pre-nucleated at 700 °C for 10 hours and without pre-nucleation are almost parallel to each other which is shown in Figure 69, and consequently the calculated crystallization activation energy is the same within experimental error, namely from 430 to 440 kJ/mol. The Kissinger plot for the powder sample has a much steeper slope and consequently higher activation energy, 790 kJ/mol and 680 kJ/mol for glass with (700 °C for 10 hours) and without nucleation heat-treatment, respectively.

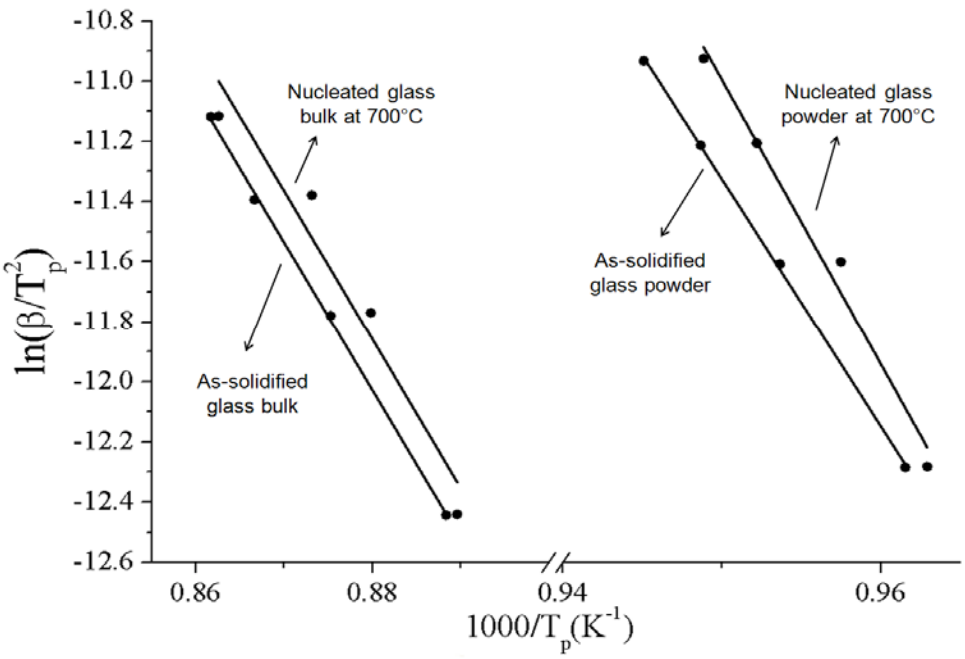

Figure 69. *Plot of $ln(\beta/T_p^2)$ versus $1000/T_p$ from which the crystallization activation energy is estimated. Comparison between as-solidified and nucleated bulk and powder MBS glass is shown in the graph. The calculated results are obtained from Figure 67.*

We believed that since crystal growth in MBS bulk glass sample occur on a fixed number of nuclei, the m value is consider to be the same as the n value. With respect to the modified Kissinger method also known as Matusita method (Eq. 61) we obtained the dimensionality of growth parameter, m, which is closely related to the Avrami exponent. A Matusita plot $\ln(\beta^n/T_p^2)$ versus $1/T_p$, yields mEg from 615 to 670 kJ/mol in the temperature range from 849 to 857 °C (Figure 70). Obtained values of activation energy multiplied with m (mEg), divided by activation energy obtained by Kissinger method yields the value of m = 1.5. This is in good agreement with the supposed crystallization mechanisms.

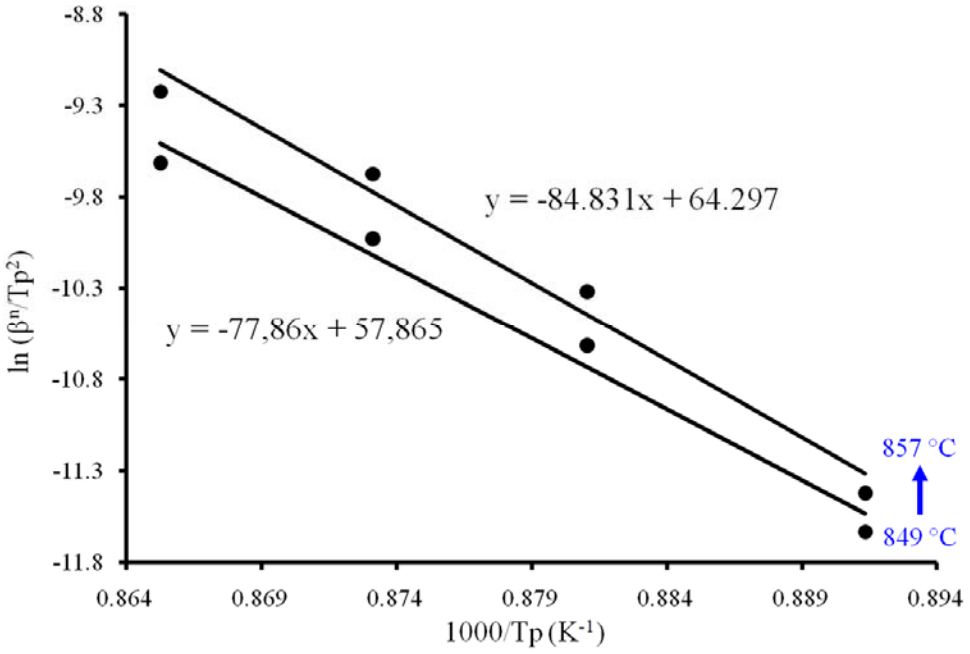

Figure 70. *Plot of $ln(\beta^n/T_p^2)$ versus $1000/T_p$ from which the crystallization activation energy multiplied with m is estimated for the MBS bulk glass nucleated at 700 °C for 10 h. The calculated results are obtained from Figure 67.*

The activation energy could be evaluated with several other methods such as Ozawa-Chen and Šatava method. The values of $E = (m/n)E_G$ for bulk MBS glass were calculated using Ozawa-Chen method (Eq 63) for the α in the range from 10 to 90 % (Figure 71). According to previous findings that n = m, the slope of the lnβ versus 1000/T correspond to $E = m/nE_G$. The activation energy for crystallization of bulk MBS glass obtained by this method was in the range from 412 to 442 kJ/mol.

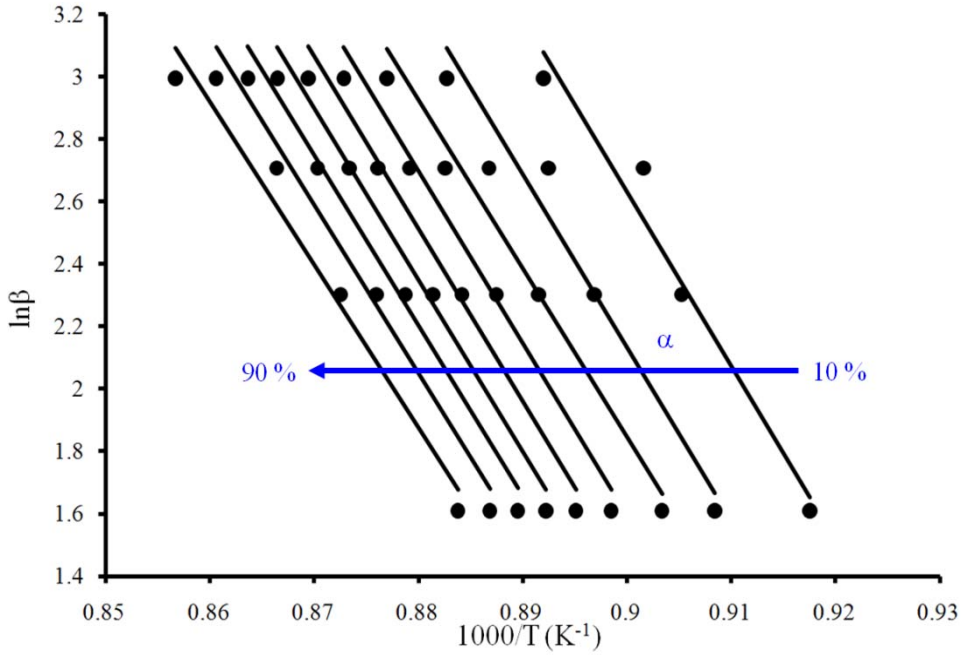

Figure 71. *Ozawa–Chen plot of ln β versus $1/T_p$ for determination of $E = (m/n)E_G$. Activation energy is calculated at different α for the MBS bulk glass nucleated at 700 °C for 10 h.*

Although Šatawa method shown in Figure 72 is regarded as the least accurate method it was (Eq. 64) also used to evaluate the values of activation energy and mEg. The thermoanalytical data, which were analyzed, were obtained at heating rates of 5, 10, 15 and 20 °C/min and α = 10-90 %. Taking into account that m = 1.5 the values of activation energy determined from the slope ln(-ln(1-α) versus 1000/T were in the range 450-500 kJ/mol (mEg = 640-720). Wide span could be expected due to less accuracy of the method.

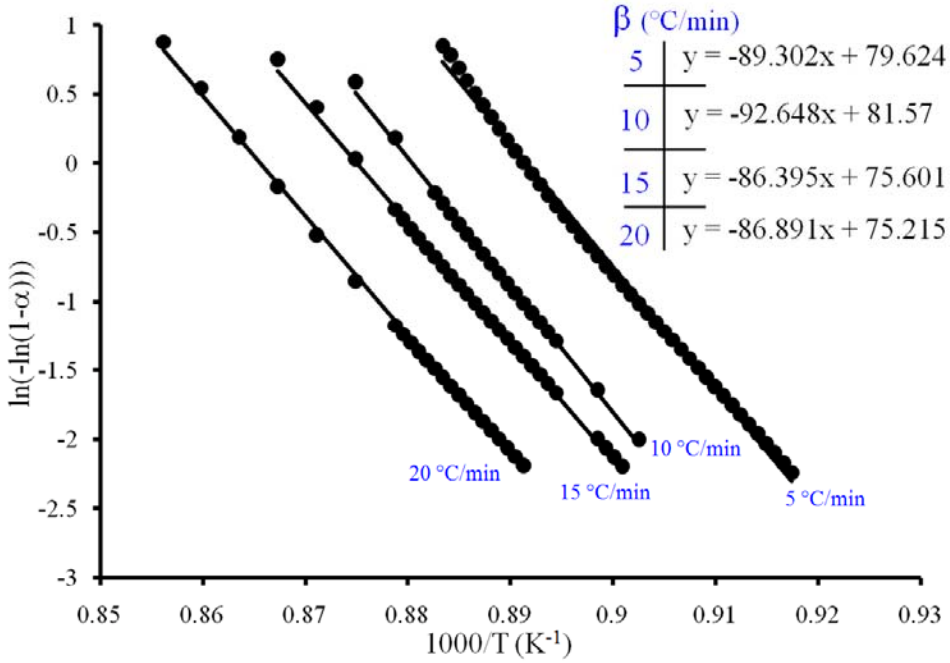

Figure 72. *Determination of mE_G according to the Šatava method by plotting ln[-ln(1-α)] versus $1/T_P$ at different heating rates for the MBS bulk glass nucleated at 700 °C for 10 h.*

Comparison of the results obtained by various methods for bulk MBS glass with variation of nucleation heat treatment time helps us to understand the crystallization mechanism. All applied analytical methods led to very similar values of activation energy for crystallization of bulk MBS glass (Table 15). Nucleation heat-treatment was also found to have no significant influence on determined values of n (1.4-1.6) and activation energy (390-450 kJ/mol). This additionally proves that bulk crystallization occurred at constant number of nuclei, with the diffusion controlled crystal growth, and proportional to $t^{-0.5}$. The similar methods as for bulk MBS glass were used for the study of crystallization kinetics of MBS glass powders. In spite of small particle size (< 50 μm) the bulk crystallization was still the prevailing crystallization mechanism (n = 1.4-1.7). Also in case of powders the nucleation heat-treatment did not significantly influence the determined values of activation energy, which are higher compared to those of bulk MBS glass (Table 15). The higher values of activation energy for powdered samples in comparison with bulk were observed also for lithium disilicate glass, where the values differed more than 2-times.[131] Despite the bulk crystallization was determined on the prevailing crystallization mechanisms in powders, surface crystallization is also expected to occur since the particle size was < 50 μm. Due to the mixed crystallization mechanisms in powders, the activation energy obtained from the kinetic study of powders has less meaningful value than that obtained for bulk glass, where the surface crystallization is negligible.

Table 15. *Comparison of activation energies calculated from different analytical methods for both bulk and powder sample.*

Methods			Activation energy, E_G (kJ/mol)				
			Glass				
			Bulk			Powder	
			/	700°C/2h	700°C/10h	/	700°C/10h
Ozawa		n	1,4-1,6	1,6-1,7	1,5-1,6	1,7-1,8	1,4-1,6
		n=m	1,5				
Kissinger		E_G	410	440	430	680	790
Matusita		E_G	390-440	430-460	410-450	750-810	600-690
Ozawa-Chen		E_G	365-470	415-425	410-440	610-720	650-860
Šatava	5°C/min	E_G	450	480	470	790	850
	10°C/min		410	430	500	770	720
	15°C/min		390	440	450	790	760
	20°C/min		380	470	460	710	730

4.2.3.3 Phase evolution of the $MgO-B_2O_3-SiO_2$ (MBS) glass-ceramic after isothermal heat-treatment

The XRD patterns of the MBS glass and glass – ceramic sintered at various temperatures from 800 to 1050 °C for 10 hours are shown in Figure 73. Crystallization was not detectable at temperatures below 800 °C. Magnesium borate ($Mg_2B_2O_5$) which has a triclinic crystal modification with the space group S.G. $P\bar{1}$ is the main crystalline phase in the XRD pattern of the glass-ceramics powder annealed at 800 °C. The broad peaks indicate the small size of the crystallites. The sharpening and increase of intensity of the majority of diffraction lines indicates the $Mg_2B_2O_5$ crystallites growth and increase of $Mg_2B_2O_5$ phase content with increase in temperature. At the annealing temperatures higher than 950 °C the $MgSiO_3$ phase appeared. The proximity of $Mg_2B_2O_5$ and $MgSiO_3$ diffraction lines caused the apparent broadening of some of the diffraction lines, especially in the 34-36 ° 2θ range. The cordierite expectedly did not form in the glass that was melted in the Pt crucible.

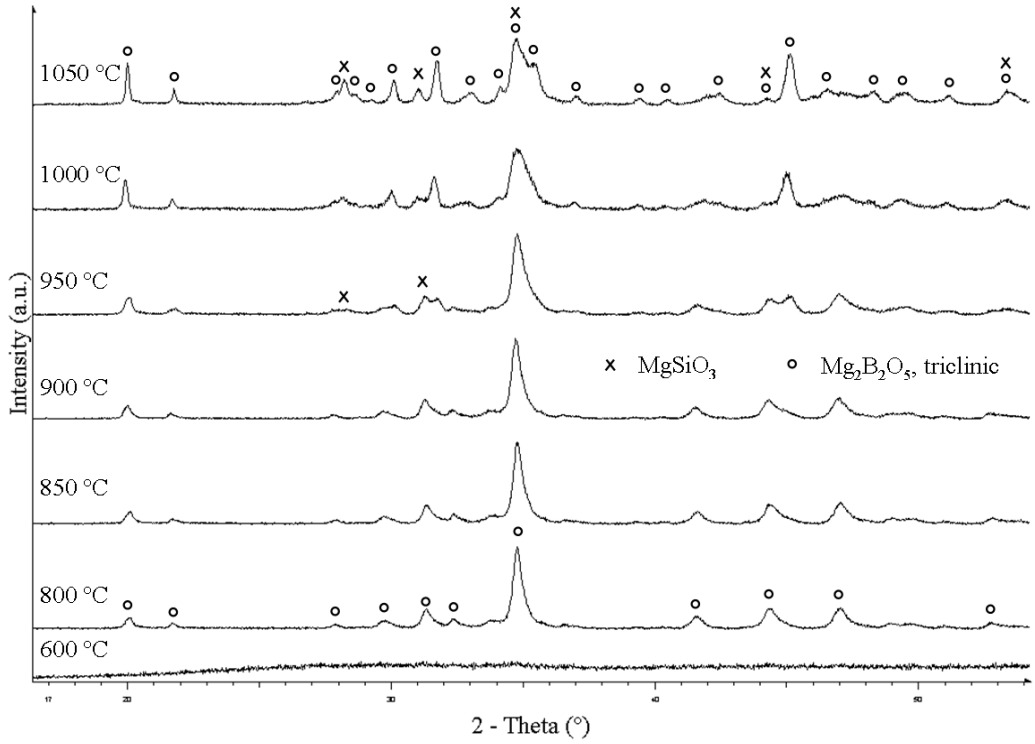

Figure 73. *Summarizes the X – ray powder diffraction results for the glass and glass – ceramic composition 43 wt.% MgO – 35 wt.% B_2O_3 – 22 wt.% SiO_2 prepared in platinum crucible. Denotation of the crystalline phases: ○ $Mg_2B_2O_5$ - triclinic, x $MgSiO_3$.*

4.2.3.4 Microstructural analyses

Figure 74 shows a sequence change of microstructure for the MBS glass sample prepared in platinum crucible with increasing temperature from 900 to 1050 °C. The samples that were heat-treated for 10 hours at certain temperature exhibits lumps of spherical growing crystals. According to the XRD results we suppose that round shaped particles appertain to the major $Mg_2B_2O_5$ phase. With regard to the chemical etching behavior we assume that the glassy phase, which is removed by chemical etching, fills the area around the particles, what is visible as dark grey area in the micrographs. The XRD results indicate that some $MgSiO_3$ should exist in the sample but we couldn‘t distinguish it from the $Mg_2B_2O_5$ phase by SEM investigations. According to the well known fact that crystallization SiO_2 is difficult, we believe that $MgSiO_3$ phase is in minority and a majority of SiO_2 remains in the glassy phase. As shown in the chemically etched micrographs (Figure 74 a) it seems that crystallization already started at 800 °C, where the size of the grains were relatively smaller than that in the specimens sintered at higher temperatures. This could be expected the grain growth increase with the increase of temperature. There was no remarkable difference in density between the

MBS samples prepared in different crucibles (corundum and Pt) (Figure 58 and Figure 74).

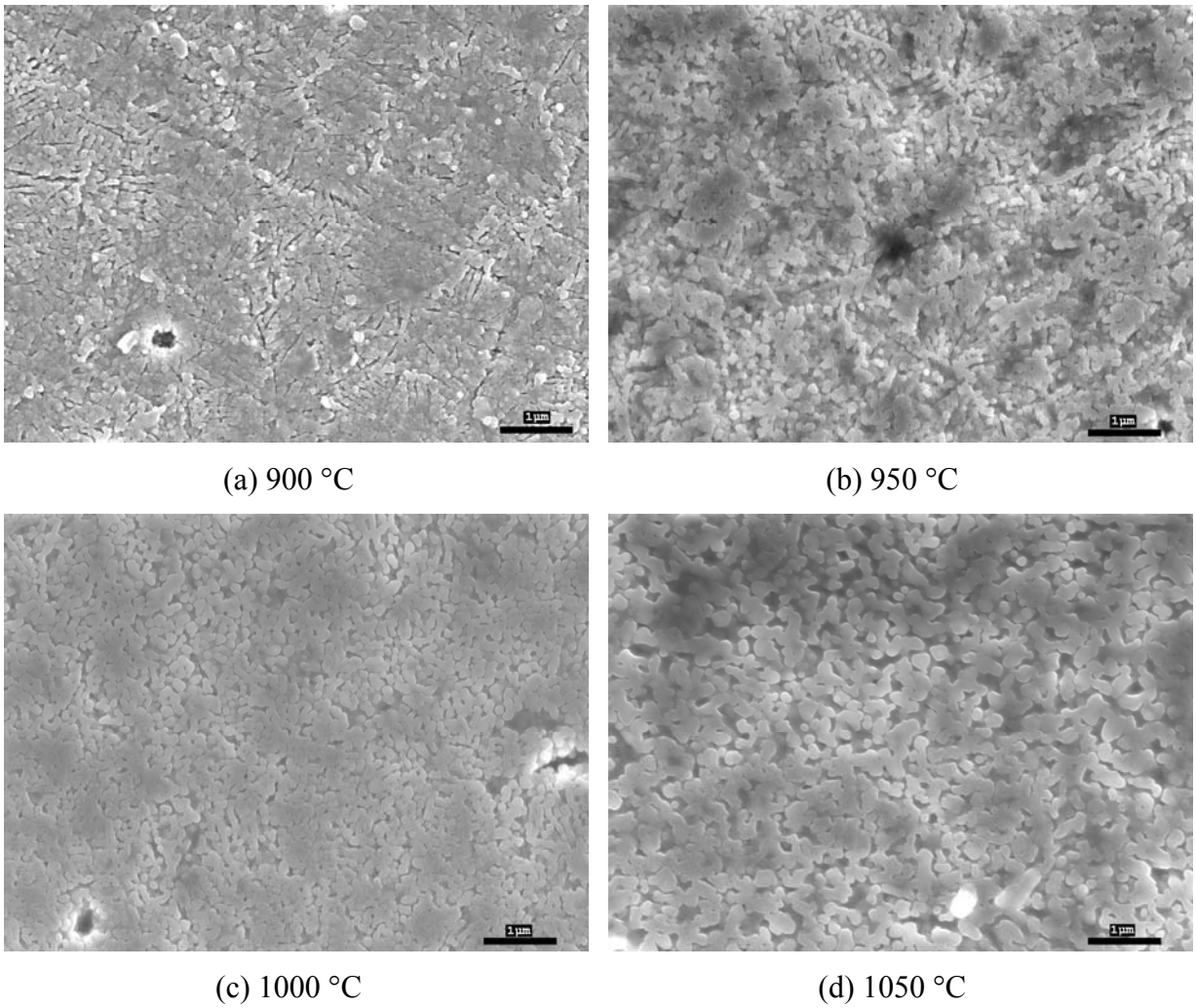

(a) 900 °C (b) 950 °C

(c) 1000 °C (d) 1050 °C

Figure 74. *FESEM images after chemical etching of 43 wt.% MgO – 35 wt.% B_2O_3 – 22wt.% SiO_2 glass – ceramics sintered for 10 hours at: (a) 950 °C, (b) 1000 °C, (c) 1050 °C.*

The dielectric properties of glass-ceramics are dependent on the microstructure. Thus, the less porous specimen could play an important role to degrade the lattice vibration and get the high Q value.

4.2.3.5 Microwave dielectric properties

The microwave dielectric properties for the 43 wt.% MgO–35 wt.% B_2O_3–22 wt.% SiO_2 glass–ceramics were examined. Previously, we declare milling conditions and from that reason the glass, which was prepared in platinum crucible, was crushed and milled 2 hours in planetarium mill.

The dielectric properties are thought to be affected by a combination of second phases, microstructural defects, specimen density, impurities and lattice defects.[134] In our study, no additives were used and no microstructural defects e.g. voids and micro-cracks were observed by SEM. Thus, dielectric properties of samples primarily result from specimen density, impurities and lattice defects. However, porosity has large impact on the dielectric constant. Figure 75 show how dielectric constant slightly decreased with increasing temperature. The ε_r value decreased from 6.2 to 5.8 with increasing the sintering temperature from 800 to 1050 °C. It implies that the decrease for ε_r of MBS ceramics with sintering temperature is due to the increase of porosity and reduced density. The low dielectric constant provides an attractive feature for minimizing cross-talk and increasing signal transmission speeds.

The dielectric loss is caused by two reasons, i.e., intrinsic contribution: such as lattice vibrational modes and ion occupation; extrinsic contribution: such as pores and secondary phases. Porosity plays an important role in affecting the dielectric loss. In general, the large grain size of well – sintered ceramics resulted in low dielectric loss. It is assumed that for materials of density less than 90 % theoretical, the decrease in Q value, due to increasing porosity may be attributed to the effects of polarization at the pore surface.[135] Such as dielectric constant also the Qxf values of MBS glass – ceramics is shown as a function of sintering temperatures in Figure 76. Qxf values increase from 4410 to 11 330 GHz with increase of sintering temperature. This improvement of the Qxf values could be attributed to better crystallization.

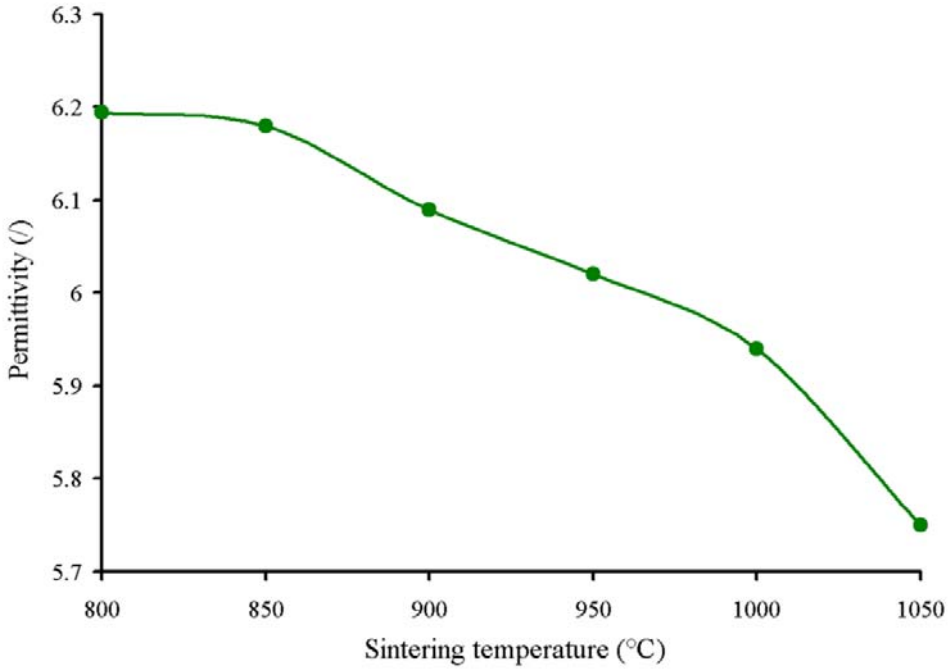

Figure 75. *Dielectric constant of the 43 wt.% MgO – 35 wt.% B_2O_3 – 22 wt.% SiO_2 glass – ceramic prepared in platinum crucible as a function of sintering temperature.*

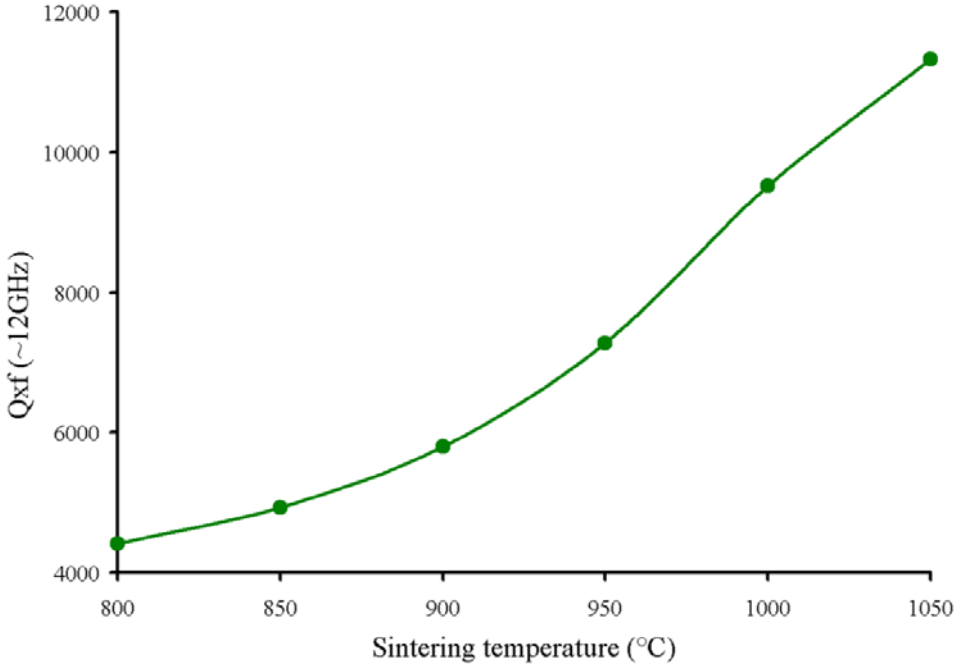

Figure 76. *Quality values of the 43 wt.% MgO – 35 wt.% B_2O_3 – 22 wt.% SiO_2 glass – ceramic prepared in platinum crucible as a function of sintering temperature.*

It can be concluded that each constituent in the glass composition is crucial to the crystallization, densification, and thus microwave dielectric properties. However, their effects are intercorrelated and, sometimes, unable to distinguish the contribution from an individual constituent. Cordierite phase, which was undesired product, was avoided with exchanging the corundum with platinum crucible. Regarding the dielectric properties, the glass-ceramic prepared in platinum crucible still exhibited high Qxf values after sintering at 1050 °C whereas the dielectric properties of glass-ceramic from Al_2O_3 were determined already at 1000 °C.

4.2.3.6 Nucleation in MBS glass with the addition of nucleating agent, TiO_2

Controlled crystallization usually involves a two-stage heat treatment, namely a nucleation stage and a crystallization stage. In the nucleation stage, small nuclei are formed within the parent glass. After the formation of stable nuclei, crystallization proceeds by growth of a new crystalline phase. It is well-known that the crystallization is facilitated by addition of nucleating agents. These additives act as heterogeneous sites at which the nucleation of desired crystalline phases may take place and therefore by adjusting the type and concentration of the nucleating agent used, it is possible to control the crystallization process. TiO_2 is commonly used nucleating agent for SiO_2 based glasses.[136] The effect of TiO_2 on the crystallization exotherm of bulk MBS glass is presented in Figure 77. The amount of added TiO_2 in concentration higher than 5 wt.% obviously influenced the shape, position and intensity of crystallization peak. With the increasing amount of TiO_2, the crystallization peaks evidently became narrower and their intensity increased, while Tx and T_p were decreased. On the contrary, Tg was only slightly shifted to lower temperatures. The increase of the crystallization peak intensity with TiO_2 content results from a larger number of nuclei, the formation of which is stimulated by the presence of the TiO_2. The narrowing of the peak width indicates that the TiO_2 enhances the bulk crystallization.

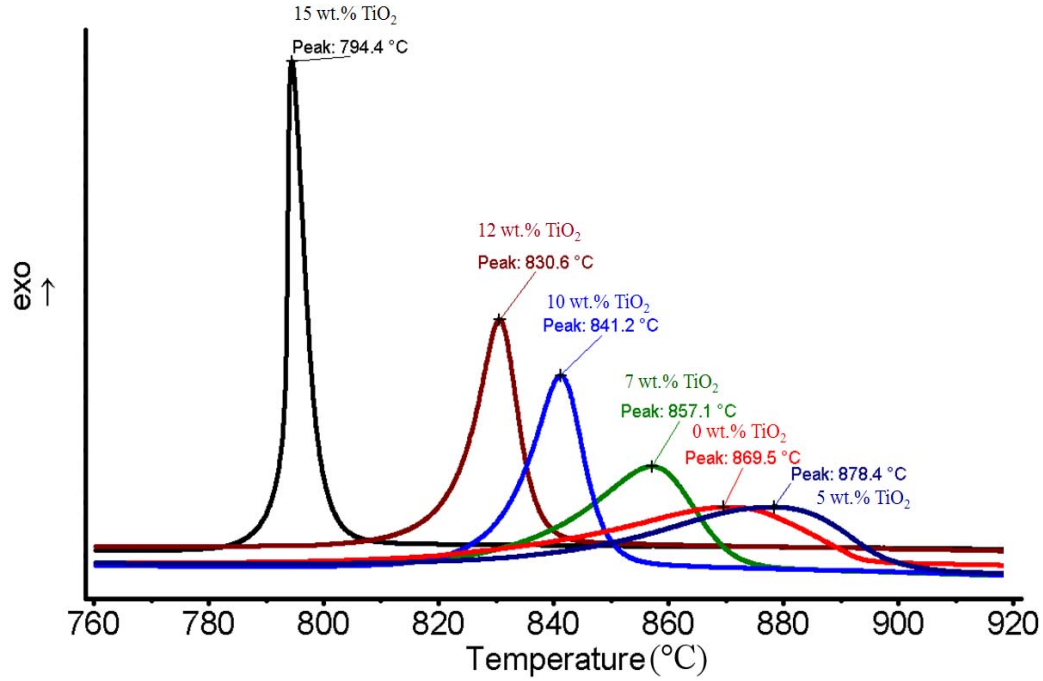

Figure 77. *DSC curves of MBS glass bulk with addition of 0, 5, 7, 10, 12 and 15 wt.% of TiO_2.*

Detailed crystallization study was performed for MBS glass with 10 wt.% of TiO_2. Determination of the Avrami exponent (n) using the Ozawa method (Eq. 62) revealed that TiO_2 change the crystallization mechanism. For the TiO_2-added MBS glass without nucleation heat treatment n was close to 4, indicating bulk crystallization with increasing number of nuclei (Figure 78). According to known crystallization mechanisms (Table 17), the dimensionality factor m is 3, considering the relation m = n-1.

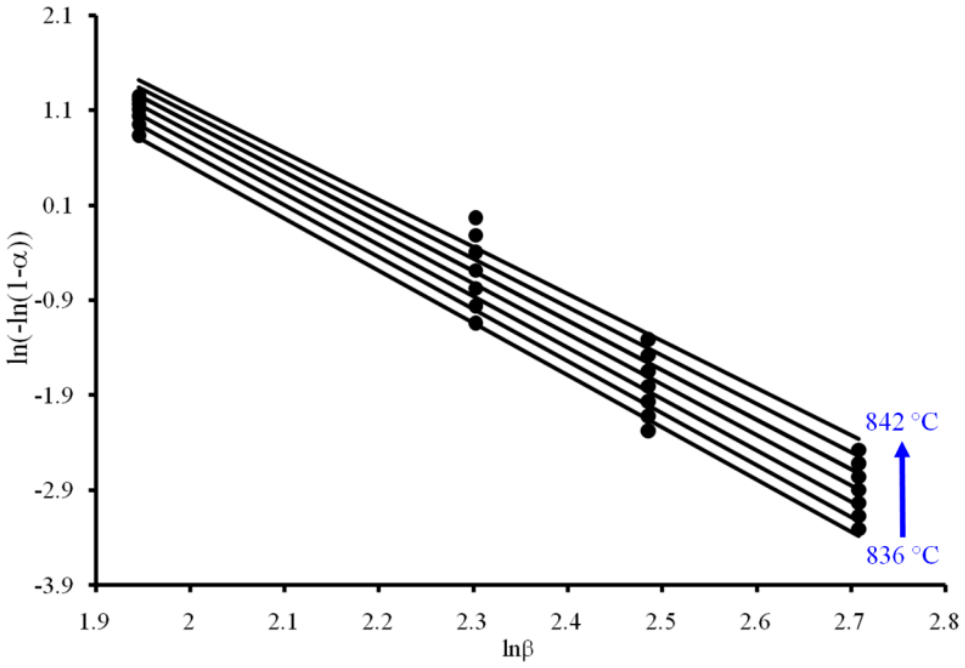

Figure 78. *Determination of n by plotting of ln[-ln(1-α)] versus lnβ for MBS glass bulk with addition of 10 wt.% of TiO_2. The Ozawa method was obtained in the temperature range from 836 to 843 °C.*

Figure 79 represents typical DSC curves for TiO_2-added MBS glass. With regard to the n = 4, m = 3, the number of nuclei changes during the DSC run. Fewer nucleuses are formed during fast than slow scanning due to the longer dwell time in the nucleation temperature range. Besides the heating rate this also influences the T_p. Since the number of nuclei is expected to increase during the DSC run, the Kissinger method gives the incorrect value of the activation energy.

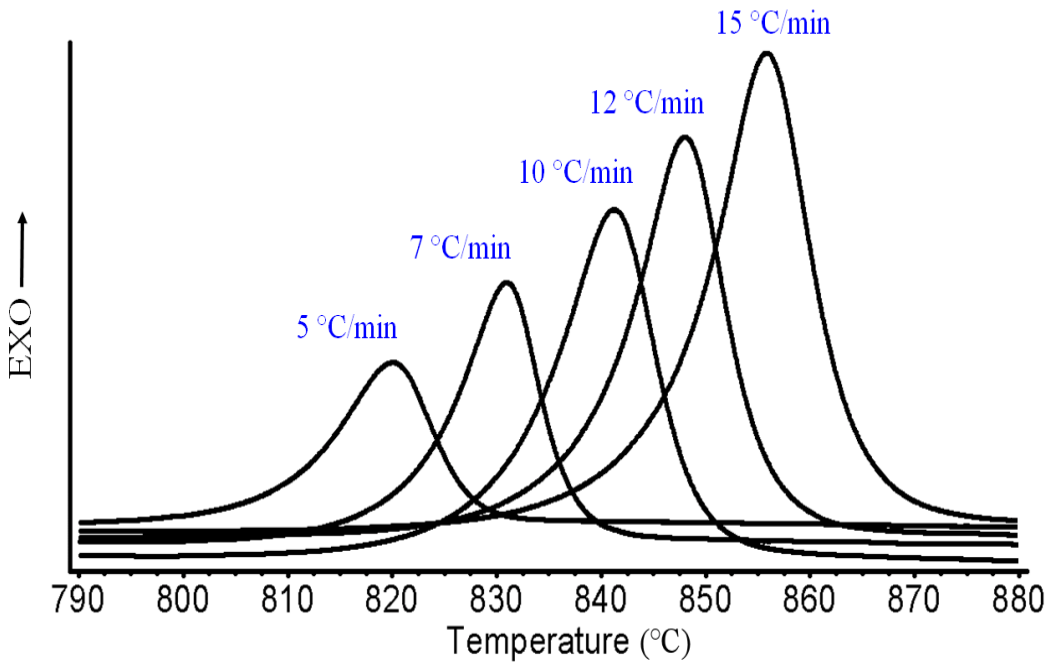

Figure 79. *Represent typical DSC curves for the MBS glass bulk with the addition of 10 wt.% of TiO_2 scanned at different heating rates in the range between 5 and 15 °C/min.*

In spite of that this method was used for the calculation of activation energy mainly due to the comparison with Matusita (Eq. 61) Ozawa-Chen (Eq. 63) and Šatava (Eq. 64) methods, which are expected to give more correct values. (Table 17, Figure 80, Figure 81 and Figure 82). The analysis of the DSC data using the later methods led to very similar values of E_G around 400 kJ/mol for the TiO_2-added MBS glass without nucleation heat treatment (Table 17). This value was only slightly lower than that determined for pure MBS-bulk glass. The Kissinger method led to lower value of 300 kJ/mol. XRD measurements revealed that the crystallization exotherm in TiO_2-added glass is associated with the crystallization of $Mg_2B_2O_5$, what is the same as in pure MBS glass (Chapter 4.2.3.).

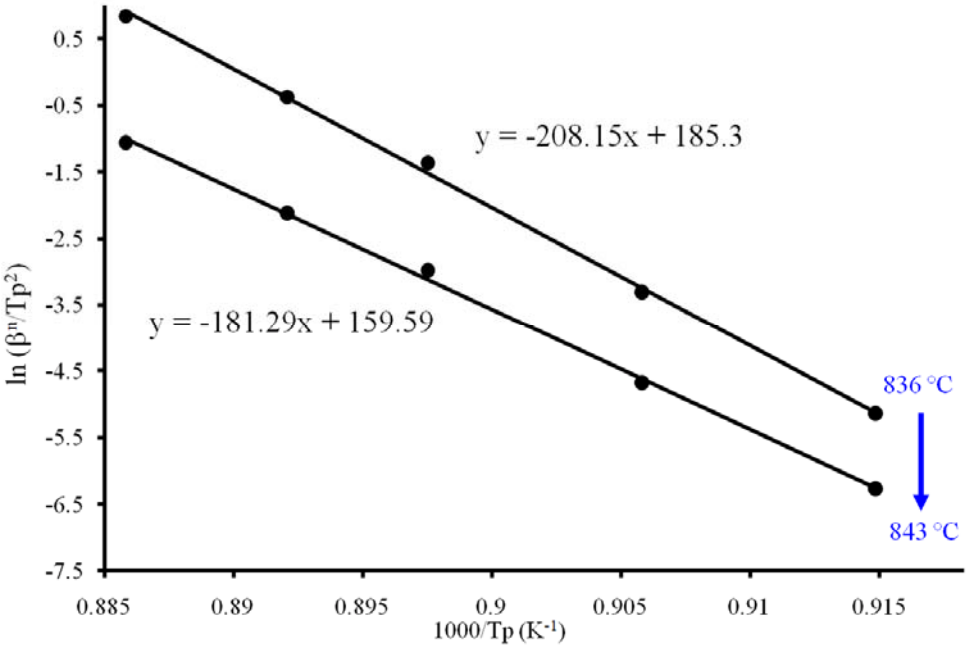

Figure 80. *Determination of mE_G according to Matusita method for the MBS glass bulk with addition of 10 wt.% of TiO_2 by plotting the $\ln(\beta^n/T_p^2)$ versus $1000/T_p$.*

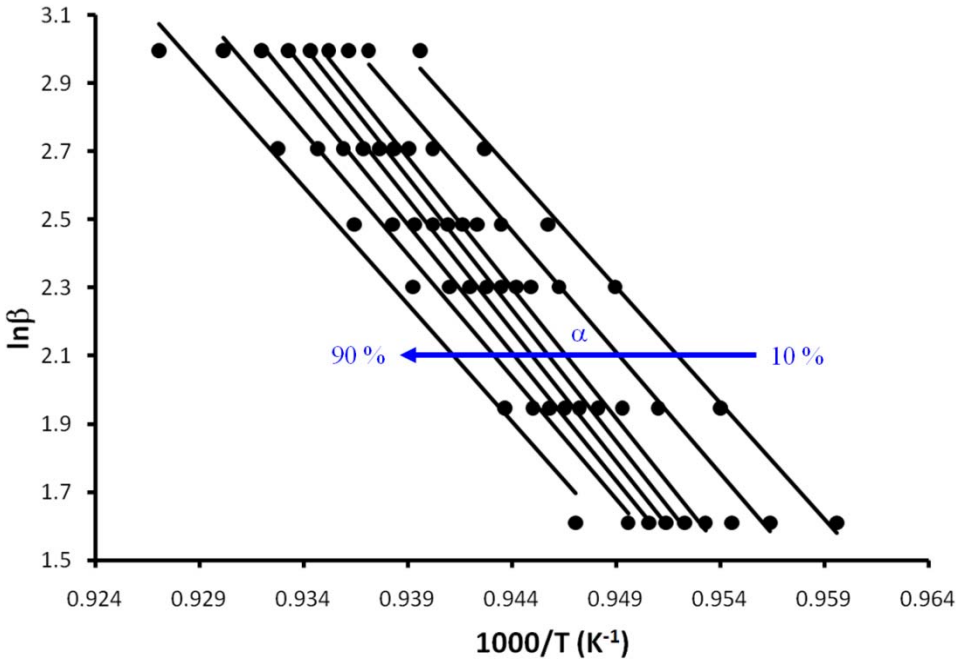

Figure 81. *Ozawa-Chen plot ($\ln\beta$ versus $1/T$) for determination of $E = (m/n)E_G$ at α values in the range from 10 to 90 % for the MBS glass bulk with addition of 10 wt.% of TiO_2.*

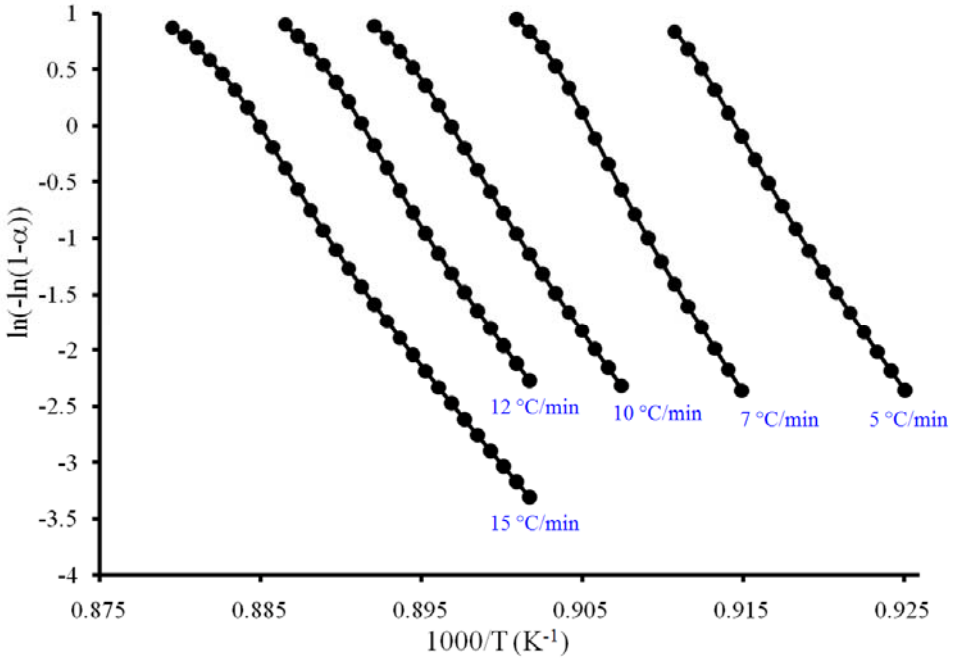

Figure 82. *Determination of mE_G according to the Šatava method by plotting the $ln(\beta^n/T_p^2)$ versus $1000/T_p$ at heating rates (5, 7, 10, 12 and 15 °C/min) for the MBS glass bulk with addition of 10 wt.% of TiO_2.*

The analysis of the DSC data is easier and more reliable for glass with constant number of nuclei. It was expected that the constant number of nuclei in the TiO_2 added MBS glass could be achieved by heating the glass at the temperatures of high nucleation rate. The temperature range, where nucleation took place was determined from the plot $1000/T_p$ versus T_n. The shape of this plot was atypical and thus differed from that of pure MBS glass (Figure 64). The nucleation rate increased at T > 600 °C, remained fairly constant in the range from 625 to 675 °C and then increased again up to 700 °C (Figure 83). Due to partial crystallization of the bulk glass nucleated at 700 °C, the lower temperature 688 °C was selected for nucleation heat-treatment.

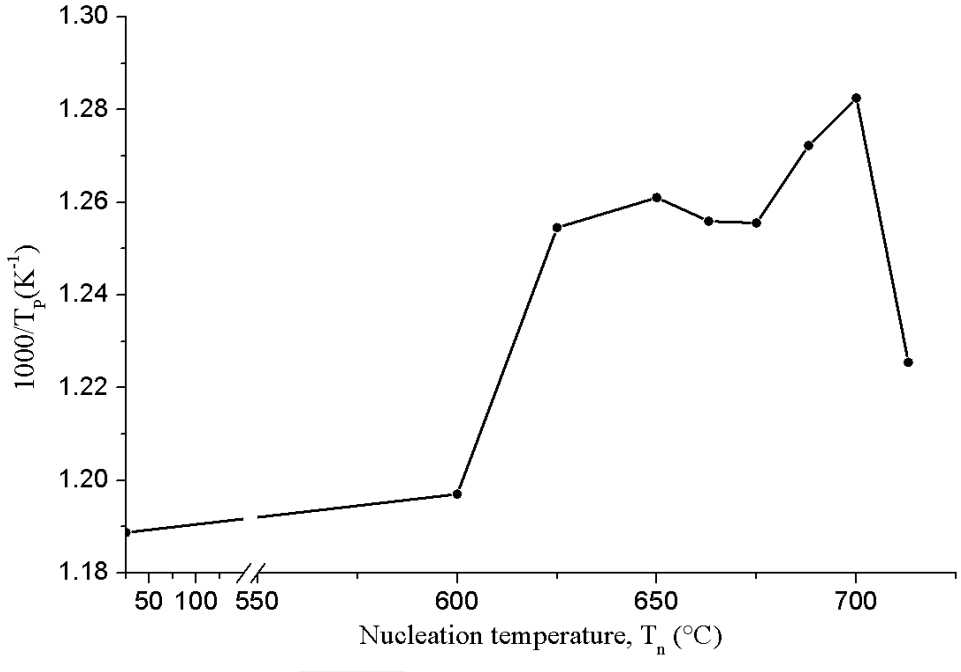

Figure 83. *The inverse of the maximum temperature crystallization peak ($1/T_p$) for TiO_2-added MBS glass as a function of nucleating temperature (10 hours).*

Figure 84 shows typical DSC curves for the nucleated TiO_2-added MBS glass (688 °C) taken at five different heating rates 7, 10, 12, 15, and 20 °C/min. All the DSC curves revealed a single very narrow exothermic peaks with the peak temperatures (T_p), which differed only for a few degrees (T_p = 783.5 (7 °C/min), 786.4 (10 °C/min), 788.8 (12 °C/min), 792.5 (15 °C/min) and 795.3 °C (20 °C/min)). The exothermal peaks are significantly shifted to higher temperatures with increasing heating rate, which is in accordance with the presumption about the thermal activation of the crystallization controlling processes. The shape of these DSC curves depends on the heating rate.

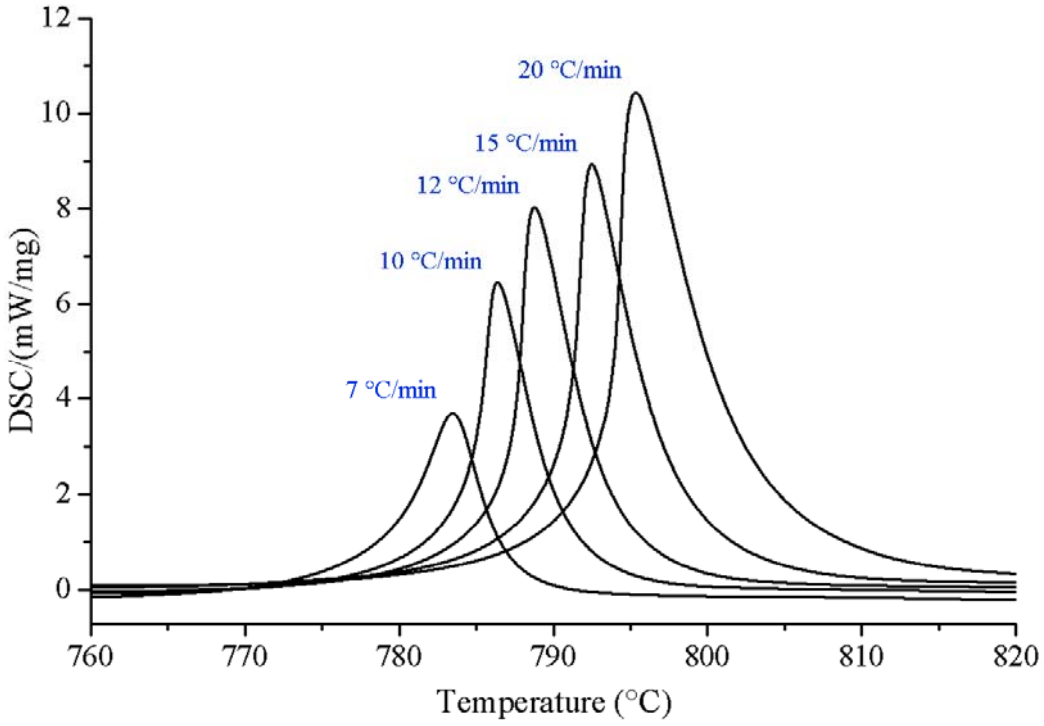

Figure 84. *A plot of the DSC thermograms of MBS glass doped with 10 wt.% of TiO_2 at five different heating rates 7, 10, 12, 15 and 20 °C/min. The bulk glass was before DSC measurements pre-nucleated for 10 hours at 688 °C.*

The Avrami exponent (n) for TiO_2-added MBS glass heat treated at the nucleation temperatures of 650 and 688 °C was determined using the Ozawa method (Eq 62). Figure 85 show plots of $\ln[-\ln(1-\alpha)]$ against $\ln(\beta)$ in which α was obtained at the same temperature from a number of crystallization exotherms taken at different heating rates (β) (Figure 84). The Avrami parameter (n) was determined from the slope of the curves and was estimated to be between 3.8 and 4.0 at the temperatures ranging from 784 to 790 °C (Table 16). Considering experimental errors, this value can be taken as n = 4. Very similar value was obtained for the glass nucleated at 650 °C. Both results revealed that the crystallization in TiO_2-added MBS glass occurs via bulk crystallization mechanism with increasing number of nuclei. This means that the constant number of nuclei was not achieved by nucleation heat treatment at 650 and 688 °C. The reason for such crystallization mechanism is most probably in the TiO_2, which acts in itself as the starting point for crystallization. The source of heterogeneous nucleation sites could be also small titanium containing crystalline precipitates. The closest match for m value that should be equal to n-1 is 3, corresponding to three-dimensional crystal growth

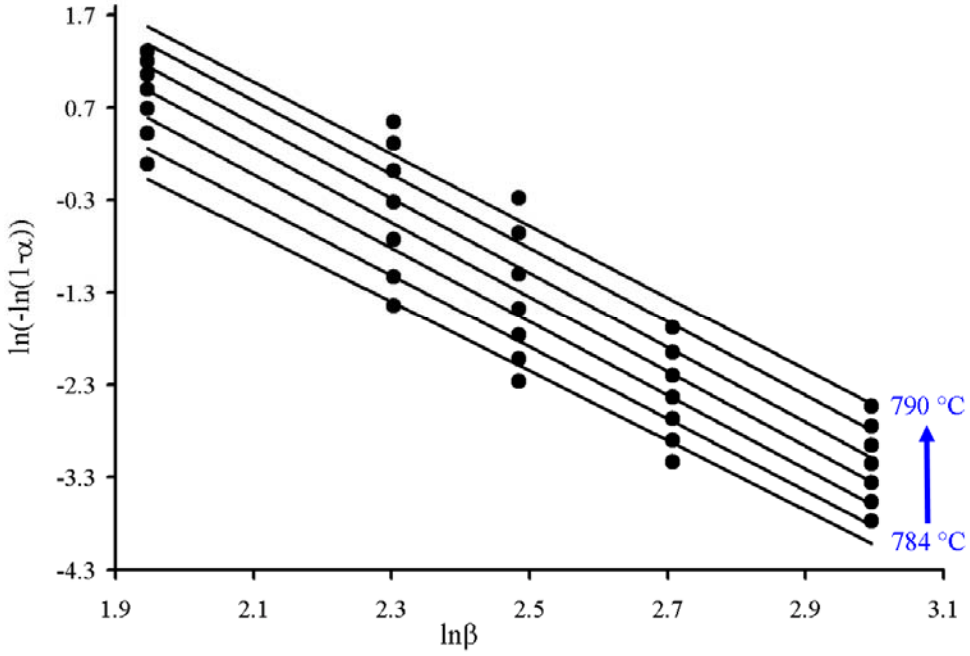

Figure 85. *Plot of ln[-ln(1-α)] versus ln β for MBS bulk-glass with the addition of 10 wt.% of TiO_2 nucleated at 688 °C/10h for β of 7, 10, 12, 15 and 20 °C/min, gives the result of E_G.*

Taking into account the crystallization mechanism, which was studied with Matusita and Ozawa-Chen methods are expected to give the most reliable values of the activation energy for the crystallization of TiO_2-added MBS glass. For the comparison the activation energy was determined also by Kissinger and Šatava method. However, according to the Matusita and Sakka[107] who claimed that Kissinger model is valid only when crystal growth occurs on a fixed number of nuclei we evaluate the activation energy with modified Kissinger model optimized by Matusita and Sakka (Eq 61). Taking into account the crystallization mechanism (n = 4, m = 3) the activation energy of 976 ± 26 kJ/mol was determined using Matusita-Sakka method from the slopes of $\ln(\alpha^n/T_p^2)$ versus $1000/T_p$ plots (Table 16).

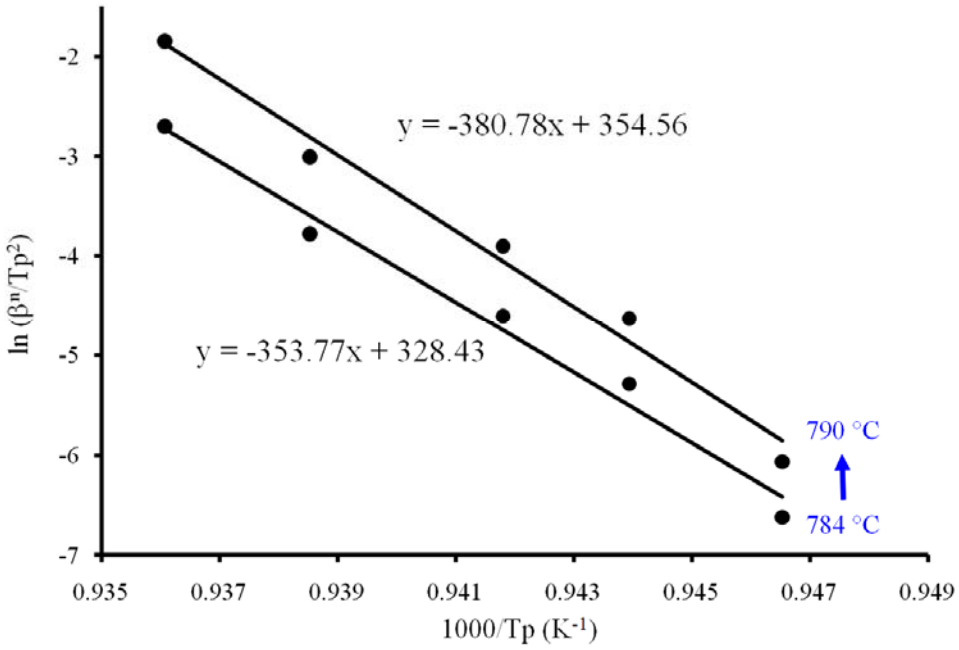

Figure 86. *The Matusita-Sakka plots ($ln(\alpha^n/T_p^2)$ versus $1000/T_p$) for the MBS glass bulk with the addition of 10 wt.% of TiO_2 nucleated at 688 °C for 10 hours.*

Table 16. *The kinetic crystallization parameters for the MBS glass bulk with 10 wt.% of added TiO_2 nucleated at 688 °C for 10 hours. Activation energy was calculated at different temperature with the help of known n and m values obtained from Ozawa and Matusita method, respectively.*

T (°C)	n	m	mE_G (kJ/mol)	E_G (kJ/mol)
784	3.75	2.75	2680.3	973.1
785	3.88	2.88	2771.0	961.9
786	3.99	2.99	2846.1	953.4
787	4.04	3.04	2885.9	949.2
788	4.04	3.04	2885.0	949.2
789	3.99	2.99	2971.5	994.1
790	3.89	2.89	2899.2	1002.4

In the Ozawa-Chen method presented in equation 63, the calculation of the activation energy is mainly based on the heating rate (β) and the peak crystallization temperature (T_p). For a set of exotherms taken at all heating rates (β) and at a fixed value of the crystallized fraction at the range of α from 10 to 90 %, value of E_G can be deduced from the slopes of the best fit of the linear relations, when lnβ is plotted against ($1/T_p$) as shown in Figure 87. From the slops of these plots the activation energy was determined with respect of n and m values. The average value of the activation energy for crystallization, considering result for all α values, is E_G = 787 ± 50 kJ/mol (Table 17).

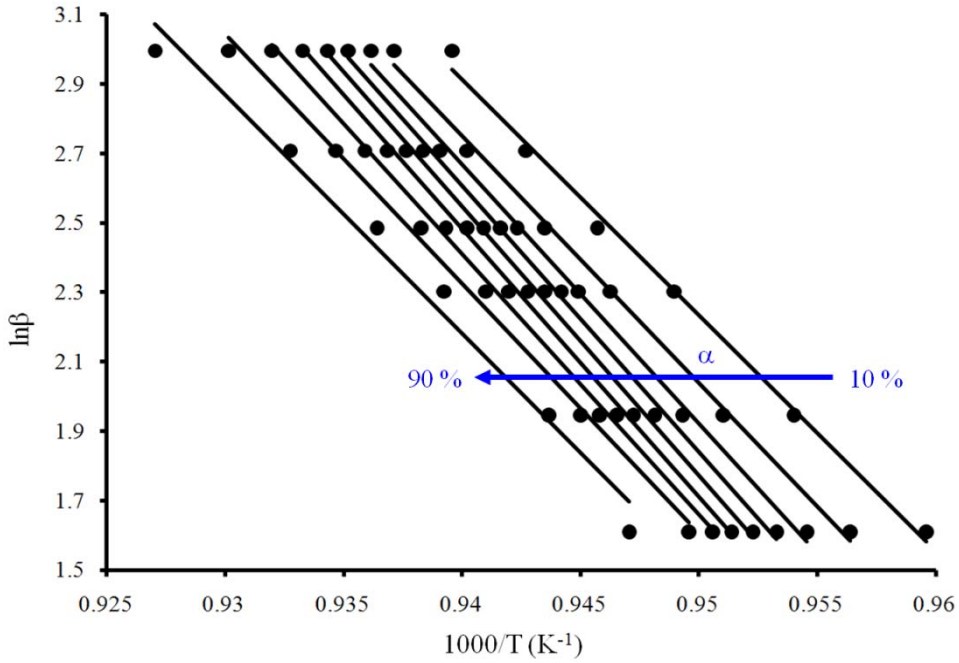

Figure 87. *Ozawa-Chen plot (lnβ versus $1/T_p$) for determination of E_G = (n/m)E at values of α ranging from 0.1 to 0.9.*

According to Šatava method (Eq. 64) the activation energy at a constant heating rate was derived from the linear slope presented in Figure 88. The slope of the obtained linear dependence of ln[-ln(1-α)] as a function of $1000/T_p$ exhibit mE_G. The activation energy depending on the volume fraction of crystals (α) in the area of 10 – 90 % is in the range from 671 to 895 kJ/mol. These values were determined at different heating rates from 7 to 20 °C/min. Comparison between the activation energy values determined from different non-isothermal methods are listed in Table 17.

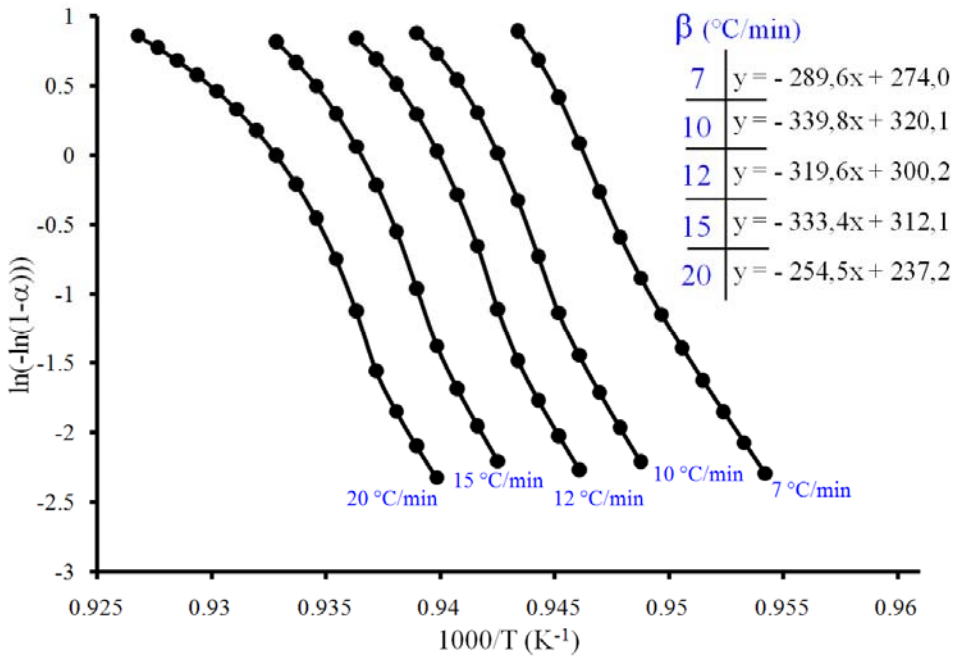

Figure 88. *Determination of mE_G according to the Šatava method by plotting ln[-ln(1-α)] versus $1/T_p$ at several heating rates (β) ranging from 7 to 20 °C.*

Table 17. *Crystallization with and without pre-nucleation at 688 °C 10h parameters of MBS glass with the addition of 10 wt.% of TiO_2.*

Methods			Activation energy, E_G (kJ/mol)	
			Bulk-Glass	
			/	688°C/10h
Ozawa		n	4	4
		n-1 = m	3	3
Matusita		E_G	365-395	950-1000
Ozawa-Chen		E_G	380-405	730-835
Šatava	5°C/min	E_G	600	/
	7°C/min		650	765
	10°C/min		575	895
	12°C/min		580	885
	15°C/min		520	880
	20°C/min		/	670

Although there were some scattering in the results, all methods revealed that the activation energy for crystallization of TiO_2-added MBS glass with previous nucleation heat treatment was higher compared to that without nucleation heat treatment, which exhibited the same activation energy as pure MBS-glass. The reason for this lies in the additional magnesium titanate phase which crystallizes in addition to $Mg_2B_2O_5$ from the nucleated glass.

4.2.3.7 Dielectric material based on TiO_2-added glass-ceramic prepared by isothermal heat-treatment

The dielectric properties of glass-ceramics strongly depend on the ratio between the amount of glassy and crystalline phase. It is well known that glassy phase lowers the Qxf values of the glass-ceramics material. With the addition of small amount of nucleating agent we can increase the content of crystallization phases and significantly influence the dielectric properties. TiO_2 is one of the most commonly used nucleating agents since it can have twofold effect on the crystallization. Firstly, TiO_2 may promote a metastable liquid–liquid phase separation which ought to be the starting point for the internal crystallisation of the glass volume.[137] This effect is enhanced in glasses possessing an increased Ti^{3+} content as obtained by melting the glasses under reducing conditions.[137] Secondly, TiO_2 can form small primary crystalline precipitates (sometimes containing other components of the host glasses). Such crystallites can readily act as heterogeneous nucleation sites for the crystallisation of the glass matrix.[138] TiO_2 used as a nucleating agent in silica-based glasses is easily miscible in the glassy networks at high temperatures but induces phase separation during cooling of the melt.[139] We added 1, 3, 5, 7, and 10 wt.% of TiO_2. When we add only 1 wt.% of TiO_2 there is now significant change in the phase formation, comparing to the MBS glass without nucleating agent prepared in a platinum crucible. Small amount of added TiO_2 is clearly not sufficient for XRD detection (Figure 89).

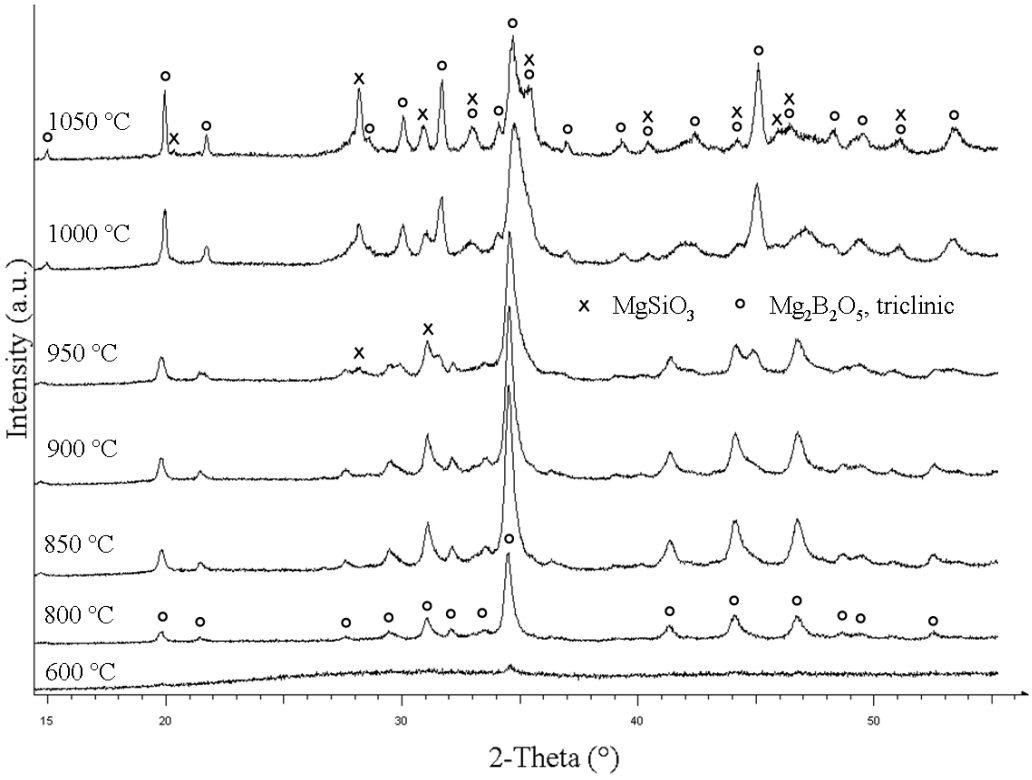

Figure 89. *XRD results for the MBS glass and glass-ceramic with 1 wt.% of TiO_2 sintered at different temperatures for 10 hours. Denotation of the crystalline phases: ○ $Mg_2B_2O_5$ - triclinic, x $MgSiO_3$.*

The XRD patterns of the MBS glass-ceramic with various amount of added TiO_2 sintered at 1050 °C for 10 hours are shown in Figure 90. When glass-ceramic contains 1 wt.% of TiO_2 only $MgSiO_3$ and $Mg_2B_2O_5$ were present. With increasing amount of nucleating agent, the additional crystalline phases started to form. Peaks of Warwickite ($Mg_3TiB_2O_8$) and Rutile doped with boron ($TiB_{0.024}O_2$) were identified for samples with higher content than 1 wt.% of TiO_2. The intensity of the crystal phase peaks increases with the TiO_2 addition. Due to the prolonged isothermal heat-treatment (10 h) at selected temperature the phase constitution of the glass-ceramics differed from that obtained after the single DSC run, which was described in previous Chapter.

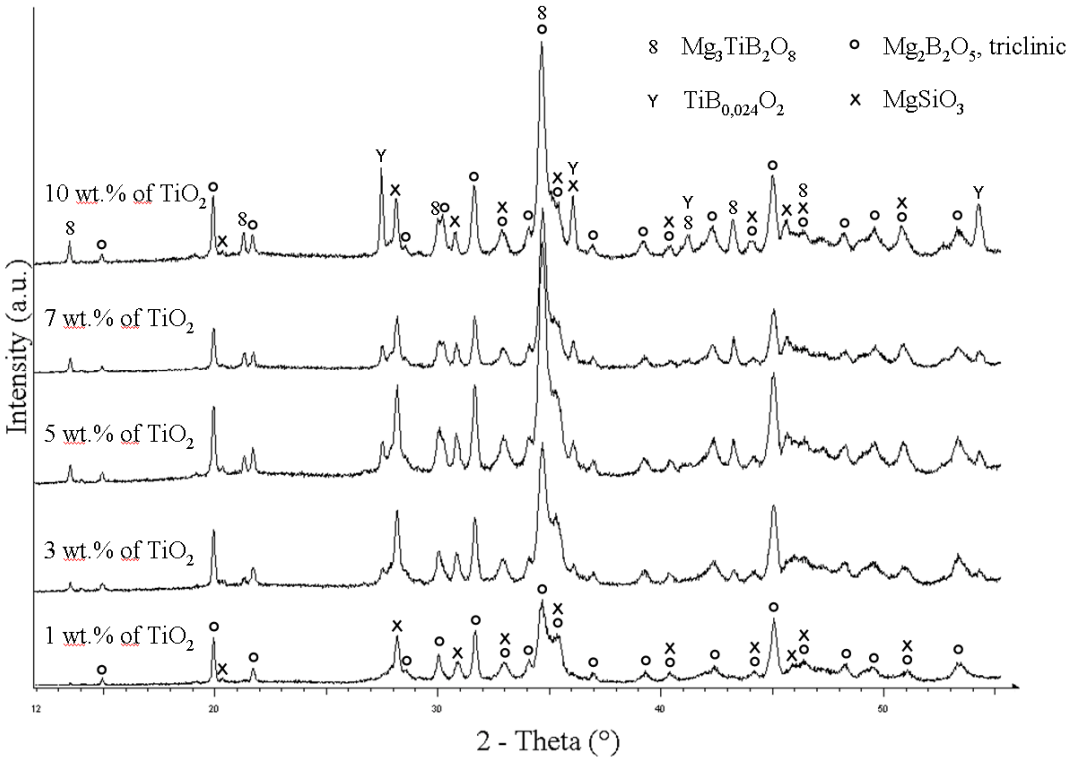

Figure 90. *X-ray diffraction patterns of MBS glass-ceramic with different amount of added TiO_2, sintered at 1050 °C for 10 hours. Denotation of the crystalline phases: ○ $Mg_2B_2O_5$ - triclinic, x $MgSiO_3$, Y $TiB_{0.024}O_2$ and 8 $Mg_3TiB_2O_8$.*

4.2.3.7.1 Microwave dielectric properties

The variation of dielectric constant and Qxf values of MBS glass-ceramics with different amount of TiO_2 (1 to 10 wt.%) against the sintering temperature are shown in Figure 92 and Figure 93, respectively. The dielectric constant decreased with the sintering temperature. Density measurements revealed that this decrease was more likely related to the lowering of density than the change in phase constitution (Figure 91). For the preparation of dense glass-ceramics the densification must occur before beginning of the crystallization. The densification of MBS glass was expected to be improved by two stage sintering. The glass was heated first to temperature slightly above Tg, annealed at this temperature for 10 hours and then heated to the final temperature, where it was annealed for additional 10 hours. It was found that the dielectric properties and the density were not improved by this annealing procedure. MBS glass-ceramics with higher amount of TiO_2 exhibited higher permittivity. This is expected because of higher dielectric polarizability of titanium. TiO_2 posses high dielectric constant ($\varepsilon_r = 105$) and high quality factor (Qxf = 40 000 GHz).[140] In contrast to the permittivity the Qxf-values increased with the sintering temperature. Qxf values also

increase with the amount of added nucleating agent. The highest Qxf values above 16 500 GHz were measured for the sample with 10 wt.% of added TiO_2 sintered at 1050 °C for 10 hours. We assume that the higher Qxf values are result of higher degree of crystallization. According to the knowledge that the presence of crystal phases doubtlessly affects the dielectric properties, we believed that pre-nucleation of the glass will increase the nuclei and in the continuation of the process increase the quantity of the crystal phases in the system.

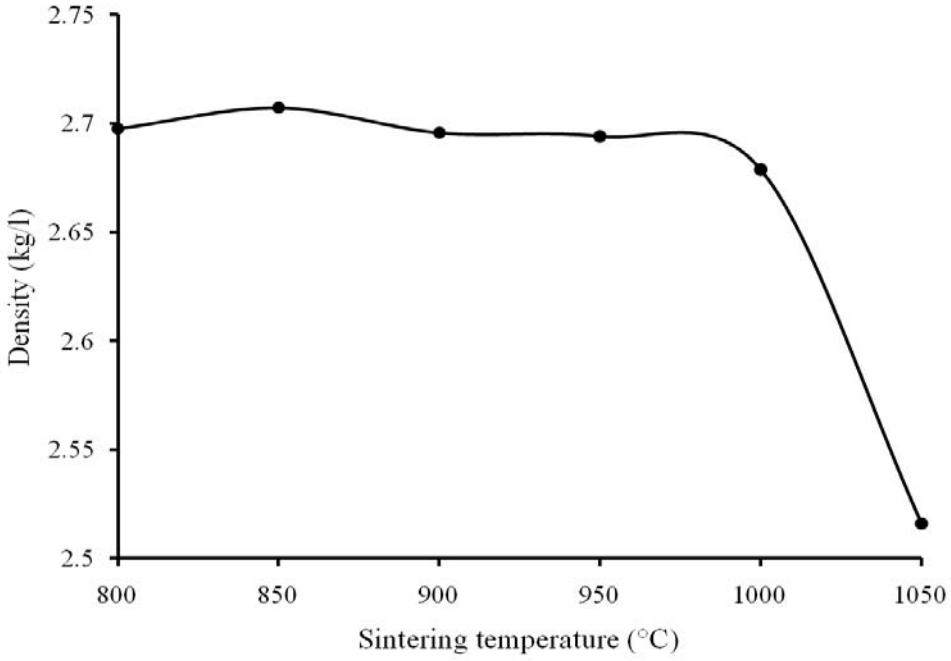

Figure 91. *The density as a function of sintering temperature of the MBS glass with 10 wt.% of added TiO_2 pre-nucleated at 688 °C for 10 hours.*

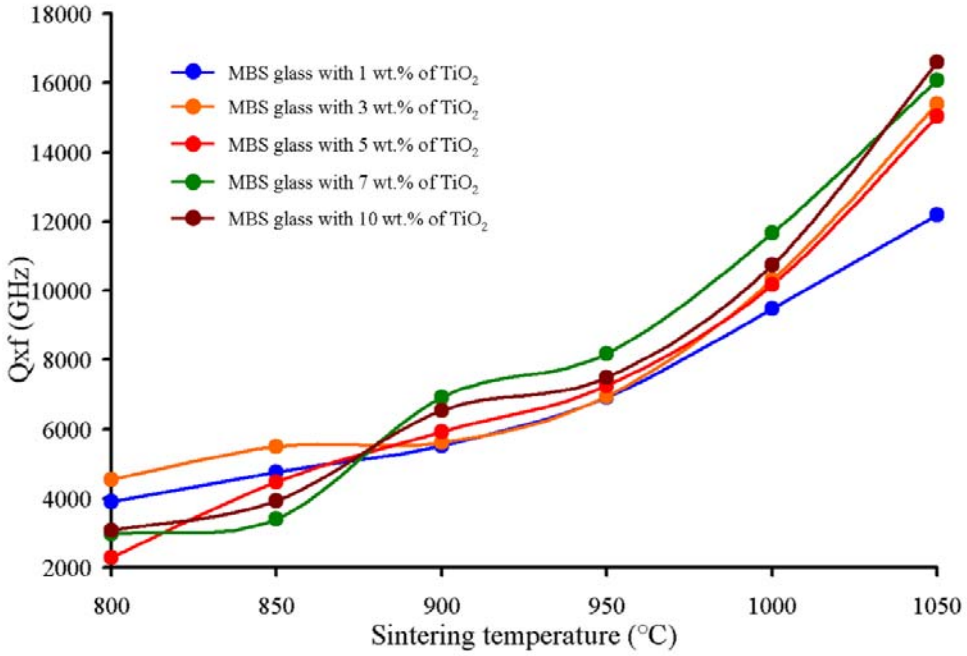

Figure 92. *Qxf values of MBS glass-ceramic with addition of 1 to 10 wt.% of TiO_2 sintered at temperatures from 800 to 1050 °C for 10 hours.*

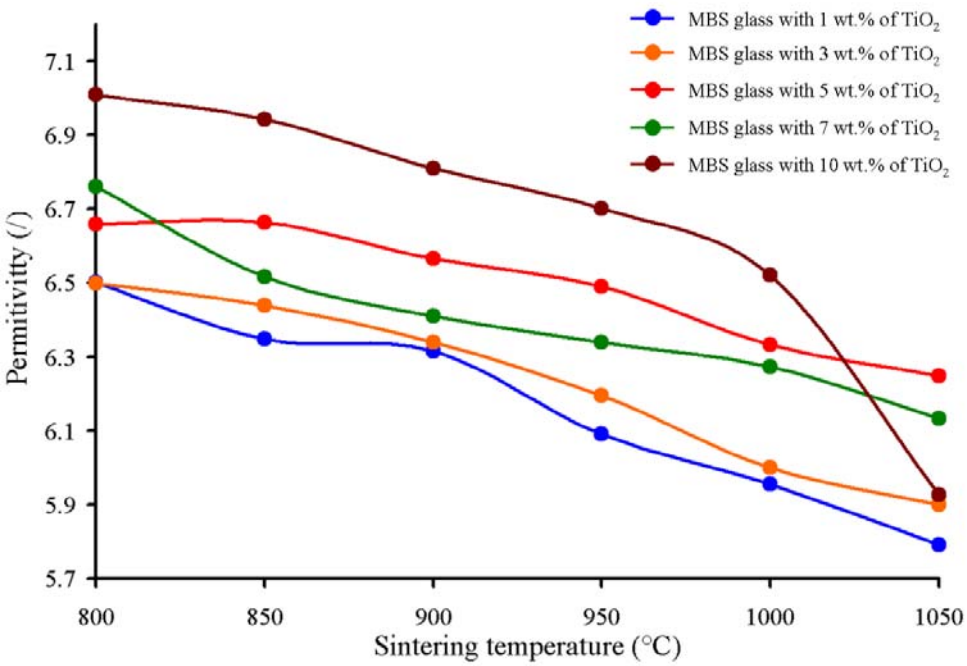

Figure 93. *Permittivity values of MBS glass-ceramic with addition of 1 to 10 wt.% of TiO_2 sintered at temperatures from 800 to 1050 °C for 10 hours.*

Figure 94 shows the variation of dielectric constant for the samples with both the addition of nucleating agent and pre-nucleation as a function of sintering temperature. In all three cases permittivity decreases with increasing of the sintering temperature. Dielectric constant for MBS glass with the addition of TiO_2 is higher at lower sintering temperature than in MBS glass without content of TiO_2. At 1050 °C the drop of the dielectric constant for the sample with TiO_2 is significant that the values become comparable with the values of the samples without nucleating agent. Pre-nucleation at 688 °C for 10 hours doesn't significantly effect on the dielectric constant comparing to the MBS sample with the addition of TiO_2 without pre-nucleation.

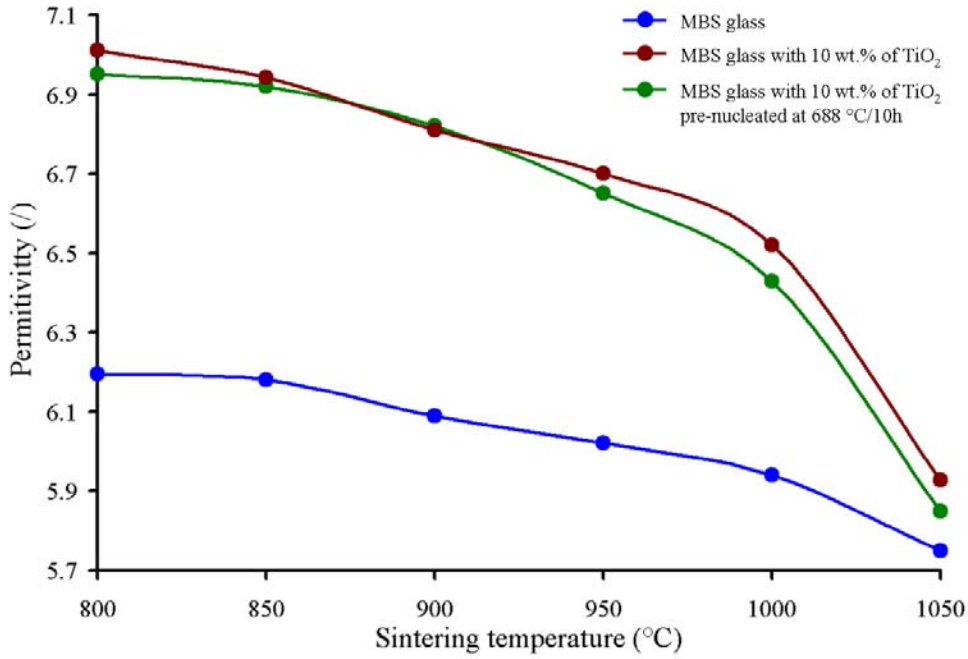

Figure 94. *The εr values of MBS glass with and without addition of TiO_2 as a function of sintering temperature.*

Figure 95 shows the relation between quality factor (Qxf) and sintering temperature. It was found that the Qxf reached the maximum value (17 370 GHz) when MBS glass with 10 wt.% of added TiO_2 was pre-nucleated at 688 °C and sintered at 1050 °C, both for 10 hours. The sample without pre-nucleation exhibit slightly lower Qxf values. Additionally, the Qxf values increased with the sintering temperature of MBS glasses and the values of Qxf in all three cases are quite comparable up to the 1000 °C. The improvement of the Qxf values due to the addition of TiO_2 was noticed at 1050 °C.

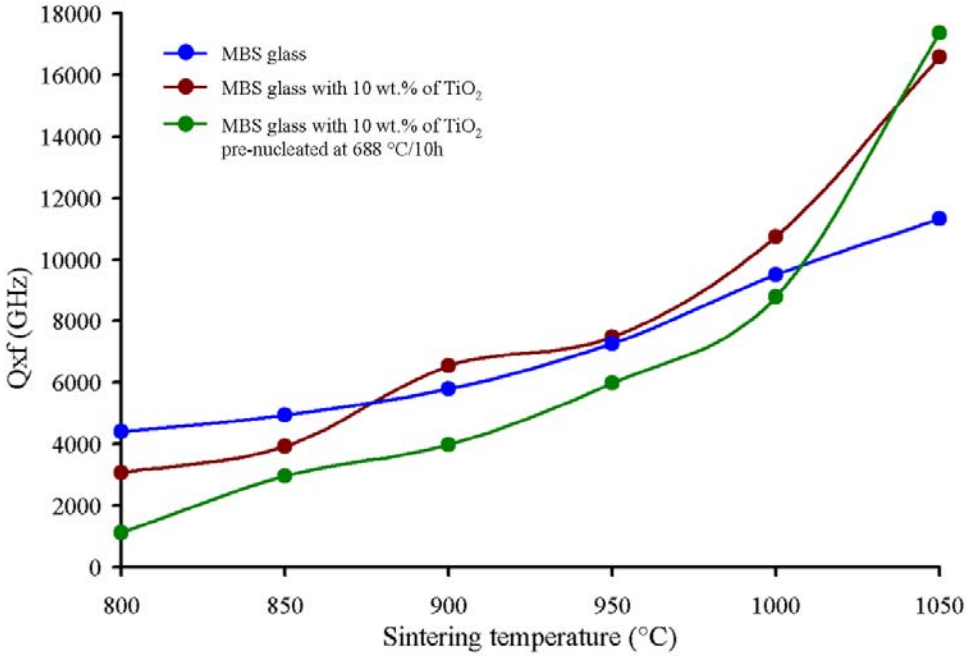

Figure 95. *Comparison between the Qxf values of MBS glass with and without addition of TiO_2 as a function of sintering temperature.*

5 Conclusions

In recent years, the application range for glass-ceramic materials in electronic industry has expanded considerably, which stimulated detail research of MgO– B_2O_3–SiO_2 (MBS) based glass-ceramic. Furthermore, crystallization of MBS glass and dielectric properties of the corresponding MBS glass-ceramic has not been reported, yet. The knowledge about the properties of the individual binary compounds from the MgO–B_2O_3 system shows an important role in the interpretation of the ternary MBS based system. Binary compounds of $Mg_2B_2O_5$ and $Mg_3B_2O_6$ are precisely described in the subsections. The main purpose of the thesis was the investigation of the nucleation and crystallization processes of MBS glass and their related dielectric properties

5.1 Binary system MgO – B_2O_3

5.1.1 $Mg_2B_2O_5$

Single-phase $Mg_2B_2O_5$ ceramics was prepared with the solid-state reaction technique. The presence of $Mg_3B_2O_6$ in the $Mg_2B_2O_5$ ceramics, prepared from stoichiometric ratio of MgO and B_2O_3, indicated the evaporation of B_2O_3, which was in further synthesis substituted by the addition of excess B_2O_3 at the beginning of the synthesis. According to the XRD results we determined that 14 wt.% of excess of B_2O_3 led to the single phase $Mg_2B_2O_5$ ceramics at 1200 °C and at 1250 °C. The Archimedes' method measured densities of sintered $Mg_2B_2O_5$ with 14 wt.% B_2O_3 ceramics revealed the values from 94 to 97 %. The permittivity for the ceramics varied from 6.2 to 7.0 and Qxf values from 18 400 to 32 100 GHz. The τ_f values were in the range from −18 to −45 ppm/°C. The microstructural investigations of the sintered $Mg_2B_2O_5$ ceramics revealed the presence of 10-μm grains.

5.1.2 $Mg_3B_2O_6$

Single phase $Mg_3B_2O_6$ was obtained after several pre-reactions and with 11 wt.% of excess B_2O_3, which was added to the stoichiometric ratio of MgO and B_2O_3 at the beginning of the synthesis. The permittivity of the $Mg_3B_2O_6$ ceramics was 6.8–7.4 and τ_f was in the range from −36 to −45 ppm/°C. The properties of the $Mg_3B_2O_6$ based ceramics from this study exceed the already reported Qxf values (150 400 GHz) for this type of ceramic. Our investigations revealed great variation of the Qxf-values and microstructural characteristics with the annealing conditions. The highest Qxf values over 220 000 GHz were observed for the ceramics that were sintered at 1300 °C and cooled slowly from the sintering temperature with a controlled cooling rate of 2 °C/min. These ceramics consisted of large grains (~1000 μm) with some closed porosity. According to the density measurements the porosity was about 4–5 %. The ceramics sintered at 1300 ºC (10 hours) and cooled rapidly contained areas of large (500–1000 μm) and small grains (10–50 μm) exhibit lower Qxf values up to 150 000 GHz. In the ceramics sintered at 1200 °C the grains were only a few tens of μm in size and the Qxf value was below 60 000 GHz.

Detailed microstructural and dielectric characterization of $Mg_3B_2O_6$ ceramics was performed in order to understand the reasons for exaggerated grain growth and to clarify the conditions for preparation of $Mg_3B_2O_6$ ceramics with extremely high Qxf-values. The reasons for exaggerated grain growth were attributed to the liquid phase that formed from the admixture of the glassy or $Mg_2B_2O_5$ phases. The presence of an amorphous phase at the grain boundaries was confirmed by TEM. The effect of $Mg_2B_2O_5$ on the grain growth was studied by its intentional addition (0-5 wt.%) to the $Mg_3B_2O_6$ before sintering. The fastest grain growth was observed for $Mg_3B_2O_6$ ceramics with 5 wt.% of $Mg_2B_2O_5$. Regardless of the amount of added $Mg_2B_2O_5$, the exaggeratedly grown grains were anisotropic with a twin boundary that extends along the anisotropic direction. EBSD, which was used for an examination of the anisotropic grains, revealed a (011) twin plane. The Qxf values increased with the prolongation of the annealing, while the permittivity remained constant at 7. The highest Qxf value of 240 000 GHz was measured for coarse-grained $Mg_3B_2O_6$ ceramics with 5 wt.% of $Mg_2B_2O_5$. In contrast, $Mg_3B_2O_6$ ceramics with 10 times smaller grains exhibited only a slightly lower Qxf value of 200 000 GHz. The decrease of the amorphous phase during the annealing could be one of the reasons for this improvement of the Qxf values.

5.2 Ternary system $MgO – B_2O_3 – SiO_2$

The glass composition 43 wt.% MgO–35 wt.% B_2O_3–22 wt.% SiO_2, chosen on the basis of the preliminary studies, was synthesized in both corundum and platinum crucible. The diffusion of aluminium, from corundum crucible to the melt, during melting process resulted in the formation of cordierite phase. The presence of cordierite phase in the glass-ceramics significantly affects the microwave dielectric properties. The maximum Qxf values were obtained for ceramics sintered at 950 °C, while with further increase of temperature to 1000 °C, the Qxf-values significantly decreased. XRD analysis shows that amount of cordierite phase was considerably reduced at this temperature. For the glass-ceramics prepared in Pt- crucible the increase of Qxf-values up to 11 330 GHz was observed. The decrease of permittivity with increase of sintering temperature was observed for both types of glass-ceramics. The range of permittivity for the glass-ceramic, which contained cordierite, was larger (6.5-4.7) than that the glass-ceramic where glass was prepared in platinum crucible (6.2-5.8). Since the amount of cordierite could not be controlled the further research was performed for the MBS glass melted in platinum crucible.

In order to understand the nucleation and crystallization processes in the MBS glass the nucleation and crystallization kinetics was investigated by means of non-isothermal DSC techniques. In the MBS glass nucleation occurs in the range from 600 to 750 °C and the maximum nucleation rate is reached at 700 °C. Avrami exponent n = 1.5, obtained by Ozawa method for both powder and bulk sample indicates three-dimensional bulk crystallization. Diffusion controlled crystal growth occurred at constant number of nuclei n = m. Activation energy of non-nucleated and nucleated bulk samples (2 and 10 h) show comparable values of 420 kJ/mol. In the case of nucleated and non-nucleated powder samples, the activation energy achieves higher values up to 810 kJ/mol. Due to the surface crystallization that takes place in powders along prevailing bulk crystallization; this value of activation energy is expected to have less physical meaning than that obtained for bulk MBS glass.

In order to promote the crystallization of MBS glass different amount of TiO_2 (1-10 wt.%) was added. $Mg_2B_2O_5$ as a main phase crystallize at ≈ 800 °C, while $MgSiO_3$ appeared at 950 °C. Warwickite ($Mg_3TiB_2O_8$) and rutile doped with boron ($TiB_{0.024}O_2$) were additionally found and identified for samples with more than 1 wt.% of TiO_2 at temperatures higher than 1000 °C. With the addition of TiO_2 the crystallization mechanism changes to bulk crystallization with an increasing number of nuclei (n = 4, m = 3). The permittivities and Qxf values was found to increase with the TiO_2 content. The improvement of the Qxf-values was attributed to the enhanced crystallization. The highest Qxf value of 17 370 GHz was measured for the MBS glass-ceramics with 10 wt.% of TiO_2, which were pre-nucleated at 688 °C and

sintered at 1050 °C, both for 10 hours. The MBS based glass-ceramics sintered in the range from 850 to 950 °C exhibited somewhat lower Qxf-values of 5000-8000 GHz and $\varepsilon = 6.1\text{-}6.9$.

6 Acknowledgements

I would like to express my deep and sincere gratitude to my supervisor, Professor Dr. Danilo Suvorov, head of Advanced Materials Department, who kindly welcomed me into the department and gave me a chance to improve my knowledge and extend my education. I would like to thank him for his unwavering trust, support and encouragement during my studies.

I am sincerely grateful to Dr. Marjeta Maček Kržmanc for her supervision and guidance throughout the studying process. I am very thankful to her because she offered valuable suggestions for my work and was always willing to help. Her scientific contribution has been more than essential for the completion of my thesis.

This work would not have been possible without the stimulating environment in the Advanced Materials Department. I would like to thank my colleagues and friends for their support and all the pleasant moments we spent together.

I am indebted to my thesis committee: Prof Dr. Dragoljub Uskoković, Assis. Prof. Dr. Miran Čeh, Assis. Prof. Dr. Boštjan Jančar.

My parents and sister deserve a special mentioning for their continuous support and encouragement throughout my studies and for raising me into an inquisitive and curious person. My parents have always encouraged me to fulfil my ambitious goals and put education as the first priority in my life.

Finally, I would like to express my heartfelt gratitude to Sabina for all her patience and understanding. During the writing of this thesis she provided me with encouragement and inspiration for which I am immensely grateful.

7 References

[1] Zhang, Q. L.; Yang, H.; Sun, H. P. A new microwave ceramic with low permittivity for LTCC applications. *Journal of the European Ceramic Society* **28**, 605-609 (2008).

[2] Ohsato, H.; Research and development of microwave dielectric ceramics for wireless communications. *Journal of the Ceramic Society of Japan* **113**, [11] 703-711 (2005).

[3] Higuchi, Y.; Sugimoto, Y.; Harada, J.; Tamura, H. LTCC system with new high-ε_r and high-Q material co-fired with conventional low-ε_r base material for wireless communications. *Journal of the European Ceramic Society* **27**, 2785-2788 (2007).

[4] Udovič, M.; Suvorov, D. Sintering and dielectric characterization of pseudoternary compounds from the Bi_2O_3- TiO_2-TeO_2 system. *Journal of the American Ceramic Society* **90**, [8] 2404-2408 (2007).

[5] Takada, T.; Wang, S. F.; Yoshikawa, S.; Jang S. J.; Newnham, R. E. Effect of glass additions on BaO-TiO_2-WO_3 microwave ceramics. *Journal of the American Ceramic Society* **77**, [7] 1909-1916 (1994).

[6] Belous, A.; Ovchar, O.; Durylin, D.; Valant, M.; Krzmanc, M. M.; Suvorov D. Microwave composite dielectrics based on magnesium titanates. *Journal of the European Ceramic Society* **27**, 2963-2966 (2007).

[7] Shin, H. K.; Shin, H.; Cho, S. Y.; Hong, K. S. Phase evolution and dielectric properties of $MgTiO_3$–$CaTiO_3$-based ceramic sintered with lithium borosilicate glass for application to low-temperature co-fired ceramics. *Journal of European Ceramic Societ* **88**, 2461–2465 (2005).

[8] Surendran, K. P.; Sebastian, M. T.; Manjusha, M. V.; Philip, J. A low loss, dielectric substrate in $ZnAl_2O_4$–TiO_2 system for microelectronic applications. *Journal of Applied Physics* **98**, 044101-9 (2005).

[9] Ohashi, M.; Ogawa, H.; Kan, A.; Tanaka, E. Microwave dielectric properties of low-temperature sintered $Li_3AlB_2O_6$ ceramic. *Journal of the European Ceramic Society* **25**, 2877-2881 (2005).

[10] Chang, C. R.; Jean, J. H. Crystallization kinetics and mechanism of low-dielectric, low-temperature, cofirable CaO-B_2O_3-SiO_2, Glass-ceramics. *Journal of the American Ceramic Society* **88**, 2461–2465 (2005).

[11] Zhang, Q. L.; Yang, H.; Zou, J. L.; Wang, H. P. Sintering and microwave dielectric properties of LTCC-zinc titanate multilayers. *Materials Letters* **59**, 880-884 (2005).

[12] Huang, W.; Liu, K. S.; Chu, L. W.; Hsiue, G. H.; Lin, I. N. Microwave dielectric properties of LTCC materials consisting of glass–$Ba_2Ti_9O_{20}$ composites. *Journal of the European Ceramic Society* **23**, 2559–2563 (2003).

[13] Lo, C. L.; Duh, J. G.; Chiou, B. S.; Lee, W. H. Low-temperature sintering and microwave dielectric properties of anorthite-based glass-ceramics. *Journal of the American Ceramic Society* **85**, [9] 2230-2235 (2002).

[14] Kim, H. T.; Kim, S. H.; Nahm, S.; Byun, J. D.; Kim, Y. Low-temperature sintering and microwave dielectric properties of zinc metatitanate–rutile mixtures using boron. *Journal of the American Ceramic Society* **82**, 3043–3048 (1999).

[15] Jantunen, H.; Rautioaho, R.; Uusimaki, A.; Leppavuori, S. Compositions of $MgTiO_3$-$CaTiO_3$ ceramic with two borosilicate glasses for LTCC technology. *Journal of the European Ceramic Society* **20**, 2331-2336 (2000).

[16] Takada, T.; Wang, S. F.; Yoshikawa, S.; Jang, S. J.; Newnham, R. E. Effects of glass additions on (Zr,Sn)TiO, for microwave applications. *Journal of the American Ceramic Society* **77**, [9] 2485-2488 (1994).

[17] Chen, C. S.; Chou, C. C.; Shih, W. J.; Liu, K. S.; Chenc, C. S.; Lin, I. N. Microwave dielectric properties of glass–ceramic composites for low temperature co-firable ceramics. *Materials Chemistry and Physics* **79**, 129–134 (2003).

[18] Tummala, R. R.; Ceramic and glass-ceramic packaging in the 1990s. *Journal of the American Ceramic Society* **74**, [5] 895-908 (1991).

[19] Kumar, C. J. D.; Sunny, E. K.; Raghu N.; Venkataramani, N.; Kulkarni, A. R. Synthesis and characterization of crystallizable anorthite-based glass for a low-temperature cofired ceramic application. *Journal of the American Ceramic Society* **91**, [2] 652–655 (2008).

[20] Jean, J. H.; Chang, C. R.; Lei, C. D. Sintering of a crystallizable $CaO–SiO_2–B_2O_3$ glass with silver. *Journal of the American Ceramic Society* **87**, [7] 1244-1249 (2004).

[21] Zhu, H.; Liu, M.; Zhou, H.; Li, L.; Lv, A. Study on properties of $CaO–SiO_2–B_2O_3$ system glass-ceramic. *Materials Research Bulletin* **42**, 1137–1144 (2007).

[22] Tulyaganov, D. U.; Agathopoulos, S.; Venura, J. M.; Karakassides, M. A.; Fabrichnaya, O.; Ferreira, J. M. F. Synthesis of glass-ceramics in the $CaO\text{-}MgO\text{-}SiO_2$ system with B_2O_3, P_2O_5, Na_2O and CaF_2 additives. *Journal of the European Ceramic Society* **26**, 1463–1471 (2006).

[23] Jean, J. H.; Fang, Y. C.; Dai, S. X.; Wilcox, Sr. D. L. Devitrification kinetics and mechanism of $K_2O\text{-}CaO\text{-}SrO\text{-}BaO\text{-}B_2O_3\text{-}SiO_2$ glass-ceramic, *Journal of the American Ceramic Society* **84**, [6] 1354–60 (2001).

[24] McMillan, P. W. *Glass-Ceramics* (Academic Press, London, 1964).

[25] Morey, G. W. *The Properties of Glass* (Reinhold, 2nd edition, New York, 1954).

[26] Vogel, W. *Glass Chemistry* (Springer Verlag, 2nd edition, Berlin, 1994).

[27] Goldschmidt, V. M. *Geochemische Verteilungsgeestze der Elemente, VII.: Die Gesetze der Kristallochemie* (Vid.-Akad. Skr., Oslo, 1926).

[28] Zachariasen, W. H. The atomic arrangement in glass. *Journal of the American Ceramic Society* **54**, 3841-3857 (1932).

[29] Biscoe, J.; Warren, B. E. X-ray diffraction study of soda-boric oxide glass. *Journal of the American Ceramic Society* **21**, 287-293 (1938).

[30] Dietzel, A. Die kationenfeldstärken und ihre beziehungen zu entglasungsvorgängen, zur verbindungsbildung und zu den schmelzpunkten von silicaten. *Zeitschrift für Elektrochemie und Angewandte Physikalische Chemie* **48**, 9-23 (1942).

[31] Tammann, G. *Der Glaszustand* (Leonard Voss, Leipzig, 1933, Moscow, 1935).

[32] Volmer, M. *Kinetik der Phasenbildung* (Th Steinkopf Verlag, Dresden, Leipzig, 1939).

[33] Kingery, W. D.; Bowen, H. K.; Uhlmann, D. R. *Introduction to Ceramics* (John Wiley & Sons, New York, 1975).

[34] Kelly, G.; Alderman, J.; Lyden, C.; Barrett, J. Microsystem packaging: lessons from conventional low cost IC packaging. *Journal of Micromechanics and Microengineering* **7**, 99-103 (1997).

[35] Al-Taei, S.; Haigh, D.; Passiopoulos, G. Multilayer ceramic integrated circuits (MCICs) technology and passive circuit design. *Proceedings of the London Communication Symposium*. 139-142 (6th Annual London Conference on Communications, 2001).

[36] Golonka, L. J. Technology and applications of low temperature cofired ceramic (LTCC) based sensors and Microsystems. *Bulletin of the Polish Academy of Sciences Technical Sciences* **54**, [2] 221-231 (2006).

[37] Jantunen, H. A Novel low temperature co-fired ceramic (LTCC) materials for telecommunication devices. Ph. D. thesis, *Department of Electrical Engineering* (University of Oulu, Finland, 2001).

[38] Anjana, P. S.; Sebastian, M. T. Microwave dielectric properties of low-temperature sintering of cerium oxide for LTCC applications. *Journal of the American Ceramic Society* **92**, [1] 96-104 (2009).

[39] Sebastian, M. T.; Jantunen, H. Low-loss dielectric materials for LTCC applications: a review. *International Materials Reviews* **53**, [2] 57-90 2008.

[40] Prudenziati, M. *Handbook of Sensors and Actuators: Thick-Film Sensors* (Elsevier Science B.
V., Amsterdam, 1994).

[41] Lange, F. F. Powder processing science and technology for increased reliability. *Journal of the American Ceramic Society* **72**, [1] 3-15 (1989).

[42] Lewis, J. A. Colloidal processing of ceramics. *Journal of the American Ceramic Society* **83**, [10] 2341-2359 (2000).

[43] Mistler, R. E. Tape casting: past, present, potential. *American Ceramic Society Bulletin* **77**, [10] 82-26 (1998).

[44] Schwartz, B. Microelectronics Packaging: 2. *American Ceramic Society Bulletin* **63**, [4] 577-581 (1984).

[45] Chowdhry U.; Sleight, A. W. Ceramic substrates for microelectronic packaging. *Annual Review of Materials Research* **17**, 323-340 (1987).

[46] Jean J. H.; Gupta, T. K. Design of low dielectric glass+ceramics for multilayer ceramic substarte. *IEEE Transactions on Components, Packaging, and Manufacturing Technology-Part B Advanced Packaging* **17**, [2] 228-233 (1994).

[47] Reaney, I. M.; Iddles, D. Microwave dielectric ceramics for resonators and filters in mobile phone networks. *Journal of the American Ceramic Society* **89**, [7] 2063-2072 (2006).

[48] Cava, R. J. Dielectric materials for applications in microwave communications. *Journal of Materials Chemistry* **11**, 54-62 (2001).

[49] Ohsato, H.; Imaeda, M. The quality factor of the microwave dielectric materials based on the crystal structure-as an example: the $Ba_{6-3x}R_{8+2x}Ti_{18}O_{54}$ (R = rare earth) solid solutions. *Materials Chemistry and Physics* **79**, 208-212 (2003).

[50] Moulson A. J.; Herbert, J. M. *Electroceramics*. (Chapman and Hall, London, 1990).

[51] Shim, K. B.; Cho, N. T.; Lee, S. W. Silver diffusion and microstructure in LTCC multilayer couplers for high frequency applications. *Journal of Materials Science* **35**, 813-820 (2000).

[52] Dai, S. X.; Huang, R. F.; Sr. Wilcox, D. L. Use of titanates to achieve a temperaturestable low temperature cofired ceramic dielectric for wireless applications. *Journal of the American Ceramic Society* **85**, [4] 828-832 (2002).

[53] Nagai, T.; Inuzuka, T.; Sugiyama, M. Contribution of dielectric constant to change in temperature coefficient of resonant frequency in $(Ba_{1-x}Sr_x)(Mg_{1/3}Ta_{2/3})O_3$ compounds. *Japanese Journal of Applied Physics* **31**, 3132-3135 (1992).

[54] Kim, D. H.; Lim, S. K.; An, C. The microwave dielectric properties of $xTiO_2(1-x)CeO_2$ ceramics.
Materials Letters **52**, 240-243 (2002).

[55] Freer, R.; Azough, F. Microstructural engineering of microwave dielectric ceramics. *Journal of the European Ceramic Society* **28**, 1433-1441 (2008).

[56] Hench, L. L.; West, J. K. *Principles of Electronic Ceramics* (John Wiley & Sons, New

York, 1990).

[57] Maex, K.; Baklanov, M. R.; Shamiryan D.; Iacopi, F.; Brongersma, S. H.; Yanovitskaya, Z. S. Low dielectric constant materials for microelectronics. *Journal of Applied Physics* **93**, [11] 8793-8841 (2003).

[58] Shannon, R. D. Dielectric polarizabilities of ions in oxides and fluorides. *Journal of Applied Physics* **73**, [1] (1993).

[59] Sebastian, M. T. *Dielectric Materials for Wireless Communication* (Elseiver, Amsterdam, 2008).

[60] Vendik, O. G.; Ter-Martirosyan, L. T.; Zubko, S. P. Microwave Losses in incipient ferroelectrics as function of the temperature and the biasing field. *Journal of Applied Physics* **84**, [2] 993-998 (1998).

[61] Astafiev, K. F.; Sherman, V. O.; Tagantsev, A. K.; Setter, N.; Kaydanova, T.; Ginley, D. S. Crossover between extrinsic and intrinsic dielectric loss mechanisms in $SrTiO_3$ thin films at microwave frequencies. *Applied Physics Letters* **84**, [13] 2385-2387 (2004).

[62] Finstrom, N. H.; Gannon, J. A.; Pervez, N. K.; York, R. A.; Stemmer, S. Dielectric losses of $SrTiO_2$ thin film capacitors with Pt bottom electrodes at frequencies up to 1 GHz. *Applied Physics Letters* **89**, 242910 (2006).

[63] Gurevich, G. L.; Tagantsev, A. K. Intrinsic dielectric loss in crystals. *Advances in Physics* **40**, 719-767 (1991).

[64] Vorobiev, A.; Rundqvist, P.; Khamchane, K.; Gevorgian, S. J. Microwave loss mechanisms in $Ba_{0.25}Sr_{0.75}TiO_3$ thin film varactors. *Journal of Applied Physics* **96**, [8] 4642-4649 (2004).

[65] Bosman, A. J.; Havinga, E. E. Temperature dependence of dielectric constants of cubic ionic compounds. *Physical Review* **129**, [4] 1593-1600 (1963).

[66] Valant, M.; Suvorov, D.; Rawn, C. J. Intrinsic reasons for variations in dielectric properties of $Ba_{6-3x}R_{8+2x}Ti_{18}O_{54}$ (R=La-Gd) solid solutions. *Japanese Journal of Applied Physics* **38**, 2820-2826 (1999).

[67] Michael, G. T.; Frank, G. S. Validation of a novel dielectric constant simulation model and the determination of its physical parameters. *Microelectronics Journal* **33**, 627–632 (2002).

[68] Kim, D. W.; Park, B. W.; Chung J. H.; Hong, K. S. Mixture behavior microwave dielectric properties in the low-fired TiO_2–CuO system. *Japanese Journal of Applied Physics* **39,** 2696–2700 (2000).

[69] Jayasundere, N.; Smith, B. V. Dielectric constant for binary piezoelectric 0–3 composites. *Journal of Applied Physics* **73**, [5] 2462–2466 (1993).

[70] Wu, C. C.; Chen, Y. C.; Su, C. C.; Yang, C. F. The chemical and dielectric properties of epoxy/$(Ba_{0.8}Sr_{0.2})(Ti_{0.9}Zr_{0.1})O_3$ composites for embedded capacitor application. *European Polymer Journal* **45**, [5] 1442-1447 (2009).

[71] Paladino, A. E. Temperature-compensated $MgTi_2O_5$-TiO_2 dielectrics. *Journal of the American Ceramic Society* **54**, 168-169 (1971).

[72] Toropov, N. A.; Konovalov, P. F. Binary system magnesium oxide-boron anhydride. *Zhurnal Fizicheskoi Khimii* **14**, [3] 1103-1109 (1940).

[73] Davis, H. M.; Knight, M. A. The system magnesium oxide-boric oxide. *Journal of the American Ceramic Society* **28**, [4] 97-102 (1945).

[74] Kuzel, H. J. Zur Kenntnis des systems MgO-B_2O_3: Synthese und röntgenographische untersuchungen der verbindung $MgO{\cdot}2B_2O_3$. *Neues Jahrbuch Mineral Monatsh* **12**, 357-360 (1964).

[75] Fletcher, B. L.; Stevenson, J. R.; Whitaker, A. Phase equilibria in the system CaO-MgO-

B_2O_3 at 900 °C. *Journal of the American Ceramic Society* **53**, [2] 95-97 (1970).

[76] Miyagawa, S.; Hirano, S. I.; Somiya, S. Phase relations in the system MgO-B_2O_3. *Bulletin of the Tokio Institute of Technology* **108**, 34-42 (1972).

[77] Mutluer T.; Timucin, M. Phase equilibria in the system MgO–B_2O_3. *Journal of the American Ceramic Society* **58**, 196–197 (1975).

[78] Furetta, C.; Kitis, G.; Weng P. S.; Chu, T. C. Thermoluminescence characteristics of MgB_4O_7: Dy, Na. *Nuclear Instruments and Methods Physics Research A* **420**, 441-445 (1999).

[79] Shahare, D. I.; Dhoble, S. J.; Moharil, S. V. J. Preparation and characterization of magnesium-borate phosphor. *Journal of Materials Science Letters* **12**, 1873-1874 (1993).

[80] Hu, Z. S.; Lai, R.; Lou, F.; Wang, L. G.; Chen, Z. L.; Chen, G. X.; Dong, J. X. Preparation and tribological properties of nanometer magnesium borate as lubricating oil additive. *Wear* **252**, 370–374 (2002).

[81] Li, Y.; Fan, Z.; Lu, J. G.; Chang, R. P. H. Synthesis of magnesium borate ($Mg_2B_2O_5$) nanowires by chemical vapor deposition method. *Chemistry of Materials* **16**, 2512–2514 (2004).

[82] Tao, X.; Li, X. Catalyst-free synthesis, structural, and mechanical characterization of twinned $Mg_2B_2O_5$ nanowires. *Nano Letters* **8**, [2] 505–510 (2008).

[83] Elssfah, E. M.; Elsanousi, H. A.; Zhang, J.; Song, H. S.; Tang, C. Synthesis of magnesium borate nanorods. *Materials Letters* **61**, 4358–4361 (2007).

[84] Zeng, Y.; Yang, H.; Fu, W.; Qiao, L.; Chang, L.; Chen, J.; Zhu, H.; Li, M.; Zou, G. Synthesis of magnesium borate ($Mg_2B_2O_5$) nanowires, growth mechanism and their lubricating properties. *Materials Research Bulletin* **43**, 2239–2247 (2008).

[85] Xu, B. S.; Li, T. B.; Zhang, Y.; Zhang, Z. X.; Liu, X. G.; Zhao, J. F. New synthetic route and characterization of magnesium borate nanorods. *Crystal Growth & Design* **8**, [4] 1218–1222 (2008).

[86] Ma, R.; Bando, Y.; Sato, T. Nanowires of metal borates. *Applied Physics Letters* **81**, [18] 3467-3469 (2002).

[87] Ma, R.; Bando, Y.; Golberg, D.; Sato, T. Nanotubes of magnesium borate. *Angewandte Chemie International Edition* **42**, 1836-1838 (2003).

[88] Zhang, J.; Li, Z.; Zhang, B. Formation and structure of single crystalline magnesium borate ($Mg_3B_2O_6$) nanobelts. *Materials Chemistry and Physics* **98**, 195-197 (2006).

[89] Watanabe, T. Kotoit, ein neues gesteinsbildendes Magnesiumborat. *Mineralogische und Petrographische Mitteilungen* **50**, 441-463 (1939).

[90] Takeuchi, Y. The crystal structure of magnesium pyroborate. *Acta Crystallographica* **5**, 574-581 (1952).

[91] Mrose, M. E.; Fleischer, M. The probable identity of magnioborite with suanite. *The American Mineralogist* **48**, 915-924 (1963).

[92] Guo, G. C.; Cheng, W. D.; Chen, J. T.; Zhuang, H. H.; Huang, J. S.; Zhang, Q. E. Monoclinic $Mg_2B_2O_5$. *Acta Crystallographica* **C51**, 2469-2471 (1995).

[93] Guo, G. C.; Cheng, W. D.; Chen, J. T.; Huang, J. S.; Zhang, Q. E. Triclinic $Mg_2B_2O_5$. *Acta Crystallographica* **C51**, 351-352 (1995).

[94] Effenberger, H.; Perttlik, F. Verfeinerung der kristallstrukturen der isotypen verbindungen $M_3(BO_3)_2$ mit M = Mg, Co und Ni (strukturtyp: Kotoit). *Zeitschrift für Kristallographie* **166**, 129–140 (1984).

[95] Bondareva, O. S.; Simonov, M. A.; Belov, N. V. The crystal structure of synthetic

Jimboite, $Mn_3(BO_3)_2$. *Soviet Physics – Crystallography* **23**, 272–273 (1978).

[96] Berger, S.V. The crystal structure of isomorphous orthoborates of cobalt and magnesium. *Acta Chemica Scandinavica* **3**, 660-675 (1949).

[97] Kuzel, H. J. Untersuchung des dreistoffsystems $MgO – B_2O_3 – SiO_2$. *Neues Jahrbuch für Mineralogie* **100**, [3] 322-338 (1963).

[98] PCPDFWIN Version 2.3, *JCPDS-International Center for Diffraction Data* (2001).

[99] Matusita, K.; Sakka, S. Kinetic study on non-isothermal crystallization of glass by thermal analysis. *Bulletin of the Institute for Chemical Research* **59**, [3] 159-170 (1981).

[100] Marotta, A.; Buri, A.; Branda, F.; Saiello, S. Nucleation in glass forming systems. A DTA study. *Thermochimica Acta* **85**, 231-234 (1985).

[101] Marotta, A.; Buri, A.; Branda, F. Nucleation in glass and differential thermal analysis. *Journal of Materials Science* **16**, 341-344 (1981).

[102] Kissinger, H. E. Variation of peak temperature with heating rate in differential thermal analysis. *Journal of Research of the National Bureau Standards* **57**, [4] 217-221 (1956).

[103] Henderson, D. W. Thermal analysis of nonisothermal crystallization kinetics in glass-forming liquids. *Journal of Non-Crystalline Solids* **30**, 301-315 (1979).

[104] Yinnon, H.; Uhlmann D. R. Applications of thermoanalytical techniques to the study of crystallization kinetics in glass-forming liquids, part I: Theory. *Journal of Non-Crystalline Solids* **54**, 253-275 (1983).

[105] Matusita, K.; Sakka, S.; Matsui, Y. Determination of activation energy for crystal Growth by differential thermal analysis. *Journal of Materials Science* **10**, 961-66 (1975).

[106] Matusita, K.; Sakka, S. Kinetic study of crystallization of glasses by differential scanning calorimeter. *Physics and Chemistry of Glasses* **20**, 81-84 (1979).

[107] Matusita, K.; Sakka, S. Kinetic study on crystallization of glass by differential thermal analysis-criterion on application of kissinger plot. *Journal of Non-Crystalline Solids* **38 & 39**, 741-746 (1980).

[108] Ozawa, T. Kinetics of nonisothermal crystallization. *Polymer* **12**, [3] 150-158 (1971).

[109] Predeep, P.; Saxena, N. S.; Saksena, M. P.; Kumar, A. Isothermal crystallization study of $Se_{70}Te_{28}Cd_2$ chalcogenide glass. *Physica Scripta* **54**, 207-209 (1996).

[110] Kolomogoroff, A. N. K statičeskoj tieorii kristallizacii mietallov. *Izwiestija Rossiiskoi Akademii Nauk SSSR Seria Matematiceskaja* **3**, 355-359 (1937).

[111] Donald, I. W. Crystallization kinetics of a lithium zinc silicate glass studied by DTA and DSC. *Journal of Non-Crystalline Solids* **345&346**, 120–126 (2004).

[112] Chen, H. S. A method for evaluating viscosities of metallic glasses from the rates of thermal transformations. *Journal of Non-Crystalline Solids* **27**, 257-263 (1978).

[113] Šatava, V. Mechanism and kinetics from non-isothermal TG traces. *Thermochimica Acta* **2**, 423-428 (1971).

[114] Krupka, J.; Derzakowski, K.; Riddle, B.; Jarvis, J. B. A dielectric resonator for measurements of complex permittivity of low loss dielectric materials as a function of temperature. *Measurement Science and Technology* **9**, 1751–1756 (1998).

[115] Sevim, F.; Demir, F.; Bilen, M.; Okur, H. Kinetic analysis of thermal decomposition of boric acid from thermogravimetric data. *Korean Journal of Chemical Engineering* **23**, [5] 736-740 (2006).

[116] Iddles, D. M.; Bell, A. J.; Moulson, A. J. Relationships between dopants, microstructure and the microwave dielectric properties of ZrO_2–TiO_2–SnO_2 ceramics. *Journal of Materials Science* **27**, 6303–6310 (1992).

[117] Silverman, B. D. Microwave absorption in cubic strontium titanate. *Physical Review* **125**, [6] 1921-1930 (1962).

[118] Valant, M.; Suvorov, D. Microstructural phenomena in low-firing ceramics. *Materials Chemistry and Physics* **79**, 104-110 (2003).

[119] Mori, N.; Sugimoto, Y.; Harada, J.; Higuchi, Y. Dielectric properties of new glass-ceramics for LTCC applied to microwave or millimeter-wave frequencies. *Journal of the European Ceramic Society* **26**, 1925-1928 (2006).

[120] Došler, U.; Kržmanc, M. M.; Suvorov, D. The synthesis and microwave dielectric properties of $Mg_3B_2O_6$ and $Mg_2B_2O_5$ ceramics. *Journal of the American Ceramic Society* **93**, [11] 3788-3792 (2010).

[121] Hennings, D. F. K.; Janssen, R.; Reynen, P. J. L. Control of liquid-phase-enhanced discontinuous grain growth in barium titanate. *Journal of the American Ceramic Society* **70**, 23–27 (1987).

[122] Došler, U.; Kržmanc, M. M.; Jančar, B.; Suvorov, D. A high-Q microwave dielectric material based on $Mg_3B_2O_6$. *Journal of the European Ceramic Society* **30**, 413-418 (2010).

[123] Rečnik, A.; Čeh, M.; Kolar, D. Polytype induced exaggerated grain growth in ceramics. *Journal of the European Ceramic Society* **21**, 2117-2121 (2001).

[124] Randle, V. *Microtexture Determination and its Applications* (Institute of Materials, Minerals and Mining, 2nd edition, London, 2003).

[125] Loretto, M. H. *Electron Beam Analysis of Materials* (Chapman and Hall, London, 1984).

[126] Chiang, C. C.; Wang, S. F.; Wang, Y. R.; Wei, W. C. J. Densification and microwave dielectric properties of $CaO–B_2O_3–SiO_2$ system glass - ceramics. *Ceramics International* **34**, 599-604 (2008).

[127] Wang, S. H.; Zhou, H. P. Densification and dielectric properties of $CaO-B_2O_3-SiO_2$ system glass ceramics. *Materials Science and Engineering* **B99**, 597-600 (2003).

[128] Marques, V. M. F.; Tulyaganov, D. U.; Agathopoulos, S.; Ferreira J. M. F. Low temperatures production of glass ceramics in the anorthite-diopside system via sintering and crystallization of glass powder compacts. *Ceramics International* **34**, 1145-1152 (2008).

[129] Beall, G. H. Refractory glass – ceramics based on alkaline earth aluminosilicates. *Journal of the European Ceramic Society* **29**, 1211–1219 (2009).

[130] Seo, Y. J.; Shin, D. J.; Cho, Y. S. Phase evolution and microwave dielectric properties of lanthanum borate-based low-temperature co-fired ceramics materials. *Journal of the American Ceramic Society* **89**, [7] 2352-2355 (2006).

[131] Ray, C. S.; Day, D. E. Determining the nucleation rate curve for lithium disilicate glass by differential thermal analysis. *Journal of the American Ceramic Society* **73**, [2] 439-442 (1990).

[132] Li, W.; Mitchell, B. S. Nucleation and crystallization in calcium aluminate glasses. Journal of Non-Crystalline Solids **255**, 199-207 (1999).

[133] Ray, C. S.; Huang, W.; Day, D. E. Crystallization kinetics of a Lithia-Silica glass: effect of sample characteristics and thermal analysis measurements techniques. *Journal of the American Ceramic Society* **74**, [1] 60-66 (1991).

[134] Azough, F.; Freer, R.; Wang, C. L.; Lorimer, G. W. The relationship between the microstructure and microwave dielectric properties of zirconium titanate ceramics. *Journal of Materials Science* **31**, 2539-2549 (1996).

[135] Zhang, S. X.; Li, J. B.; Cao, J.; Zhai, H. Z.; Zhang, B. Preparation, microstructure and microwave dielectric properties of $Zr_xTi_{1-x}O_4$ (x=0.40–0.60) ceramics. *Journal of European Ceramic Societ* **21**, 2931–2936 (2001).

[136] Kashif, I.; Soliman, A. A.; Farouk, H.; Sanad, A. M. Effect of titanium addition on crystallization kinetics of lithium borosilicate glass. *Journal of Alloys and Compounds* **475**, [1-2] 712-717 (2009).

[137] Höland, W.; Wange, P.; Naumann, K.; Vogel, J.; Carl, G.; Jana, C.; Götz, W. J. Control of phase formation processes in glass-ceramics for medicine and technology. *Journal of Non-Crystalline Solids* **129**, 152-162 (1991).

[138] Carl, G.; Höche, T.; Voigt, B. Crystallisation behaviour of a MgO-Al_2O_3-SiO_2-TiO_2-ZrO_2 glass. *Physics and Chemistry of Glasses* **43C**, 256-258 (2002).

[139] Lacerda, S. R.; Oliveira, J. M.; Correia, R. N.; Fernandes, M. H. V. TiO_2-induced phase separation and crystallization in SiO_2-$3CaOP_2O_5$-MgO glass. *Journal of Non-Crystalline Solids* **221**, 255-260 (1997).

[140] Yoon, S. H.; Kim, D. W.; Cho, S. Y.; Hong, K. S. Phase analysis and microwave dielectric properties of LTCC TiO_2 with glass system. *Journal of the European Ceramic Society* **23**, 2549–2552 (2003).

Index of Figures

Index of Tables

Appendix

Original scientific article

1. DOŠLER, Urban, MAČEK, Marjeta, JANČAR, Boštjan, SUVOROV, Danilo. A high-Q microwave dielectric material based on $Mg_3B_2O_6$. *J. Am. Ceram. Soc.*, 2010, vol. 93, no. 11, str. 3788-3792.

2. DOŠLER, Urban, MAČEK, Marjeta, SUVOROV, Danilo. The synthesis and microwave dielectric properties of $Mg_3B_2O_6$ and $Mg_2B_2O_5$ ceramics. *J. Eur. Ceram. Soc.*. [Print ed.], 2010, vol. 30, no. 2, str. 413-418.

Published scientific conference contribution

3. DOŠLER, Urban, MAČEK, Marjeta, SUVOROV, Danilo. Nucleation and crystallization of MgO-B_2O_3-SiO_2 glass. V: First International Conference for Students and Young Scientists on Materials Processing Science, 10-13 October 2010, Tbilisi, Georgia. *Programme and book of manuscripts*. [S. l.]: Georgian Ceramic Society, 2010, str. 126-130.

Published scientific conference contribution abstract

4. DOŠLER, Urban, UDOVIČ, Marko, SUVOROV, Danilo. Sinteza in dielektrične lastnosti stekel v MgO-B_2O_3-SiO_2 sistemu = Processing and dielectric properties of glasses from the MgO-B_2O_3-SiO_2 system. V: JENKO, Monika (ur.). 15. konferenca o materialih in tehnologijah = 15th Conference on Materials and Technology, 8-10 October, 2007 Portorož, Slovenia. *Program in knjiga povzetkov*. Ljubljana: Inštitut za kovinske materiale in tehnologije], 2007, str. 34.

5. DOŠLER, Urban, MAČEK, Marjeta, UDOVIČ, Marko, SUVOROV, Danilo. The synthesis and dielectric properties of $Mg_3B_2O_6$ and $Mg_2B_2O_5$. V: Electroceramics XI, August 31 - September 4,2008, Manchester, UK. *Abstracts and CD proceedings*. [S. l.: s. n.], 2008.

6. DOŠLER, Urban, MAČEK, Marjeta, UDOVIČ, Marko, SUVOROV, Danilo. The synthesis and dielectric properties of the glass ceramic composite $MgO-B_2O_3-SiO_2$. V: USKOKOVIĆ, Dragan (ur.). Tenth Annual Conference of the Yugoslav Materials Research Society YUCOMAT 2008, Herceg Novi, Montenegro, September 8-12,2008. *Programme and the book of abstracts*. Belgrade: Institute of Technical Sciences of SASA, 2008, str. 98.

7. DOŠLER, Urban, MAČEK, Marjeta, UDOVIČ, Marko, SUVOROV, Danilo. Dielektrične lastnosti rekristaliziranega stekla na osnovi $MgO-B_2O_3-SiO_2$ = Dielectric properties of recrystallized glass in the $MgO-B_2O_3-SiO_2$. V: GLAVIČ, Peter (ur.), BRODNJAK-VONČINA, Darinka (ur.). Slovenski kemijski dnevi 2008, Maribor, 25. in 26. september 2008. *Zbornik povzetkov referatov s posvetovanja*. Maribor: FKKT, 2008, str. 33.

8. DOŠLER, Urban, MAČEK, Marjeta, SUVOROV, Danilo. The correlation between the dielectric losses and the grain size of $Mg_3B_2O_6$ ceramics. V: 11th International Conference and Exhibition of the European Ceramic Society, Krakow, 21-25 June 2009. *Conference programme and book of abstracts*. Krakow: ECERS, 2009, str. 80.

9. DOŠLER, Urban, MAČEK, Marjeta, SUVOROV, Danilo. Sinteza in mikrovalovne dielektrične lastnosti $Mg_3B_2O_6$ in $Mg_2B_2O_5$. V: ISKRA, Jernej (ur.), MILOŠEV, Ingrid (ur.). *Dan mladih raziskovalcev 2009*. Ljubljana: Institut "Jožef Stefan", 2009, 1 str.

10. DOŠLER, Urban, MAČEK, Marjeta, SUVOROV, Danilo. Low-temperature sintering and microwave dielectric properties of $MgO-B_2O_3-SiO_2$ - based glass ceramics. V: SRDIĆ, Vladimir V. (ur.), RANOGAJEC, Jonjaua (ur.). The Eighth Students' Meeting Processing and Application of Ceramics, SM 2009, December 2-5, 2009, Novi Sad, Serbia. *Programme and book of abstracts*. Novi Sad: Faculty of Technology, University of Novi Sad, 2009, str. 14.

11. DOŠLER, Urban, MAČEK, Marjeta, SUVOROV, Danilo. Sooodvisnost dielektričnih izgub in velikosti zrn v $Mg_3B_2O_6$ keramiki = The correlation between the dielectric losses and the grain size of $Mg_3B_2O_6$. V: GLAVIČ, Peter (ur.), BRODNJAK-VONČINA, Darinka (ur.). *Zbornik povzetkov referatov s posvetovanja*. Maribor: FKKT, 2009, str. 34.

12. BRAČKO, Ines, VEBER, Asja, OTONIČAR, Mojca, ŠETINC, Tina, DOŠLER, Urban, ŽUNIČ, Vojka. Predstavitev mladih raziskovalcev Odseka za raziskave sodobnih materialov. V: ŠETINA, Barbara (ur.), JUNKAR, Ita (ur.), KALUŽA, Boštjan (ur.), ELERŠIČ, Kristina (ur.). 1. študentska konferenca Mednarodne podiplomske šole Jožefa Stefana, 19. - 20. maj 2009, Ljubljana, Slovenija = 1st Jožef Stefan International Postgraduate School Student's Conference, 19th - 20th May 2009, Ljubljana, Slovenia. *Zbornik prispevkov*. Ljubljana: Mednarodna podiplomska šola Jožefa Stefana, 2009, str. 8-9.

13. DOŠLER, Urban. Sinteza in dielektrične lastnosti steklo-keramike na osnovi MgO-B_2O_3-SiO_2 sistema. V: ŠETINA, Barbara (ur.), JUNKAR, Ita (ur.), KALUŽA, Boštjan (ur.), ELERŠIČ, Kristina (ur.). 1. študentska konferenca Mednarodne podiplomske šole Jožefa Stefana, 19. - 20. maj 2009, Ljubljana, Slovenija = 1st Jožef Stefan International Postgraduate School Student's Conference, 19th - 20th May 2009, Ljubljana, Slovenia. *Zbornik prispevkov*. Ljubljana: Mednarodna podiplomska šola Jožefa Stefana, 2009, str. 14-15.